2015

Signal Subspace Processing in the Beam Space of a True Time Delay Beamformer Bank

Nathan Allen Wilkins
Wright State University

SIGNAL SUBSPACE PROCESSING IN THE BEAM SPACE OF A TRUE TIME DELAY BEAMFORMER BANK

A dissertation submitted in partial fulfillment of the requirements for the degree of Doctor of Philosophy

By

Nathan A Wilkins
B.S., Southern Illinois University at Edwardsville, 1984
M.S., Texas Tech University, 1989

WRIGHT STATE UNIVERSITY

GRADUATE SCHOOL

May, 2015

I HEREBY RECOMMEND THAT THE DISSERTATION PREPARED UNDER MY SUPERVISION BY Nathan A Wilkins ENTITLED Signal Subspace Processing in the Beam Space of a True Time Delay Beamformer Bank BE ACCEPTED IN PARTIAL FULFILLMENT OF THE REQUIREMENTS FOR THE DEGREE OF Doctor of Philosophy.

Arnab K. Shaw, Ph.D.
Dissertation Director

Ramana Grandhi, Ph.D.
Ph.D. in Engineering Program Director

Robert E. W. Fyffe, Ph.D.
Dean, Graduate School

Committee on Final Examination

Arnab K. Shaw, Ph.D.

Kefu Xue, Ph.D.

Marty Emmert, Ph.D.

Ronald G. Riechers, Ph.D.

Mohsin Jamali, Ph.D.

ABSTRACT

Wilkins, Nathan Allen, Engineering Ph.D. Program, Department of Electrical Engineering, Wright State University, 2015. Signal Subspace Processing in the Beam Space of a True Time Delay Beamformer Bank.

A number of techniques for Radio Frequency (RF) source location for wide bandwidth signals have been described that utilize coherent signal subspace processing, but often suffer from limitations such as the requirement for preliminary source location estimation, the need to apply the technique iteratively, computational expense or others. This dissertation examines a method that performs subspace processing of the data from a bank of true time delay beamformers. The spatial diversity of the beamformer bank alleviates the need for a preliminary estimate while simultaneously reducing the dimensionality of subsequent signal subspace processing resulting in computational efficiency. The pointing direction of the true time delay beams is independent of frequency, which results in a mapping from element space to beam space that is wide bandwidth in nature. This dissertation reviews previous methods, introduces the present method, presents simulation results that demonstrate the assertions, discusses an analysis of performance in relation to the Cramer-Rao Lower Bound (CRLB) with various levels of noise in the system, and discusses computational efficiency. One limitation of the method is that in practice it may be appropriate for systems that can tolerate a limited field of view. The

application of Electronic Intelligence is one such application. This application is discussed as one that is appropriate for a method exhibiting high resolution of very wide bandwidth closely spaced sources and often does not require a wide field of view. In relation to system applications, this dissertation also discusses practical employment of the novel method in terms of antenna elements, arrays, platforms, engagement geometries, and other parameters. The true time delay beam space method is shown through modeling and simulation to be capable of resolving closely spaced very wideband sources over a relevant field of view in a single algorithmic pass, requiring no course preliminary estimation, and exhibiting low computational expense superior to many previous wideband coherent integration techniques.

TABLE OF CONTENTS

LIST OF FIGURES

LIST OF TABLES

ACKNOWLEDGEMENT

I would like to acknowledge the support and guidance of my dissertation advisor, mentor and friend, Dr. Arnab Shaw. His seminal work in this field, depth of understanding in a broad range of related areas and relentless pursuit of rigor made this work possible. Throughout the process he was always thorough, challenging, and persistent in driving home the idea that mediocrity was unacceptable. That persistence challenged me to continually improve the research and documentation so that it ultimately formed a result of which I am proud. His contribution to the development of the theory was indispensible. I thank each of my other committee members, who all had important and useful suggestions that improved this dissertation: Dr. Kefu Xue, Dr. Marty Emmert and Dr. Ronald Riechers, all of Wright State University. I especially thank also my committee member from the University of Toledo, Dr. Mohsin Jamali, who contributed substantially to the work, having participated as visiting summer faculty in my office. His contribution is very much appreciated and complimented the theory developed herein quite nicely. I thank the many fellow students at Wright State and the University of Toledo, my many colleagues at the Air Force Research Laboratory too numerous to mention, but very much integral to the process of research and development.

This research is the culmination of many years of stimulating discussions, influences of related developments, trial and error, going back to the drawing board, rigorous improvement, and pressing on in the face of struggles when I could have easily given up. I sincerely thank the United States Air Force, Wright State University and the Dayton Area Graduate Studies Institute for financial support without which this effort would not have been possible. I would be remiss in not acknowledging the support of family and friends who contributed in so many ways and put up with way too much grief while I struggled through this process.

DEDICATION

I dedicate this work first and foremost to God. My faith in him has guided my every move. I dedicate it also to my wife, Melissa, who has stayed by my side throughout every struggle and victory; to my children, Nathan Allen, Jr., Joshua David and Daniel Russell; to my parents who supported me in so many ways; to all my friends along the way who made a difference by offering prayers, kind words, encouragement and sometimes tough love that made the difference. This work was only possible due to all of your help and support.

1 INTRODUCTION

1.1 Motivation

This dissertation examines signal-processing aspects of the Direction Finding (DF) problem for wide bandwidth Radio Frequency (RF) sources. The DF problem in this context involves processing of the data received on an array of antennas in the far field of the emission sources. Recent advances in a variety of fields such as radio transmission, digital signal processing, information technology and others have resulted in the proliferation of wideband systems. Along with this proliferation has come a corresponding need to locate such emission sources. This dissertation presents a novel technique for efficient high-resolution DF using signal subspace processing in the beam space of a true time delay beamforming bank. A beamformer bank block diagram is shown in Fig. 1. The antenna array contains M elements and the beamformer bank contains K beamformers. Each beamformer is characterized by time delays, $\tau_{B:m,k}$, and weights, w_m, from each element to be defined.

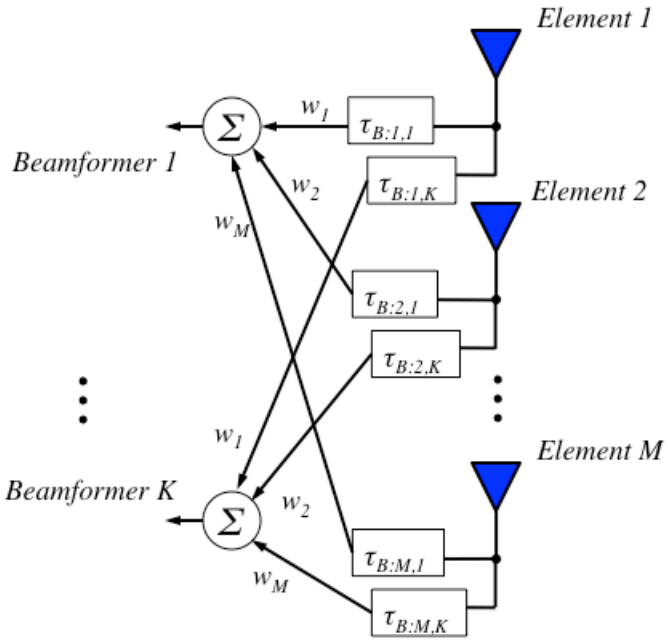

Fig. 1. Block diagram of a true time delay beamformer bank.

An example military application for such a system is an airborne array designed to receive radio frequency signals from sources beyond the range of enemy anti-aircraft missiles. Fig. 2 depicts a top view of a generic large-body aircraft line drawing of the type that could support such a Signals Intelligence (SIGINT) application. The antenna array could be mounted on the side of the aircraft fuselage inside a radio transparent structure called a radome. Operator workstations connected to receivers and signal-processing equipment could be housed inside the aircraft.

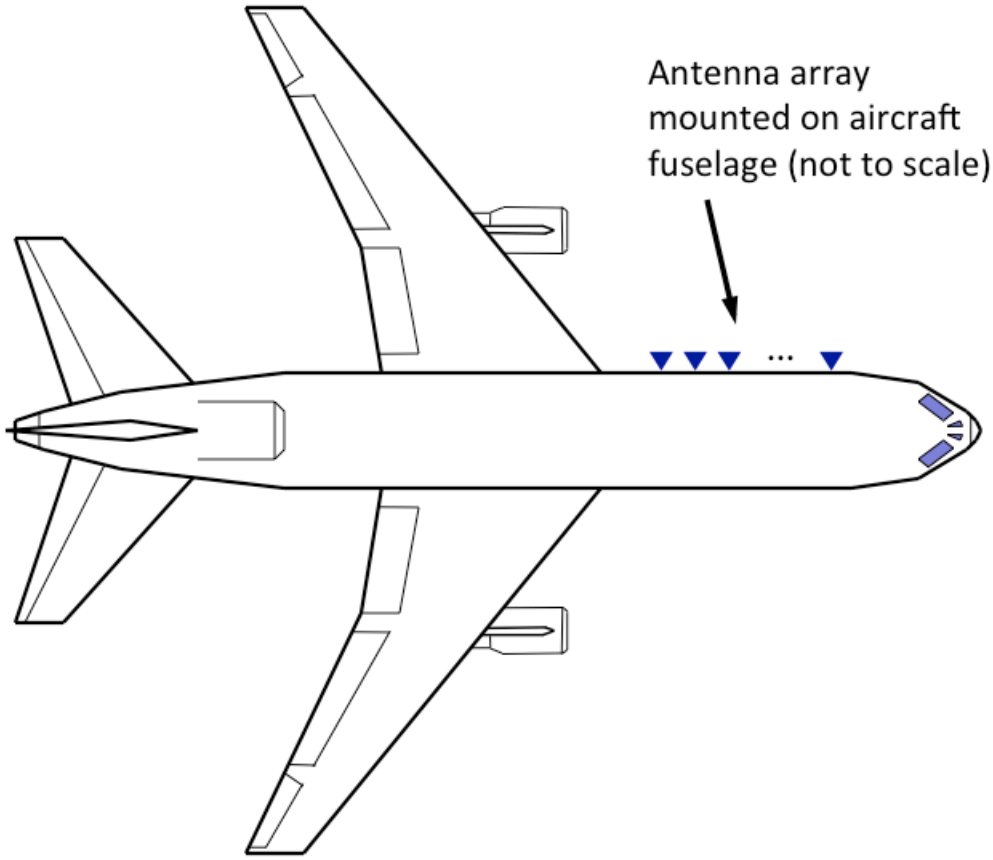

Fig. 2. Generic large body aircraft with antenna array.

Fig. 3 shows a depiction of a mission geometry consistent with this type of aircraft. The airborne array receives signals such as those being emitted by the ground-based radar sources shown. The radars may be deployed in a defensive position such as along a coastline to contribute to the search, acquisition, tracking and guidance for surface-to-air missile systems. The airborne receive array has a characteristic field of view for which it is designed. The field of view is a circular sector whose center is at the receive array and which is associated with some reference radial line segment from which angles of arrival are measured. Angles of arrival are angles between the lines from the

sources to the airborne array and the defined reference line. Typically the reference line for angle measurement may be the line extending straight out the front of the aircraft with the array boresight being at 90° azimuth as shown. Note that the standoff range is defined to be that which is large enough that enemy anti-aircraft missiles cannot reach the aircraft.

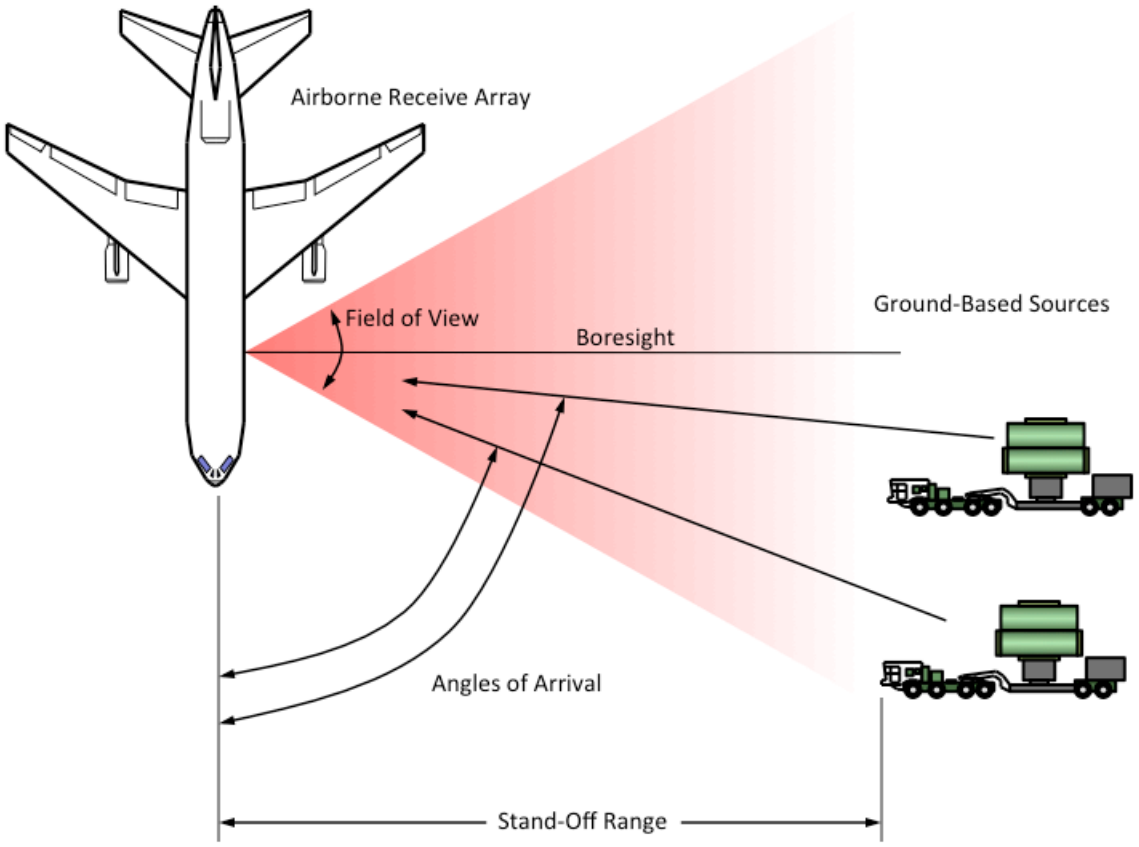

Fig. 3. Example Mission Geometry (not to scale).

The SIGINT mission to locate and characterize emission sources depends on the capability to spatially resolve closely spaced sources and potentially extract signal

characteristics in a cluttered and noisy spectral environment. Signals of wide instantaneous bandwidth in particular may be difficult to detect and resolve at long ranges using conventional techniques [1].

In recent years wideband RF signals have proliferated and reasons for their utilization are numerous. In the communications field, the handheld devices and smart phones often rely on spreading codes to permit multiple users to access the same frequency channel [2]. The bandwidth of the signal is purposefully increased beyond that required to transmit the embedded information in order to permit multiple users to access the same channel. For data transfer purposes, the demand for bandwidth intensive applications such as streaming video to portable devices has precipitated an enormous growth in wideband cellular infrastructure worldwide, typically referred to as 3G and 4G wireless networks [3].

In the radar field, signal bandwidth is directly related to range resolution. The radar signal's bandwidth can be increased simply by decreasing the length of the transmitted pulse, but this implies a corresponding increase in *instantaneous* transmit power in order to maintain range according to the radar range equation [4]. Radar system designers realized early on that the instantaneous power requirement could be moderated by spreading the power over time by modulating the pulse with a changing frequency, such as Linear Frequency Modulation (LFM), commonly known as a chirp signal. Other types of wideband radar signals in use today include phase code modulation and long codes made up of low power wideband pulses and frequency

hopping (rapidly changing carrier frequency synchronized between transmitter and receiver). A so-called fast hopper could change carrier frequencies many times within the time of a pulse length using a pseudorandom pattern. For a receiver that does not have the advantage of a priori knowledge of the hop pattern, the system designer may require the system to receive the entire hopped bandwidth through the intermediate frequency. Even if the frequencies can be tracked and digitally processed separately after analog to digital conversion, certain applications may be ineffective unless the response to energy in multiple frequency bins can be coherently integrated [5].

In military communications or other covert applications, users often desire to freely transmit data, signals or carry on communications while still making it difficult for an unfriendly entity to detect the transmission. A wideband signal can often successfully operate at or below the noise level as long as the intended user has knowledge of the way the signal was spread in frequency in order to perform some type of detection, such as a matched filter. Wide bandwidth techniques are thus frequently part of a tactic to reduce the probability that the signal will be detected and processed by unfriendly forces. This tactic is known as Low Probability of Intercept/Low Probability of Detection (LPI/LPD). Signal types that incorporate bandwidth broadening for the purpose of avoiding detection include modulation with noise-like codes, Gaussian pulses and frequency hopping [6].

Chirp radars exhibit high range resolution by compressing the transmitted pulses in time when they are received. The figure of merit typically associated with pulse

compression is the compression ratio, or the related time bandwidth product. Sidney Darlington at Bell Labs received a patent for Chirp radar in the year 1954 in which he published a time bandwidth product of 34 [7]. The Massachusetts Institute of Technology Lincoln Laboratory (MIT-LL) was a pioneer in the field of chirp radar technology. MIT-LL engineers were instrumental in the development of surface acoustic wave devices for radar signal processing applications that achieved time bandwidth products up to 1500 by the year 1972 [8]. Today, time bandwidth products in excess of one million are common [7].

The capability to generate and process ever-broadening bandwidths has been fueled by dramatic increases in processing power. MIT-LL was also instrumental in the development of digital signal processing for radar pulse compression. The Lincoln Laboratory Digital Convolver System (DCS) achieved time bandwidth products in excess of 4000 by the year 1979 and was roughly the size of several racks of equipment [9]. Although the first digital systems proved to be quite bulky, digital signal processing integrated circuits soon developed at manufacturers to include Texas Instruments whose TMS320Cxx series of chips became a staple in the industry [10]. Today, the Field Programmable Gate Array (FPGA) technology is gaining a prominent role in the digital signal processing discipline due to the power and flexibility in being able to readily reconfigure a dense array of digital processing elements. For example one of the recent more capable FPGA devices currently available from the Xilinx Corporation, the Virtex-6 XC6VLX760 device, contains $758{,}784$ configurable logic cells on a single device [11].

Fig. 4 depicts a chirp pulse in the time domain. The change in frequency of the signal from low to high as time increases is easily seen in this example. In general, a chirp signal need not vary the frequency linearly, but this example does implement LFM. It also has a window applied that defines the pulse envelope. This has implications for facilitation of the physical realization and helps reduce certain undesirable effects such as ringing in the frequency domain.

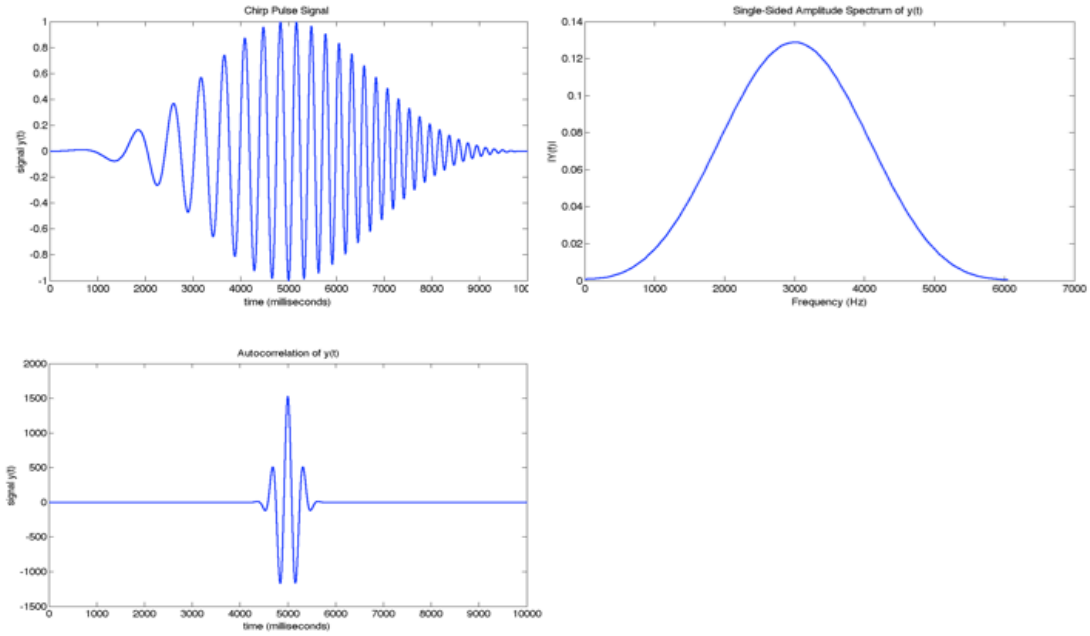

Fig. 4. Chirp pulse example.

The spectral representation of the LFM pulse is shown in the upper right plot of Fig. 4 and the autocorrelation of the chirp pulse is shown in the lower left. The

autocorrelation is an indication of the typical pulse compression performance that can be expected from this type of signal. Note that in Fig. 4 the pulse and its autocorrelation are plotted on the same time scale so the compression of the pulse from the broad LFM pulse to the compressed autocorrelation function is clearly indicated. This phenomenon is exploited to great effect in high-resolution radar where the narrow pulse compressed returns provide a much more precise indication of range than would be possible from a narrow bandwidth signal.

The spectrum of the windowed chirp signal exhibits a broad smooth spectrum in the frequency domain that may be desirable for many high-resolution radar applications, but difficult for conventional narrow bandwidth receivers to detect and track if the frequency modulation is unknown. Applications that require detection and tracking of signals without prior knowledge of modulation characteristics include SIGnals INTelligence (SIGINT) systems that attempt to passively characterize unfriendly RF emitters, often from long ranges. The general category of SIGINT includes both COMmunications INTelligence (COMINT) for communications signals and ELectronic INTelligence (ELINT) for radar signals [12].

The Defense Advanced Research Projects Agency (DARPA) performed a review of the state of the art in Ultra-Wideband (UWB) technology in 1990 [13]. DARPA defined UWB as any signal whose total bandwidth is greater than or equal to 25% of the center frequency. The signal property of the ratio of bandwidth to center frequency is termed fractional bandwidth. Wideband signals are those with fractional bandwidth between

1% and 25%, while those with fractional bandwidth less than or equal to 1% are considered narrowband [13].

Another class of wideband signals is represented by a Gaussian impulsive type signal. These types of signals rely on the well-known Fourier analysis principle that a perfect impulse possesses infinite bandwidth. They commonly achieve fractional bandwidths well in excess of 25% [14]. Examples of Gaussian impulses of different lengths along with their corresponding spectra are shown in Fig. 5. The system designed using a psuedorandomly timed sequence of such ultra-wideband pulses is capable of high range resolution, has favorable propagation characteristics for many applications, is suitable for detection avoidance and is unlikely to interfere with other RF systems [14].

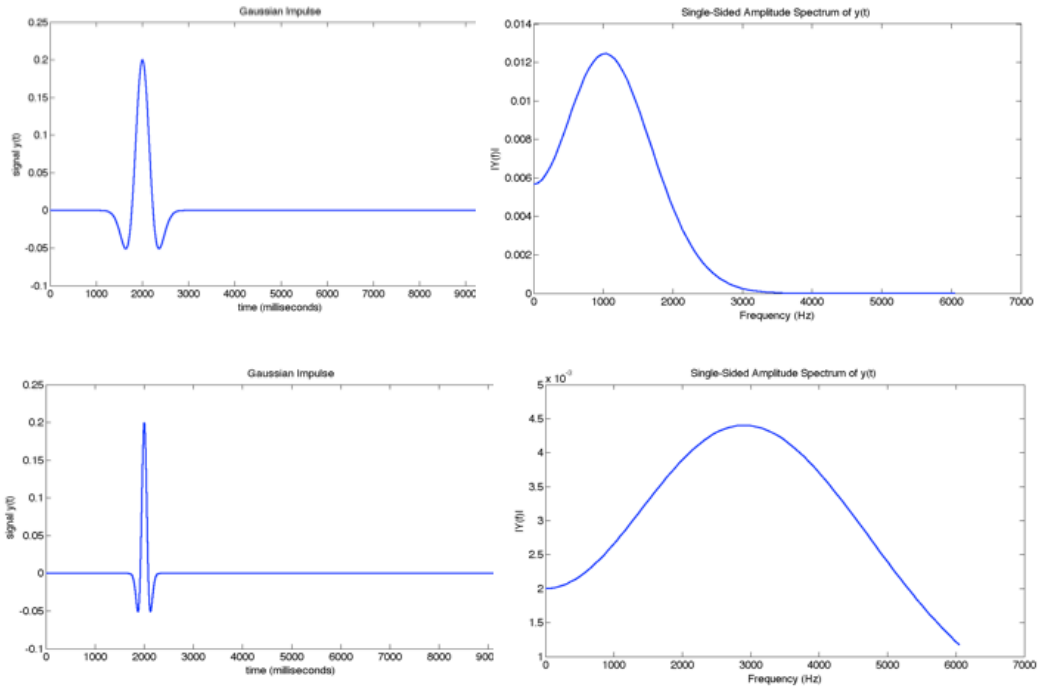

Fig. 5. Gaussian impulse example.

The spectra of the signals in Fig. 5 are shown on the right side of the figure. These signals are sometimes used in systems due to the smooth characteristic of the spectrum and relative ease with which the time domain signal can be generated on a small time scale. Notice that the length of the time domain signal on the bottom of Fig. 5 is shortened in time but the spectrum becomes wider. In recent years, these types of signals have been used in many new low transmit power, short range applications in the automotive, security, appliances, manufacturing and other industries. Typical applications are low power because the power must be concentrated in the impulse

rather than spread in time as in some other pulse types [15].

One advantage of ultra-wideband impulses is their characteristic to tend to be able to penetrate various solid materials. Since the radiated emission is not concentrated within a narrow frequency band that may be particularly susceptible to attenuation in a given type of material, it is generally accepted to possess a greater probability of penetration through a wider variety of materials than a narrowband emission [16].

Lawrence Livermore National Laboratory (LLNL) has developed the Micropower Impulse Radar (MIR) that was spawned as an offshoot of their research in digital transient sampling of nuclear events. The research has resulted in small low cost transmitter and receiver modules that have been licensed to commercial developers for many applications. The MIR utilizes wideband impulsive type signals. A summary of several claimed application areas is shown in Table 1 that was presented in [16]. Such proliferation of wideband signals for numerous applications is significant because overlapping broadband sources often appear to other broadband receivers as a general increase in the noise floor [2]. Applications such as SIGINT must contend with this complex environment as they attempt to locate various sources, characterize them and determine which may have military significance [1], [5].

TABLE 1

APPLICATIONS OF THE LLNL MICROPOWER IMPULSE RADAR

Commercial Sector	Applications
Automotive	Parking assistance; backup warning; precollision detection; cruise control; airbag deployment; electronic dipstick
Security	Home intrusion and motion sensing; keyless locks; automatic doors; child monitoring; vehicle theft alarm; radar trip wire; perimeter surveillance
Appliances	Stud finder; wireless thermostat; automatic dispenser; automatic tool shutoff; gaming
Manufacturing	Fluid level monitoring; proximity sensing; robotic sensing; industrial automation

Other types of wideband signals include spread spectrum communication systems that commonly incorporate Code Division Multiple Access (CDMA) that spreads waveform bandwidth by direct modulation with a spreading code and wideband radars that utilize coded phase modulation, frequency hopping, or other means to spread the spectrum in an effort to intentionally render them difficult to detect and process by non-cooperative systems [17].

The need to locate the sources of wideband signals results from their proliferation in the fields of consumer communications, data transfer, radar and other applications. Law enforcement agencies use source location methods to locate stolen items or wanted individuals known to use particular wireless devices [18]. In military applications, some weapons are designed to guide to the location of an emission source [19]. Intelligence, Surveillance and Reconnaissance (ISR) military platforms use RF

source location to track emitters and in conjunction with beamforming to mitigate co-channel interference [20]. Location of mobile CDMA devices for Emergency-911, smart antennas or other applications has been one area of research and development [21]. Modern LPI radars may be designed to incorporate so called “war modes” whose emission characteristics have remained unobserved during system tests [22]. In future battlefield scenarios, reliable efficient methods for detection and estimation of wideband emitter parameters will be essential to maintaining accurate Electronic Order of Battle (EOB) data [23]. One of the most important emitter parameters is the Angle of Arrival (AOA) since it is frequently used to determine locations of emitters of interest. The process of determining the AOA of an electro-magnetic wave is frequently referred to as radio Direction Finding (DF) [24].

With wideband signals increasing in the RF environment, wideband source location is a growing need for civil and military users, but many common phase measurement based methods are inherently narrowband in nature [25]. Many efforts to extend narrowband signal processing techniques to wideband simply apply the narrowband technique repetitively across multiple sub-bands, adding cumbersome complexity, computational expense and cost to the system [26].

This dissertation introduces methods to perform source location processing at the output of a bank of true time delay beamformers. The true time delay beamformers simultaneously introduce spatial diversity and frequency independence [27]. This permits the system to maintain its wideband nature while performing spatial processing

to locate emission sources. Unlike many previous methods that rely on frequency domain concepts such as sub-banding and coherent recombination of sub-bands using transformation matrices, the novel methods introduced here operate primarily in the time domain. Depending on the particular system design, the number of beamformers could be less than the number of antenna elements, effectively reducing the number of channels that have to be processed and thus providing an advantage in terms of computational expense. Sections 1.2 through 1.4 contain some brief introductory remarks about related work. Some of these will be discussed in greater mathematical detail in 2.

1.2 Related Work in True Time Delay Beamforming

Beamforming is a process that separately adjusts the magnitude, phase, and/or time delay for signals received on multiple spatially displaced antennas then coherently sums the signals. The process results in an aggregate antenna beam pattern that differs from that of the individual antenna elements. The most common and readily implementable type of array antenna architecture is the phased array antenna for which the phase at each element is adjusted. Since phase at a single frequency is equivalent to a time delay, phased array antennas and time delay beamformers have comparable performance for narrow bandwidth operation. Since phase is frequency dependent, phased array antennas suffer from the phenomenon referred to as beam squint for wide bandwidth

operation. Beam squint manifests as a change in the beam direction at different frequencies. Since true time delays are not frequency dependent, True Time Delay (TTD) beamforming minimizes beam squint and is suitable for wide bandwidth operation.

W. F. Gabriel at the Naval Research Laboratory laid out much of the groundwork for true time delay beamforming [28], [29], [30], [31]. Gabriel had previously described the application of high-resolution techniques that had been developed for spectral estimation to the spatial source location problem [28]. Subsequently he developed criteria for versatile RF array systems with large baselines for good resolution and few degrees of freedom to maintain efficient processing [29], [30], [31]. These criteria along with others that will be considered in greater mathematical detail in Section 2.6 of this document led Gabriel to conclude that TTD beamforming would be required to achieve the desired performance at broad bandwidths.

TTD beamforming is fairly straightforward conceptually, but difficult to practically implement with precision for RF systems. This is due to the typical time delay differences and precision control in time delays between adjacent array elements being on the order of picoseconds or less. A numerical example of a typical time delay is presented in Section 2.6. As another example in the literature, [27] states that, "the most large time delay error of $1.6ps$ corresponds to the radiation angle error of $2.1°$ from the main beam direction of $28.7°$." for an $x-band$ radar application. Among the concepts for achieving practical implementation of TTD beamforming systems are

optical and acousto-optical architectures. Gesell and colleagues have led much of the research in this area. They used an acousto-optic Bragg cell as a continuous delay line that was tapped at selected points to provide the time delay output. A prototype system of this type was constructed and demonstrated [32], [33], [34].

Some more recent efforts have focused on development of miniature hardware modules for TTD implementation such as Monolithic Microwave Integrated Circuit (MMIC) modules. TTD modules developed by the Air Force Research Laboratory (AFRL) Sensors Directorate, Wright-Patterson Air Force Base, OH [35] and Cobham Sensor Systems, Richardson, TX [36] have been integrated into an aircraft pod to demonstrate a wideband beamforming capability. L3 ComCept, Rockwall, TX, performed the integration into their Miniature Reconfigurable Beamformer (MRB) cards. The pod, depicted in Fig. 6, is said to provide a $13\times$ size reduction, a $6\times$ reduction in weight, and $3.8\times$ less power than comparable TTD units currently fielded.

Fig. 6. True Time Delay (TTD) beamformer pod used to demonstrate wideband beamforming capability by the US Air Force Research Laboratory [image courtesy AFRL/RY Sensors Directorate].

Much of the work in TTD systems such as the beamformer pod shown in Fig. 6 has been hardware-oriented work that is focused on investigation into techniques that achieve the precise control of the time delays necessary for successful implementation. Private communication with a representative of the development team for this pod at the Air Force Research Laboratory (AFRL) indicated that testing on the integrated pod was primarily limited to measurement of formed beams with a single source. The team did not investigate DF algorithms or performance with multiple sources [37]. Much less is found in the literature that takes the approach of development of signal processing

algorithms that exploit the frequency invariant nature of TTD beamformer banks. Chen, Yao and Hudson's 2002 review article, [37], discussed wideband source location in the context of acoustic sensors. They mentioned time delay for acoustic arrays, but did not address coherent subspace processing that takes advantage of the frequency invariant beams. Wagner et al. provided a good representation for the sector of the literature that investigated algorithms for formation of single TTD beams [39]. Hussain presented a space-time processing approach that referenced TTD beamforming, but the formulation depended on a Gaussian impulse signal model such that the results do not necessarily apply to other signal types [40].

Gabriel's work as represented by [31] does involve significant signal processing for TTD beamforming systems. His focus involved side lobe cancellation whereby a reference beam was combined with adaptive nulls formed in beam space to result in beams of high signal to interference ratio for wide bandwidths. The formation of nulls in the direction of interfering signals utilized source location estimates, but he obtained these estimates in element space. Here element space is defined as the output data of the antenna array and beam space is defined as the output data of an array beamformer matrix [41]. The formulation did not explicitly address spatial spectra in TTD beam space [31]. Section 2.6 provides additional clarification of element space processes contrasted with beam space processes.

This dissertation builds on the previous work of primarily Hong, Russer [41], Gabriel [31], Burg [42], Schmidt [43], Wang and Kaveh [44] in their respective fields of wideband

beamformers, spatial signal processing, and wideband source location. It introduces methods to exploit the wideband nature of TTD beam space. It presents methods to formulate spatial spectra of high-resolution without the need for preliminary location estimation or iteration. We demonstrate that the simultaneous spatial diversity and wide bandwidth nature of the TTD beamformer bank provides the domain whereby high-resolution, low computational cost, wide bandwidth source location processing is achieved. This contribution will enhance TTD system capabilities by enabling efficient estimation of source locations for wideband systems.

1.3 Related Work in Narrow Bandwidth Signal Processing

Jenkins [45] and Lipsky [46] both provide good reviews of the general narrowband radio direction-finding problem. Gething also provides such a review and includes high-resolution as a significant component of the discussion [47]. Wax includes a thorough discussion of maximum likelihood estimation of superimposed signals [48]. Wax and Kailath expanded the discussion to include detection of the number of signals in a given data set by minimizing the information criteria for model selection, the information theoretic approach [49]. Kumaresan, Scharf and Shaw drew a connection between fitting exponential models and pole-zero modeling [50] and their resulting algorithm was validated by Bresler and Macovski who presented a unified framework for maximum likelihood estimation of superimposed signals that applied equivalently to

spectral estimation and array signal processing [51]. They pointed out that certain other methods based on modifications of algorithms that perform well with no noise are often sensitive to the added noise level. Their maximum likelihood formulation derived an expression in terms of the linear prediction polynomial of the signal [51].

Some seminal developments in narrowband spatial processing applicable to the source location problem include the high-resolution spectral analysis concepts introduced by Capon [52] and the covariance processing of Pisarenko [53]. Burg postulated that the most appropriate spectral estimate for a given data set is the one that possesses the maximum randomness, or maximum entropy, of any spectrum that is consistent with the data [42]. Reddi introduced the minimum norm method that is based on the Eigen decomposition of the data covariance matrix and subsequent solution of a polynomial equation with coefficients obtained from the Eigen vectors [54]. Tufts and Kumaresan further elaborated on the minimum norm method and discussed its benefits in performance in low signal-to-noise ratio scenarios and tendency to lack spurious detections [55]. Kay reviewed the state of the art in spectral estimation as of the writing of his well-known text [56]. Schmidt expanded on the signal subspace and noise subspace concepts. He also introduced the Multiple Signal Classification (MUSIC) subspace processing method that utilizes the noise subspace Eigen vectors [43]. Other significant developments include the Estimation of Signal Parameters via Rotational Invariance Techniques (ESPRIT) of Paulraj, Roy and Kailath, that relies on the rotational invariance property of arrays with translational invariance structures, such as pair-wise

matched, codirectional element doublets [57] and the Root-MUSIC variation of the MUSIC algorithm that represents a fast implementation for uniform linear arrays. Rao and Hari presented a thorough analysis of the performance of Root-MUSIC [58]. Numerous variations of these and other formulations for spatial processing for RF emitter location are extensive in the literature. Therrien also reviewed many of these topics and related ones in his text [59].

Stoica and Nehorai discussed the MUSIC algorithm in the context of operating in element space and beam space [60]. Their results are primarily applicable within the context of computational expense savings when operating in conventional beamformer beam space as opposed to element space without addressing bandwidth concerns. Recently Tidd, Zhao and Huang reported results of experiments with a variation of Stoica and Nehorai's beam space MUSIC using a circular array of narrow bandwidth elements [61]. This work reports performance results for beam space MUSIC comparable to the element space counterpart, but with a significant advantage in computational efficiency, but again is only described for the conventional narrow bandwidth case.

1.4 Related Work in Wide Bandwidth Spatial Signal Processing

For wide bandwidth specific spatial signal processing, important advances include the incoherent integration approach of Wax and Kailath [48], [49]. The incoherent

integration approach essentially entails executing some type of narrowband processing in multiple sub-bands prior to integration into a wideband result. Wang and Kaveh introduced the Coherent Signal Subspace (CSS) method, a technique to coherently transform data in multiple frequency bins to a reference frequency that can then be processed post-integration by a narrowband method [44], [62]. Following coherent integration, the data can be processed using a technique such as MUSIC. Unfortunately the data transformation from sub-bands to reference frequency relies on construction of transformation matrices that are focused around specific angles in the AOA spectrum determined by preliminary processing using conventional means. The results depend on the accuracy of the preliminary estimates and results for multiple focusing angles or inaccurate initial estimates may require iteration of the algorithm. Hung and Kaveh improved the technique by using unitary focusing matrices in the Rotational Signal Subspace (RSS) method [63]. The RSS technique performs the least squares minimization of the measurement norm between the transformed location matrix for each frequency bin and the focusing matrix subject to the unitary constraint. Shaw and Kumaresan [64] incorporated Henderson's rank reduction technique using a bilinear transformation [65] to overcome the need for a preliminary estimate. This technique incorporates an approximation that relies on closely spaced sensing elements rendering it impractical in some applications, however closely spaced elements can be useful for applications in which miniaturization is critical such as cell phones.

Krolik and Swingler introduced the steered covariance matrix method that was shown

to result in lower source location bias errors than CSS when errors are present in the transformation matrices, [66], [67]. The technique is computationally intensive however, requiring a covariance matrix computation for each bearing angle of interest. They later focused their research on spatial resampling to achieve frequency invariance [67]. Spatial resampling of a linear array entails utilization of uniform element spacing that varies by frequency resulting in array characteristics that are frequency invariant. An infinite number of array elements is unfortunately required to achieve perfect invariance using this technique. Optimization and interpolation can be used to achieve minimal errors in performance for a given finite array, but the technique once again becomes quite computationally intensive.

Lee applied frequency invariant beamforming matrices to wideband direction finding [68]. The technique uses reference beams with desired properties for a given array at a reference frequency, and then minimizes a measurement norm between the reference beams and beamforming matrices at other frequencies of interest. Once these beamforming matrices have been defined with similar characteristics at all frequencies of interest, the data can be transformed from element space to frequency invariant beam space. Lee then used the beam space data to perform CSS processing in a manner similar to previously published research [68]. The spatial sampling involved in the beamforming matrices alleviates the need for preliminary AOA estimation. Ward, Ding and Kennedy [69] extended the technique based on further frequency invariant techniques discussed by Ward, Kennedy and Williamson [70]. Their method is similar to

Lee's except that their beamforming matrix is composed of beam shaping Finite Impulse Response (FIR) filters that focus the beams in the time domain. The technique eliminates any need for frequency decomposition. It is a considerable improvement in efficiency over previous methods, but is generally only discussed in the context of linear arrays with limited fields of view. Hong, Demmel and Russer used a technique similar to Lee as well, but extended it to arbitrary arrays [71]. Ward and Abhayapala once again updated the beam space approach to include operation in the near field [72]. In [41], Hong and Russer combined spatial interpolation in a manner similar to the technique of Krolik and Swingler [66] with the beam space processing method. The subspace processing of this combination method does not take advantage of the full bandwidth of the beamforming matrices, but it is shown to result in higher resolution of closely spaces sources than some other methods for detected signals.

Valee and Kabal discussed some alternate approaches including least squares techniques [73], [74]. Their formulation is once again an extension of the CSS technique, but relies on the observation that if the product of the transformation matrix and its conjugate transpose is uniform over the frequency range of interest, then the focusing is lossless. This optimizes performance, but increases computational complexity as compared to many of the other methods. Agrawal and Prasad reviewed several of the signal subspace based techniques and harkened also to least squares and maximum likelihood approaches [75]. They show that an advantage in processing complexity can be obtained by considering only spatial aspects of the data rather than the spatio-

temporal framework of most formulations. They also show that although incomplete, spatial only modeling of the data can yield adequate results in many practical situations.

Several researchers have utilized a priori knowledge of specific signal types as an advantage in processing those signals [76], [77], [78], [79]. In particular, Gershman and Amin discussed AOA estimation for Frequency Modulated (FM) signals using the space time-frequency distribution approach [76]. Upon breaking the signals into their constituent components in space, time and frequency, this approach then uses techniques related to MUSIC to perform the AOA estimation. Feng, Zhao and Yin utilized chirplet-based transforms [77]. Cong and Zhuang considered a hybrid Time Direction of Arrival (TDOA) and AOA approach for direct sequence spread spectrum type signals [78]. Gelli and Izzo considered signals that exhibit cyclostationarity as many man-made signals do [79].

A number of other developments in wideband AOA estimation have occurred. Delmas and Meurisse evaluated the performance of various narrowband approaches in processing wideband data [80]. Hawkes and Nehorai [81] analyzed arrays of vector sensors, as did Chen and Zhao [82]. In [81], the authors discuss fast wideband algorithms for vector sensor arrays and consider performance limits in this context. Chen and Zhao formalized a vector sensor construct for CSS processing by extending the theory to the vector case and showing that a straightforward extension of the scalar transformation focusing matrices is sufficient in the vector case [82]. Yoon, Kaplan and McClellan extend wideband AOA estimation to the case of arbitrarily shaped arrays, but

their formulation is based on the computationally complex approach of forming signal and noise subspaces for each of many frequency bins, then combining them incoherently [83]. In a related topic, several researchers have studied tracking of the AOA for multiple wideband moving targets. These include Yan and Fan who exploited the cyclostationary signal property for a least squares tracking algorithm as well as a Kalman filter [84]. El-Keyi, Kirubarajan and Gershman tracked the adaptive wideband beamformer weights with an extended Kalman filter [85]. Sellone updated the RSS technique and provided an excellent review of many of the preceding methods [86]. He showed that the RSS technique results in a family of solutions rather than a unique solution for the case where the number of antenna elements is greater than the number of sources. His solution, the Robust Coherent Signal Subspace Method (R-CSM), exploited this extra dimensionality to include additional constraints to build robustness to AOA into the process. In this way, he was able to alleviate the need for preliminary AOA estimation, but once again, the method has increased computational expense when compared to CSS due to the additional iterations introduced to obtain robustness [86].

This dissertation extends signal subspace array processing methods to a form that operates in the beam space of a true time delay beamformer bank. These extensions are described in section 3. The methods presented provide the advantage of resolution superior to conventional methods such as element space periodogram while being less computationally costly than fully coherent element space methods but still capable of

processing signals of wide instantaneous bandwidth in moderate signal-to-noise environments as demonstrated via simulation results in section 7. We demonstrate mean squared error performance for the beam space methods comparable to that of element space coherent signal subspace processing. A price is paid in absolute resolution performance when compared to fully coherent element space methods. However the computational advantage is such that true time delay beam space processing may be suitable in cases where the number of true time delay beamformers is less than the number of array elements and a limited field of view can be tolerated. An example of such a potential application is the airborne intelligence, surveillance and reconnaissance system as discussed in sections 1.1, 5 and 7.7.

1.5 Guiding Principles and Assumptions

Throughout this work the author makes a number of common assumptions. Many of these simplify the demonstration of the concepts described, without any loss of generality. Among these are the assumptions of ideal $0dBi$ antenna elements and the use of a Uniform Linear Array (ULA). The ULA facilitates the implementation of models and simulations, but the equations presented herein permit the application of entirely arbitrary arrays through the antenna manifold construct. The antenna manifold represents measurement of the array response without regard to its physical configuration, but is relatively easy to compute for the ULA as a uniform phase or time

shift. For the antenna array, the author assumes that the elements are identical, and that they are ideal elements with uniform spectral responses across the bandwidth of interest. The author also assumes that the RF wavefronts that impinge on the array are planar, that is the sources of RF emission are in the far field of the antenna array. The research and analysis herein examines signal processing aspects of the wide bandwidth source location problem and assumes the availability of a broadband antenna array for the input, although some practical issues for the array itself are considered in Chapter 5.

Noise in the system is assumed to be White Gaussian Noise (WGN) unless otherwise specified. Although the beamformer bank may introduce some coloration in the noise, it is shown to be uncorrelated between the beamformer outputs, which justifies the diagonal noise term in the system model. The simulation results utilize primarily wideband chirp (linear frequency modulation) signals due to the ease with which these can be shifted and resampled. In general, the techniques are applicable to any wideband signal. Much of the previous wideband source location work focused on noise-like signals which are relatively easy to model in a spatial characterization that relies on phase shifting within sub-bands, but physical memory and processor constraints made it impractical to use these types of signals to demonstrate the results of signal subspace processing in true time delay beam space. For this reason, the author chose to use chirp signals that can be more readily shifted and resampled.

Although the technology and signal processing methodology discussed in this dissertation are intended to be generally applicable for a variety of system types and

applications, the discussion will frequently be framed in the context of airborne radio direction finding. This is not intended to constrain its use, but simply due to the application paradigm within which the related research and development has taken place. It is often helpful to consider not only the theoretical basis for the problem and solution, but also its practical application. The airborne radio direction finding application is simply one example to which the theory can be applied.

One of the fundamental concepts in this dissertation is that the beam direction of true time delay beamforming is independent to changes in the frequency content of the signal to be processed by the beamformer [27]. We assume that this is true for a system composed of ideal components. In practice components are not ideal and nearly all parts of the system will exhibit some frequency dependence. In particular the antenna elements for a practical system design will have significant frequency dependence compared to the beamformer. With judicious system design and thorough calibration procedures, the author assumes that the effects of antenna element frequency dependence can be minimized. Therefore within the context of applying the signal processing concepts to the array data, the true time delay beam space is assumed to be independent of frequency. The accompanying explanation of Section 3.1 provides additional detail regarding the relationship of TTD beamforming and frequency dependence.

We assume that the form of the Power Spectral Density (PSD) is generally known a priori. For the examples treated in simulation results, the PSD is approximately uniform

across the bandwidth of interest.

1.6 Original Contributions

This dissertation introduces and evaluates methods to execute high-resolution signal subspace processing in the beam space of a bank of true time delay beamformers. The resulting processes of beam space MUSIC and beam space Minimum Variance Distortionless Response (MVDR) are original contributions. The developments that result in the equations for these novel methods as well as the analyses of their performance rely heavily on the works of Schmidt ([43] and [87]), Wang and Kaveh ([44] and [62]), and Capon [52]. To the best of our knowledge, similar developments have not been applied previously to the beam space of a bank of true time delay beamformers. Signal subspace processing in true time delay beam space simultaneously introduces spatial diversity and frequency independence of the time delays that control the beamformer into the data model. This alleviates the need for a transformation that requires preliminary AOA estimation. It enables source location mean squared error performance similar to CSS coherent integration while gaining an advantage in computational expense. Unlike CSS it permits instantaneous source location across the field of view without requiring a preliminary AOA estimation step and without requiring iterations using updated AOA estimates. Also unlike CSS and similar methods it is primarily a time and spatial domain based method as opposed to a frequency domain

based method. This dissertation demonstrates this result for the case where the number of beams in the beamformer bank is less than the number of array elements. Although a price may be paid in absolute resolution performance as compared to fully coherent element space methods, resolution is still superior to conventional beamforming. The beam space methodology is particularly well suited for applications that can tolerate a limited instantaneous field of view, require high-resolution of wide bandwidth sources and low computational cost. We posit the long-range airborne intelligence, surveillance and reconnaissance application as a well suited one. We summarize the contributions as follows:

- We present an original derivation for multiple source classification in TTD beam space. The novel formulation is presented in Section 3.2.1 is a key aspect of the TTD beam space method.
- We present an original derivation for minimum variance distortionless response (MVDR) source location estimation in TTD beam space.
- Another key to the operation of processing in the beam space of a true time delay beamformer bank is the beam space manifold. A novel detailed derivation of the beam space manifold is presented in Appendix B.
- We claim that the mean squared error performance for TTD beam space MUSIC is comparable to that of element space CSS at moderate SNR.
- We claim that the computational cost for beam space processing is less than that for element space CSS for the case where the number of beams is less

than the number of array elements. We give original derivations of the computational cost for CSS and beam space MUSIC methods and validate the theoretical derivation of computational cost via Monte-Carlo simulation study.

- We claim that resolution performance for TTD beam space MUSIC is superior to conventional methods such as the periodogram and MVDR for the conditions discussed.
- Unlike CSS, the existing baseline element space approach, the proposed method does not require initial estimates of DOAs for focusing. Instead, TTD beamforming is used to steer at any arbitrary angular direction.
- Also unlike CSS, the proposed approach is capable of estimating closely spaced as well as disparately separated sources simultaneously without requiring refocusing. This is achieved by beam steering at multiple angular directions simultaneously. The penalty to achieve this capability is a limited field of view, but this limitation is appropriate for many applications.
- We claim that TTD beam space processing simultaneously incorporates spatial diversity and frequency independence of the time delays that control the beamformers to permit a non-iterative result for wideband sources. This is demonstrated by simultaneously processing closely and disparately spaced sources that neither CSS nor conventional methods can successfully process for the conditions discussed.

1.7 Dissertation Outline

Chapter 2 provides a background by reviewing significant previous work in the fields of signal subspace processing, wideband source location, TTD beamforming and the optimization of array signal processing system configurations. Chapter 3 discusses the problem formulation, solution and analysis of signal subspace processing in the true time delay beam space. It also discusses the formulation of the Cramer-Rao Lower Bound (CRLB), the theoretical limit for accuracy in the measured angle using the wideband source location methods. Chapter 4 examines computational expense for the various wideband source location methods. Chapter 5 considers practical and system considerations, such as those involved in mounting physical arrays with limited capabilities on vehicles. Chapter 6 discusses optimization of system parameters, particularly in the area of array and signal processing configurations. Chapter 7 presents the results of simulations performed to demonstrate the concepts discussed throughout the dissertation. Finally, Chapter 8 gives the conclusions of the dissertation.

2 BACKGROUND

This chapter discusses aspects of the body of knowledge present in the literature relevant to the dissertation topic. Section 2.1 discusses the background of minimum variance distortionless response source location estimation for narrow bandwidth sources. Section 2.2 discusses signal subspace and related signal processing techniques for narrow bandwidth sources. Section 2.3 presents the background for Multiple Signal Classification (MUSIC) in the narrow bandwidth case. Section 2.4 describes the Root-MUSIC technique. Section 2.5 discusses efforts to develop wide bandwidth processes such as those that extend the narrow band techniques to wide bandwidths. These include variants of both non-coherent and coherent integration of wide bandwidth data filtered into many narrow sub-bands. Among them are Section 2.5.1, coherent signal subspace, Section 2.5.2, rotational signal subspace, Section 2.5.3, bilinear transformation, Section 2.5.4, steered covariance matrix, Section 2.5.5, beamforming invariance coherent signal subspace, Section 2.5.6, specific signal type model-based

approaches, Section 2.5.7, test of orthogonality of projected subspaces, and Section 2.5.8, robust coherent signal subspace. Section 2.6 provides some background to compare and contrast element space and beam space architectures. Section 2.7 deals with the background of true time delay beamforming as an inherently wide bandwidth technique that alleviates the beam squint phenomenon common to narrow bandwidth phased array antenna systems. Section 2.8 discusses the concept of optimization of antenna array and signal processing configurations that is generally applicable to either narrow or wide bandwidth systems, but may be very application dependent. Finally Section 2.9 addresses the general notion of multiple source resolution that is applicable to all sources of emission without regard to their bandwidth.

2.1 Minimum Variance Distortionless Response (MVDR) Estimation - Narrowband Case

Capon developed a method for high-resolution spectral estimation in the context of wavenumber analysis for seismic sensor arrays. The formulation relied on the assertion that conventional power spectral density analysis has resolution limited by the array beam pattern with a fixed wavenumber window. Capon's high-resolution formulation introduced a window that changes as a function of the wavenumber [52].

Without loss of generality, we consider the case of a Uniform Linear Array (ULA) of M antenna elements receiving radiation from L monochromatic point sources in the far field under the constraint of element spacing $d \leq \frac{\lambda}{2}$, the half wavelength. Fig. 7 depicts

such an array with an illustration of the ULA along the $x - axis$ with phase center at the origin and depictions of the azimuth and elevation angles. For convenience, unless otherwise specified, we consider the azimuth only case with AOA characterized by the single angle, θ.

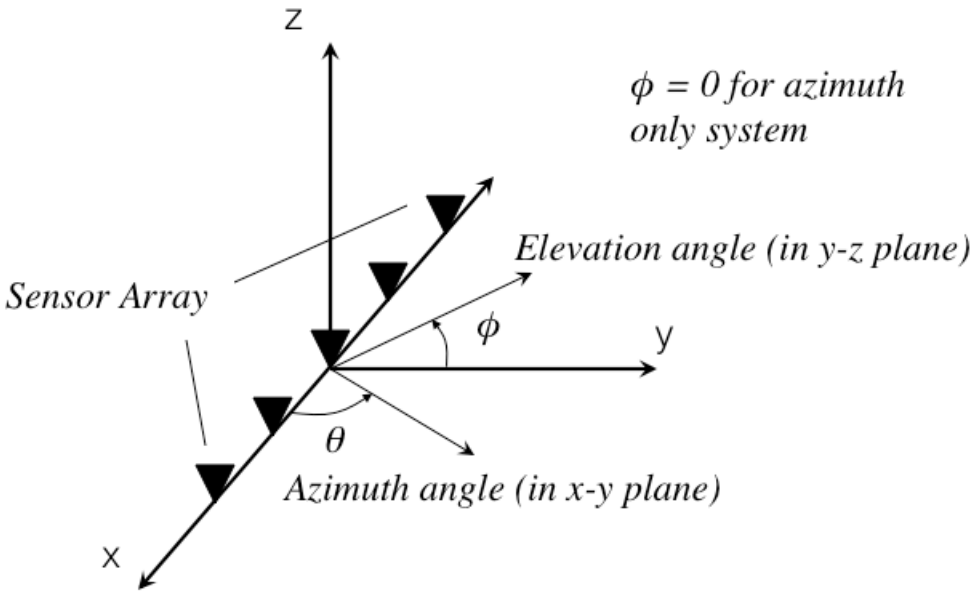

Fig. 7. Illustration of azimuth and elevation angles for uniform linear array on x-axis with phase center at the origin.

Therrien [59] described the motivation for Capon's method as one that applies a narrowband filter with impulse response, $h_{\omega_0}[n], n = 1,2, \ldots N_s$, that is constrained to

frequency response $H_{\omega_0}(e^{j\omega})$ of unity magnitude and zero phase at the frequency ω_0 for number of data points N_s and measured column N_s-vector on sensor, m,

$$\boldsymbol{x}_m = \begin{bmatrix} x_{1m} \\ x_{2m} \\ \vdots \\ x_{N_s m} \end{bmatrix}, m = 1, \dots M \,, \tag{2.1}$$

for M sensors. Note that throughout this dissertation, a bold lower case symbol in equations is used to signify vectors and a bold upper case symbol in equations is used to signify matrices. This unity constraint filter characteristic ensures a distortionless response. We may then construct the data matrix for the sensor array, $\boldsymbol{X}$, as

$$\boldsymbol{X} = \begin{bmatrix} \boldsymbol{x}_1^T \\ \boldsymbol{x}_2^T \\ \vdots \\ \boldsymbol{x}_M^T \end{bmatrix} = \begin{bmatrix} x_{11} & x_{12} \cdots & x_{1N_s} \\ x_{21} & x_{22} \cdots & x_{2N_s} \\ \vdots & \vdots \cdots & \vdots \\ x_{M1} & x_{M2} \cdots & x_{MN_s} \end{bmatrix}. \tag{2.2}$$

Since the N_s-length column vectors, $\boldsymbol{x}_m$, are transposed to form the rows of $\boldsymbol{X}$, the data matrix $\boldsymbol{X}$ is $M \times N_s$ and we follow the matrix element subscript numbering convention $element_{row\ column}$. The data correlation matrix, $\boldsymbol{R} \stackrel{\text{def}}{=} E\{\boldsymbol{X}\boldsymbol{X}^H\}$, is estimated by the sample correlation matrix,

$$\widehat{\boldsymbol{R}} = \frac{1}{N_s}\boldsymbol{X}\boldsymbol{X}^H \tag{2.3}$$

where $E\{\cdot\}$ is the expectation operator and the superscript H denotes the Hermitian or complex conjugate transpose [59]. Simultaneously a minimum noise variance constraint is applied such that the filter weights satisfy $\min(\boldsymbol{h}_0^H \widehat{\boldsymbol{R}} \boldsymbol{h}_0)$. This latter constraint minimizes the average power of the filter output and is the impetus for the descriptor "minimum variance." Therrien [59] then went on to derive the filter weight vector relation

$$\boldsymbol{h}_0 = \frac{\boldsymbol{R}^{-1}\boldsymbol{a}(\theta_0)}{\boldsymbol{a}(\theta_0)^H \boldsymbol{R}^{-1}\boldsymbol{a}(\theta_0)}. \tag{2.4}$$

The column mode vector, $\boldsymbol{a}(\theta_0)$, for a spatial sensor array is the angle dependent sensor response also known commonly as the array manifold vector for angle of arrival (AOA) θ_0 [43]. The mode vector is given by

$$\boldsymbol{a}(\theta_0) = \begin{bmatrix} a_1(\theta_0) \\ a_2(\theta_0) \\ \vdots \\ a_M(\theta_0) \end{bmatrix} \tag{2.5}$$

The matrix made up of the collection of all such mode vectors for all measured angles is denoted as $\boldsymbol{A}_{tot}(\theta)$. For the M-element ULA, the components of $\boldsymbol{a}(\theta_0)$ are given by $a_m(\theta_0) = e^{i\left[\frac{2\pi}{c} f d(m-1)\sin\theta_0\right]}, m = 1, \ldots, M$, for frequency, f, sensor spacing, d, and $i = \sqrt{-1}$.

Reference [59] calculates the output power of the filter as

$$\mathcal{P} = \boldsymbol{h_0}^H \boldsymbol{R h_0} = \frac{\boldsymbol{a}(\theta_0)^H \boldsymbol{R}^{-1} \boldsymbol{R} \boldsymbol{R}^{-1} \boldsymbol{a}(\theta_0)}{[\boldsymbol{a}(\theta_0)^H \boldsymbol{R}^{-1} \boldsymbol{a}(\theta_0)]^2} = \frac{1}{\boldsymbol{a}(\theta_0)^H \boldsymbol{R}^{-1} \boldsymbol{a}(\theta_0)} . \quad (2.6)$$

Since the same filter response structure holds for any AOA, $0 \leq \theta_0 \leq 2\pi$, the Minimum Variance Distortionless Response (MVDR) estimator is defined by substitution of variable θ for θ_0 in equation (2.6) resulting in [59]

$$P_{MVDR}(\theta) = \frac{1}{\boldsymbol{a}(\theta)^H \boldsymbol{R}^{-1} \boldsymbol{a}(\theta)} . \quad (2.7)$$

2.2 Signal Subspace Processing - Narrowband Case

Burg laid considerable groundwork for signal subspace processing in his seminal dissertation on maximum entropy spectral analysis [42]. Burg's work was developed in the context of estimation of the power density spectra for stationary time series based on the data correlation matrix. His thesis was that the spectral estimate possesses the most random, or has maximum entropy, of any possible estimate. This estimation process led to a technique that was claimed to be of greater resolution than conventional techniques with moderate additional computational cost, but was not immediately applied to the Radio Frequency (RF) source location problem.

Signal subspace processing for RF source location as described in publications such as [54] and [43] considers multichannel data as a linear combination of RF source wavefronts incident upon an arbitrary antenna element array. Fig. 8 depicts such an

arbitrary array for a 3-element case so that the signal space can be visualized in three dimensions. In physical space, the example shows two emitters whose wavefronts, assumed to be far field planar wavefronts, impinge on the array with directions of propagation angles θ_1 and θ_2, the Angles Of Arrival (AOA's), with respect to the x-axis in the array coordinate system. The collected data, $\boldsymbol{X}$, are modeled as a linear combination of incident wavefronts, $\boldsymbol{S}$, plus noise, $\boldsymbol{N}$. For the visualized case of two signals ($L = 2$) and three elements ($M = 3$), the three vector responses on the three elements make up the collected signal matrix,

$$\boldsymbol{X} = \boldsymbol{AS} + \boldsymbol{N} = \begin{bmatrix} \boldsymbol{x}_1^T \\ \boldsymbol{x}_2^T \\ \boldsymbol{x}_3^T \end{bmatrix} = [\boldsymbol{a}(\theta_1) \quad \boldsymbol{a}(\theta_2)] \begin{bmatrix} \boldsymbol{s}_1 \\ \boldsymbol{s}_2 \end{bmatrix} + \begin{bmatrix} \boldsymbol{n}_1 \\ \boldsymbol{n}_2 \\ \boldsymbol{n}_3 \end{bmatrix}. \tag{2.8}$$

The $\boldsymbol{a}(\theta_1)$ and $\boldsymbol{a}(\theta_2)$ 3×1 coefficient vectors are AOA dependent mode vectors that represent components of the array manifold of general form $\left[e^{i\left[\frac{2\pi f}{c}\zeta_1(\theta)\right]} \; e^{i\left[\frac{2\pi f}{c}\zeta_2(\theta)\right]} \; e^{i\left[\frac{2\pi f}{c}\zeta_3(\theta)\right]}\right]^H$. Each $\boldsymbol{s}$ is a $1\times N_s$ signal vector. Each $\boldsymbol{n}$ is a $1\times N_s$ noise vector that correspond to each of the 3 elements. $\zeta_m(\theta)$ is a general function of the sensor array configuration which for the ULA is $\zeta_m(\theta) = d(m-1)\sin\theta$. The mode vector for AOA θ_i, the column M-vector $\boldsymbol{a}(\theta_i) = [a_1(\theta_i)\, a_2(\theta_i) \cdots a_M(\theta_i)]^H$, is the relative array response due to the signal from a particular direction of arrival. The signals $\boldsymbol{s}_1$ and $\boldsymbol{s}_2$ are the individual wavefronts due to the RF sources impinging on the sensors.

In general for an M-element array and L RF sources, the M collected signal vectors are

of length N_s, and we have the $M \times M$ data correlation matrix

$$\widehat{\boldsymbol{R}} = \frac{1}{N_s}\boldsymbol{X}\boldsymbol{X}^H \tag{2.9}$$

where the superscript H denotes the complex conjugate transpose.

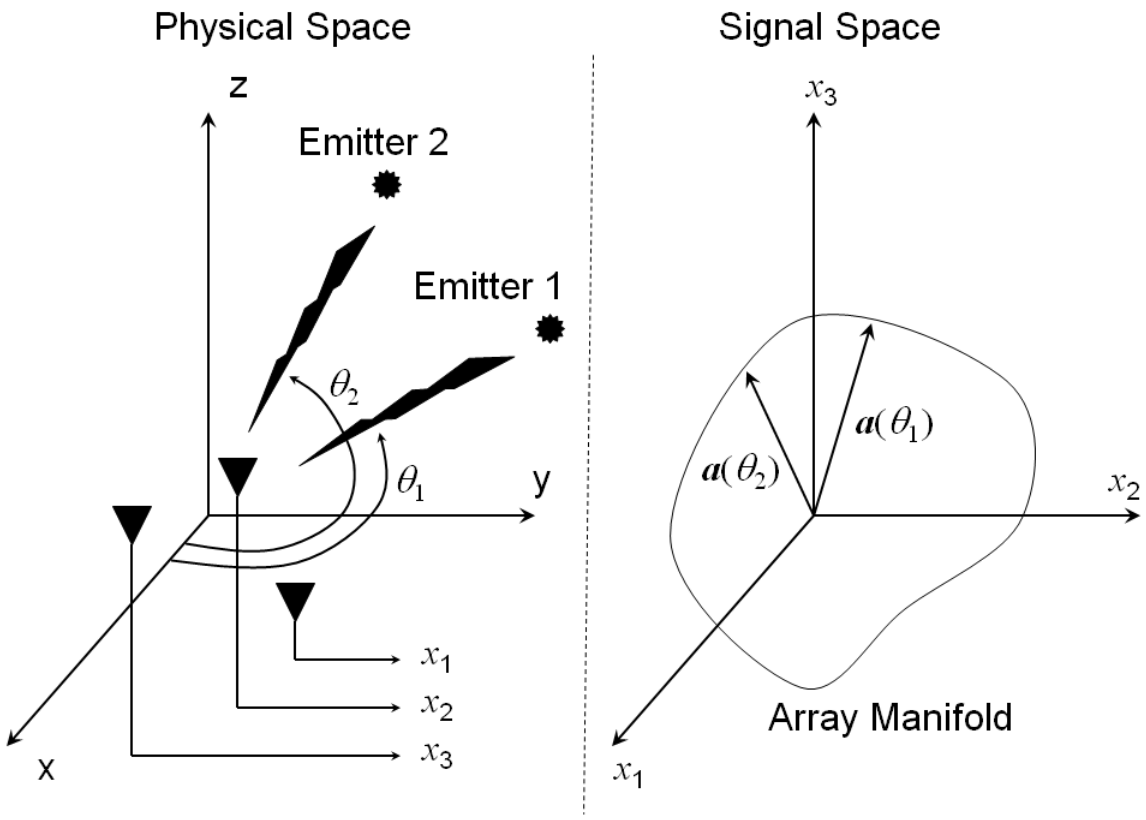

Fig. 8. Geometrical depiction of the direction finding problem.

Following [54] and [43] we express the general modeled system in terms of the Eigen structure and write

$$\boldsymbol{R} = \boldsymbol{APA}^H + \lambda_{min}\boldsymbol{S}_0 \tag{2.10}$$

where $\boldsymbol{S}_0$ is the normalized noise covariance matrix such that $\text{trace}(\boldsymbol{S}_0) = M$, $\boldsymbol{P}$ is the spatial power spectrum, and λ_{min} is the smallest Eigenvalue for the solution of

$$|\boldsymbol{R} - \boldsymbol{\lambda S}_o| = 0 \tag{2.11}$$

with the M Eigenvalues are

$$\lambda_1 \geq \lambda_2 \geq \cdots \geq \lambda_L \geq \cdots \geq \lambda_{M-1} \geq \lambda_M = \lambda_{min} \tag{2.12}$$

for L sources under the assumption that the noise is uniform on all channels. We assume uniform white Gaussian noise in which case

$$\lambda_{min}\boldsymbol{S}_0 = \sigma^2\boldsymbol{I} \tag{2.13}$$

where σ^2 is the noise variance. The corresponding Eigenvectors are

$$\boldsymbol{e}_1, \boldsymbol{e}_2, \cdots, \boldsymbol{e}_M \tag{2.14}$$

with

$$\mathcal{S}_s = span(\boldsymbol{e}_1, \boldsymbol{e}_2, \cdots, \boldsymbol{e}_L) \tag{2.15}$$

being the signal subspace and

$$\mathcal{S}_N = span(\boldsymbol{e}_{L+1}, \boldsymbol{e}_{L+2}, \cdots, \boldsymbol{e}_M) \tag{2.16}$$

being the noise subspace. The L largest Eigenvalues indicate the signals while the associated Eigenvectors serve as an estimate of the signal subspace, $\boldsymbol{E}_L = [\boldsymbol{e}_1|\boldsymbol{e}_2|\dots|\boldsymbol{e}_L]$. Similarly, the $M-L$ smallest Eigenvalues indicate the noise while the associated Eigenvectors serve as an estimate of the noise subspace, $\boldsymbol{E}_N = [\boldsymbol{e}_{L+1}|\boldsymbol{e}_{L+2}|\dots|\boldsymbol{e}_M]$. The minimum Eigenvalue, λ_{min}, typically represents the nominal noise level for the system.

The solution can be viewed geometrically as an intersection of the signal subspace plane with the array manifold for the case of two signals in a three element system as shown in Fig. 9 [89]. The two Eigenvectors corresponding to the two largest Eigenvalues, $\boldsymbol{e}_1$ and $\boldsymbol{e}_2$, lie in a plane that intersects the array manifold. Orthogonality of $\boldsymbol{e}_3$ to the signal subspace plane is shown in [90]. These intersections of $\boldsymbol{e}_1$ and $\boldsymbol{e}_2$, with the array manifold indicate the estimate of the AOA's of the incident wavefronts.

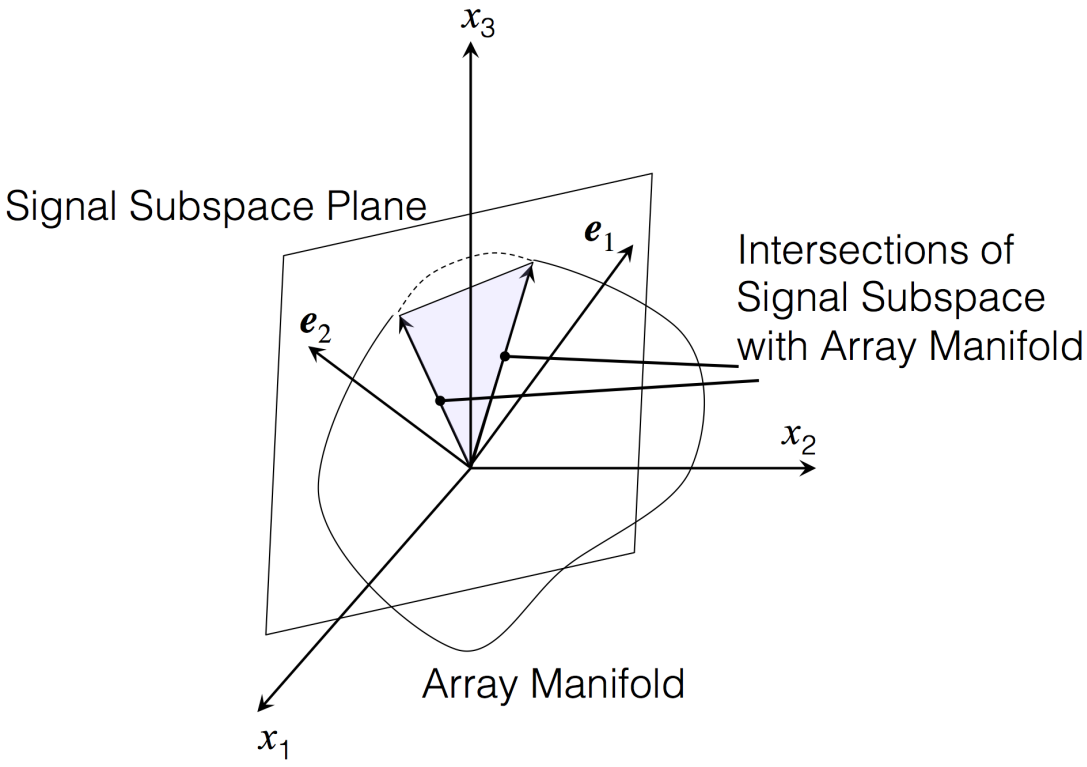

Fig. 9. The intersections of a signal subspace plane with the array manifold in a geometrical representation for three elements.

For the general case of L incident waveforms from multiple directions of arrival impinging on an M-element antenna array, the measured response, $\boldsymbol{X}$, is characterized by

$$[\boldsymbol{x}_1 \quad \boldsymbol{x}_2 \quad \cdots \quad \boldsymbol{x}_M]^T = [\boldsymbol{a}(\theta_1)^T \quad \boldsymbol{a}(\theta_2)^T \cdots \quad \boldsymbol{a}(\theta_L)^T] \begin{bmatrix} \boldsymbol{s}_1 \\ \boldsymbol{s}_2 \\ \vdots \\ \boldsymbol{s}_L \end{bmatrix} + \begin{bmatrix} \boldsymbol{n}_1 \\ \boldsymbol{n}_2 \\ \vdots \\ \boldsymbol{n}_M \end{bmatrix}$$

$$\text{or } \boldsymbol{X} = \boldsymbol{A}\boldsymbol{S} + \boldsymbol{N} \tag{2.17}$$

where $\boldsymbol{S}$ is the signal, $\boldsymbol{N}$ is the noise, and $\boldsymbol{A}$ is made up of L column M-vector components of the array manifold. The array manifold is the set of response M-vectors

on the M-element array obtained by incrementing the direction of arrival of a source through a predetermined pattern, such as many individual azimuth angles, θ, in a calibration procedure.

2.3 Multiple Signal Classification (MUSIC) – Narrowband Case

Schmidt also described conventional beamforming in the signal subspace context as

$$P_{BF}(\theta) = \boldsymbol{a}(\theta)\widehat{\boldsymbol{R}}\boldsymbol{a}(\theta)^{\boldsymbol{H}} \tag{2.18}$$

which is viewed as a correlation of the received signal data with the array manifold. By exploiting the principle that the square of the Euclidean distance from a vector $\boldsymbol{y}$ to the estimate of the noise subspace is

$$d^2 = \boldsymbol{y}^H \boldsymbol{E}_N \boldsymbol{E}_N^H \boldsymbol{y}\,, \tag{2.19}$$

for arbitrary signal space vector, $\boldsymbol{y}$. Schmidt then defined the Multiple Signal Classification (MUSIC) spatial spectrum as

$$P_{MU}(\theta) = \frac{1}{\boldsymbol{a}(\theta)\boldsymbol{E}_N\boldsymbol{E}_N^H\boldsymbol{a}(\theta)^{\boldsymbol{H}}}\,. \tag{2.20}$$

Since the denominator of equation (2.20) represents the square of the distance from the noise subspace estimate to the array manifold, P_{MU} can reasonably be expected to exhibit peaks in the locations of the incident signals [91]. Frequency dependence for

$\boldsymbol{a}(\theta)$ is typically ignored and processing performed as if the system were monochromatic. Wide tuning bandwidths (as opposed to wide instantaneous bandwidth) can be treated by measuring $\boldsymbol{a}(\theta)$ for many discrete frequencies and interpolating in between.

2.4 Root-MUSIC – Narrowband Case

Barabell introduced the root-MUSIC method, [92], that was later thoroughly analyzed by Rao and Hari, [93], that generates estimated source location solutions from the roots of a polynomial derived from the MUSIC spectrum. The root-MUSIC method is typically restricted to Uniform Linear Array (ULA) type sensor so that the denominator of the MUSIC spectrum can be written as

$$P_{MU}^{-1}(\theta) = \boldsymbol{a}(\theta)\boldsymbol{E}_N\boldsymbol{E}_N^H\boldsymbol{a}(\theta)^{\boldsymbol{H}} = \sum_{p=-M+1}^{M-1} c_p e^{-j2\pi p(\frac{d}{\lambda})\sin(\theta)} \tag{2.21}$$

where c_p is a coefficient given by the sum of the elements on the pth diagonal of the data correlation matrix,

$$c_p = \sum_{pth\ diagonal} \boldsymbol{E}_N\boldsymbol{E}_N^H \ . \tag{2.22}$$

The roots of the polynomial, equation (2.21), then provide a direct estimate of the source locations without a need to find spectral peaks. [92] and [93] discussed instances where root-MUSIC gave accurate source arrival direction estimates for closely

spaced sources that spectral-based MUSIC did not resolve.

2.5 Wideband Source Location

Although signal subspace processing methods produced many advances, particularly in terms of resolution of closely spaced sources, they were still primarily monochromatic in nature due to the phase based measurement processes for the received signals and antenna manifold. A number of authors have also examined wideband RF reception and processing, but these often refer to large tuning bandwidth rather than instantaneous bandwidth as in [94]. This dissertation investigates processes compatible with wideband sources of large instantaneous bandwidth or large bandwidth excursions within the processing interval such as chirp sources. Systems designed for a large tuning bandwidth may still be required only to process sources within a narrow bandwidth during any single processing interval.

Today, the estimation of wideband emitter characteristics is becoming increasingly important due to the proliferation of spread spectrum systems. Such systems commonly incorporate techniques to increase the signal bandwidth beyond that necessary to transmit the requisite information. Reasons for spreading the bandwidth of signals may be to provide multiple access, increase radar range resolution, desire to operate undetected, or others [2], [3], [4], [5]. Along with the proliferation of such signals, the desire to locate their sources is becoming important for many civil and

military applications.

Also of note in the wideband RF sensor array field is the work of [95] that considers a spatially continuous distributed sensor so that element spacing need not be considered. Messer analyzed the effect of considering specific signal spectral content [96]. Ji and Kwong extended estimation techniques to sparse arrays of vector sensors [97]. The following sections review some of the prominent methods previously devised for wide bandwidth source location.

2.5.1 Coherent Signal Subspace (CSS)

A significant body of work exists in the literature to describe methods to calculate the AOA for wideband signals. Many of these are wideband extensions of the previously described narrowband techniques. Subsequent to the seminal development of Wax, Shan, and Kailath who introduced an incoherent integration approach [98], Wang and Kaveh developed the Coherent Signal Subspace (CSS) method, [44] and [62], that coherently integrates many frequency sub-bands of data into a common reference band whose data can then be processed by signal subspace techniques. Unfortunately the data transformation from each sub-band to the reference band relies on construction of transformation matrices that are focused around specific angles in the AOA spectrum determined by preliminary processing using conventional means. The results depend on the accuracy of the preliminary estimates and results for multiple focusing angles or inaccurate initial estimates may require iteration of the algorithm. We follow the signal

subspace processing for wideband cases introduced by Wang and Kaveh by coherently integrating pre-processed data from multiple filtered sub-bands into a common reference frequency, f_0, [44], [62]. The signals from L sources on M elements are collected over D independent subintervals, or data snapshots of duration ΔT each. The Discrete Fourier Transform (DFT) of the ith data snapshot is $X_i(f_j)$ for $i = 1, \dots, D$ and for the J sub-band frequencies $f_j, j = 1, \dots, J$. The authors of [62] give the spatial covariance matrix as

$$\operatorname{cov}\left(\boldsymbol{X}_i(f_j)\right) = \frac{1}{\Delta T}\boldsymbol{P}_X(f_j) = \frac{1}{\Delta T}\boldsymbol{A}(f_j)\boldsymbol{P}_S(f_j)\boldsymbol{A}^H(f_j) + \frac{\sigma_N^2}{\Delta T}\boldsymbol{P}_N(f_j) \tag{2.23}$$

for $\boldsymbol{P}_X(f_j)$, the Cross-Spectral Density Matrix (CSDM) of the array output, $\boldsymbol{A}(f_j)$, the frequency dependent array manifold, $\boldsymbol{P}_S(f_j)$, the signal spectral density matrix, $\boldsymbol{P}_N(f_j)$, the noise spectral density matrix, and σ_N^2, the noise power. This is a frequency domain representation of the familiar additive noise model. For the narrow bandwidth case, the frequency dependence of the array manifold was neglected, but now must be taken into account. The array manifold is made up of row vectors, $\boldsymbol{a}(f_j, \theta)$, that parametrically represent the response to a single source at frequency f_j as a function of the source angle, θ, given by

$$\boldsymbol{a}(f_j, \theta) = \left[a_1(f_j, \theta) \;\; a_2(f_j, \theta) \cdots a_M(f_j, \theta)\right]. \tag{2.24}$$

The $a_m(f_j, \theta), m = 1, \dots, M, j = 1, \dots, J$ values are the characteristic response on

element m at frequency f_j and AOA θ_0. The general form of a mode vector is $a_m(f_j,\theta) = \left[e^{i\left[\frac{2\pi f_j}{c}\zeta_1(\theta)\right]} \; e^{i\left[\frac{2\pi f_j}{c}\zeta_2(\theta)\right]} \; e^{i\left[\frac{2\pi f_j}{c}\zeta_M(\theta)\right]}\right]^H$ with $\zeta(\theta) = d(m-1)\cos\theta$ for the ULA that we consider in this dissertation.

Accounting for frequency dependence in the source response the mapping from each sub-band center frequency, f_j, $j = 1, \ldots, J$, to common band, f_0, is given by

$$\boldsymbol{T}_j = \text{diag}\left[\frac{a_1(f_0,\theta_0)}{a_1(f_j,\theta_0)} \quad \frac{a_2(f_0,\theta_0)}{a_2(f_j,\theta_0)} \cdots \quad \frac{a_M(f_0,\theta_0)}{a_M(f_j,\theta_0)}\right] \tag{2.25}$$

for initial direction of arrival estimate, θ_0. The CSS method requires preliminary processing to determine the approximate source locations since this mapping is dependent on an initial course direction of arrival estimate, θ_0. The method must be applied iteratively to cases with multiple widely spaced sources since these will typically be characterized by different initial course estimates.

The data, $\boldsymbol{X}_i(f_j)$, are reduced to the sample correlation matrices

$$\widehat{\boldsymbol{R}}_{Xj} = \frac{1}{D}\sum_{i=1}^{D} \boldsymbol{X}_i(f_j)\boldsymbol{X}_i^H(f_j)\,. \tag{2.26}$$

The data are transformed according to

$$\widehat{\boldsymbol{R}}_{Yj} = (\Delta T)\boldsymbol{T}_j\widehat{\boldsymbol{R}}_{Xj}\boldsymbol{T}_j^H \tag{2.27}$$

and modeled according to

$$\widehat{\boldsymbol{R}}_Y = \frac{\Delta T}{J}\sum_{j=1}^{J} \boldsymbol{T}_j \widehat{\boldsymbol{R}}_{Xj} \boldsymbol{T}_j^H \ , \tag{2.28}$$

the coherently integrated signal, and

$$\widehat{\boldsymbol{R}}_N = \frac{\Delta T}{J}\sum_{j=1}^{J} \boldsymbol{T}_j \boldsymbol{P}_N(f_j) \boldsymbol{T}_j^H \ , \tag{2.29}$$

the coherently integrated noise.

Once the data are transformed and coherently integrated, they can be processed using one of the narrowband techniques such as discussed in Section 2.2. One popular method for processing the coherently integrated data is MUSIC. The signal and noise subspaces must be determined by first solving the Eigenvalue and Eigenvector problem

$$\widehat{\boldsymbol{R}}_Y \boldsymbol{E}_{i-CSS} = \lambda_{i-CSS} \widehat{\boldsymbol{R}}_N \boldsymbol{E}_{i-CSS}, \ i = 1, \dots, M \tag{2.30}$$

with the noise subspace given by the span of $\boldsymbol{E}_{N-CSS}$ formed by the Eigenvectors associated with noise Eigenvalues, in order of ascending magnitude, $\lambda_M, \lambda_{M-1}, \dots, \lambda_{M-L}$, where L is the estimated number of sources. The CSS MUSIC spatial spectrum for the coherently integrated data is then

$$P_{CSS}(\theta) = \frac{1}{\boldsymbol{a}^H(f_0,\theta)\boldsymbol{E}_{N-CSS}\boldsymbol{E}_{N-CSS}^H \boldsymbol{a}(f_0,\theta)} \ . \tag{2.31}$$

The CSS spectra displayed in the simulation results of Chapter 7 are idealized results in that the solution of the generalized Eigenvalue problem assumes perfect knowledge of the noise samples. While this is not practical in real world application, it does permit

comparison with the best result that CSS provides.

Sivinand, Yang and Kaveh subsequently developed time domain focusing filters using the digital FIR technique as preprocessors for a CSS-like method. This technique derived the filters that were the time domain equivalents of the frequency domain-based preprocessing of CSS. The authors showed that the time domain filter construction combined with signal subspace processing produced results similar to CSS. The method is unlike the novel method of this dissertation in that it does not constitute a beamformer bank in the preprocessing scheme. Since it is essentially CSS with a different, but equivalent, preprocessor, it suffers from limitations similar to CSS and still involves significant processing complexity [99].

2.5.2 Rotational Signal Subspace (RSS)

Hung and Kaveh augmented CSS by using unitary focusing matrices in the Rotational Signal Subspace (RSS) method [63]. The RSS method injected an important constraint into the wideband source location discussion but is still computationally expensive. It seeks to minimize the square of the Frobenius norm of the difference between the transformed array at frequency f_j and the reference frequency array subject to a unitary transformation matrix such as

$$\boldsymbol{T}_{j,RSS} = \arg\left\{\min_{\boldsymbol{T}} \left\|\boldsymbol{T}\boldsymbol{a}(f_j,\theta) - \boldsymbol{a}(f_0,\theta)\right\|_F^2 \text{ subject to } \boldsymbol{T}^H\boldsymbol{T} = \boldsymbol{I}_M\right\}, j = 1,2,\cdots,J. \quad (2.32)$$

The Frobenius norm, $\|\cdot\|_F$, is simply the root sum square of the matrix elements. The authors showed that this constraint necessarily results in a lossless focusing matrix whereas earlier transformation matrices did not. Focusing loss is defined as the ratio of the array signal to noise after focusing to the array signal to noise ratio before focusing. The closed form solution to the constrained optimization of equation (2.32) is

$$\boldsymbol{T}_{j,RSS} = \boldsymbol{V}_j \boldsymbol{U}_j^H \tag{2.33}$$

where $\boldsymbol{V}_k$ and $\boldsymbol{U}_k$ represent the solution to the singular value decomposition

$$\boldsymbol{a}(f_j, \theta)\boldsymbol{a}^H(f_0, \theta) = \boldsymbol{U}_k \boldsymbol{\Lambda}_k \boldsymbol{V}_k^H. \tag{2.34}$$

2.5.3 Bi-Linear Transformation (BLT) Method

One of the limitations of the CSS method is the requirement to perform a preliminary coarse AOA estimation to use in the calculation of the transformation matrices. The Bi-Linear Transformation (BLT) method of Shaw and Kumaresan eliminates the need for a preliminary AOA estimate for wideband sources by incorporating Henderson's rank reduction technique [64], [65]. The transform, B, is an $M \times M$ matrix constructed from the coefficients of the polynomials

$$p_k(z) = (1+z)^{M-k}(1-z)^{k-1}, k = 1,2,\dots,M \tag{2.35}$$

for polynomial order $M-1$. The BLT method alleviates the need for preliminary AOA

estimation, resulting in excellent results in a single processing stage, without iteration. The authors showed that the BLT matrix is not dependent on the angle of arrival of the source signal. It does however utilize an approximation that relies on closely spaced array elements rendering it not applicable to arbitrary array configurations. As mentioned previously closely spaced elements can be useful for particular applications like those for which miniaturization is critical, cell phones being an example.

2.5.4 Steered Covariance Matrix (SCM)

The Steered Covariance Matrix (SCM) method of Krolik and Swingler is based on the previous CSS method and constitutes an extension of it. The authors showed that it results in lower source location bias errors than the standard CSS method when errors are present in the transformation matrices [66]. It is said to provide greater statistical stability and threshold observation times than previous common methods. The technique is also computationally intensive however, requiring a covariance matrix computation for each bearing angle of interest. It expresses the steered array output as

$$y_{SCM}(t,\theta) = \sum_{j=1}^{J} \boldsymbol{T}_j(\theta)\boldsymbol{Y}_{SCM}(f_j)e^{j\omega_j t} \tag{2.36}$$

with

$$\boldsymbol{T}_j(\theta) = \begin{bmatrix} e^{j\omega_j T_0(\theta)} & 0 & \cdots & 0 \\ 0 & e^{j\omega_j T_m(\theta)} & & \vdots \\ \vdots & & & \\ 0 & & \cdots & e^{j\omega_j T_{M-1}(\theta)} \end{bmatrix} \tag{2.37}$$

yielding the steered covariance matrices

$$\boldsymbol{R}_{SCM}(\theta) = \sum_{j=1}^{J} \boldsymbol{T}_j(\theta)\, \boldsymbol{R}(f_j) \boldsymbol{T}_j(\theta)^H \,, \tag{2.38}$$

where ω_j is the angular frequency $\frac{2\pi j}{\tau}$ corresponding to frequency f_j, and the conventional covariance matrix for the sub-band at frequency f_j is

$$\boldsymbol{R}\big(f_j\big) = E\big\{Y(f_j)Y(f_j)^H\big\}\,. \tag{2.39}$$

Clearly from this formulation the covariance matrix is steered to each angle of interest. Krokik and Swingler characterized their SCM as a special case of CSS as it takes, "the same form as the coherently focused covariance matrix proposed by Wang and Kaveh for the case where all sources in the group are in the same group." They later focused their research on spatial resampling to achieve frequency invariance [67]. Spatial resampling of a linear array entails utilization of uniform element spacing that varies by frequency resulting in array characteristics that are frequency invariant. An infinite number of array elements is unfortunately required to achieve perfect invariance using this technique. Optimization and interpolation can be used to achieve minimal errors in performance for a given finite array, but the technique once again becomes quite computationally intensive.

2.5.5 Beamforming Invariance Coherent Signal Subspace (BI-CSS)

The method of Lee is known as the Beamforming Invariance Coherent Signal Subspace (BI-CSS) technique. It applied frequency invariant beamforming matrices to wideband direction finding, but the technique requires reference beams with desired properties for a given array at a reference frequency. It then minimizes a measurement norm between the reference beams and beamforming matrices at other frequencies of interest [68]. The $\boldsymbol{T}_{k,BI-CSS}$ matrices developed by Lee are very similar to the transformation matrices of the previous methods in terms of problem formulation. They differ significantly in the fact that they are formulated as frequency invariant beamforming matrices as well as transformation matrices. Whereas the $\boldsymbol{T}_{k,RSS}$ and $\boldsymbol{T}_{k,R-CSM[i]}$ matrices are frequency dependent and AOA dependent, the $\boldsymbol{T}_{k,BI-CSS}$ matrices are frequency independent and AOA dependent. The AOA dependence is implemented as a series of digital beamforming matrices over the field of view that effectively mitigate the need for an initial estimate of AOA. The solution for Lee's method is given by the solution to

$$\boldsymbol{T}_{k,BI-CSS} = arg\left\{\min_{\boldsymbol{T}} \int_{-\frac{1}{2}}^{\frac{1}{2}} \|\boldsymbol{T}\boldsymbol{a}(f_k,\theta) - \boldsymbol{T}_0\boldsymbol{a}(f_0,\theta)\|_F^2 w(\theta) d\theta\right\}, k = 1,2,\cdots,K-1\ . \tag{2.40}$$

The solution is given by

$$\boldsymbol{T}_{k,BI-CSS} = \boldsymbol{T}_0\boldsymbol{S}_k^H\boldsymbol{U}_k^{-H} \tag{2.41}$$

where

$$\boldsymbol{S}_k = \int_{-\frac{1}{2}}^{\frac{1}{2}} \boldsymbol{a}(f_k, \theta)\boldsymbol{a}^H(f_0, \theta)w(\theta)d\theta \tag{2.42}$$

and

$$\boldsymbol{U}_k = \int_{-\frac{1}{2}}^{\frac{1}{2}} \boldsymbol{a}(f_k, \theta)\boldsymbol{a}^H(f_k, \theta)w(\theta)d\theta \ . \tag{2.43}$$

$\boldsymbol{T}_0$ is the reference focusing matrix and $w(\theta)$ is a generic weighting function. Ward, Ding and Kennedy [69] extended Lee's method based on further frequency invariant techniques discussed by Ward, Kennedy and Williamson [70]. Their method is similar to Lee's except that their beamforming matrix is composed of beam shaping Finite Impulse Response (FIR) filters that focus the beams in the time domain. The technique eliminates any need for frequency decomposition. It is a considerable improvement in efficiency over previous methods, but is generally only discussed in the context of linear arrays with limited fields of view.

Hong, Demmel and Russer used a technique similar to Lee as well, but extended it to arbitrary arrays [71]. Ward and Abhayapala once again updated the beam space approach to include operation in the near field [72]. Such a near field formulation is clearly not applicable to most airborne applications that are the primary concern of the present research.

In [41], Hong and Russer combined spatial interpolation in a manner similar to the

technique of Krolik and Swingler [67] with the beam space processing method. This technique is said to incorporate Spatially Interpolated Wideband Beamformers (SIWB). In order to account for a wide bandwidth, the authors chose to utilize anisotropic elements with element spacing larger than the typical half wavelength of the frequencies of interest. The directionality of the elements helps to reduce undesirable sidelobes and ambiguities. The authors construct beamformer networks of such SIWB's and process the beam space output with narrowband MUSIC. With respect to signal subspace processing in frequency invariant beam space, the method is similar to signal subspace processing in true time delay beamformer bank beam space, but the beamforming construct is very different. Although the method is shown to result in higher resolution of closely spaces sources than CSS for detected signals, the authors limit its use in several ways. The SIWB beamformer network is frequency invariant, but not spatially diverse, with the field of view being evidently limited by the element gain. The field of view given for the example demonstrated by simulation is $70°$ to $110°$, half that of the preponderance of examples demonstrated in this dissertation. In addition, the fractional bandwidth is limited as well with the modeled signals having 28.6% bandwidth, while this dissertation demonstrates the methods with signals of 40% bandwidth. Despite these limitations, Hong and Russer show that this method "enhances the resolution of spectral estimation and reduces root mean square error of AOA estimation without increasing the number of array elements."

Lee's method and extensions to it are perhaps the most similar developments to the

novel method introduced in this dissertation and share certain properties with it such as elimination of the need for preliminary, iterative estimation and operation within a limited field of view. They differ in that the beamformers are implemented as conventional beamformers with phase shifters rather than exploiting the properties of a true time delay beamformer bank.

Valee and Kabal discussed some alternate approaches including least squares techniques, [73] and [74]. Their formulation is once again an extension of the CSS technique, but relies on the observation that if the product of the transformation matrix and its conjugate transpose is uniform over the frequency range of interest, then the focusing is lossless. This optimizes performance, but increases computational complexity as compared to many of the other methods. Agrawal and Prasad reviewed several of the signal subspace based techniques and harkened also to least squares and maximum likelihood approaches [75]. They show that an advantage in processing complexity can be obtained by considering only spatial aspects of the data rather than the spatio-temporal framework of most formulations. They also show that although incomplete, spatial only modeling of the data can yield adequate results in many practical situations.

2.5.6 Specific Signal Model-Based Approaches

A model of process construction useful in certain circumstances is that which uses knowledge of a particular signal type in the design of the signal processor. Use of the

signal type in this manner is thought to potentially provide some benefit in efficiency or effectiveness in the process. Consider for example the work of Gershman and Amin in AOA estimation for Frequency Modulated (FM) signals using the space time-frequency distribution [76]. The method is again based on CSS, but utilizes a transformation with the constraint,

$$\boldsymbol{T}^H(f_j)\boldsymbol{a}(f_j(t),\theta) \approx \boldsymbol{a}(f_0,\theta)\,, \tag{2.44}$$

such that the frequency response is a function of time. Thus the coherent integration is said to involve a set of time-frequency points rather than frequency-only points as in the previous CSS method. This approach breaks the signals into their constituent components in space, time and frequency, and then uses techniques related to MUSIC to perform the AOA estimation. Feng, Zhao and Yin built on this approach and utilized chirplet-based transforms [77]. The chirplet is said to be a windowed frequency modulated pulse whose joint time-frequency energy density is the Wigner-Ville distribution. Cong and Zhuang considered a hybrid Time Direction of Arrival (TDOA) and AOA approach for direct sequence spread spectrum type signals [78]. The method is developed in the context of very inexpensive cellular device receiver location and thus utilizes application specific approximations and assumptions that are not generally applicable. Gelli and Izzo introduced a method that is based on CSS and exploits the cyclostationarity property commonly exhibited by man-made signals [79]. This method could be useful for cases where similarly modulated signals occupy the same bandwidth

such as multiple access spread spectrum communications, but once again is computationally expensive.

Among the numerous other developments in wideband AOA estimation is the method of Delmas and Meurisse who systematically evaluated the performance of various narrowband approaches in processing wideband data [80]. They characterized various methods in terms of their performance with respect to changing fractional bandwidth

$$\beta = \frac{MB}{f_0} \tag{2.45}$$

for signal bandwidth B and center frequency f_0 and quite interestingly found that the standard MUSIC algorithm is robust up to $\beta = 1.8$ for moderate signal to noise ratio. These results are consistent with the results for MUSIC performance in the center sub-band to be discussed in 7. The mean square error estimator was also found to be robust up to approximately $\beta = 1.8$.

Various authors have investigated the extension of array principles to vector sensor arrays. We define a vector sensor to be one that has the form

$$\boldsymbol{X}_I(t) = [x_1(t), x_2(t), \dots, x_I(t)] \tag{2.46}$$

where each $x_i(t)$ is a waveform component of the I-vector, $\boldsymbol{X}_I(t)$. In [81], Hawkes and Nehorai discussed fast wideband algorithms for vector sensor arrays and consider performance limits in this context. They developed a weighted least squares approach and presented results for a vector acoustic sensor array for underwater applications.

Wide bandwidths were discussed but not fully exploited as the focus was on application specific topics with limits on the bandwidth. Chen and Zhao formalized a vector sensor construct for CSS processing by extending the theory to the vector case and showing that a straightforward extension of the scalar transformation focusing matrices is sufficient in the vector case.

2.5.7 Test of Orthogonality of Projected Subspaces (TOPS)

Yoon, Kaplan and McClellan developed yet another extension of the CSS method called the Test of Orthogonality of Projected Subspaces (TOPS) method. This method extended wideband AOA estimation to the case of arbitrarily shaped arrays and is said to not require a course initial AOA estimate, but is still shown to be of greater computational complexity than several other methods including standard CSS [83]. The method uses a transformation matrix based on equation (2.25) for each AOA of interest which is given by

$$\boldsymbol{T}_j(\theta_j) = \begin{bmatrix} e^{j\omega_j v_0 sin(\theta_j)} & 0 & \cdots & 0 \\ 0 & & e^{j\omega_j v_m sin(\theta_j)} & \vdots \\ \vdots & & & \\ 0 & & \cdots & e^{j\omega_j v_{M-1} sin(\theta_j)} \end{bmatrix}. \tag{2.47}$$

The TOPS method incorporates an orthogonality test between the signal and noise subspaces for each resulting transformation. The authors suggested that if orthogonality is preserved, then the AOA should be considered a true AOA [83]. In a

related topic, several researchers have studied tracking of the AOA for multiple wideband moving targets. These include Yan and Fan who exploited the cyclostationary signal property for a least squares tracking algorithm as well as a Kalman filter [84] and El-Keyi, Kirubarajan and Gershman, who tracked the adaptive wideband beamformer weights with an extended Kalman filter [85].

2.5.8 Sellone's Robust Coherent Signal-Subspace Method (R-CSM)

Sellone's method can be viewed as a series of special cases of the RSS technique. His paper also provided an excellent review of many of the preceding methods, however these are typically computationally expensive or exhibit other limitations [86]. He showed that the RSS technique results in a family of solutions rather than a unique solution for the case where the number of antenna elements is greater than the number of sources. Sellone pointed out that for the case of $M > L$, i.e., the number of elements greater than the number of sources, the RSS solution leads to a class of lossless transformation matrices rather than a single unique solution. He exploited this trait to interject additional constraints to optimize the process for inaccuracies in frequency alignment and AOA estimation accuracy. He calls his updated process the Robust Coherent Signal-Subspace Method (R-CSM). It is an iterative technique similar to RSS except that it imposes additional constraints appropriate for each processing step. For the first step it imposes an integral over the array field of view to increase robustness to AOA since the first processing step is performed without any preliminary estimate of

source AOA. The first step of R-CSM is given by the jth frequency sub-band to reference frequency transformation matrix

$$\boldsymbol{T}_{R-CSM,j}(0) = \boldsymbol{V}_j \boldsymbol{U}_j^H \tag{2.48}$$

where $\boldsymbol{V}_j$ and $\boldsymbol{U}_j$ result from the singular value decomposition of the matrix

$$\boldsymbol{Q}_j = \int_{0^\circ}^{180^\circ} \boldsymbol{a}(f_j,\theta)\boldsymbol{a}^H(f_j,\theta)w(\theta)d\theta = \boldsymbol{U}_j \boldsymbol{\Lambda}_j \boldsymbol{V}_j \, . \tag{2.49}$$

for a system with field of view in the interval $[0^\circ, 180^\circ]$. Subsequent processing iterations of R-CSM utilize the knowledge of estimated source AOA from the previous step or iteration by limiting the integral to selected regions of the field of view in the vicinity of these AOA estimates as in the $\boldsymbol{Q}_{j,i}$ matrix for singular value decomposition associated with transformation matrix for iteration i,

$$\boldsymbol{Q}_{j,i} = \int_{\theta_1}^{\theta_2} \boldsymbol{a}(f_j,\theta)\boldsymbol{a}^H(f_j,\theta)w(\theta)d\theta \tag{2.50}$$

where the integral is over the interval $[\theta_1, \theta_2], 0^\circ \leq \theta_1 < \theta_2 \leq 180^\circ$. It is clear from the description of these transformations that the integral bounds can be made successively narrower as the algorithm progresses. Sellone uses the term robustness boundaries for the integral bounds. The transformation matrices resulting for all algorithm iterations following the initial processing stage are described in two steps. The first step utilizes the vector of estimated AOAs from the previous stage to obtain interim transformation matrices and the second step yields the unique focusing matrix

using the previously calculated interim matrices and the integral around selected regions in the vicinity of the estimated AOAs. The integral regions are somewhat arbitrary, but Sellone suggests exponentially narrowing them around the estimated AOAs as processing proceeds. The method yields excellent results in many cases, but significantly increases computational expense beyond the previous methods.

2.5.9 Summary of Wideband Methods

This section considers the wideband processes discussed in the previous sections and the manner in which they operate on their respective domain data. For any typical wide method, the data across some wide frequency range are collected and processed over some length of time over some spatial extent. The spatial domain may represented by the physical array made up of many individual antenna elements (element space), or may be the output of beamformers whose data are made up of combinations of the element data (beam space). Our qualitative view may be thought of in terms of a process flow of space-frequency domain data as depicted in Fig. 10 through Fig. 13.

Methods such as CSS and RSS that require a preliminary estimate in order to construct the transformation matrices are depicted in Fig. 10 that shows a feed forward mechanism to symbolize the construction. The processing can then be viewed as collapsing in the frequency domain into a single reference frequency in element space for processing as if it were a narrowband process. The coherent integration process by which CSS and RSS are seen to result in a compression of frequencies of interest into a

single reference frequency has been shown to result in the ability to successfully process signals whose signal to noise ratios are lower than those successfully processed by incoherent methods such as processing sub-bands separately then incoherently integrating the results. Both of these methods are iterative due to errors caused by inaccuracies in AOA estimation since the transformation matrices are dependent on the estimates.

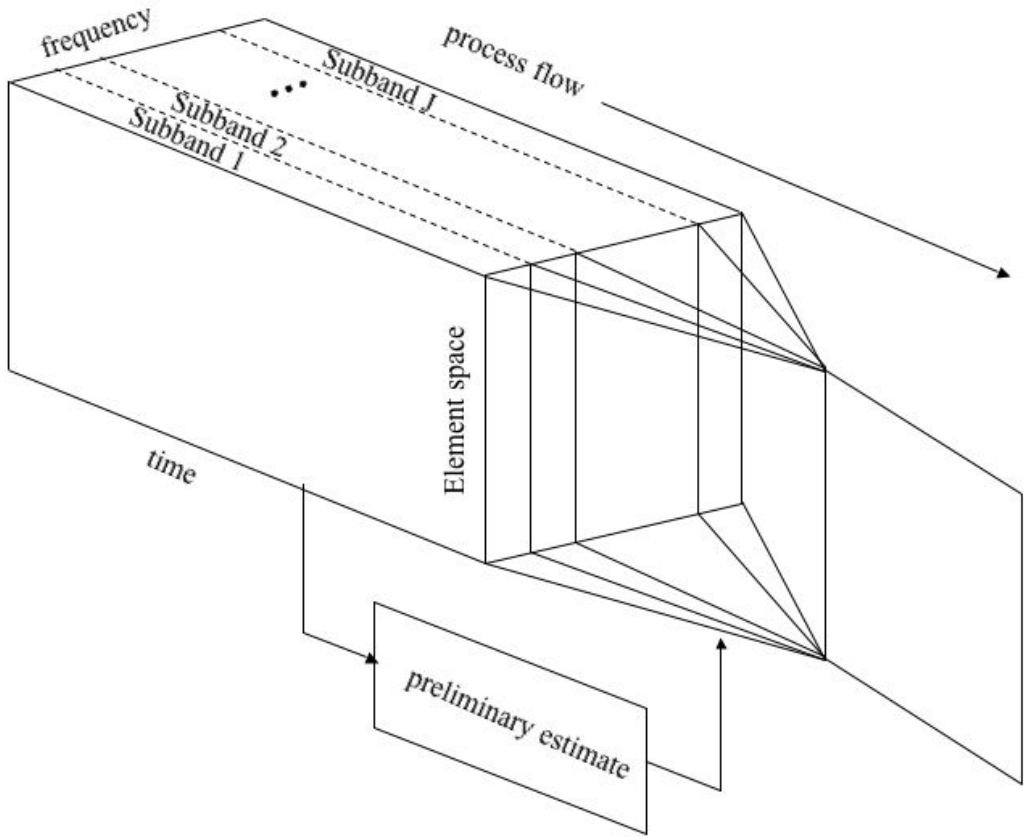

Fig. 10. Wideband methods such as CSS and RSS filter the data into sub-bands. Transformation matrices map all sub-bands into a single reference band that depends on a preliminary angle of arrival estimate.

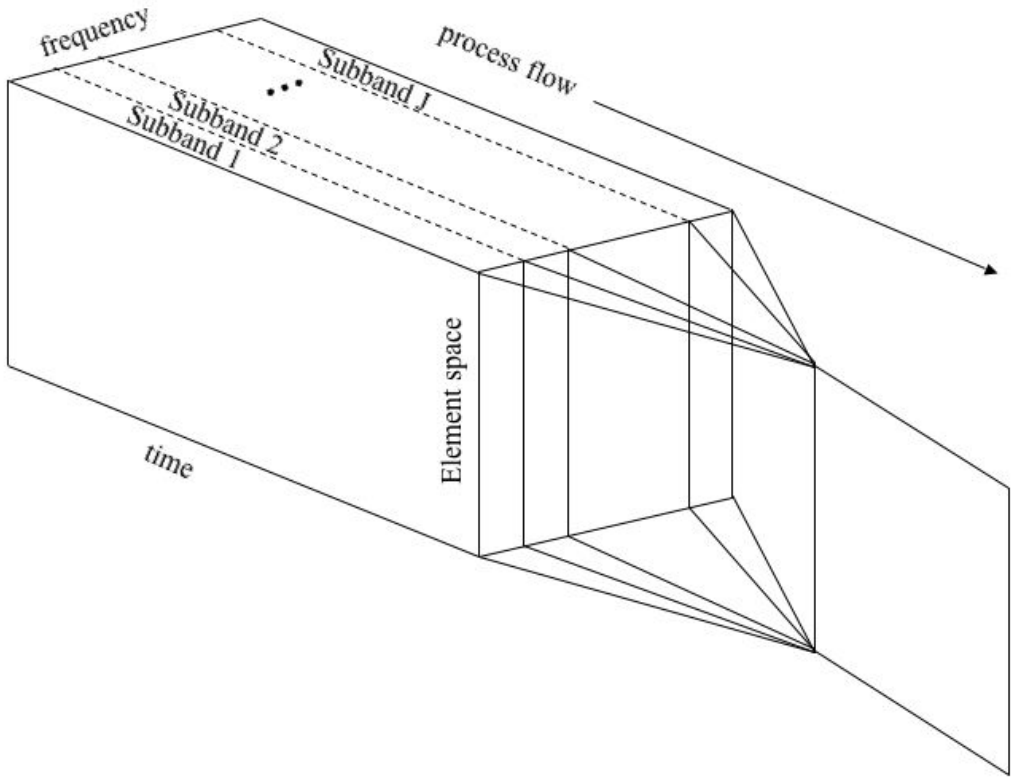

Fig. 11. Methods such as R-CSM and BLT transform the data by filtering, but do not require a preliminary estimate. The data are processed in element space.

Fig. 11 is similar, but depicts methods that do not require a preliminary estimate such as R-CSM and BLT. The elimination of the preliminary estimate requirement is an advantage, but the data for these methods are still in element space implying significant computational expense for systems that need large numbers of elements due to high gain or other requirements. R-CSM and BLT are very similar in terms of process flow, but do not require an initial estimate. They differ from each other in that R-CSM is iterative and BLT is not.

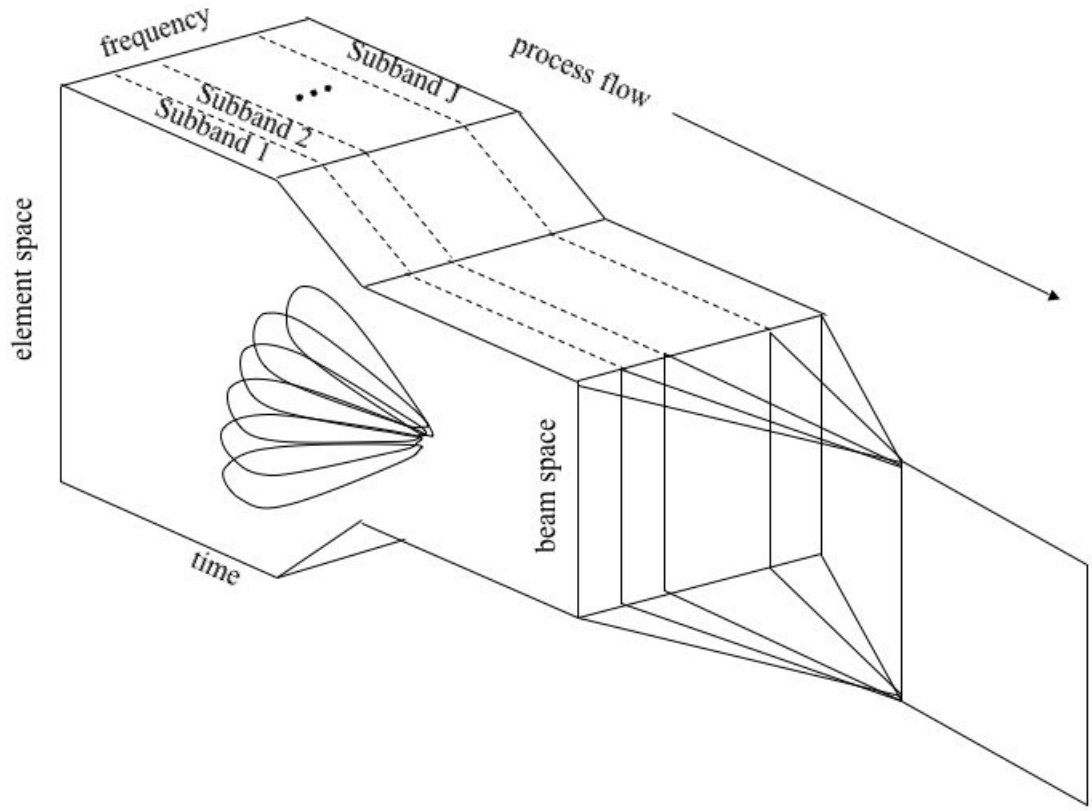

Fig. 12. BI-CSS seeks to reduce computational expense by processing in beam space rather than element space. It requires a beamformer bank for each sub-band, then frequency transformation in beam space.

Methods such as BI-CSS utilize banks of beamformers to transform the data from element space to beam space outside of the process that collapses the data in the frequency domain. This represents an improvement in signal subspace processing computational expense, but adds additional steps to the preprocessing. Some such methods, including BI-CSS, require a complete beamformer bank for each sub-band across the frequency domain.

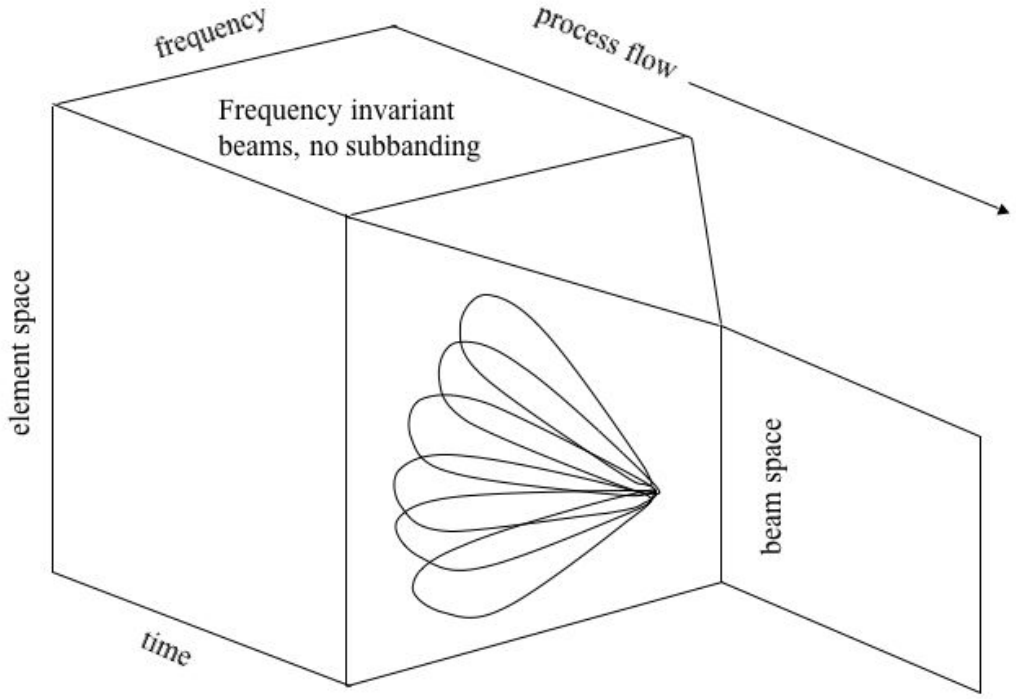

Fig. 13. Greater efficiency might be obtained by a beamformer bank transformation that could simultaneously process all frequencies into beam space.

Alternately, Fig. 13 depicts a concept for simultaneously performing a reduction in the scale of processing expense by utilizing beamformers constructed from frequency independent time shifts. The beamformer bank in this case accounts for frequency diversity and spatial diversity simultaneously. A beamforming technique such as digital true time delay implements beam space transformation and frequency compression simultaneously.

2.6 Element Space Versus Beam Space

We make a distinction between processing in the element space as opposed to the beam space. Fig. 14 shows some block diagrams of example architectures by which we contrast these spatial domains. Fig. 14*a*) is an example of element space signal processing that implements some process on the data from individual antenna elements. Note that for sake of clarity we ignore other components possibly associated with the element data stream that are not pertinent to the present discussion such as filters and tuners. The element space process can be any one that operates on the element data or combines the element data.

Fig. 14*b*) is a typical M-element space beamformer that includes M phase shifts or time delays, M beamformer weights for beam shaping such as sidelobe suppression, and a summer that combines the M-element data streams into a formed beam. The distinction between element space processing and the element space beamformer is largely a question of terminology as observation of the diagrams makes it obvious that the element space beamformer can be viewed as a special case of the element space processor. The element space processor is simply a more general term for any process that operates on the element data, while the element space beamformer is a particular element space process that forms a beam.

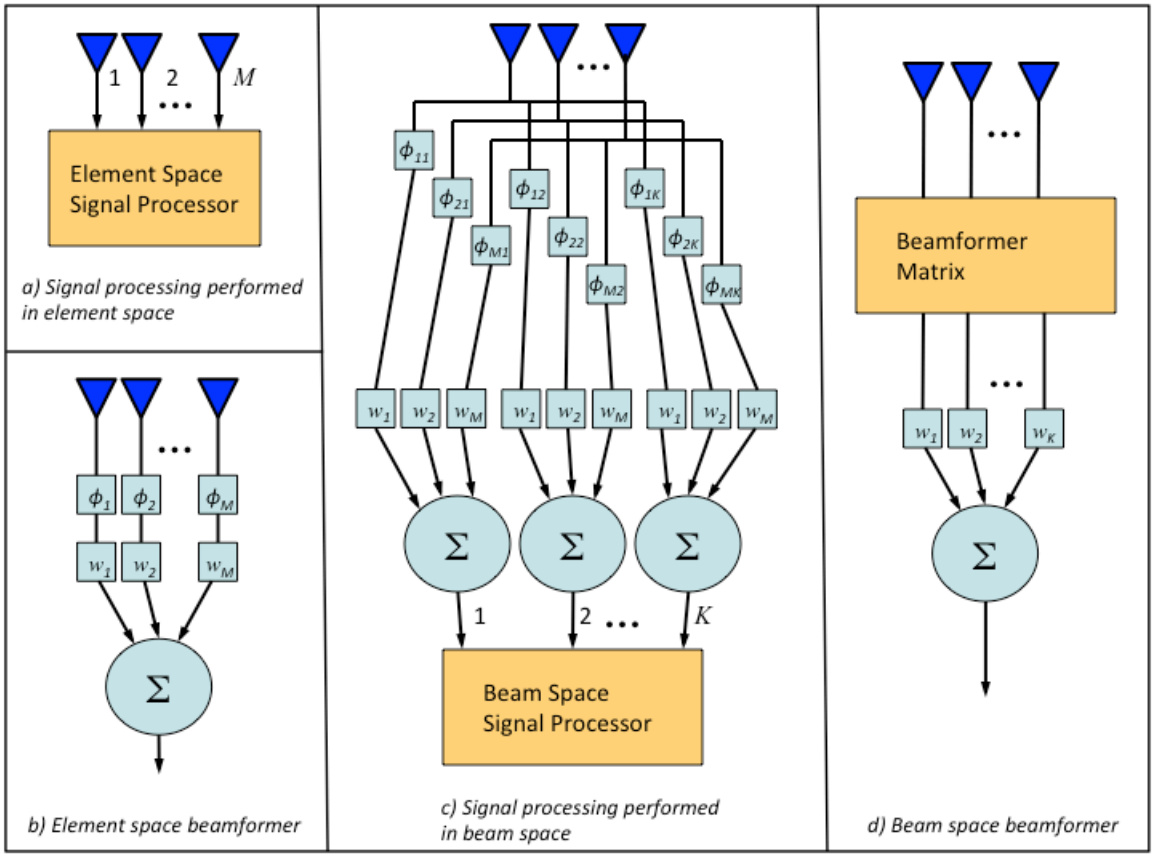

Fig. 14. Examples of element space and beam space architectures.

Fig. 14*c*) shows an architecture for beam space signal processing. Beam space processing implements K element space beamformers that produce K beam data streams. The beam space process can be any one that operates on the beam data or combines the beam data. *d*) shows an example block diagram of a beam space beamformer that, similar to the element space description, can be viewed as a special case of a beam space processor. The beamformer matrix may be implemented in any number of ways to include Fourier Transform beamformers. Reference [100] provides a good review of such algorithms suitable for use in the beamformer matrix block.

The novel methods described in this dissertation primarily fall into the category of beam space processing methods as shown in Fig. 14*c*) that take advantage of the ϕ_{mk}'s being implemented as true time delays, not phase shifts.

2.7 True Time Delay Beamforming

Conventional beamforming using phase control is subject to frequency dependence. A number of efforts have demonstrated wide bandwidth antenna arrays and beamformers using True Time Delay (TTD). Ideally the time delay is uniform over all processed frequencies permitting frequency independent beam patterns in the system. Examples of relevant efforts are documented in [27], [31], [34], [35], [36], [100], [102], and [103].

Consider a comparison of phase shift control beam steering to TTD control beam steering as depicted in [27]. Referring to Fig. 15 the physical distance the wavefront travels from one antenna element to its nearest neighbor is

$$\Delta R = d\cos(\theta) \tag{2.51}$$

where d is the element-to-element spacing of the antenna elements and θ is the steering direction for the beamformer. The phase shift required to correspond to the distance ΔR for a waveform of wavelength λ is

$$\Delta\phi = 2\pi\frac{\Delta R}{\lambda}. \tag{2.52}$$

In turn the corresponding beam direction θ is

$$\theta = \cos^{-1}\frac{\Delta R}{d} = \cos^{-1}\frac{\lambda\Delta\phi}{d2\pi} \tag{2.53}$$

which is obviously a function of the wavelength of the processed emission. Fig. 15(a) shows the phase shift control case. Alternatively TTD control as depicted in Fig. 15(b) utilizes a delay unit length $\Delta L = \Delta R$ and corresponding time delay of

$$\Delta\tau = \frac{\Delta R}{c} = \frac{d\cos(\theta)}{c} \tag{2.54}$$

for speed of the radiation, c, which is not a function of wavelength, i.e., the time-delays are independent of source signal frequency.

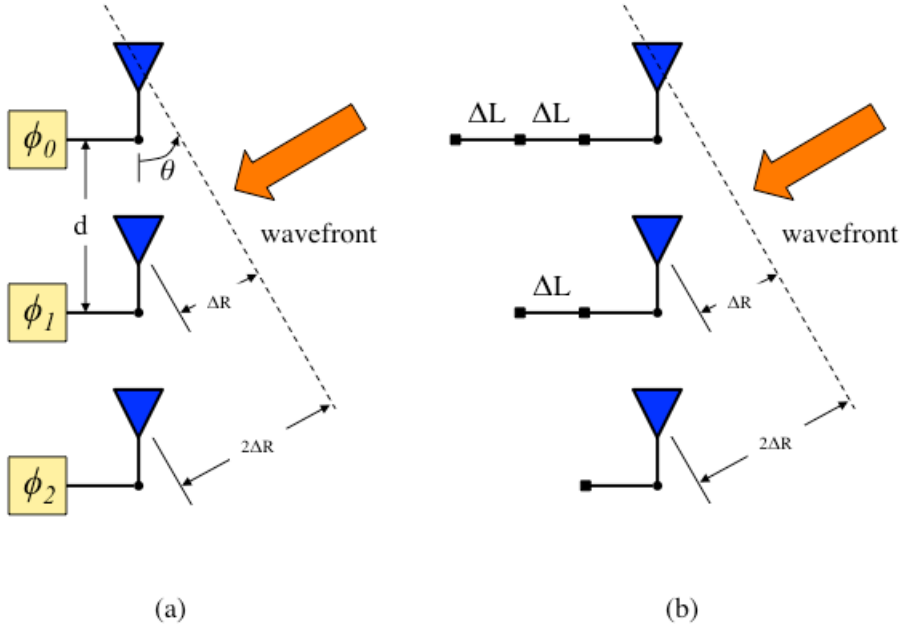

Fig. 15. Comparison of beam steering with (a) phase shifter control and (b) time delay lines.

We can further examine the array factor associated with steering the beam with phase shifters and that associated with steering the beam with time delays. It can be shown that the array factor for phase shifter control for the ULA is, [104], [105],

$$G_{ap}(\theta,\lambda) = \frac{\sin^2[M\pi d\left(\frac{\cos\theta}{\lambda}-\frac{\cos\theta_0}{\lambda_0}\right)]}{M^2\sin^2[\pi d\left(\frac{\cos\theta}{\lambda}-\frac{\cos\theta_0}{\lambda_0}\right)]}, \tag{2.55}$$

where θ_0 is the angle for the desired steering direction and λ_0 is the fixed wavelength

used to determine the particular phase shift,

$$\Delta\phi_0 = \frac{2\pi d\,\cos\theta_0}{\lambda_0}, \tag{2.56}$$

that is used to steer the array such that $\Delta\phi - \Delta\phi_0 = 0$. The array factor associated with the particular time delay,

$$\Delta\tau_0 = \frac{d\,\cos(\theta_0)}{c}, \tag{2.57}$$

is by substitution [104]

$$G_{a\tau}(\theta,\lambda) = \frac{\sin^2[M\pi\frac{d}{\lambda}(\cos\theta - \cos\theta_0)]}{M^2\sin^2[\pi d(\cos\theta - \cos\theta_0)]}. \tag{2.58}$$

The array factors of equations (2.55) and (2.58) are plotted in Fig. 16 where a) is the result for phase shift steering and b) is the result for time delay steering. These results are for 3 different frequencies using a 64-element linear array with element spacing of $\frac{\lambda}{2}$ at $12GHz$ with phase shifter values computed based on the center frequency of $10GHz$ and for steering direction, $\theta_0 = 20^\circ$ [104]. Fig. 17 depicts similar plots for beams steered to $\theta_0 = 75^\circ$ using the modeled parameters of Chapter 7, a 16-element linear array with element spacing of $\frac{\lambda}{2}$ at $1.2GHz$ with phase shifter values computed based on the center frequency of $1GHz$.

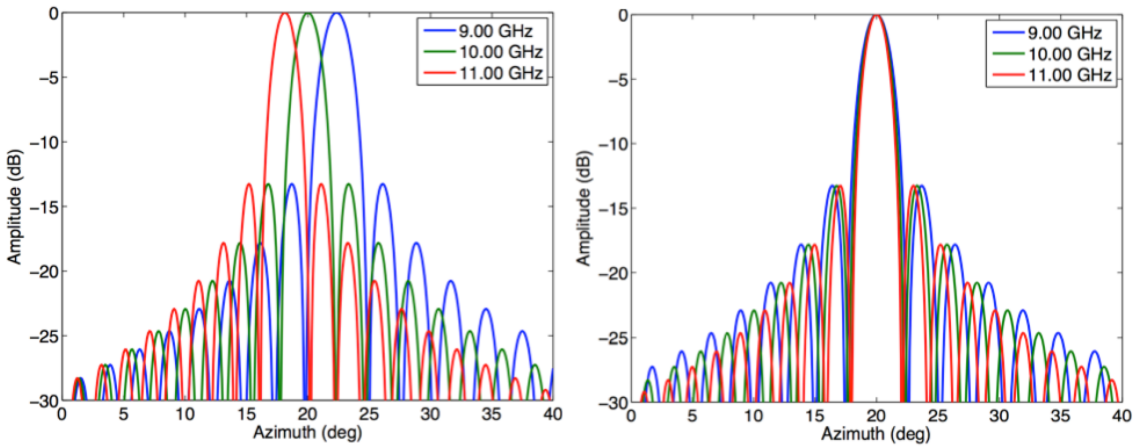

a) Beams steered by phase shifters

b) Beams steered by time delays

Fig. 16. Plots of beams at varying frequencies steered to $20°$ by a) phase shifters, and b) time delays from [104].

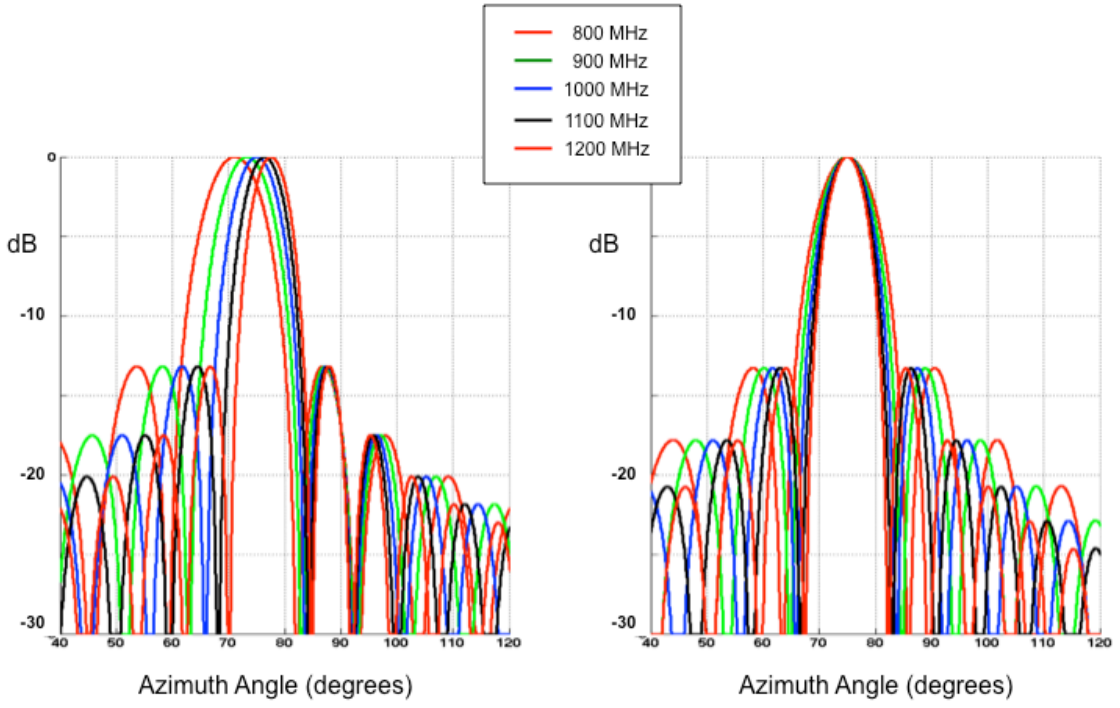

a) Beams steered by phase shifters

b) Beams steered by time delays

Fig. 17. Plots of beams using parameters from the array modeled in Chapter 7 steered to $75°$ by a) phase shifters, and b) time delays.

The distinction between phase shift and time delay also becomes clear when we consider two monochromatic waveforms at different frequencies as depicted in Fig. 18. The black solid line is a sinusoid of frequency f_0 and the blue dashed line is a sinusoid of frequency $2f_0$. This figure is meant to convey the organic signals prior to phase shifting or time delaying so that the effect of these operations may be considered. For phase shift control beamforming [27], a set of phase shifts designed for $\sin(\theta)$ will not in general present the correct phases for similar beam pointing direction. Array antenna designers refer to the phased array phenomenon that results in the distortion of the beam pointing direction due to the frequency dependence of the phase as beam squint [27]. Beam squint manifests as a deformation of the beam as the processed frequency deviates from the design frequency.

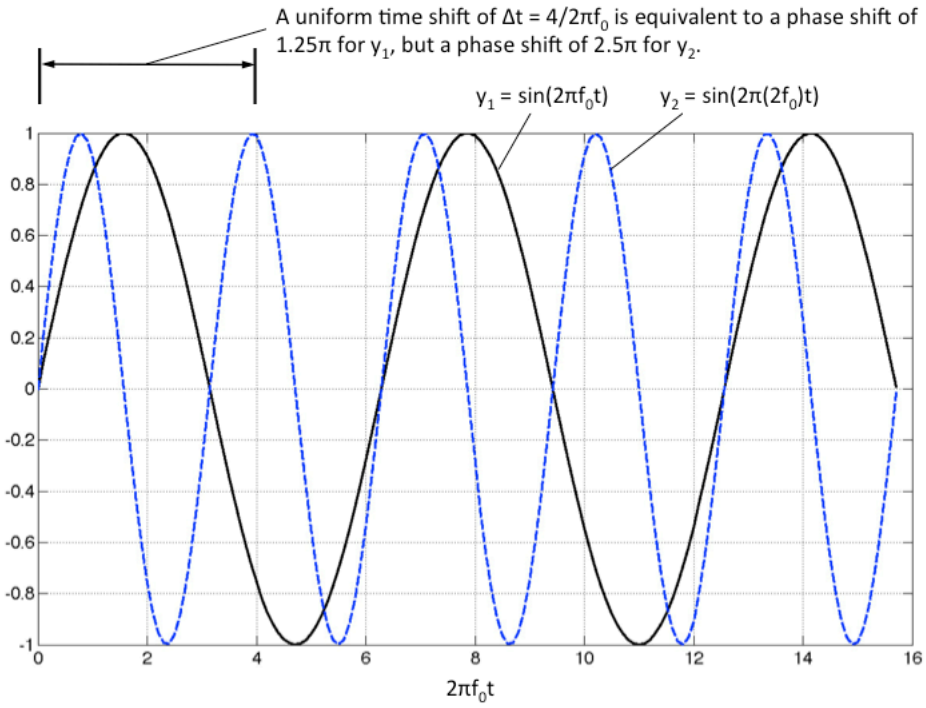

Fig. 18. Comparison of monochromatic waveforms at different frequencies.

Phase shift control of a beamforming system thus exhibits the frequency dependent behavior referred to as beam squint. Fig. 19 depicts examples of beam patterns that display beam squint for a simulated 8-element array described in [35]. For this example, the authors characterized the beam squint as, "a $\pm 4^{\circ}$ beam squint across a $2GHz$ instantaneous bandwidth." Fig. 16 and Fig. 19 are explained mathematically by the array factor of equation (2.55) for their respective array configurations and steering directions.

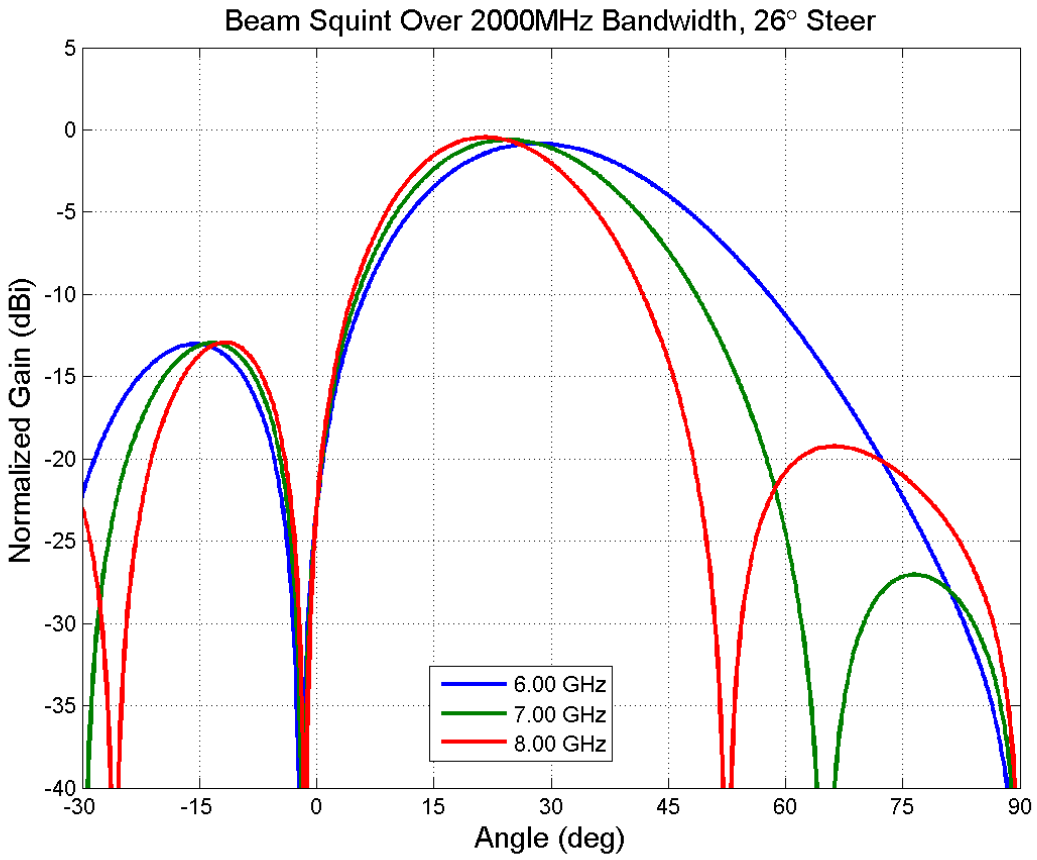

Fig. 19. Example of beam squint modeled over $2\,GHz$ bandwidth for beams steered to $26°$ with conventional phase shifter technology [35].

Fig. 20 shows a plot similar to Fig. 19 but for the parameters modeled in Chapter 7. The relevant parameters are $400MHz$ bandwidth, a 16-element linear array with element spacing of $\frac{\lambda}{2}$ at $1.2GHz$, and with phase shifter values computed based on the center frequency of $1GHz$.

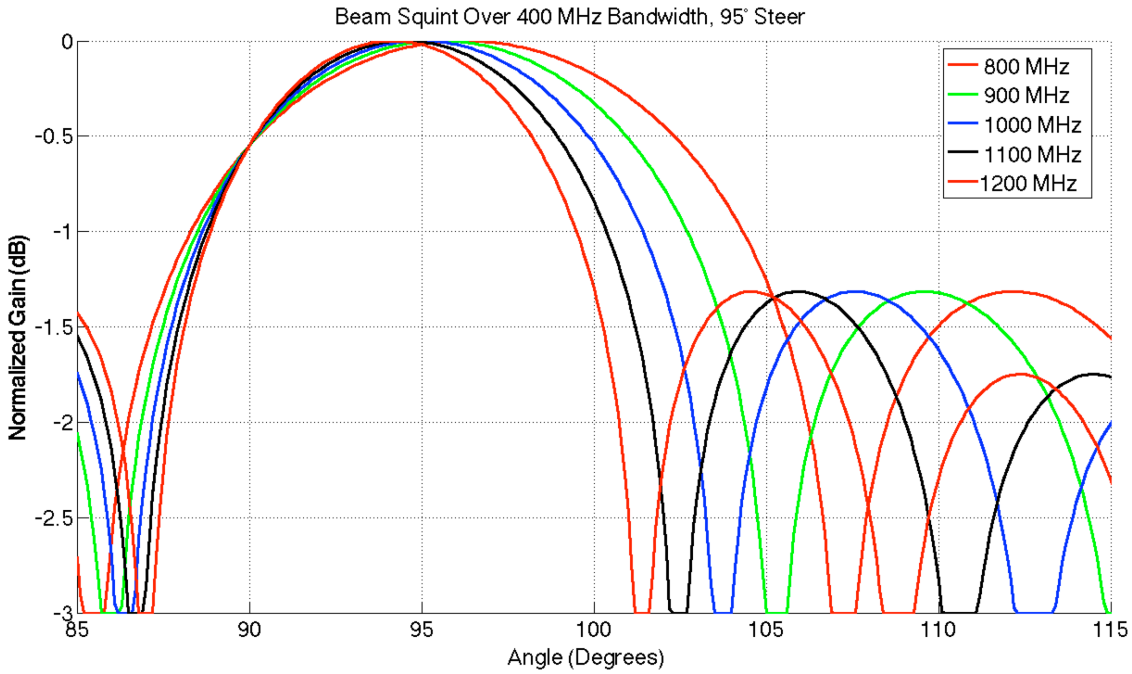

Fig. 20. Example of beam squint modeled over $400 MHz$ bandwidth for beams steered to $95°$ with conventional phase shifter technology

As a numerical example of a typical time delay for implementation of a TTD beamformer, consider a planar wavefront impinging on a ULA such as that shown in Fig. 15. For $\theta = 2^{\circ}$ and element spacing of $d = 0.15m$, which is consistent with half-wavelength spacing for radiation of frequency $1GHz$, the delay line unit length, ΔL, is

$$\Delta L = d\cos(\theta) = 5.23\times10^{-3}m\,. \tag{2.59}$$

This unit length corresponds to a time delay of

$$\Delta\tau = \frac{\Delta R}{c} = \frac{\Delta L}{c} = 17.5ps \tag{2.60}$$

by substitution into equation (2.57).

For wideband systems, the signal processing system analyst must consider the characteristic of group delay. Group delay is the signal delay through a specified portion of the system as a function of frequency, f. Group delay from point a to point b in the system is expressed as

$$\mathrm{T}_{ba} = \frac{1}{2\pi}\frac{\partial \phi_{ba}}{\partial f} \tag{2.61}$$

where ϕ_{ba} is the phase of the signal waveform [104]. Since the ideal TTD component exhibits a characteristic delay that does not vary across the frequency range of interest it thus has group delay, $\mathrm{T}_{ba} = \tau_{ba}$, a constant. Unfortunately realized hardware is never ideal and significant effort is expended to minimize the non-uniformity in group delay for TTD implementations. In particular such realizations as those with optical fiber delay lines and other non-ideal components may require corrections to maintain group delay within desired specifications.

Also of interest are recent developments in photonic architectures for TTD realizations. Among these is [107] that presented results of digital optical formulations that demonstrated 80% bandwidth using fiber optic Bragg gratings. Chen et al. developed a reconfigurable TTD feed designed for increased compactness for wide bandwidth systems [108]. In [109] Lee, Jeon and Jung presented an optical TTD architecture using a tunable laser and dispersion compensating fiber that was said to achieve a wide angle of rotation for the beam pattern.

2.7.1 Reflections on Gabriel's Method

Leading up to Gabriel's advocacy for TTD beamforming systems, in [28] he was an early proponent of the application of spectral estimation techniques to the problem of signal processing of antenna array data for source location. He examined the maximum likelihood method and the maximum entropy method for source location and demonstrated improved resolution as compared to previous techniques for the narrowband case. In [29] he focused on the characteristics of such antenna arrays and discussed the concept of partial adaptivity. Partially adaptive arrays may be more suitable than fully adaptive arrays for certain applications. In particular Gabriel showed that for partially adaptive arrays, the application of high-resolution spectral estimation techniques could exhibit benefits over fully adaptive systems such as faster response, lower processing expense, and system design flexibility. This work is relevant because as Gabriel began to examine extensions to sensor array systems, particularly in terms of broadening of instantaneous bandwidth, TTD beamforming became an important factor in development of such systems.

By the development discussed in [30] and [31] Gabriel's research had led him to consider a set of constraints for effective location of wideband sources. These constraints included a large aperture for high-resolution performance, a scheme that employed few degrees of freedom for efficient processing and low cost, a concession to trade off instantaneous field of view based on spatial sector information, and ease of

frequent calibration. Gabriel found that in order to meet these constraints it was beneficial to utilize TTD beam steering to achieve the desired wideband performance. The TTD system was constructed to utilize spatial linear prediction filters with reference beams. Gabriel considered this construction to represent an alternative implementation of the Wang and Kaveh CSS method with the focusing adjustments realized by the time delays. The primary differences between Gabriel's work and the novel developments described in this dissertation are that Gabriel used the spatial linear prediction filters rather than the formulations presented herein, although at a conceptual level, the constraints described by Gabriel are similar in some respects to those herein. In addition he used a shaped reference beam to constrain the data to a spatial sector as opposed to the design of the beamformer bank presented herein. Note that Gabriel forms his correlation matrices in the frequency domain like the CSS method whereas the novel methods of this dissertation are performed in the temporal and spatial domains.

Gabriel's system, depicted in Fig. 21, was formulated to address several simultaneous constraints. Among these are large aperture size, low cost, and restriction of the instantaneous field of view to a narrow search sector [31].

Gabriel desired to use the maximum available aperture size to achieve high-resolution performance. This constraint is imposed while at the same time not requiring $\frac{\lambda}{2}$ element spacing. The desire for high-resolution is consistent with the same desire we place on the TTD beam-space formulation. In the TTD beam-space method, we maintain a $\frac{\lambda}{2}$

element spacing to avoid ambiguities in the processing result, while Gabriel used a supplementary reference beam. Note in the block diagram of Gabriel's system that the reference beam elements do have $\frac{\lambda}{2}$ element spacing but do not traverse the entire aperture width. In addition, the phase center of the reference beam is displaced from the phase center of the sparse array. Note that Gabriel also refers to the Butler matrix beamformer as an interferometer beamformer. The formulation is permitted to employ sparse array techniques to lower the cost of the system by lowering the number of expensive front-end components compared to a $\frac{\lambda}{2}$-spaced array of similar aperture size.

Referring to Fig. 21, the sparse array element signals are input into a Butler matrix beamformer. Nine beams are constructed from the nine sparse elements, but not all nine are utilized in every processing example. The Butler matrix beams then pass into a beam assignment selector. The beam assignment selector is used to select which beam signals will be utilized in subsequent processing. The number of beams selected by the beam assignment selector is either all nine beams, or some subset of the nine beams. The selected beams are then filtered by the Finite Impulse Response (FIR) filter matrix, which is also termed a transversal filter. Gabriel stated that the purpose of the transversal filter is to permit "adaptivity in the time/frequency domain, in addition to adaptivity in the spatial domain" provided by the spatial beamforming [31]. Note that Gabriel considers the transversal filter parameters such as number of filter taps to be adjustable, and indeed the transversal filter may be bypassed altogether for a given example. The transversal filter outputs and the reference beam signal are then fed into

the estimation algorithm signal processor that combines the weights for both arrays according to

$$\boldsymbol{W}_0 = \boldsymbol{S}^* - \sum_{k=1}^{K} \boldsymbol{W}_k \boldsymbol{b}_k \,, \tag{2.62}$$

using Gabriel's notation, where $\boldsymbol{S}^*$ is the set of beamformer weights for the reference beam, the $\boldsymbol{b}_k$'s are the Butler matrix weights and $\boldsymbol{W}_k$ is the adaptive weight for the kth beam of K total number of beams. When only a subset of K_g of the K beams is used, the associated computational burden for sample matrix inversion on the sample covariance matrix, $\widehat{\boldsymbol{R}}$, is of dimensionality $K_g \times K_g$ rather than $K \times K$.

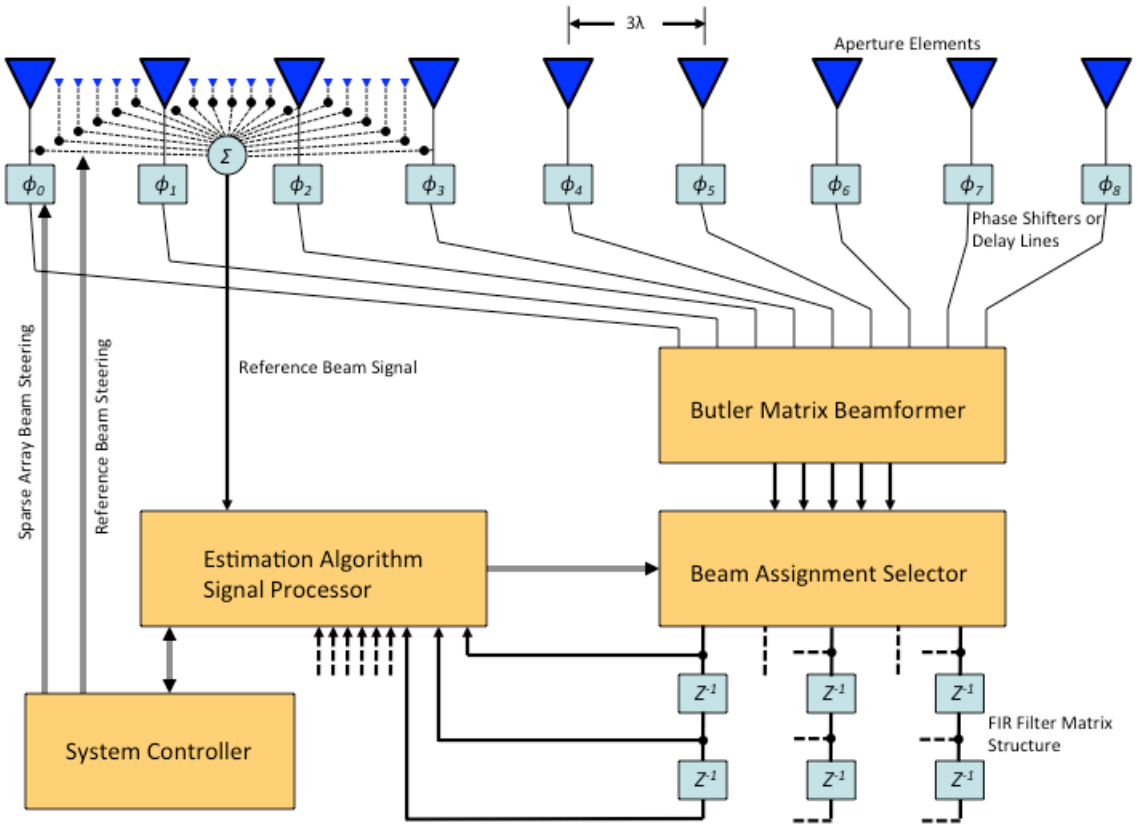

Fig. 21. Block Diagram of Gabriel's System.

The constraints Gabriel described in [31] led to a very specific array design that is not amenable to direct comparison with the ULA's used in the simulations of Chapter 7. The need for a large aperture size while trying to keep the cost for front-end components low led him to choose 3λ as the spacing for the sparse array portion of the system. The filled reference array phase center is displaced 7.5λ from that of the sparse array. Gabriel states that "this displacement is essential to achieving robust spatial estimation performance in our Spatial Linear Prediction Filter (SLPF) systems because it produces a sensitivity to source location in a beam space system in addition to the amplitude

sensitivity derived from beam shapes." On the other hand, the TTD beam space formulation developed in this dissertation is demonstrated to operate without the need for a supplemental reference array.

One of the interesting statements made by Gabriel in [31] is with regard to the number of degrees of freedom required to process a given signal set. Upon using all nine beams to process three signals, the resulting nine Eigenvalues are observed to contain three unique values. Gabriel then states that this corresponds to "the minimum number associated with three spatial point sources … and would permit us to reduce the matrix dimension down to three degrees of freedom, i.e., only three assigned beams for this particular case." Gabriel stopped short of actually providing the details of such an example. In Section 7.4 of this dissertation we consider an example of two sources of similar percent of Rayleigh resolution limit to Gabriel's signal set successfully resolved by only three beams and corresponding 3×3 sample correlation matrix.

2.8 Optimization of Array and Signal Processing Configurations

The source location system can be quite complex. System designs can incorporate antenna arrays that must conform to vehicle outer surfaces such as on an airborne platform and signal processing configurations that must efficiently process large amounts of data with limited resources. Reference [110] reported results of optimization experiments for multiple process, multiple Digital Signal Processing (DSP) processor configurations using a genetic algorithm to improve efficiency of signal

subspace processing for source location problems. In this context the processes can be any procedure that contributes to the solution, uses processor resources, and communicates with one or more other processes. The paper examined cases such as that of Fig. 22 that shows a data flow diagram for a multiple processor DSP configuration. The particular example that was reported utilized an off the shelf DSP card incorporating four TI TMS320C40 DSP chips. Consider for such a configuration that several processes interact in complex ways, that any process can reside on any one of the multiple processors, and that each process can access its processors own dedicated memory as well as memory that is shared among all the processors. One criterion for optimizing this configuration is the time for a given set of data to be processed and produce the data output result. Even for a small number of processors this DSP configuration can be difficult to optimize by hand. The paper showed that the genetic algorithm was capable of generating a process configuration that utilized the available processors and memory more efficiently than the original manually generated configuration.

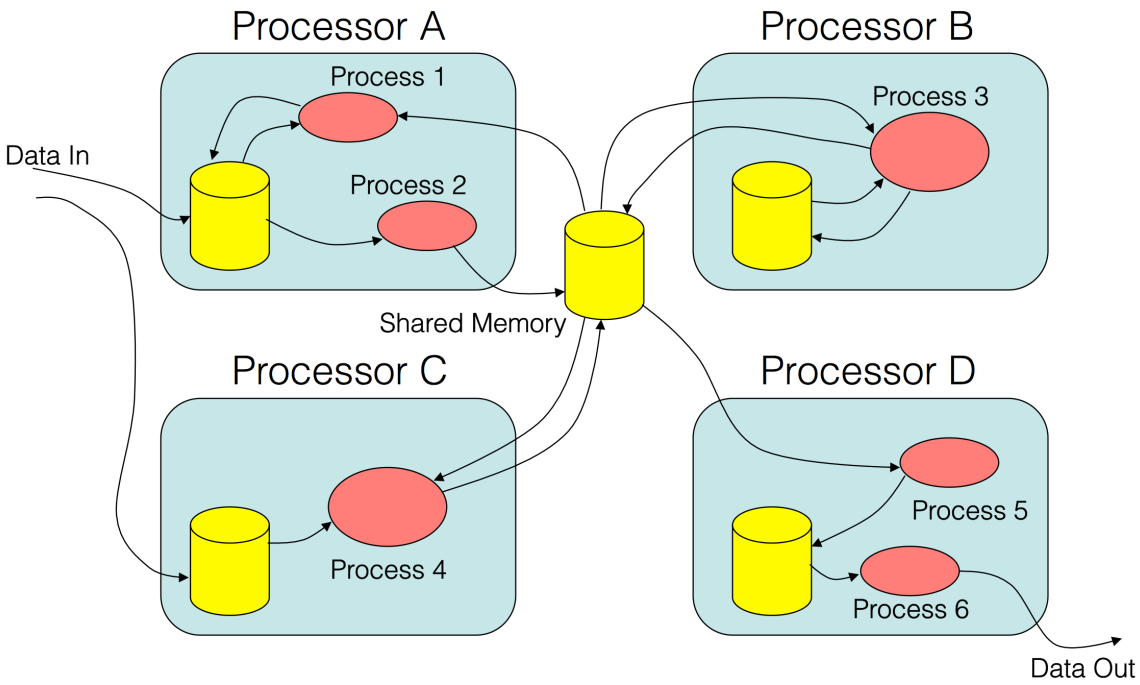

Fig. 22. Hypothetical multiple processor configuration.

Efficient implementation of signal subspace processing algorithms on another DSP configuration was described in [111]. This development specifically targeted wideband applications by examining an implementation of the CSS algorithm that includes:

- Compute 64 sets of 64-point Fast Fourier Transforms (FFT),
- Compute 33 covariance matrices of size 16×16,
- Computation of initial angle estimate using MUSIC,
- Computation of CSS focusing matrix,
- Computation of number of sources,
- Separation of signal and noise subspaces, and

- Compute focused angles of arrival using MUSIC algorithm.

The CSS algorithm was implemented in C and executed on a DIOPSISTM 740 by Atmel. The DIOPSISTM 740 (D740) is a high performance dual-core processing platform for real time applications. The CSS algorithm was modified to comport with the parallel architecture of the selected hardware. The covariance matrices for all the frequency components were estimated and combined to form a single focused covariance matrix so that the narrowband MUSIC algorithm could be applied to the resulting focused covariance matrix. As describe previously in Section 2.2, the CSS algorithm is based on matrix computations and orthogonal transformations, which are computationally intensive. The Eigen decomposition problem is a very important part of this spatial spectrum estimation algorithm. Finding the Eigenvalues and Eigenvectors of the covariance matrix is needed to construct the signal and noise subspaces that the CSS algorithm will use. The particular implementation used the Householder and QR algorithms to compute the Eigenvalues and Eigenvectors of the symmetric covariance matrix [112], [113]. The Householder algorithm is used to reduce the bandwidth of the covariance matrix by transforming it into tridiagonal form. The Eigenvalues and Eigenvectors were then computed using the QR algorithm. The computational cost needed for computing the Eigenvalues and Eigenvectors of a tridiagonal matrix is much smaller than that of the original symmetric matrix.

To implement this CSS algorithm in real-time, hardware capable of executing millions of operations per second is required. A general purpose DSP was selected for

implementation because of its ease of programming. Also, the DSP is suitable for matrix and floating-point computations. The DIOPSISTM 740 (D740) is a high performance dual core-processing platform for real time applications [114]. The D740 is optimally suited for floating point applications complex domain computations. The ARM7TDMI (ARM) embedded microcontroller core is also incorporated into the DSP architecture. It is equipped with several peripherals and on-chip memories. The main components of the DSP subsystem are the core processor, the on-chip memories and the interfaces to and from the ARM subsystem. The DSP has four on-chip memory blocks: the program memory, the data memory, the data buffer, and the dual ported memory shared with the ARM processor. An external memory interface multiplexes the data accesses and the program accesses to and from the external memory. The program memory stores the Very Long Instruction Word (VLIW) program to be executed.

The development in [111] also incorporated the Multicore Application Development Environment (MADE) which is an Integrated Development Environment (IDE) that can be used to develop D740 applications [114]. It includes the C compilers for both ARM and DSP based on GNU compiling tools known as the GNU Compiler Collection (GCC). The C compiler includes a library composed of over 220 functions such as Fast Fourier Transform (FFT), Infinite Impulse Response (IIR) and Finite Impulse Response (FIR) filter creation. Using these tools, a parallel architecture for implementation the CSS algorithm was developed. The parallel architecture was simulated using a single DSP by executing the parallel processes sequentially with the performance measured using the

longest running process in that sequence in terms of number of clock cycles. The purpose of the simulations was to detect and estimate the angles of arrival of two sources located at 20° and 20° using 40 iterations for the QR algorithm. The performance analysis showed that the most computationally intensive tasks were the QR algorithm, the Householder algorithm and the power spectrum computation. Table 2 shows the comparison between the computation time of the single DSP and the computation time of the parallel architecture.

Table 2

PERFORMANCE RESULTS FOR SINGLE DSP AND PARALLEL ARCHITECTURE

Task	Single DSP		Parallel architecture	
	Cycles	Seconds	Cycles	Seconds
Covariance matrix	140000	0.014	42000	0.00042
Householder	260000	0.026	30000	0.0003
QR	100000000	1	2100000	0.021
Power Spectrum	1400000	0.014	47000	0.00047
Total	210000000	2.1	5300000	0.053

Clearly significant advantages in algorithm execution time can be achieved by applying the principles of optimization to signal processing configurations. Much recent activity in signal processing application has involved FPGA development. In [115] the authors considered the development of an FPGA based signal processor targeted specifically for the wide bandwidth direction-finding problem. This work considered operations necessary to implement the CSS algorithm for estimation of the AOA of a signal with a bandwidth of $4GHz$. This requires a high-speed digital signal processor with sampling at a frequency of at least $8GHz$. In order to process the data continuously, a throughput of 8 gigasamples per second (GSa/s) must be maintained throughout the system. The

paper reported the design and simulation of a 64-point Fast Fourier Transform (FFT) processor capable of the required throughput. This FFT processor represents a key building block for the CSS wideband AOA estimation algorithm and was implemented as a radix-4 64-point FFT per the block diagram in Fig. 23.

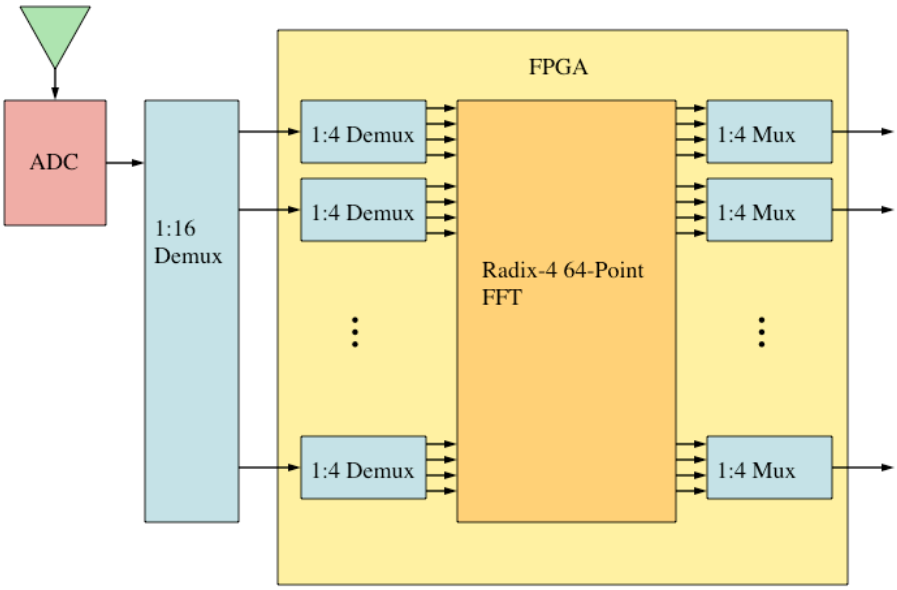

Fig. 23. FFT implementation for CSS algorithm building block.

The device chosen for the implementation was the Xilinx Virtex V. With clock frequencies up to $550MHz$ and up to 1200 input/output (I/O) pins, the Virtex V is ideal for high-throughput applications. With regards to high-speed digital signal processing, the Virtex V contains up to 640 dedicated arithmetic units known as DSP48E slices. Two FFT processors were developed, one with 8-bit samples, and another with 10-bit

samples from the ADC. Both the 8-bit and 10-bit FFT processors meet the timing constraints and yield throughputs of $8.01GSa/s$ and $8.02GSa/s$ respectively. The development resulted in a highly parallel and pipelined architecture for a FPGA based, high speed, FFT processor for wideband AOA applications.

The design of the antenna array for airborne radio direction finding systems is also often not as straightforward as it may at first appear. Many conflicting constraints can often arise in such designs. For example the system architect may desire to simultaneously widen the bandwidth, reduce the radar cross section, maintain high-resolution performance throughout a wide field of view, eliminate ambiguities, maintain a design whose characteristics can be readily modeled in computer simulations and conform to the shape of the platform airframe for aerodynamic purposes. These and other constraints interact in numerous and complex ways, making it virtually impossible, or at least impractical, to attempt to optimize the array by hand. Fortunately system designers can often use experience and engineering judgment to obtain acceptable performance and many tools exist to automate further optimization of the design within the bounds of practical constraints. Engineers have used global optimization algorithms such as genetic algorithms, simulated annealing and others for the design of antenna arrays, for example [116] and [117].

An example of a commercially available direction finding array is that marketed by the Randtron Antenna Systems subsidiary of L3 Communications Corporation. The company has marketed these radio direction-finding arrays for airborne applications such as

Electronic Support Measures (ESM). One of the company's designs is depicted in Fig. 24. Note the multiple sizes of array elements for wide bandwidth application and lack of circular symmetry in the photograph. A circularly symmetric array could tend to exhibit a characteristic uniformity of performance in azimuth, but may also possess undesirable ambiguities. The Randtron documentation states that the array design for airborne applications is designed for good source location estimation performance while incorporating multiple simultaneous constraints such as operational bandwidth, phase tracking, gain, low radar cross section on the installed platform, and aerodynamic properties. These results are achieved by utilizing simulation and modeling tools to predict the performance for these various constraints [118].

Fig. 24. Example wideband airborne radio direction finding array [Image courtesy L3].

The design of such antenna arrays can be quite complex involving numerous engineering trade-offs. It is typically system dependent and application dependent. While the intricacies of the array design are not the focus of this dissertation, it should be noted that this is not an insignificant aspect of the design of a practical system. Additional aspects of the practical application of wideband signal processing in physical systems will be briefly addressed in 5.

2.9 Angle of Arrival Resolution

One of the important capabilities for DF systems is resolution of closely spaced sources. The Rayleigh limit for resolution is defined to be the condition for two beams that occurs when the first null of one beam pattern coincides with the peak of the main lobe of the second beam pattern [119]. This condition is conveniently illustrated in Fig. 25 using $sinc(x) = \frac{\sin(x)}{x}$ functions. The two main lobes are said to be just resolved since the Rayleigh condition applies. As a rule of thumb, the Rayleigh limit is also approximately equal to the $3dB$ beamwidth. Since the concept of resolution is somewhat of a subjective one, we will consider the beamwidth [120] of

$$b = \sin^{-1}\left(\frac{\lambda}{D}\right) \tag{2.63}$$

to be the resolution limit for the conventional beamformer process where D is the aperture width. Using the M-element ULA with d element-to-element spacing, we have

the boresight condition $D = (M-1)d$. Using the example array chosen for the simulation results in Chapter 7, λ is $0.3m$, the center band wavelength, d is $0.125m$, the half wavelength at the upper frequency limit, and M is 16 yielding a beamwidth of $b \approx 9.2^{\circ}$. We use an example of source separation of $7°$ in Section 7.1 to demonstrate resolution of sources beyond the Rayleigh limit.

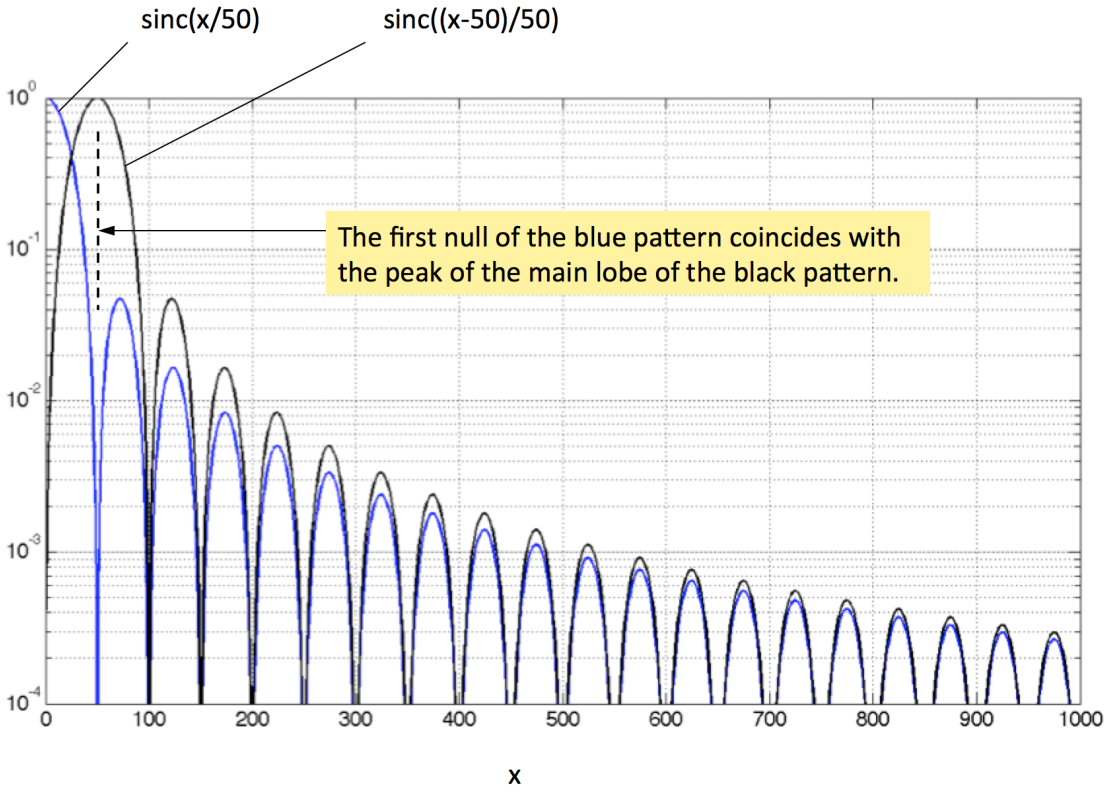

Fig. 25. An illustration of beams that are said to be just resolved.

3 SUBSPACE PROCESSING IN TRUE TIME DELAY BEAM SPACE

3.1 Frequency Independence of the beamformer control

We wish to develop a process that results in a high-resolution estimate of the AOA for multiple wideband sources utilizing the beam space of a bank of a True Time Delay (TTD) beamformers. Fig. 26 shows the same K beamformer bank of M elements as shown in Fig. 1, but now with multiple sources shown as well. We assume the L sources to be in the far field resulting in planar wavefronts with time delays due to the source direction related to each element as $\tau_{s:l,m}$ for the lth source and mth element.

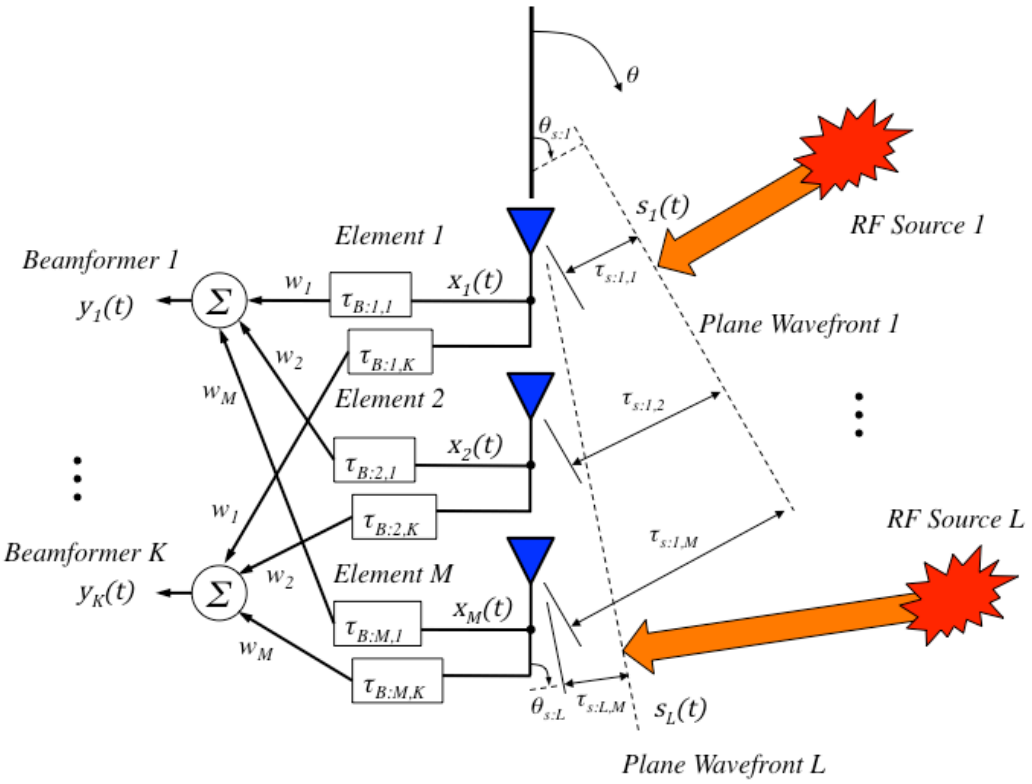

Fig. 26. Beamformer bank block diagram with multiple sources.

Note that the method of Lee, certain extensions to Lee's method, and the work of Gabriel all share some similarity of traits with signal subspace processing in the beam space of a true time delay beamformer bank [30], [31], [41], [68], [69], [70], [71], and [72]. These methods are described, compared and contrasted to the present method in Sections 2.5.5, 2.5.9, and 2.7.1.

The desired characteristic of the process is to exhibit uniform behavior across the frequency range of interest. To this end we express the general kth beamformer for the M element array,

$$y_k(t) = \sum_{m=1}^{M} \mathcal{F}\{x_m\} w_m, m = 1, \dots, M, k = 1, \dots, K, \quad (3.1)$$

where $\mathcal{F}\{\cdot\}$ is a general operator and w_m is a general weighting factor. The weighting factors are used to shape the beam pattern. In particular, as Dolph recognized, Chebyshev coefficients can be used as weights to produce uniformly low sidelobes [121]. Lee mentioned the use of Chebyshev beamformers for a similar application [68]. Frequency independence of the TTD beamformer control mechanism is observed by considering the effect of the mechanism across the frequency range of interest. Consider the TTD beamformer,

$$y_k(t) = \sum_{m=1}^{M} x_m\big(t - \tau_{B:m,k}(\theta_{B:k})\big) w_m, \ k = 1, \cdots, K \quad (3.2)$$

where $\tau_{B:m,k}(\theta_{B:k})$ is the general TTD for the kth beamformer steered to beam direction $\theta_{B:k}$ and associated with the mth element. The w_m coefficients are weights that together with the TTD's define the beam pattern. The precise form of $\tau_{B:m,k}(\theta_{B:k})$ depends on the particular antenna array configuration. For the ULA, the TTD's take the form,

$$\tau_{B:m,k}(\theta_{B:k}) = \frac{d}{c}(m-1)\cos\theta_{B:k} \ . \quad (3.3)$$

Since the TTD beamformer kernel function

$$\mathcal{F}\{x_m\} = x_m(t - \tau_B) \quad (3.4)$$

is only a function of a time delay, we consider the time delay property of the Fourier transform

$$\mathfrak{F}\{x(t \pm \tau_0)\} = e^{\pm j\omega\tau_0}\mathfrak{F}\{x(t)\}\,. \tag{3.5}$$

Observe that the time shift operator results only in an effect on the phase of the frequency spectrum and that the magnitude of the spectrum is unmodified from the spectrum of the function that is not shifted. As stated by Poularikas and Seely, "The effect of time shifting is…that only the phase spectrum is modified [122]." Using the True Time Delay (TTD) beamformer construct, this invariance results in beams at different frequencies that are not identical, but the pointing direction is preserved for all frequencies. This alleviates the beam squint observed in conventional phase shift control beamformers. The use of Chebyshev coefficients in the beamformers helps maintain uniformly low sidelobes that mitigate variations in the beam sidelobes across the spatial and frequency domains.

3.2 Multiple Signal Classification in TTD Beam Space

Consider a wide bandwidth antenna array and associated bank of TTD beamformers. Without loss of generality and in order to examine the signal processing aspects of the system, we assume ideal elements with uniform spectral response across the bandwidth of interest. Issues of practical application involving physical constraints of antennas and systems will be briefly addressed in Chapter 5. Ideally the time delay is independent of

the frequency over the range of processed frequencies. For a K-beam bank, we express the kth beamformer, $k = 1, \dots, K$, using equations (3.2) and (3.3) for the ULA.

For coherent signal subspace processing in the TTD beam space, we express the received response as a linear combination of the time delayed incident wavefront with additive noise as

$$x_m(t) = \sum_{l=1}^{L} s_l\big(t - \tau_{s:l,m}(\theta_{s:l})\big) + n_m(t), m = 1, \cdots, M \tag{3.6}$$

where $\theta_{s:l}$ is the AOA for the lth source, $s_l(t)$ is the waveform of the lth source expressed as a function of time, $n_m(t)$ is the noise for the mth element expressed as a function of time, and $\tau_{s:l,m}$ is the time delay for the lth source at the mth element. Fig. 26 depicts the relevant time delays and other parameters associated with the array for multiple incident wavefronts and a K beamformer bank. Note that the figure does not show all time delays for sake of clarity. The kth beamformer TTD's, $\tau_{B:m,k}(\theta_{B:k})$, are functions of the known beam pointing angles, $\theta_{B:k}$, defined above. The signal model time delays for the lth source, $\tau_{s:l,m}(\theta_{s:l})$, are functions of the unknown angles of arrival, $\theta_{s:l}$, expressed by similarity to equation (2.57) as,

$$\tau_{s:l,m}(\theta_{s:l}) = \frac{d}{c}(m-1)\cos(\theta_{s:l}). \tag{3.7}$$

3.2.1 Formulation of the Beam Space Manifold

Others have previously developed wide bandwidth beam space formulations in the

frequency domain. See, for example [71], which developed frequency domain frequency invariant beamformers by judicious design of the beamformer weights at various frequencies. Reference [70] utilized FIR filters in the design of frequency invariant beamformers and [69] used these same types of beamformers to implement a beam space AOA estimation. We desire to utilize the wideband TTD beam space in the time domain and thus require a time domain-based representation of the manifold of the array beamformer network.

Agrawal and Prasad investigated AOA estimation in the time domain for wideband sources using a harmonic source model [123]. The harmonic source model utilizes a summation of multiple monochromatic sources to represent the single wideband source. Although their approach models the sources as wideband, the Iterative Quadratic Maximum Likelihood (IQML)-based [51] estimation technique does not necessarily result in a unique AOA solution for all frequencies of interest. To alleviate this concern, they developed a post processing technique "whereby the separate estimates at multiple frequencies can be combined into a single estimate … in an appropriately defined least squares sense [123]."

Grenier also developed a time domain-based technique for wideband source location [124]. The method is based on a wideband extension to the Maximum Entropy Method (MEM) of Burg [42]. It implements estimates of the frequency wavenumber spectrum along with averaging of the covariance matrix. Gernier posits that such a frequency wavenumber spectral analysis is appropriate for finding the direction of the wideband

sources [124]. One of the key aspects of this technique is to model the mode vectors as a linear combination of parameterized basis functions. The basis functions may be chosen so as to obtain a set of parameters that are independent of frequency. The time domain representation is obtained by taking the Fourier Transform of the frequency domain representation with the frequency independent parameters remaining identical for both representations. Gernier's time domain representation [124] has some relevance to the TTD beam space formulation as will be articulated in the following paragraphs, although it is a wideband element space technique.

The present method is motivated by the desire to provide a spatial separation of the received signals for subsequent spatial signal subspace processing in a manner that is independent of frequency, i.e. a manner that exhibits no beam squint. It was reasoned that a TTD beam space domain representation of the received signals and array modes would provide such a mapping from array element space to wideband beam space. It was further reasoned that this approach would permit spatial signal subspace processing to be performed on the entire wide bandwidth simultaneously. The desire to process signals in wideband TTD beam space implies the need for a wideband beam space manifold. It was posited that if multiple monochromatic sources across the bandwidth of interest were used to generate a set of beam space mode vectors, that as an approximation these mode vectors could be averaged across the frequency bandwidth since the TTD beamformers preserve a frequency independent spatial relationship with the sources (no beam squint). Thus we proceed with the wideband

manifold formulation in TTD beam space.

Referring to Fig. 26, each of L sources is modeled as a wide bandwidth source as,

$$s_l(t) = \sum_{j=1}^{J} \alpha_{j,l} e^{i2\pi f_j t}, l = 1, \dots, L, \tag{3.8}$$

for spectral coefficients, $\alpha_{j,l}, j = 1, \dots, J, l = 1, \dots, L$. The multiple signal, $L > 1$, case is extended from the single source, $L = 1$, case presented in the derivation of the beam space manifold in Appendix B.

We assume J frequency sub-bands such that f_j is the center frequency of the sub-band defined by, $\frac{f_j + f_{j+1}}{2} - \frac{f_{j-1} + f_j}{2} \ll B$ which can be treated as narrowband for all $1 \leq j \leq J$. The signal impinging on each sensor element is then

$$x_m(t) = \sum_{l=1}^{L} s_l\left(t - \tau_{s:l,m}(\theta_{s:l})\right) + n_m(t)$$

$$= \sum_{l=1}^{L} \sum_{j=1}^{J} \alpha_{j,l} e^{i2\pi f_j (t - \tau_{s:l,m}(\theta_{s:l}))} + n_m(t), m = 1, \dots, M. \tag{3.9}$$

The kth beamformer response may then be formed as

$$y_k(t) = \sum_{m=1}^{M} w_m x_m(t - \tau_{B:m,k}(\theta_{B:k}))$$

$$= \sum_{m=1}^{M} w_m \sum_{l=1}^{L} \sum_{j=1}^{J} \alpha_{j,l} e^{i2\pi f_j (t - \tau_{s:l,m}(\theta_{s:l}) - \tau_{B:m,k}(\theta_{B:k}))} + n_k(t), k = 1, \dots, K, \tag{3.10}$$

where $n_k(t), k = 1, \dots, K$, is the accumulated noise at each beamformer output assumed to conform to white Gaussian structure. For each sub-band frequency,

$f_j, j = 1, \ldots, J$, the sub-band is considered narrowband [62] and thus we may apply both equations (2.56) and (2.57) for beamformer phase shift and time delay. Recall the beamformer time delays, equation (3.3), $\tau_{B:m,k}(\theta_{B:k}) = \frac{(m-1)d}{c}\cos\theta_{B:k}$, and those associated with the signal planar wavefronts impinging on the ULA, equation (3.7), $\tau_{s:l,m}(\theta_{s:l}) = \frac{(m-1)d}{c}\cos\theta_{s:l}$. We define the parameter,

$$\beta_{j,l}(t) \stackrel{\text{def}}{=} \alpha_{j,l}e^{i2\pi f_j t}, \tag{3.11}$$

rearrange the order of summation, and substitute the time delay expressions for $\tau_{s:l,m}(\theta_{s:l})$ and $\tau_{B:m,k}(\theta_{B:k})$ to obtain

$$y_k(t) = \sum_{j=1}^{J}\sum_{m=1}^{M} w_m \sum_{l=1}^{L} \beta_{j,l}(t)e^{-i2\pi f_j \frac{d}{c}(m-1)cos(\theta_{B:k})}e^{-i2\pi f_j \frac{d}{c}(m-1)cos(\theta_{s:l})} +$$

$$n_k(t), k = 1, \ldots, K. \tag{3.12}$$

We may now express equation (3.12) in matrix-vector form as,

$$\boldsymbol{y}_K \stackrel{\text{def}}{=} \begin{bmatrix} y_1(t) \\ y_2(t) \\ \vdots \\ y_K(t) \end{bmatrix} = \left(\sum_{j=1}^{J}\left[\boldsymbol{\Phi}_{jB}\left(\boldsymbol{W}_{M\times L} \circ \boldsymbol{\Phi}_{js}\right)\right]\boldsymbol{\beta}_j(t)\right) + \begin{bmatrix} n_1(t) \\ n_2(t) \\ \vdots \\ n_K(t) \end{bmatrix}, \tag{3.13}$$

where the symbol "∘" denotes the element-wise, or Hadamard product,

$$\boldsymbol{\beta}_j(t) \stackrel{\text{def}}{=} \begin{bmatrix} \beta_{j,1}(t) \\ \beta_{j,2}(t) \\ \vdots \\ \beta_{j,L}(t) \end{bmatrix} = e^{i2\pi f_j t} \begin{bmatrix} \alpha_{j,1} \\ \alpha_{j,2} \\ \vdots \\ \alpha_{j,L} \end{bmatrix} \stackrel{\text{def}}{=} e^{i2\pi f_j t} \boldsymbol{\alpha_j} \,, \tag{3.14}$$

$$\boldsymbol{\Phi}_{jB} = \begin{bmatrix} 1 & e^{-i2\pi f_j \frac{d}{j_c} \cos\theta_{B:k=1}} & e^{-i2\pi f_j \frac{d}{j_c}(2)\cos\theta_{B:k=1}} & \cdots & e^{-i2\pi f_j \frac{d}{j_c}(M-1)\cos\theta_{B:k=1}} \\ \vdots & & \vdots & & \vdots \\ 1 & e^{-i2\pi f_j \frac{d}{j_c} \cos\theta_{B:K}} & e^{-i2\pi f_j \frac{d}{j_c}(2)\cos\theta_{B:K}} & \cdots & e^{-i2\pi f_j \frac{d}{j_c}(M-1)\cos\theta_{B:K}} \end{bmatrix}, \tag{3.15}$$

$$\boldsymbol{W}_{M\times L} = \begin{bmatrix} w_1 & \cdots & w_1 \\ \vdots & \cdots & \vdots \\ w_M & \cdots & w_M \end{bmatrix}, \text{ and} \tag{3.16}$$

$$\boldsymbol{\Phi}_{js} = \begin{bmatrix} 1 & \cdots & 1 \\ e^{-i2\pi f_j \frac{d}{j_c} \cos\theta_{s:l=1}} & \cdots & e^{-i2\pi f_j \frac{d}{j_c} \cos\theta_{s:L}} \\ e^{-i2\pi f_j \frac{d}{j_c}(2)\cos\theta_{s:l=1}} & \cdots & e^{-i2\pi f_j \frac{d}{j_c}(2)\cos\theta_{s:L}} \\ \vdots & \vdots & \vdots \\ e^{-i2\pi f_j \frac{d}{j_c}(M-1)\cos\theta_{s:l=1}} & \cdots & e^{-i2\pi f_j \frac{d}{j_c}(M-1)\cos\theta_{s:L}} \end{bmatrix}. \tag{3.17}$$

Alternatively, using equations (3.14) in (3.13), $\boldsymbol{y}_K$ can be written as,

$$\boldsymbol{y}_K = \sum_{j=1}^{J} e^{i2\pi f_j t} \left(\left[\boldsymbol{\Phi}_{jB} \left(\boldsymbol{W}_{M\times L} \circ \boldsymbol{\Phi}_{js} \right) \right] \boldsymbol{\alpha_j} \right) + \boldsymbol{n}_K \,, \tag{3.18}$$

Note once again that the matrices, $\boldsymbol{\Phi}_{js}$ and $\boldsymbol{\Phi}_{jB}$, are formulated here for the ULA. Sensor configurations other than ULA may differ in the details of their construction, but the system equations, (3.13) and (3.14), hold for the general configuration. The detailed derivation of equation (3.16) is presented in Appendix B.

In a qualitative sense, the operation of signal subspace processing in wideband true

time delay beam space can be viewed as an inversion of the principle implemented by Wang and Kaveh in CSS (as well as Gabriel and many others). CSS integrates the data over a wide bandwidth using transformation matrices in the frequency domain so that the integrated data may be processed using a narrowband manifold. The TTD beam space method maintains the wideband nature of the data through the TTD beamformer bank in the time domain so that the wideband data may be processed using a multi-frequency integrated manifold. A key benefit of this approach is that for typical applications, the manifolds are pre-calculated in a system calibration procedure so that they need not be determined on the fly. On the other hand, a CSS-like process that integrates the data may require significant integration on the fly rendering it unsuitable for many real-time applications.

3.2.2 Beam Space MUSIC Spectrum

The beam space data at the beamformer bank output is thus assumed to conform to the linear model of equation (3.13) as a linear combination of the beam space mode vectors and additive noise. The individual $x_{B,l}, l = 1, \ldots, L$ signals represent the response of the individual wavefronts at the beamformer bank output. The mode vectors, wavefront responses, and noise are assumed to be mapped through the same time delay network and the noise is assumed additive white Gaussian. Using this beam space characterization, we follow the reasoning of Schmidt in [43] and [87] and consider

the TTD beam space data correlation matrix estimate,

$$\widehat{\boldsymbol{R}}_B = \boldsymbol{Y}_K \boldsymbol{Y}_K^H, \tag{3.19}$$

with $\boldsymbol{Y}_K = [\boldsymbol{y}_1 | \boldsymbol{y}_2 | \cdots | \boldsymbol{y}_N]$ the matrix formed by the K vectors, $\boldsymbol{y}_k \in K \times 1, k = 1,2,\cdots,N$ being the uniformly sampled beamformer output vectors obtained by sampling the continuous beamformer output signal, $\boldsymbol{y}_k(t)$, in the interval $[0, t_{max}]$.

Under the assumption that the additive noise is uncorrelated with the sources and that the noise power is uniform across the beamformer bank, we model the beam space covariance matrix as

$$\boldsymbol{R}_B = \boldsymbol{A}_B \boldsymbol{P}_B \boldsymbol{A}_B^H + \sigma_B^2 \boldsymbol{I} \tag{3.20}$$

with σ_B^2 representing the noise power, $\boldsymbol{P}_B$ is the beam space so-called, "signal-in-space covariance matrix [92]," and $\boldsymbol{I}$ is the identity matrix. Although the noise, when observed through the true time delay beamformers, may not be truly white, the K beamformers are shown in Appendix C to possess noise samples that are uncorrelated with each other. Thus the diagonal noise model is justified. Assuming the number of sources, L, is less than the number of beamformers, K, we utilize the conventional Eigenstructure-based signal subspace construction and write

$$\widehat{\boldsymbol{R}}_B = \boldsymbol{E}_{B,S} \boldsymbol{\Lambda}_{B,S} \boldsymbol{E}_{B,S}^H + \boldsymbol{E}_{B,N} \boldsymbol{\Lambda}_{B,N} \boldsymbol{E}_{B,N}^H \tag{3.21}$$

where $\boldsymbol{\Lambda}_{B,S}$ is the diagonal of the beam space signal Eigenvalues, $diag(\lambda_{B,max} =$

$\lambda_{B,1}, \lambda_{B,2}, \ldots, \lambda_{B,L})$, and $\boldsymbol{\Lambda}_{B,N}$ is the diagonal of the beam space noise Eigenvalues, $\sigma_B^2 \boldsymbol{I}$, with $\sigma_B^2 = \lambda_{B,L+1}$ $\sigma_B{}^2$ = $\lambda_{B,L+1}$ = $\lambda_{B,L+2}$ =…= $\lambda_{B,K}$ = $\lambda_{B,min}$. The beam space signal subspace is represented by the Eigenvectors corresponding to the beam space signal Eigenvalues,

$$\mathcal{S}_{B,S} = span\left(\boldsymbol{E}_{B,S}\right) = span(\boldsymbol{e}_{B,1}, \boldsymbol{e}_{B,2}, \cdots, \boldsymbol{e}_{B,L}) \,. \tag{3.22}$$

The beam space noise subspace is represented by the Eigenvectors corresponding to the beam space noise Eigenvalues,

$$\mathcal{S}_{B,N} = span\left(\boldsymbol{E}_{B,N}\right) = span(\boldsymbol{e}_{B,L+1}, \boldsymbol{e}_{B,L+2}, \cdots, \boldsymbol{e}_{B,K}) \,. \tag{3.23}$$

With analogy to the narrow band signal subspace processing paradigm described in Section 2.2, the L largest Eigenvalues indicate the signals while the associated Eigenvectors serve as an estimate of the signal subspace, $\boldsymbol{E}_{B,S} = \left[\boldsymbol{e}_{B,1} \middle| \boldsymbol{e}_{B,2} \middle| \ldots \middle| \boldsymbol{e}_{B,L}\right]$. Similarly, the K-L smallest Eigenvalues indicate the noise while the associated Eigenvectors serve as an estimate of the noise subspace, $\boldsymbol{E}_{B,N} = \left[\boldsymbol{e}_{B,L+1} \middle| \boldsymbol{e}_{B,L+2} \middle| \ldots \middle| \boldsymbol{e}_{B,K}\right]$. In similarity to the element space condition found in practice [87], the beam space noise Eigenvalues are not identically equal in practice and the beam space Eigenvalues in descending order become

$$\lambda_{B,max} = \lambda_{B,1} \geq \lambda_{B,2} \geq \cdots \geq \lambda_{B,K} = \lambda_{B,min} \geq 0 \,. \tag{3.24}$$

By analogy with the discourse found in [119], the TTD beam space noise subspace, the

span of the associated Eigenvectors $\boldsymbol{E}_{B,N} = \left[\boldsymbol{e}_{B,L+1}\middle|\boldsymbol{e}_{B,L+2}\middle|\ldots\middle|\boldsymbol{e}_{B,K}\right]$, is assumed orthogonal to the TTD beam space signal subspace, the span of Eigenvectors $\boldsymbol{E}_{B,S} = \left[\boldsymbol{e}_{B,1}\middle|\boldsymbol{e}_{B,2}\middle|\ldots\middle|\boldsymbol{e}_{B,L}\right]$. Thus we reason that the inverse of the Euclidean distance squared from the beam space manifold continuum to the noise subspace yields the beam space MUSIC spatial spectrum

$$P_{B,MU} = \frac{1}{\boldsymbol{a}_B^H(\theta)\boldsymbol{E}_{B,N}\boldsymbol{E}_{B,N}^H\boldsymbol{a}_B(\theta)} \tag{3.25}$$

where $\boldsymbol{E}_{B,N}$ is the beam space noise subspace obtained from the Eigenvalue-Eigenvector decomposition of $\widehat{\boldsymbol{R}}_B$, and the vector $\boldsymbol{a}_B(\theta_s, t = t_{max})$ is as described in Appendix B, equation (B.13) to preserve causality [127], [128].

With the previous discussion in this section as background, we now summarize the algorithm used to obtain the wideband beam space manifold for the M-element ULA. Note that the manifold functions have been expressed using the angles of arrival of the source planar wavefronts, $\theta_{s:l}, l = 1, \ldots, L$, but in order to search for unknown angles of arrival in simulations, we use N_a equally spaced angles to evaluate the functions.

Step 1. Sample Nsnapshots of beamspace output $\boldsymbol{Y}_K$ of size $K \times N$ across the array field of view in a time interval, $[0, t_{max}]$.

Step 2. Calculate the TTD beamspace data correlation matrix estimate, $\widehat{\boldsymbol{R}}_B = \boldsymbol{Y}_K\boldsymbol{Y}_K^H$.

Step 3. Perform the eigenvector decomposition of $\widehat{\boldsymbol{R}}_B$ to obtain the beamspace noise subspace, $E_{B,N}$.

Step 4. For each of J narrowband frequency sub-bands across the bandwidth of

interest, i.e., $j = 1,2,\dots,J$:

a) Calculate $\boldsymbol{\Phi}_{jB}$ according to equation (3.15), a $K\times M$ matrix of phase shifts that corresponds to the known beamformer time delays from each antenna element to individual beamformer outputs in the TTD bank.

b) Calculate the element manifold vectors, $\boldsymbol{\phi}_{js}$, according to equation (B.4) at angle θ being evaluated for.

Step 5. Calculate, $\boldsymbol{a}_B(\theta_s,t) = \sum_{j=1}^{J} e^{i2\pi f_j t}\left[\boldsymbol{\Phi}_{jB}\left(\boldsymbol{W}_{M\times 1}\circ\boldsymbol{\phi}_{js}\right)\right]$, a $K\times 1$ steering vector at each θ_s, over the potential domain of AOA solutions $\theta_{s:l=1,\dots,N_a}$. Set, $t = t_{max}$ to preserve causality. This implements equation (B.13) and is the wideband beamspace manifold for unknown source angles over all frequencies.

Step 6. Use the beam space manifold and noise subspace to calculate the TTD beam space MUSIC spectrum, $P_{B,MU} = \frac{1}{\boldsymbol{a}_B^H(\theta)\boldsymbol{E}_{B,N}\boldsymbol{E}_{B,N}^H\boldsymbol{a}_B(\theta)}$.

Step 7. The simulation code searches one θ_s angle at a time at N_a equally spaced angles across the field of view.

Step 8. Determine the peak positions of the TTD beamspace MUSIC spatial spectrum.

3.3 Capon's MVDR in TTD Beam Space

Next consider the MVDR estimation for TTD beam space. For white Gaussian noise the joint Probability Density Function (PDF) for $\boldsymbol{Y}$ assuming N_M independent trials takes the well-known Gaussian form

$$\boldsymbol{p}(\boldsymbol{Y}) = |\pi\sigma^2\Sigma_0|^{-N_M} e^{-\left[\frac{1}{\sigma^2} tr(\boldsymbol{Y}-\boldsymbol{U})^H \Sigma_0^{-1}(\boldsymbol{Y}-\boldsymbol{U})\right]} \tag{3.26}$$

for arbitrary $M \times N_M$ mean matrix $\boldsymbol{U}$ and diagonal matrix of noise Eigenvalues, Σ_0. The PDF in turn leads to the log likelihood function

$$\ln\big(\boldsymbol{p}(\boldsymbol{Y})\big) = -N_M \ln(\pi) - N_M \ln(\sigma^2) - N_M \ln(|\Sigma_0|) - \frac{1}{\sigma^2} tr(\boldsymbol{Y}-\boldsymbol{U})^H \Sigma_0^{-1}(\boldsymbol{Y}-\boldsymbol{U}) \,. \tag{3.27}$$

Setting the derivative equal to zero we have

$$\frac{d\ln(\boldsymbol{p}(\boldsymbol{Y}))}{d\sigma^2} = 0 = -\frac{N_M}{\hat{\sigma}^2} + \frac{1}{(\hat{\sigma}^2)^2} tr\big(\boldsymbol{Y}-\widehat{\boldsymbol{U}}\big)^H \Sigma_0^{-1}(\boldsymbol{Y}-\widehat{\boldsymbol{U}}) \tag{3.28}$$

and solving for the MVDR estimate of σ^2,

$$\widehat{\sigma\_M}^2 = \frac{1}{N_M} tr\big(\boldsymbol{Y}-\widehat{\boldsymbol{U}}\big)^H \Sigma_0^{-1}(\boldsymbol{Y}-\widehat{\boldsymbol{U}}) \tag{3.29}$$

Once again following the reasoning of Schmidt in [88] we observe that to maximize the log likelihood function, we must minimize $tr(\boldsymbol{Y}-\boldsymbol{U})^H \Sigma_0^{-1}(\boldsymbol{Y}-\boldsymbol{U})$ subject to $rank(\boldsymbol{U}) = L$. We obtain for

$$\widehat{\boldsymbol{U}} = \Sigma_0 \boldsymbol{E}_L \boldsymbol{E}_L^H \boldsymbol{Y} \tag{3.30}$$

the MVDR estimate for TTD beam space σ^2 of the form

$$\widehat{\sigma\_M}^2 = \frac{1}{N_{ML}K} \sum_{i=L+1}^{K} \lambda_{B,i} \tag{3.31}$$

and associated beam space MVDR spatial spectrum

$$P_{B,MVDR} = \frac{1}{\boldsymbol{a}_B^H(\theta)\boldsymbol{R}_B^{-1}\boldsymbol{a}_B(\theta)} \tag{3.32}$$

Note that the results of equations (3.25) and (3.32) may also be obtained by direct substitution of $\boldsymbol{E}_{B,N}$ for $\boldsymbol{E}_N$, $\boldsymbol{R}_B$ for $\boldsymbol{S}$ and $\boldsymbol{a}_B(\theta)$ for $\boldsymbol{a}(\theta)$ into the formulation developed by Schmidt in [43] even though his formulation applied only to narrow bandwidth sources where $\boldsymbol{S}$ is the notation for the data correlation matrix in Schmidt's paper. Next consider the Cramer-Rao Lower Bound (CRLB) for wide bandwidth source location estimation.

3.4 Formulation of the Cramer-Rao Lower Bound

We apply the derivation for the Cramer-Rao Lower Bound (CRLB) described by [44]. Although this formulation is derived in the frequency domain, it will serve as a basis for comparison of performance of identical wide bandwidth signals processed by both Wang and Kaveh's CSS method and TTD beam space methods. The derivation is repeated here for convenience.

Consider a set of random variables, χ, with probability density $p(\chi|\theta)$ for parameter $\theta = (\theta_1, \dots, \theta_L)$ for L wideband sources with

$$\mathrm{cov}\left(\hat{\theta}\right) \geq \boldsymbol{J}^{-1}(\theta) \tag{3.33}$$

where $\boldsymbol{J}(\theta)$ is the Fisher information matrix

$$[\boldsymbol{J}(\theta)]_{i,j} = -E\left\{\frac{\partial^2 \log p(\chi|\theta)}{\partial\theta_i \partial\theta_j}\right\}, i,j = 1,\cdots,L. \tag{3.34}$$

For the wideband source location problem, we let $\chi = X_i(f_j)$, $i = 1,\dots,L$ and $j = 1,\dots,J$. Substituting for the covariance matrix for the case of two sources,

$$\log p(\chi|\theta_1,\theta_2) = c - \sum_{j=1}^{J} \log\left[\det\left(\operatorname{cov}\left(\boldsymbol{X}(f_j)\right)\right)\right] - \sum_{j=1}^{J} \operatorname{tr}[\hat{C}\left(\boldsymbol{X}(f_j)\right)\operatorname{cov}^{-1}(\boldsymbol{X}(f_j))] \tag{3.35}$$

where c is a constant and

$$\hat{C}\left(\boldsymbol{X}(f_j)\right) = \frac{1}{L}\sum_{i=1}^{L} \boldsymbol{X}_i(f_j)\boldsymbol{X}_i^H(f_j). \tag{3.36}$$

By linearity equation (3.35) can be expressed as

$$J_{11} = -E\left\{\frac{\partial^2}{\partial\theta_1^2}\log p(\chi|\theta_1,\theta_2)\right\} \approx \frac{\partial^2}{\partial\theta_1^2}\left\{\sum_{j=1}^{J}\log\left[\det\left(\operatorname{cov}\left(\boldsymbol{X}(f_j)\right)\right)\right]\right\} + \sum_{j=1}^{J}\operatorname{tr}\left\{\operatorname{cov}(\boldsymbol{X}(f_j))\frac{\partial^2}{\partial\theta_1^2}\operatorname{cov}^{-1}(\boldsymbol{X}(f_j))\right\} \tag{3.37}$$

$$J_{12} = J_{21} = -E\left\{\frac{\partial^2}{\partial\theta_1\partial\theta_2}\log p(\chi|\theta_1,\theta_2)\right\} \approx \frac{\partial^2}{\partial\theta_1\theta_2}\left\{\sum_{j=1}^{J}\log\left[\det\left(\operatorname{cov}\left(\boldsymbol{X}(f_j)\right)\right)\right]\right\} + \sum_{j=1}^{J}\operatorname{tr}\left\{\operatorname{cov}(\boldsymbol{X}(f_j))\frac{\partial^2}{\partial\theta_1\theta_2}\operatorname{cov}^{-1}(\boldsymbol{X}(f_j))\right\} \tag{3.38}$$

and

$$J_{22} = -E\left\{\frac{\partial^2}{\partial\theta_2^2}\log p(\chi|\theta_1,\theta_2)\right\} \approx \frac{\partial^2}{\partial\theta_2^2}\left\{\sum_{j=1}^{J}\log\left[\det\left(\operatorname{cov}\left(\boldsymbol{X}(f_j)\right)\right)\right]\right\} + \sum_{j=1}^{J}\operatorname{tr}\left\{\operatorname{cov}(\boldsymbol{X}(f_j))\frac{\partial^2}{\partial\theta_2^2}\operatorname{cov}^{-1}(\boldsymbol{X}(f_j))\right\} \tag{3.39}$$

4 COMPUTATIONAL EXPENSE

Consider the computational expense for various methods of signal subspace processing. In order to compare the various methods, neglect the determination of the number of sources. Even though this may for some cases be a significant computation, it is nominally common to all methods, and thus need not factor into the comparison. Also neglect the initial AOA estimate for CSS since similar methods exist that do not require the initial estimate. For CSS the data are divided into K_{CSS} segments, sub-banded by Fast Fourier Transform (FFT) processing, and formed into the data correlation matrices prior to transformation from the sub-bands into the coherently integrated reference band. The FFT's are performed for each data segment and for each element, therefore, the computational expense for the FFT's is

$$\xi_{CSS,1} = O\left(K_{CSS} M \frac{N}{K_{CSS}} \log\left(\frac{N}{K_{CSS}}\right)\right) = O(MNlog(\frac{N}{K_{CSS}})) \tag{4.1}$$

where $O(\psi)$ indicates a magnitude of number of computations on the order of ψ , N is the total number of data points for a processing interval and M is the number of

elements. The number of frequencies resulting from the FFT's is $\frac{K_{CSS}}{2}+1$. The data correlation matrices must be calculated for each frequency and each data segment. The computational expense for calculation of the data correlation matrices is thus

$$\xi_{CSS,2} = O\left(\left(\frac{K_{CSS}}{2}+1\right)K_{CSS}M^2\frac{N}{K_{CSS}}\right) = O\left(\left(\frac{K_{CSS}}{2}+1\right)M^2N\right). \quad (4.2)$$

Next the transformation matrices are constructed and applied. We need not consider the actual construction of the transformation matrices since this may entail mostly rearrangement of data in memory. There are some calculations necessary to obtain the transformations, but these are assumed to be relatively minor compared to other components of the overall computation. For some of the methods it entails only calculations along the diagonal. In addition, the transformation matrices are the primary difference between several of the wideband coherent integration methods, so in order to obtain a common low order of magnitude estimate for these the cost of construction of the transformation matrices is neglected. The application of the transformation matrices is an $M\times M$ matrix computation for each of the frequency sub-bands yielding

$$\xi_{CSS,3} = O\left(\left(\frac{K_{CSS}}{2}+1\right)M^3\right) \quad (4.3)$$

Finally we must account for the calculation of the estimate using the coherently integrated data using a narrowband technique such as MUSIC. Assume that the

predominant computational expense in this step is the eigen-decomposition of the correlation matrix, neglecting other more minor aspects of the computation, so that the expense of this step is

$$\xi_{CSS,4} = O(M^3) \tag{4.4}$$

The total computational expense for CSS is thus

$$\xi_{CSS} = \xi_{CSS,1} + \xi_{CSS,2} + \xi_{CSS,3} + \xi_{CSS,4} \tag{4.5}$$

Next consider the computational expense for narrow bandwidth MUSIC in the center sub-band. We still must perform the sub-banding of the data in order to obtain the center band. Therefore the first step in finding the computational expense for narrow bandwidth MUSIC is to perform the same FFT's whose expense is estimated by equation (4.1) so that

$$\xi_{NBM,1} = \xi_{CSS,1}. \tag{4.6}$$

Next the data correlation matrix must be computed for the single band:

$$\xi_{NBM,2} = M^2 N. \tag{4.7}$$

Finally the matrix inversion that represents the final processing stage is

$$\xi_{NBM,3} = M^3, \tag{4.8}$$

and the total computational expense for the narrow bandwidth MUSIC method is

$$\xi_{NBM} = \xi_{NBM,1} + \xi_{NBM,2} + \xi_{NBM,3} \quad . \tag{4.9}$$

Since the TTD beamformer bank would typically be fixed in a direction finding system, the time delays are considered fixed and need not be considered in the computational expense. The computational expense for TTD signal subspace processing is thus assumed to be on the order of the sum of the data correlation matrix processing for K beams of N length data and the generation of eigen-subspace matrix for K beams which is

$$\xi_{TTD} = O(K^2N + K^3). \tag{4.10}$$

Fig. 27 shows the calculated computational expense for data sequence lengths of various sizes along with points measured using Monte-Carlo simulations of 1000 runs for each data point. The calculation assumes a 16-element array, CSS parameters from [44], and an 8-beamformer bank for TTD signal subspace processing.

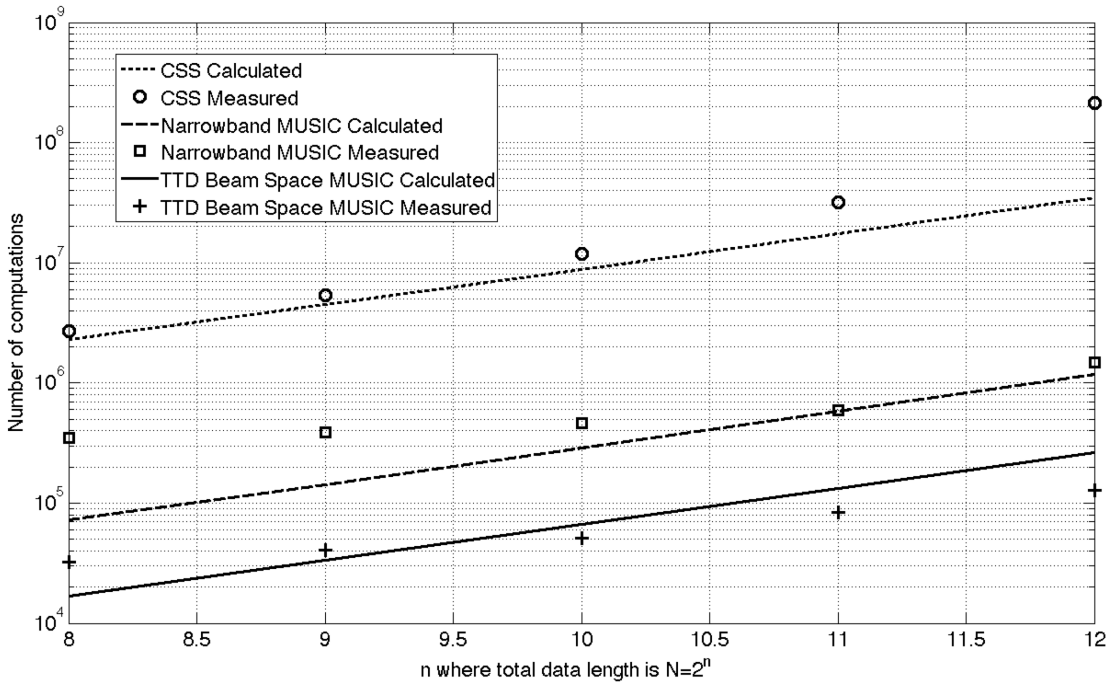

Fig. 27. Order of magnitude of computational expense.

5 Practical and System Considerations

5.1 A Representative Platform

The system architect must consider many factors when developing a system for estimation of emitter characteristics. The TTD beam space system may not be suitable for all applications, but would fit well with one requiring high-resolution of very wideband emitters in a constrained field of view such as a standoff Electronic Intelligence (ELINT) platform. In order to constrain the bounds of the discussion, consider the ELINT application. An airborne ELINT platform engagement geometry is shown in Fig. 28. It depicts an aircraft viewed from above that serves as the platform for the antenna array with the antenna elements represented by the blue triangles along the airframe. The beam pattern shown is an aggregate of 8 true time delay beams formed from a 16-element uniform linear array that will be modeled in detail in Chapter 7. This aggregate beam pattern represents the field of view of the direction finding system. The typical application will be for the ELINT platform to fly a track perpendicular to the general direction of suspected emitters outside the range of antiaircraft missiles. The term standoff refers to this long-range geometry. Because of this required range, the ELINT receivers must have excellent sensitivity and the system

must be stable and well calibrated to produce the AOA accuracy to support precise geolocation of the emitters. For this type of geometry with the emitters of interest ground based and at long ranges, an azimuth only system is often adequate. For other applications, azimuth and elevation AOA estimation may be necessary.

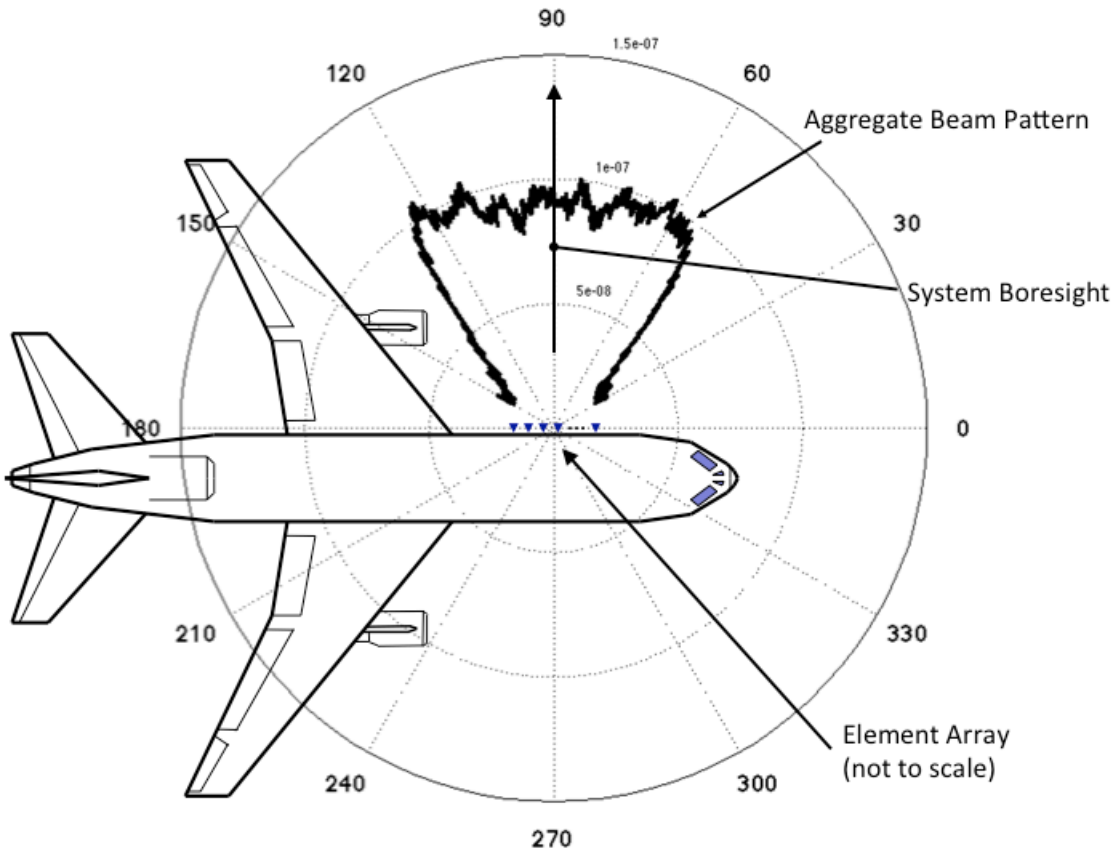

Fig. 28. Representative geometry for an airborne ELINT application.

The purpose of the ELINT system is to detect and characterize ground based radar and other sources of RF emission. One of the primary characteristics that the system must estimate is geolocation, or location on the surface of the earth, from which a given source is emitting. Fig. 29 depicts a representative geometry for geolocation from AOA

measurements. Each AOA measurement is an angle relative to the antenna array. The AOA must be combined with the state vector data of the airframe; pitch, roll, and yaw, to calculate a Line Of Bearing (LOB) that is relative to the geographical reference frame. As multiple LOB's are calculated as the platform moves along its flight path, the LOB's for a particular emitter will tend to intersect near the emitter's geolocation. With accurate LOB's, precise state vector data and Digital Terrain Elevation Data (DTED), an accurate geolocation estimate for the emitter may be obtained. Typically, the intersections of LOB's form into a cluster to which the geolocation algorithm will fit an elipse as shown.

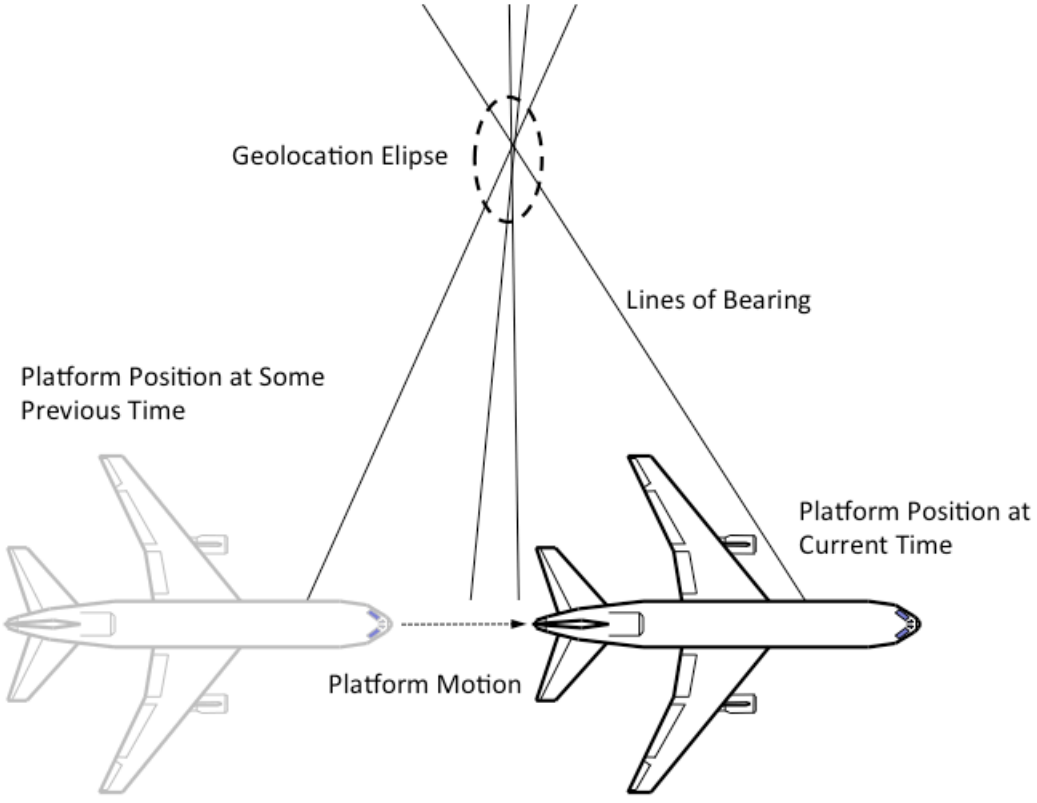

Fig. 29. Representative geolocation geometry.

5.2 The Antenna Array

The antenna array need not be linear; in fact the constraints imposed by the need to mount the elements on the airframe as well as aerodynamic constraints may preclude linearity. For an example of a realized system that incorporates a complex non-uniform array of antenna elements consider the US Army's RC-12x. Fig. 30 shows a photograph of the recently upgraded RC-12x, Guardrail Common Sensor, aircraft. The Guardrail, as it is commonly known, has been in service since 1971. The upgraded version operates in extended frequency bands as compared to the previous version and operates together with ground stations to perform spatial processing as a system to provide precision source location estimates in dense signal environments [133].

Fig. 30. US Army's Guardrail Common Sensor Platform [image courtesy US Army].

It is evident from the Guardrail photograph why observers sometimes refer to the platform as an antenna farm. The system has been modified numerous times over many years. It has several arrays at multiple frequency bands and varying degrees of performance, but is a solid proven system due to the engineering execution of the system integrators.

Consider a true time delay beamforming array. The time delay mechanism can be implemented in a number of ways. Scientists and engineers at the Naval Research

Laboratory (NRL) have investigated photonic true time delay beamforming architectures [134]. The photonic technology has been used for ultra-wide bandwidths and frequencies extending into millimeter wave, $30GHz$ to $300GHz$.

Digitizing the down-converted RF signal and applying appropriate digital delays to each channel can implement digital true time delay. Analog RF integrated circuits or mixed signal devices are another approach to true time delay beamforming.

The true time delay mechanism itself may approach frequency independence, but the overall system is frequency dependent as long as RF energy is coupled into physical antenna elements that are frequency dependent. The characteristics of the antenna elements must be accounted for in the system design. Element characteristics that effect system performance include:

- Element radiation pattern,
- Element spectral response,
- Field polarization,
- Losses,
- Element to element uniformity of characteristics, reproducibility.

Personnel from the Ansoft Corporation recently presented results of a design activity for a UWB spiral antenna intended for ELINT like applications [135] and [136]. Fig. 31 depicts the resulting spiral antenna, both the computer model version on the left and the realized design on the right. The engineers reported results of simulations for the

gain across the spectrum of interest as well as that measured in an anechoic chamber. A number of such elements could be used to form an array for a TTD beamformer bank system.

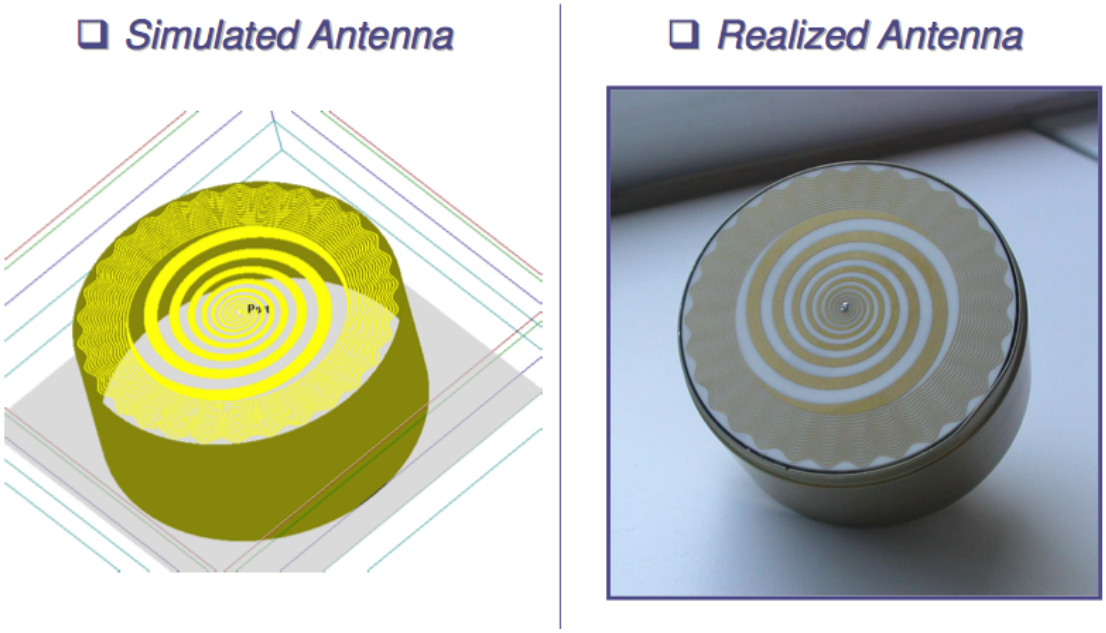

Fig. 31. Spiral wide bandwidth antenna elements, modeled on left, realized on right [image courtesy Ansoft Corporation].

Fig. 32 shows the simulated and measured spectral response of the spiral element. The response is nominally $4 \pm 2dBi$ from 3 to $27GHz$, a fractional bandwidth of 62.5%. The performance may be adequate for receipt of signals on individual elements in many cases, but the variation is such that system designers would have to determine how to account and calibrate for it to obtain accurate array measurements. The details of the various issues involved in such determinations would be specific to a given system

design and are beyond the scope of this dissertation.

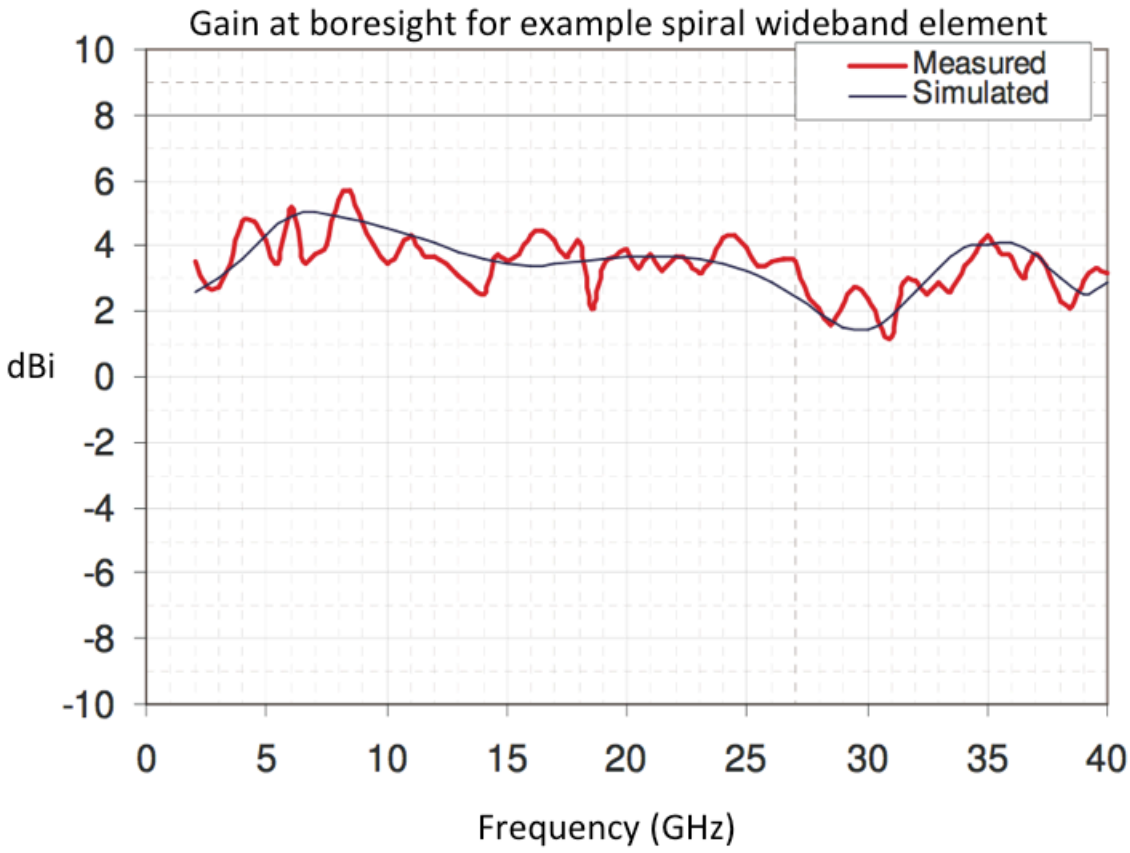

Fig. 32. Spectral gain for representative spiral element [135], [136] [image courtesy Ansoft Corporation].

For many typical airborne applications that must receive signals emitting from the ground, antennas are mounted on the bottom of an aircraft. The antennas often receive not only the direct signal from the emitter, but also correlated signals originating from the ground emitter then reflected off other portions of the airframe. This condition is called multipath. Schmidt treated the reflected multipath signal condition

for the case of narrowband emitters [91]. The extension of the treatment to the wideband case should be straightforward and is a topic for future investigation.

6 Optimization of System Parameters

6.1 Optimization Overview

A system that incorporates RF source location technology can be very complex. Often the source location component of such a system is integrated into the overall system in something of a support role. For example, on an airborne ISR platform, the RF source location results may be used to provide cues to point other sensors such as imaging optical, infrared or synthetic aperture radar. For systems that incorporate beamforming to extract meaningful data from a dense co-channel interference environment, the source location information may integrated into the beamforming solution to position the beams and nulls of the array pattern. In such cases, the array used for source location may also support other system functions. In addition the sensors on an airborne platform must often conform to the shape of the aircraft body and incorporate aerodynamic constraints. The implication is that a very complex set of constraints affect the design of the system. System architects must integrate the system within these many constraints while ensuring good performance across a wide range of sensing capabilities.

Platform constraints often play a significant role in system design. During the last

decade and a half, AFRL developed a concept to build an airborne vehicle around the desired sensor capability rather than the typical design process that begins with a platform and fits the sensor system into it. Known as Sensorcraft, this concept, depicted in Fig. 33, was conceived, as a guiding concept not intended to necessarily result in a full program development. It served as a focal point for sensor subsystem development. The idea of Sensorcraft was to envision an airborne vehicle that considered the sensor performance as paramount from the inception of platform design. As noted in an article from the Armed Forces Communications and Electronics Association (AFCEA) [133]:

> ***"Designers tapped the expertise of the AFRL Sensors Directorate to visualize the ideal airborne sensor platform. The concept configuration, resembling two boomerangs in a V-shaped joint-wing construction, is adapted to suit the best sensor configuration for air-to-air and air-to-ground ISR. The sensors are based on the outboard portion of the aircraft for an unobstructed field of view around the vehicle. The UAV version has no cockpit and features an efficient platform for aerodynamic, propulsion and sensor integration.***
>
> ***The subsonic craft would operate for about 60 to 80 hours at an altitude of about 60,000 feet. Perdzock allows that the sensorcraft could be quite large with a singular wingspan of more than 100 feet. Its speed would be in the 300- to 400-knot range.***
>
> ***A large portion of the craft's sensor suite would be dedicated to radio frequency (RF) functionality. However, it also would incorporate electro-optic, infrared, long-range imaging and long-range RF sensors. The sensorcraft would have the capability to distribute data directly to operations centers and even aircraft in theater of operations, if required.***
>
> ***One main difference between the sensorcraft and existing long-endurance UAVs such as Global Hawk would be its greater variety of apertures. The sensorcraft could accommodate lower frequency RF apertures, which are larger than those of higher frequencies. "We are looking at this as a next-generation Global Hawk," Perdzock analogizes."***

Fig. 33. Artist's depiction of AFRL Sensorcraft concept vehicle [image courtesy AFRL/RY Sensors Directorate].

Developments such as Sensorcraft are very much the exception rather than the rule. More often, organizations with limited budgets must accept suboptimal constraints by fitting sensors such as RF antenna arrays onto platforms that have been designed with primarily aerodynamic constraints in mind. An array may be constrained to conform to a curved surface simply by virtue of the shape of the airframe. Additional constraints could be imposed by platforms designed with Low Observable (LO) characteristics such as stealth aircraft. These types of platforms may prohibit system integrators from permanently mounting antennas on the external airframe at all.

Similarly for digital signal processing systems that process the array data the trend in system design in recent years has been toward utilization of Commercial Off-The-Shelf

(COTS) hardware rather than custom designed hardware that represents a precise fit to the problem at hand. COTS hardware and development tools have increased dramatically in capability and power while costs for such hardware tends to reduce as the quantity of fielded systems grows. System architects often find that the most cost effective approach for a signal processing system is to incorporate COTS solutions whenever possible even though they may be suboptimal.

The system designer may consider optimality in numerous ways In terms of the signal processing algorithms. The maximum likelihood estimator is typically based on the assumed model of signal embedded in white Gaussian noise along with other assumptions such as linearity and trial independence. In [48] Wax pointed out that certain assumptions commonly used to derive closed form expressions for MLE do not necessarily hold in general. Schmidt showed that Capon's MVDR (called "MLE in [52]), Burg's maximum entropy method [42], the least squares estimator, and AR modeling all result in identical estimators given his model formulation and that the differences in the literature result from the variations in the underlying data model assumptions [88].

In light of the complexity of modern systems, the lack of optimality for realizations that do not conform to the design model, and the difficulty of derivation of closed form solutions for designs with numerous constraints, the system designer my opt to utilize a heuristic method for some aspects of the design. One such approach to system design for a complex set of constraints is utilization of an automated optimization algorithm. The literature contains a large body of research on optimization algorithms that use

various criteria to perform searches of defined problem spaces. Consider a set of processes that must be constrained to operate on a fixed signal processing hardware system or an antenna array with complex element patterns, complex element interactions and non-planar array geometry. A general means of attempting to determine an optimal configuration for an array or a set of processes is to define a fitness function that deterministically measures performance and can be used to rapidly compare the performance of many different configurations. An automated algorithm performs a search through many configurations with the intent of finding the configuration that results in the best fitness function value. Some popular algorithms that perform a search of a global cost function are pattern search, simulated annealing and the genetic algorithm. Use of each of these three algorithms as implemented in the Matlab Global Optimization Toolbox to configure an antenna array for a specific modeled DF problem is demonstrated in section 7.6. Other similar algorithms as well as variations on these three exist, but these three will be described in the following sections.

6.2 Pattern Search

A pattern search optimization problem takes the form

$$\psi = \min\big(g(\boldsymbol{x})\big), subject\ to\ c(\boldsymbol{x}) = 0\ and\ optionally\ \boldsymbol{A}\boldsymbol{x} \geq b \tag{6.1}$$

for cost function g, inequality constraints $\boldsymbol{A}$ and equality constraints c. We will present

an example optimization problem by simulation result in Section 7.6. For the example problem of optimization of an antenna array beamformer bank for TTD beam space processing, we let the cost function be the sum of the MSE of the TTD MUSIC peak detections for two closely spaced sources at various regions of the field of view. The 8-beamformer bank was constrained such that all 8 beamformers had pointing directions within the field of view in the interval $[50^{\circ}, 130^{\circ}]$. The element locations for the 16-element ULA were fixed. Thus x represents the beamformer pointing direction vector, $c(x)$ the fixed field of view limitation constraint. The optional inequality constraint for $\boldsymbol{A}$ was not used in the example. In order to keep the total optimization processing times within reasonable limits and demonstrate the concept, the cost function was implemented as a measure of the MSE for only three sets of two closely spaced sources, one near the center of the field of view, one close to the left edge, and one close to the right edge.

The pattern search forms a geometrical mesh around the starting point, evaluates points on the mesh, and reduces the mesh spacing as the algorithm progresses [129]. It performs iterations with dynamically changing numbers of fitness function evaluations per iteration. It is useful for situations where the derivatives of g and c are unavailable or unreliable and is based on a variation of the augmented Lagrangian method. One advantage of the pattern search is that it requires no derivatives of the fitness function. The price for this is that execution time may be longer than some other methods and the optimization may tend to settle into local extrema.

6.3 Simulated Annealing

Simulated annealing optimization models the physical annealing process by repeatedly injecting energy into the system (heating) and allowing the energy to dissipate (cooling). We consider the particular variant of simulated annealing used in the Matlab Global Optimization Toolbox known as Adaptive Simulated Annealing (ASA) [130]. As the energy in the system dissipates, the system tends to settle into various states of optimality. In the simulated annealing context, the energy in the system is represented by the magnitude of the cost function. The temperature of each variable characterizes its state at any given point in the process. The ASA generating function takes the form

$$g(\boldsymbol{y}) = \prod_{i=1}^{D} \frac{1}{2(|y^i|+T_i)\ln\left(1+\frac{1}{T_i}\right)} \tag{6.2}$$

for i-dimensional random variable y^i and temperature T. For the example results presented in Section 7.6, $\boldsymbol{y}$ represents the beamformer pointing direction vector. To demonstrate the application to array optimization for TTD beam space processing, the beamformer pointing directions were constrained to the same field of view range as described for pattern search. The same cost function input conditions of three sets of two closely spaced sources was used as well. It follows that the cumulative probability distribution is

$$G_T(y) = \frac{1}{2} + \frac{\mathrm{sgn}(y^i)\ln\left(1+\frac{|y^i|}{T_i}\right)}{2\ln\left(1+\frac{1}{T_i}\right)}. \quad (6.3)$$

The process that adjusts the temperature to inject energy into or remove energy from the system is called the annealing schedule. A common annealing schedule is an exponential schedule. The annealing schedule used by Ingber in [130] is an exponential schedule that is shown under certain conditions to lead statistically to a global minimum. In practice, for discrete time steps and reasonable total annealing times, a global minimum is not guaranteed.

6.4 Genetic Algorithm

Genetic algorithm optimization models the biological process of combinatorial genetics by repeatedly generating populations of individuals [131]. Each individual corresponds to a single fitness function evaluation. Each iteration is termed a generation in the genetic algorithm context. Traits of well performing individuals in a given generation are combined to produce new individuals for the subsequent generation. Periodically, mutations are injected into the generation by utilizing randomness in the production of new individual traits. This has the potential to permit the optimization process to escape local minima.

Numerous variations of genetic-type algorithms and evolutionary computation algorithms exist. Whitley describes the particular genetic algorithm implemented in the

$Matlab\ Global\ Optimization\ Toolbox$ [131]. A binary string of length N_{GA} represents each individual in the population with the potential pool of individuals being conceptualized by an N_{GA}-dimensinal hypercube, $\mathcal{H}$. In genetic algorithm jargon, the individual binary string may be referred to as a genotype or a chromosome. For the purposes of demonstrating array optimization for TTD beam space processing, the binary string is simply the encoded beamformer pointing directions. Once again the beamformer pointing directions were constrained to the fixed field of view as described for pattern search and simulated annealing with the same cost function input conditions. Each iteration of the algorithm is performed in two phases; the selection phase and the recombination phase. In the selection phase, the current population of binary strings is operated according to their fitness function result by

$$\mathcal{M}(\mathcal{H}, t_{+}) = \mathcal{M}(\mathcal{H}, t)\frac{g(\mathcal{H},t)}{g_{avg}} \tag{6.4}$$

where t_{+} is the time at the intermediate generational stage, $g(\mathcal{H}, t)$ is the fitness function for the individual, $\mathcal{H}$ is the beamformer pointing direction vector, and g_{avg} is the average of all individual fitness functions for the generation. The selection phase vets individuals in terms of their performance to ensure that traits of high performers are preserved and selects pairs of individuals to combine for the subsequent generation. The process of performing a crossover implements the combination of a pair of individuals to form two offspring in the recombination phase. A crossover is performed by swapping bits in the two parent strings in only a predefined portion of the string.

We visualize the population pool hypercubes by considering a 3-digit binary string and corresponding 3-dimensional cube in the upper left of Fig. 34. Each corner of the cube is labeled as a possible individual member of the population. Now we consider a 4-digit binary string and represent it by the 4-dimensional hypercube in the lower right of Fig. 34. The hypercube is represented by one cube inside another. The corners of the outer cube are labeled similarly to the 3-dimensional cube with an additional 0 in the string while the corners of the inner cube are labeled similarly to the 3-dimensional cube with an additional 1 in the string. Note that for sake of clarity, not all corners are labeled. Whitley described how combining strings using the crossover process results in a sampling of hyperplane partitions in the N_{GA} -dimensional hyperspace [131].

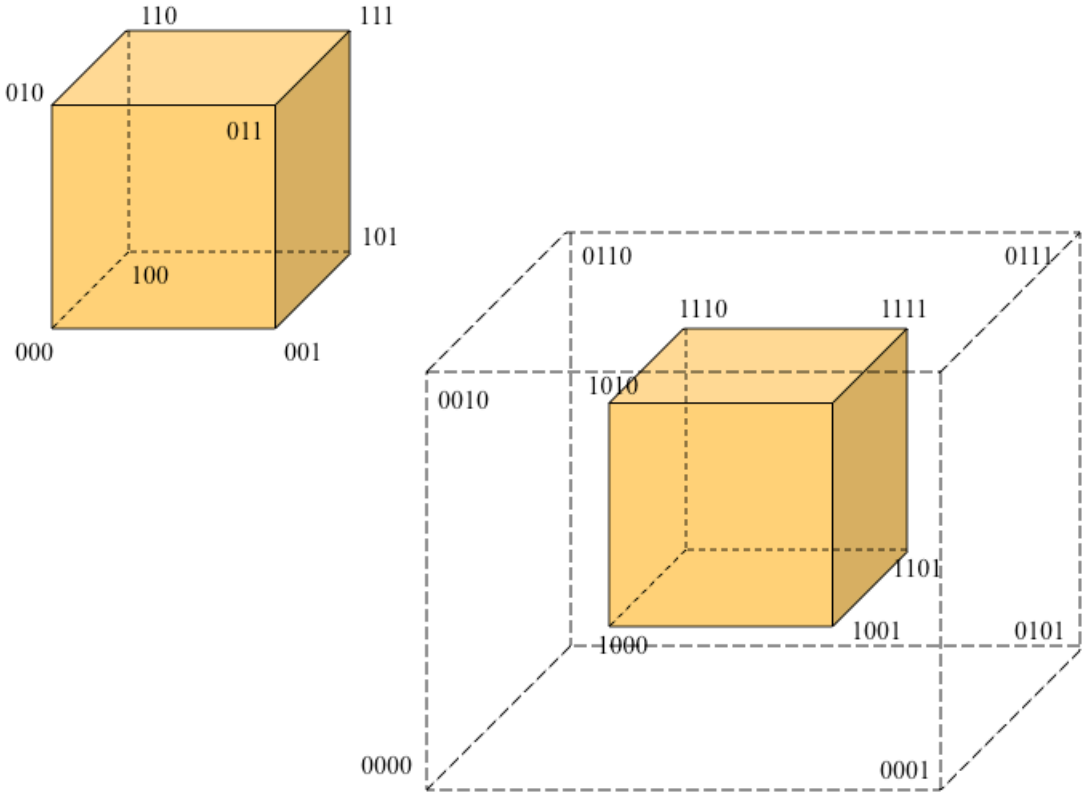

Fig. 34. Representation of a 3-dimensional cube for 3-digit binary string in the upper left and a 4-dimensional hypercube for 4-digit binary string in the lower right.

Following the crossover process a mutation stage may be implemented within the recombination phase of the genetic algorithm. With the proper tuning of algorithm parameters, permitting the genetic algorithm to iterate over many generations tends to result in a solution that approaches the global optimum [131].

7 SIMULATION RESULTS

Much of the advantage of operating in the beam space of a TTD beamformer bank will be gained by reducing the dimensionality of signal subspace processing from element space to beam space. In order to readily compare methods, consider a 16-element Uniform Linear Array (ULA) similar to that assumed by Wang and Kaveh [44], [62]. Many other researchers have used similar 16-element ULA's to facilitate the comparison of methods from simulation results. Since we desire to reduce the dimensionality, let us first consider a 4-beamformer bank. With this array we can compare processing methods with CSS using the same algorithmic parameters that Wang and Kaveh used.

We define a muliple beamformer bank as a number of fixed beamformers with common elements, each steered to a different direction. We typically use a uniform spacing between adjacent beam pointing directions. Fig. 35 depicts an example plot of the beam patterns for an 4-beam bank TTD beamformer using a 16-element Uniform Linear Array (ULA) of spacing $d = \frac{\lambda}{2}$ for $f = 1200MHz$ whose weights are Chebyshev coefficients chosen so that the uniform sidelobes are $40dB$ below the main beams. Other weighting schemes could be chosen, but Chebyshev coefficients offer the advantage of designed uniformity of the sidelobes and are sufficient for demonstration

of the techniques. The beamformer bank is steered to the vector $[67.5° \; 82.5° \; 97.5° \; 112.5°]$. The upper frequency of the desired bandwidth of $800MHz$ to $1200MHz$ was chosen to define the element spacing for 40% bandwidth. The field of view for this bank would be approximately $60°$ in the interval $[60°, 120°]$ with boresight at $90°$ perpendicular to the linear array. Since the time delays used to form the TTD beams are independent of frequency, the beam space resulting from a bank of TTD beamformers provides a multi-dimensional spatial representation of the data mapped from the element space. Note that all simulations described herein executed using $Matlab \; R2010a$ within the $Macintosh \; OS \; X \; 10.6.8$ operating system.

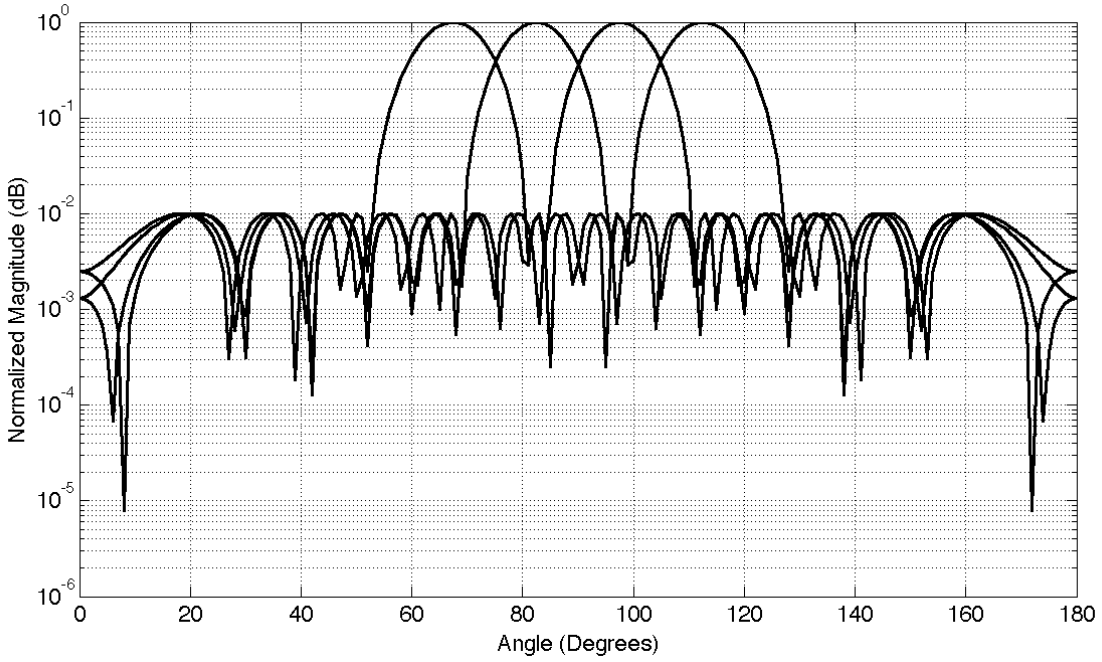

Fig. 35. Four-beamformer bank centered at $90°$ boresight.

The four-beamformer bank aggregate pattern can be viewed by calculating the sum of all the beamformers throughout the field of view. Fig. 36 depicts the aggregate pattern

for the 4-beamformer bank just described in both rectangular and polar coordinates. The pattern is quite nonuniform through the field of view making it undesirable for many applications. The beamformer bank steering vector could be chosen such that the beams are closer together, but this would reduce the instantaneous field of view and we initially desire to investigate a somewhat wider field of view. The number of beams and beamformer bank construction is of course a trade-off with computational expense since the signal subspace computations for the 4-beam space will be considerably less than that of a greater number of beamformers. Others have pointed out similar trade-offs involving attempts to reduce the number of degrees of freedom for processing [31], [41], [61].

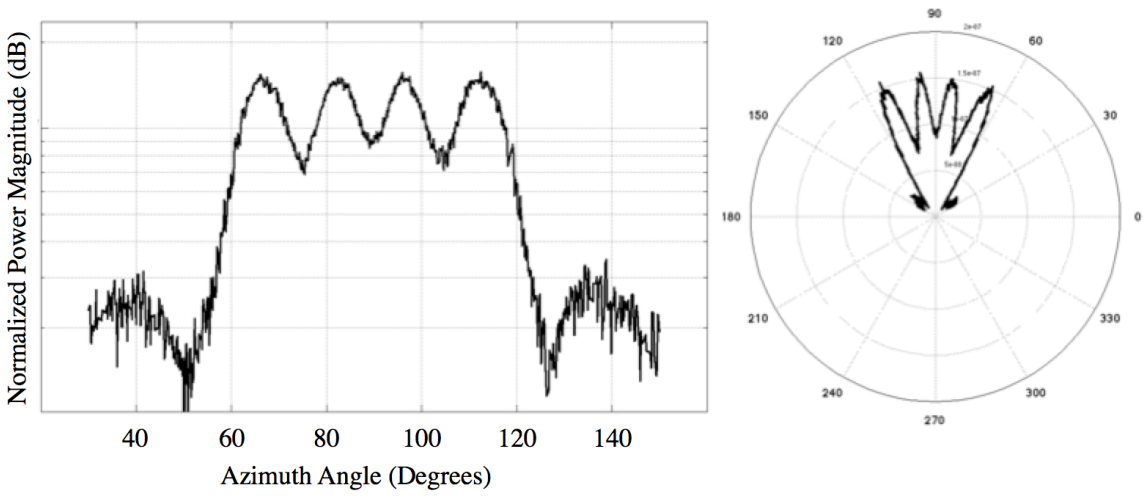

Fig. 36. Aggregate pattern for 4-beamformer bank across the field of view.

Next consider an 8-beamformer bank from the same 16-element array. The 8-beam bank is also oriented such that $90°$ is the boresight perpendicular to the array. The beams are steered to the vector $[55° \; 65° \; 75° \; 85° \; 95° \; 105° \; 115° \; 125°]$. This

beamformer bank possesses a larger field of view than the previous 4-beamformer bank of approximately $80°$ in the interval $[50°, 130°]$. Fig. 37 depicts the 8-beam bank using the same type of Chebyshev TTD beamformer as described for the 4-beam bank. The expectation for the aggregate pattern for this bank is that it would exhibit greater uniformity since the beam spacing is closer than that of the 4-beam bank.

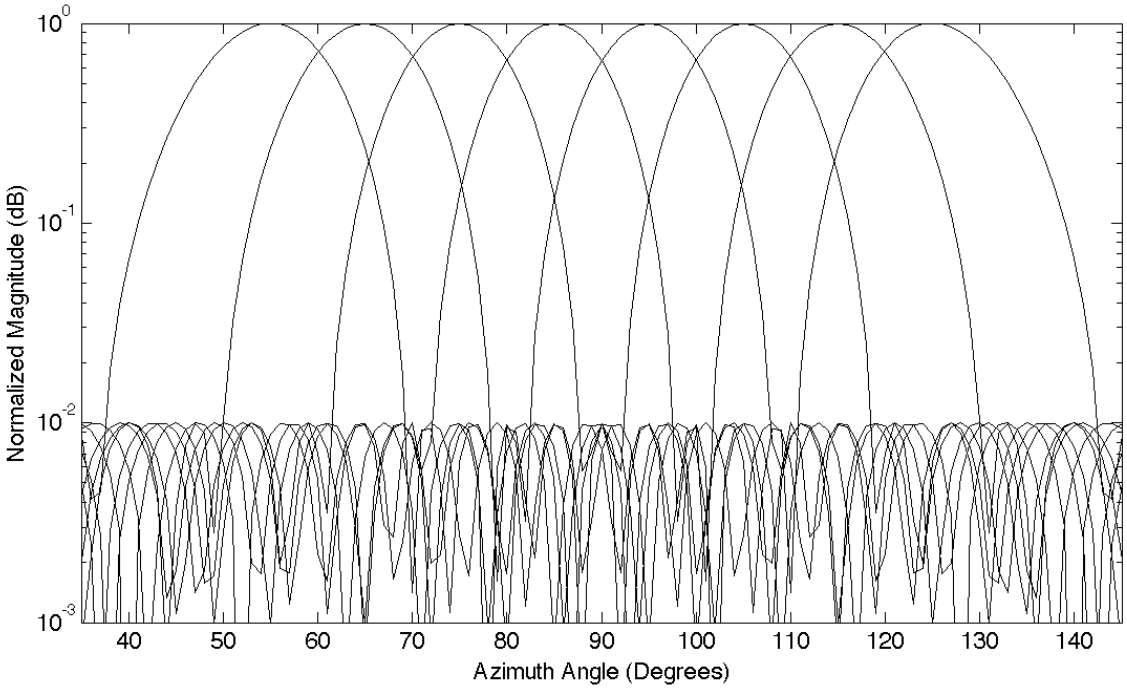

Fig. 37. Beam patterns for example TTD 8-beamformer bank.

Indeed as observed in Fig. 38 the plot, shown in both rectangular and polar coordinates, of the sum of the signal received from all beams across the field of view yields the aggregate pattern that exhibits greater uniformity than that of the 4-beam bank. The beamformer bank is designed for operation within a field of view defined by the $3dB$ window of approximately $50°$ to $130°$. The uniformity is quantified by the total

received power that is within $\pm 1dB$ over 88% of the field of view. Although a given beamformer bank configuration would typically be system and application dependent, this 8-beamformer bank appears to have adequate uniformity, field of view, and dimensionality reduction to serve as a representative selection for a comparative study. The ELINT application described in Chapter 5 is an appropriate application for such a bank. In fact the polar aggregate system pattern shown in Fig. 28 was generated from this same 8-beamformer bank.

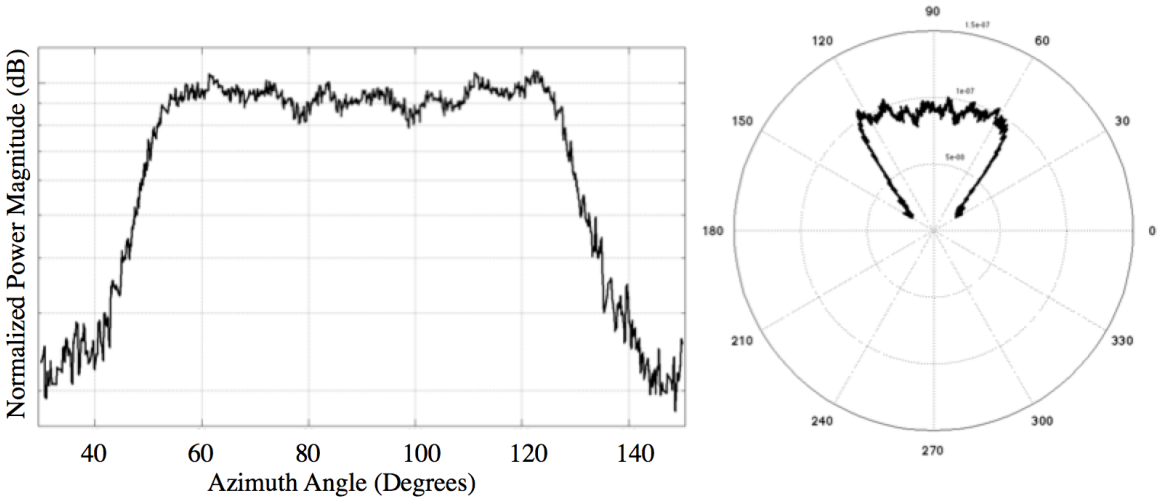

Fig. 38. Power magnitude from all beams across the field of view.

The frequency dependence of a beamforming system has a significant impact on the system design and application. The beam squint phenomenon as discussed in Section 2.6 must be taken into account for systems using traditional phase shifting technology. The frequency stability of the simulated TTD system for a single beam pattern across a wide frequency range is observed in Fig. 39 that shows the 16-element Chebyshev

weighted TTD beamformer at boresight. The frequency range is $800MHz$ to $1.2GHz$, 40% bandwidth.

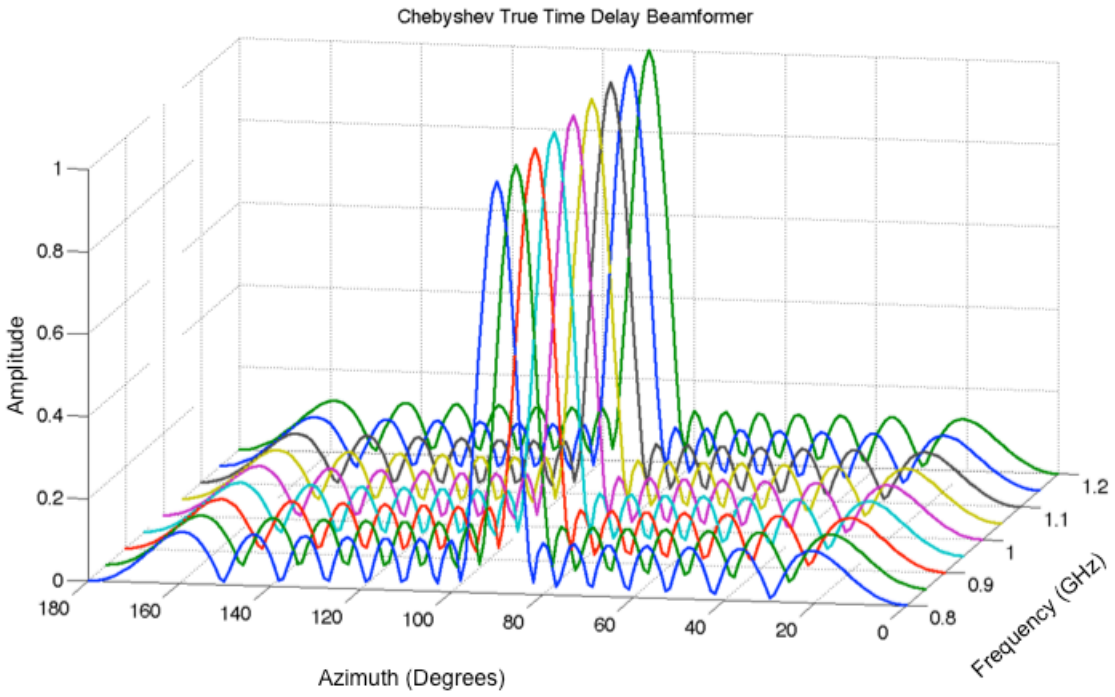

Fig. 39. Single Beamformer Across a Wide Frequency Range.

For all simulations, unless otherwise stated, the RF sensor elements make up a 16-element uniform linear array. The sources are wideband frequency modulated waveforms of $400MHz$ bandwidth centered at $1GHz$. Fig. 40 shows an example of the signals at all 16 elements for the 2 signal case described in Section 7.1 of this chapter. The signals at each element result from the superposition of the signals arriving from different source directions. To facilitate implementation of simulations and to ensure

that no frequency components were lost in the shifting of signal data, the signals were implemented as periodic pulse trains using circular shifts with the pulse start time and end time being asynchronous with the data capture window. This approach alleviates any requirement for the data collection window to precisely begin and end near any particular data point. In addition, when independent signals are generated, the signal generation code implements a random offset in the source start times to ensure that the independent pulses are not time coincident. In Fig. 40, slight differences can be observed in the signal envelope from element to element due to the superposition of the two independent planar wavefronts arriving from different AOA's.

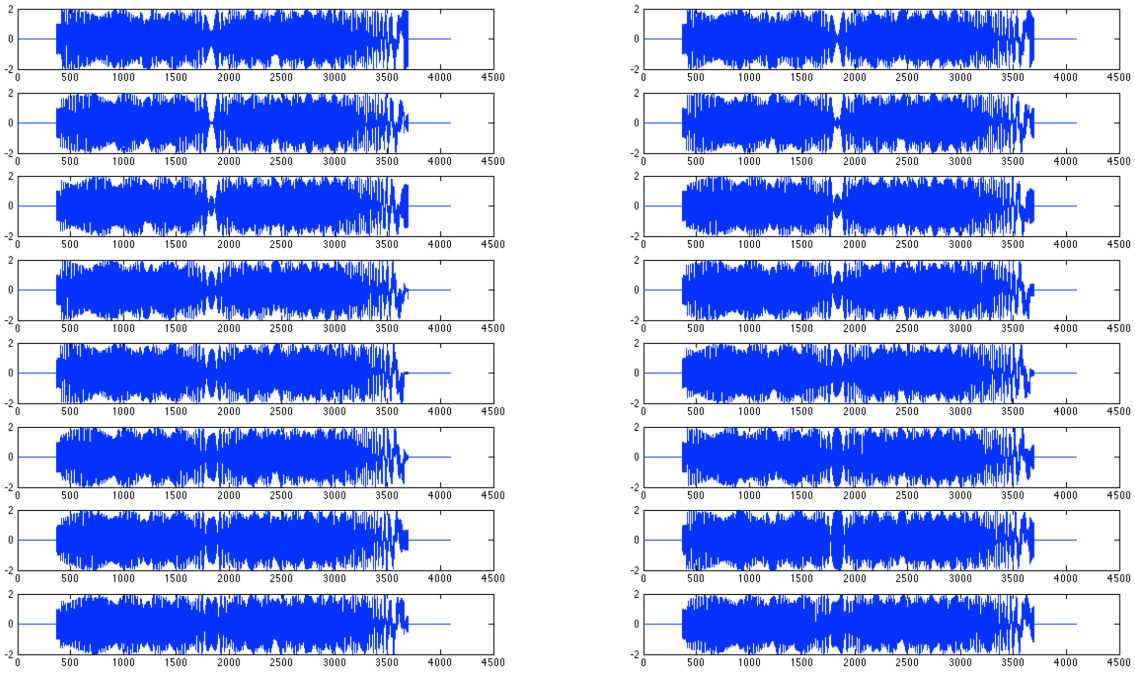

Fig. 40. Superposition of two signals on all elements.

Now consider several methods for estimation of the AOA of incident wavefronts. Throughout this investigation we refer to the plot of the AOA estimate versus angle as a spatial spectrum. For each case considered, several methods were calculated. For narrow bandwidth methods, the data were still filtered using the FFT configuration for CSS, but only the data from the center sub-band were used to process. For reference the conventional solution was considered by calculation of the correlation DF method using $\boldsymbol{a}^H(\theta)\widehat{\boldsymbol{R}}\boldsymbol{a}(\theta)$ as discussed for equation (2.18). Fig. 41 shows the result of narrow bandwidth correlation DF for 5 independent runs of a single 40% bandwidth chirp signal at $25dB$ Signal to Noise Ratio (SNR) impinging on the array from an angle of $78°$. All the 40% bandwidth chirp signals used for demonstration of results in this chapter have $B = 400MHz$ bandwidth, $800MHz$ to 1200MHz frequency modulation, with a center frequency of $1GHz$. The true AOA of the wavefront is indicated in the plot by a vertical dashed line.

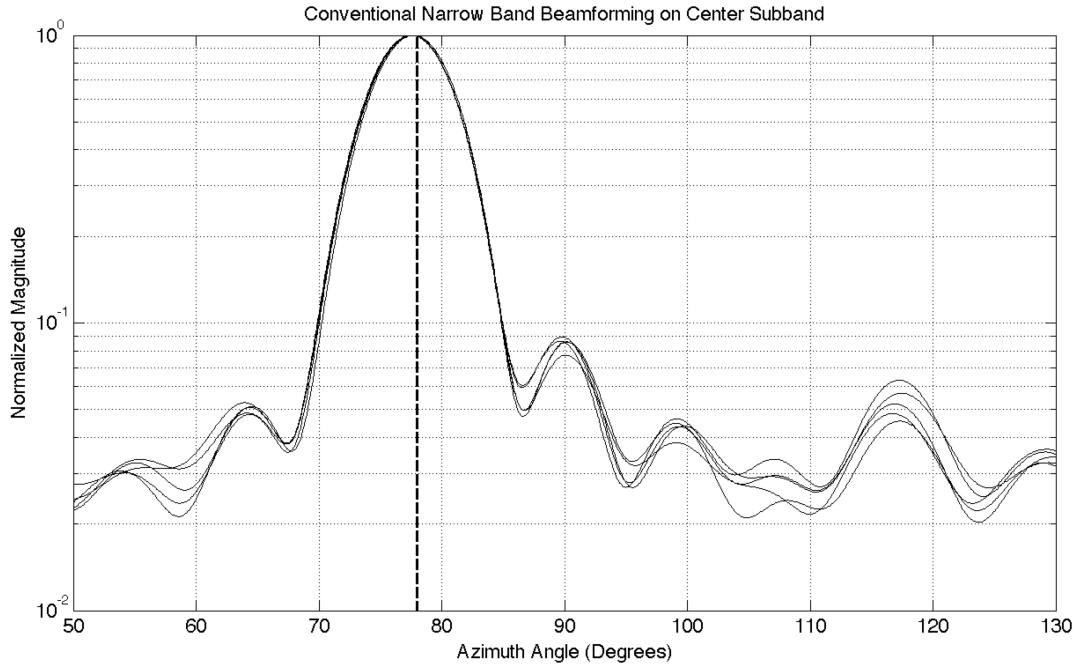

Fig. 41. Central sub-band processed using correlation DF with element data.

Narrow bandwidth MUSIC was calculated using equation (2.20) with the central sub-band data. Fig. 42 depicts the narrow bandwidth MUSIC spatial spectrum for 5 independent runs at the same SNR. Note that for all the MUSIC processes in this investigation, the number of signals was assumed known to be the true number of incident wavefronts since algorithms for estimation of the number of signals is not a focus of this investigation. The narrow bandwidth MUSIC result is for the same 40% bandwidth chirp signal as that of the correlation DF result. It is at an SNR of $25dB$ and impinges on the array from a true angle of $78°$. Note the much more narrow peak and low sidelobe characteristics of the MUSIC spectrum as compared to the narrow bandwidth correlation DF spectrum.

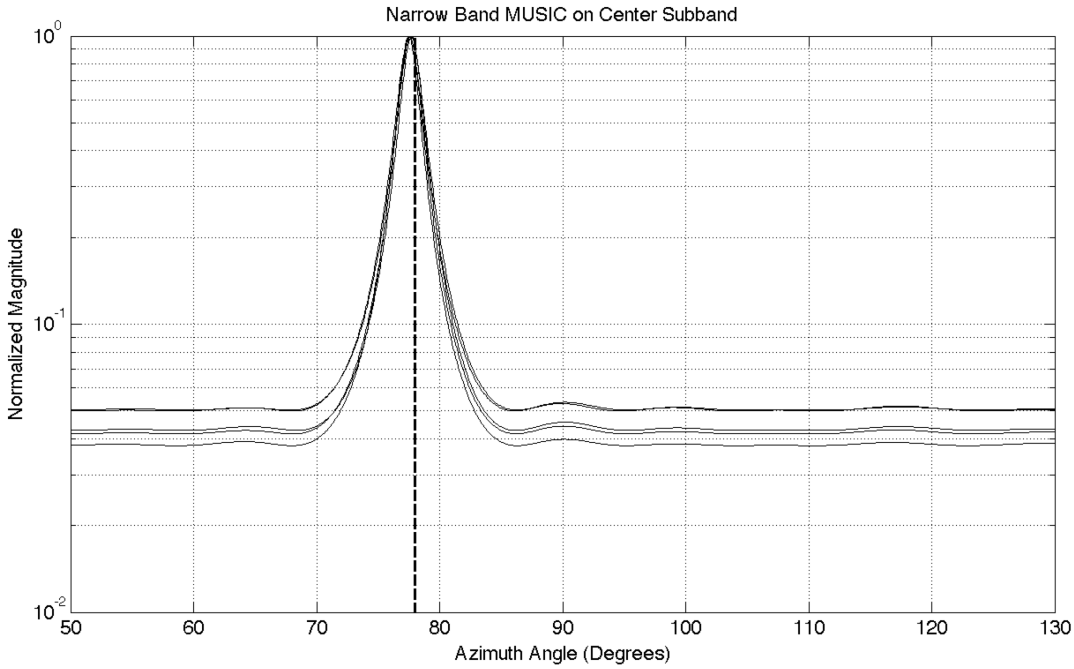

Fig. 42. Central sub-band processed using MUSIC with element data.

The wide bandwidth data were coherently integrated using the transformation matrices of equation (2.25) as described by Wang and Kaveh [44]. Following the wide bandwidth coherent integration, the data were processed using the CSS method spatial spectrum of equation (2.31) as if they were narrow bandwidth data. We used parameters similar to [44] of data segment lengths of $D = 64$ with 64 samples each at a sampling frequency of $f_s = 2B$ and sub-banded into $J = 16$ frequency bands equal of equal bandwidth. The initial estimate assumption for calculation of the transformation matrices was simply the true angle of the incident wavefront of $78°$ in order to yield the best result. The true angle is appropriate in this case since the initial single source case is just a preliminary demonstration that the method works and does not involve resolution of multiple sources. Wang and Kaveh utilized noise like signals at a lower

frequency, but still at a 40% bandwidth, so comparable results are obtained. This investigation used wideband chirp signals both since one of the main potential application areas is ELINT and due to the relative ease with which these can be shifted and resampled in simulations. Fig. 43 shows the result of CSS processing of 5 independent runs of the $5dB$ SNR wide bandwidth chirp signal. We depict the result for this noise level in order to highlight the multiple independent runs.

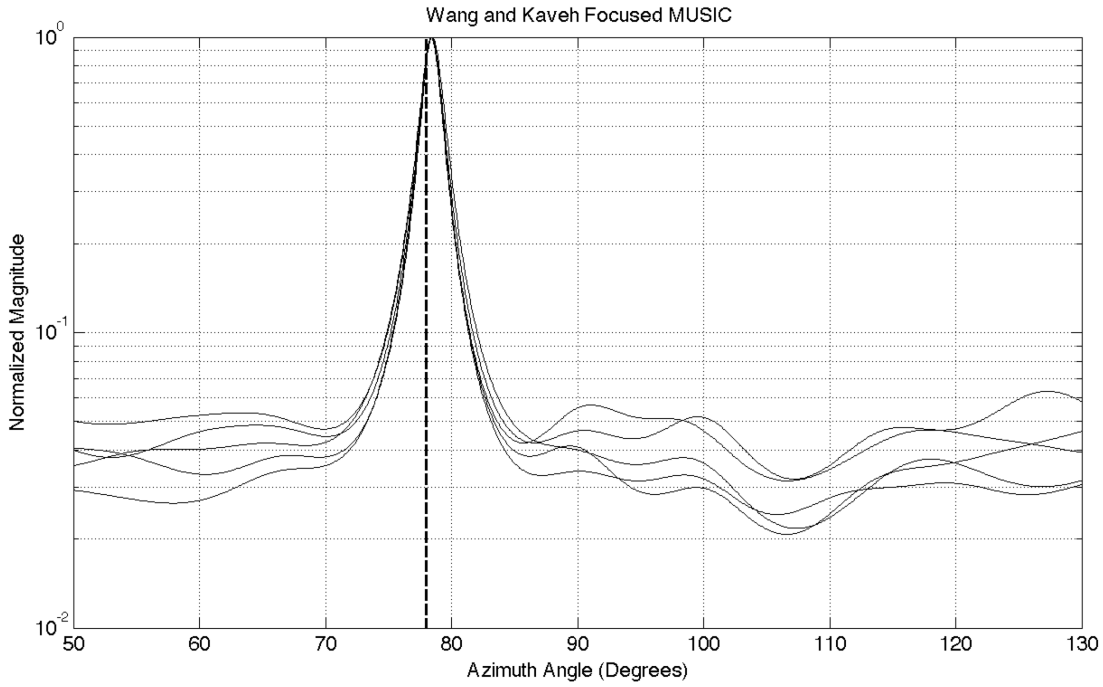

Fig. 43. All sub-bands coherently integrated with CSS then processed by MUSIC.

Next consider signal subspace processing in TTD beam space. For this processing, the element data were subjected to the fixed 8-beamformer bank depicted in Fig. 37. The output of the beamformer bank was then used to process the data in beam space. Fig. 44 shows the result of calculation of the TTD beam space MVDR spatial spectrum for 5

independent runs at $5dB$ SNR.

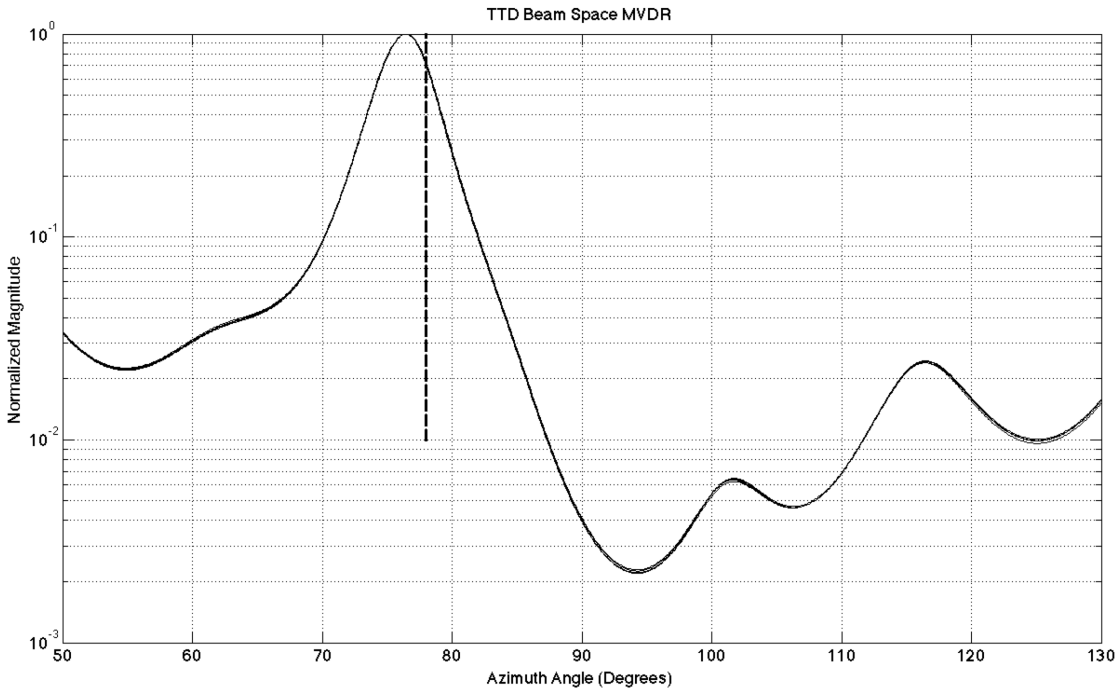

Fig. 44. TTD beam space data processed by Capon MVDR spectrum estimator.

The TTD beam space MUSIC spatial spectrum is plotted in Fig. 45 for 5 independent runs at $5dB$ SNR. Note the narrower peak and low sidelobe characteristics as compared to the TTD beam space MVDR spectrum.

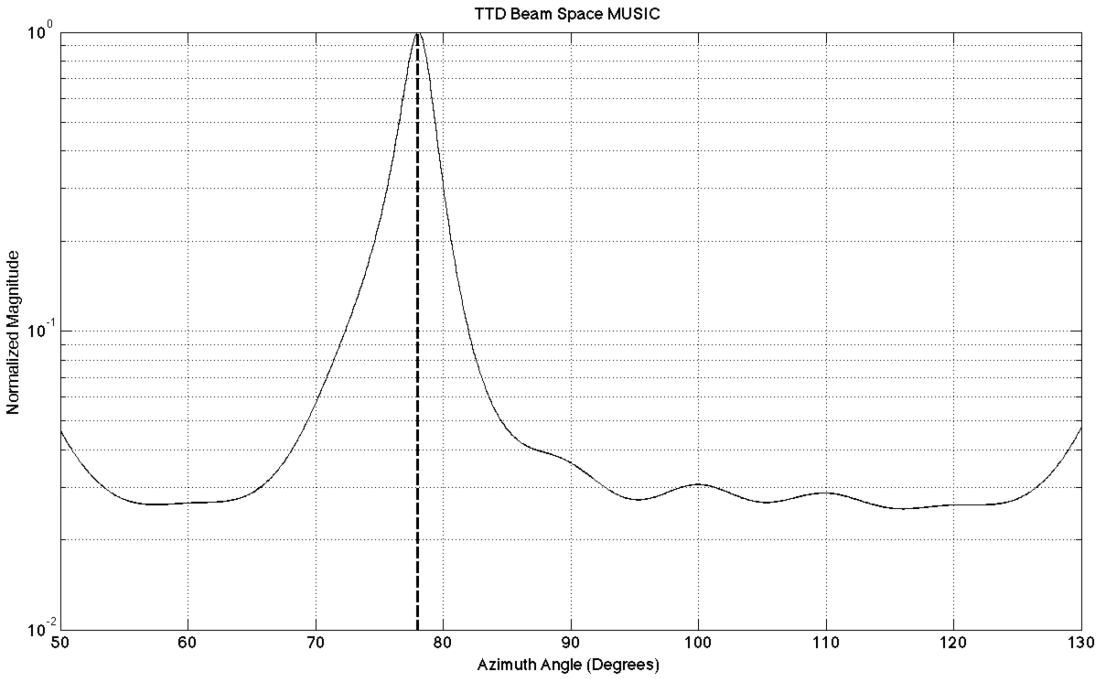

Fig. 45. TTD beam space MUSIC.

Fig. 46 shows the spatial spectra for these methods plotted together for the $B = 400MHz$ bandwidth waveform centered at $1GHz$ impinging on the array at an angle of arrival of $78°$ at an SNR of $25dB$. The initial estimate used to generate the transformation matrices for CSS was assumed given as $78°$. For these simulations the field of view was limited to the range of $50°$ to $130°$, although the methods described are readily extended to arbitrary array and beamformer bank configurations with larger fields of view.

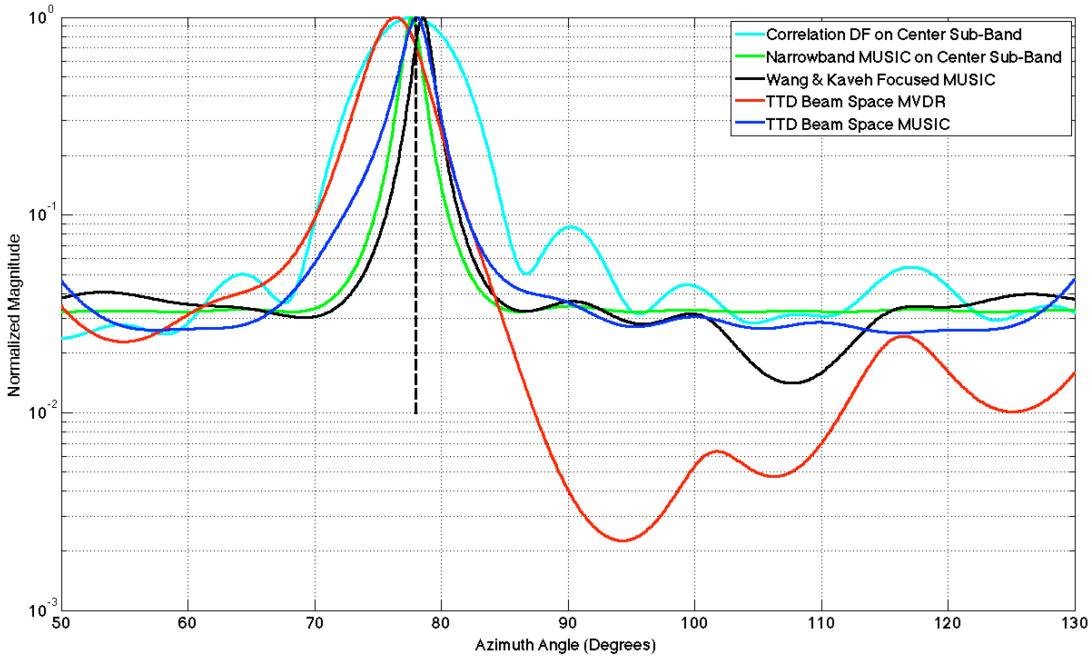

Fig. 46. Spatial spectra for location of a single 40% bandwidth $25dB$ SNR source.

7.1 Two Signal Example

Next we desire to examine resolution performance for closely spaced sources. For the case of two incident signals, consider one up-chirp at $72°$ and one down-chirp at $78°$, at $25dB$ SNR. The initial estimate used to calculate the transformation matrices for CSS was $75°$. All other signal and processing parameters were the same as those described for the single signal case. Fig. 47 shows the spatial spectrum for narrow bandwidth correlation DF for these signals. Once again the vertical dashed lines indicate the true AOA's for the incident wavefronts. Note the failure of correlation DF to resolve the two sources for this case. This is reasonable since the source separation is $7°$ and the approximate beamwidth is $9.2°$.

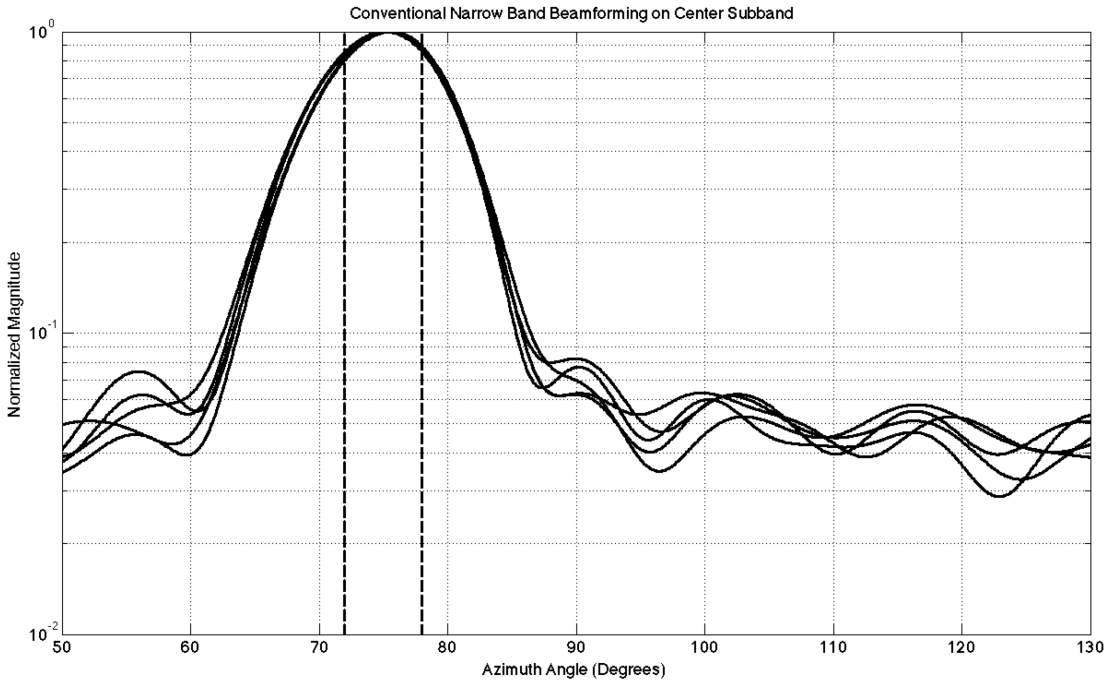

Fig. 47. Two signals $25dB$ SNR center sub-band correlation DF.

Fig. 48 shows the narrow bandwidth MUSIC spectrum result for the center sub-band in the two-signal case. The signals are clearly now resolved. Fig. 49 shows the two-signal case processed by CSS MUSIC and Fig. 50 shows the case for TTD beam space MUSIC, all with five independent runs shown for each method.

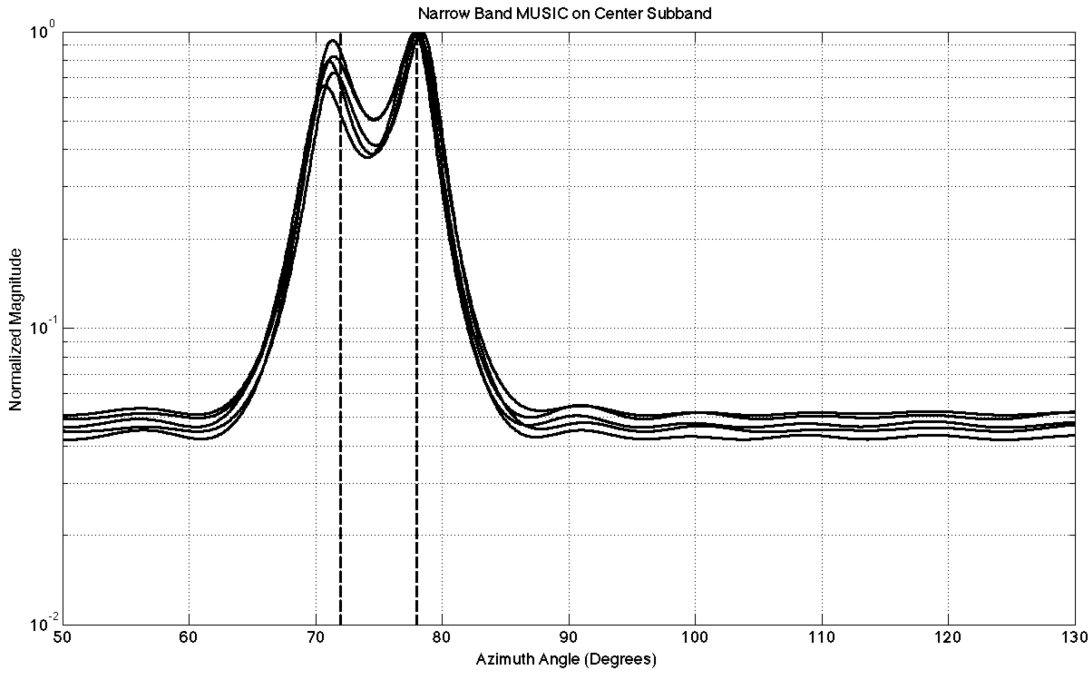

Fig. 48. Two signals $25dB$ SNR center sub-band MUSIC.

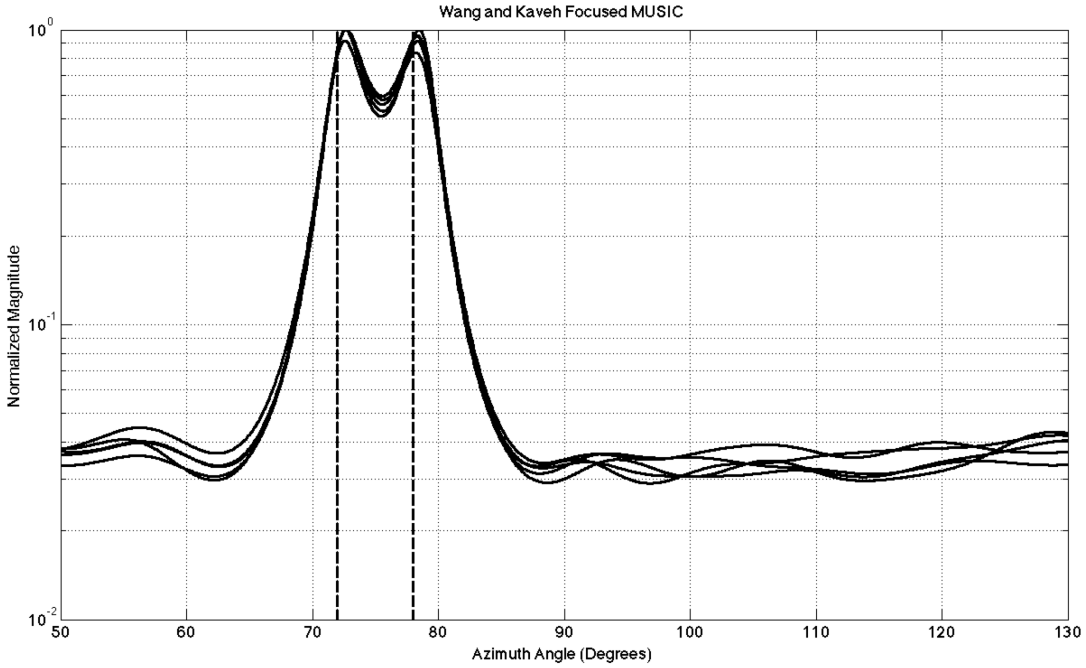

Fig. 49. Two signals $25dB$ SNR CSS MUSIC.

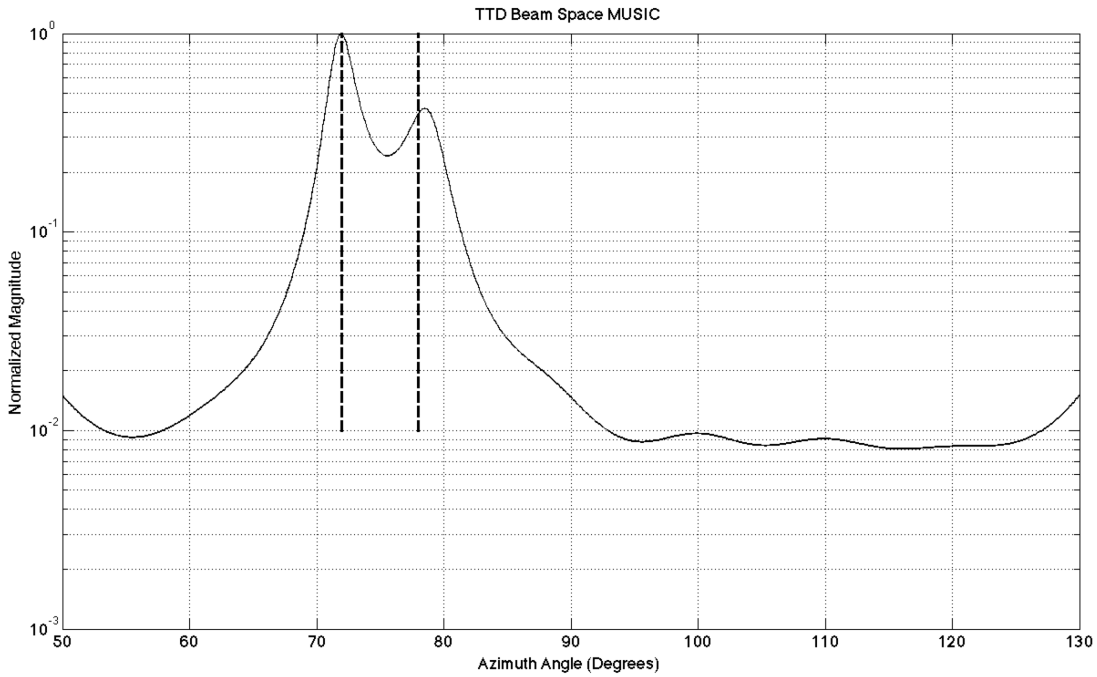

Fig. 50. Two signals $25dB$ SNR TTD beam space MUSIC.

Fig. 51 shows the various methods of element space and beam space processing for the two-signal case at $25dB$ SNR plotted together. All methods considered resolved this case except for narrow bandwidth correlation DF. Note that for comparison of multiple methods on the same plot, identical noise samples were used for all methods.

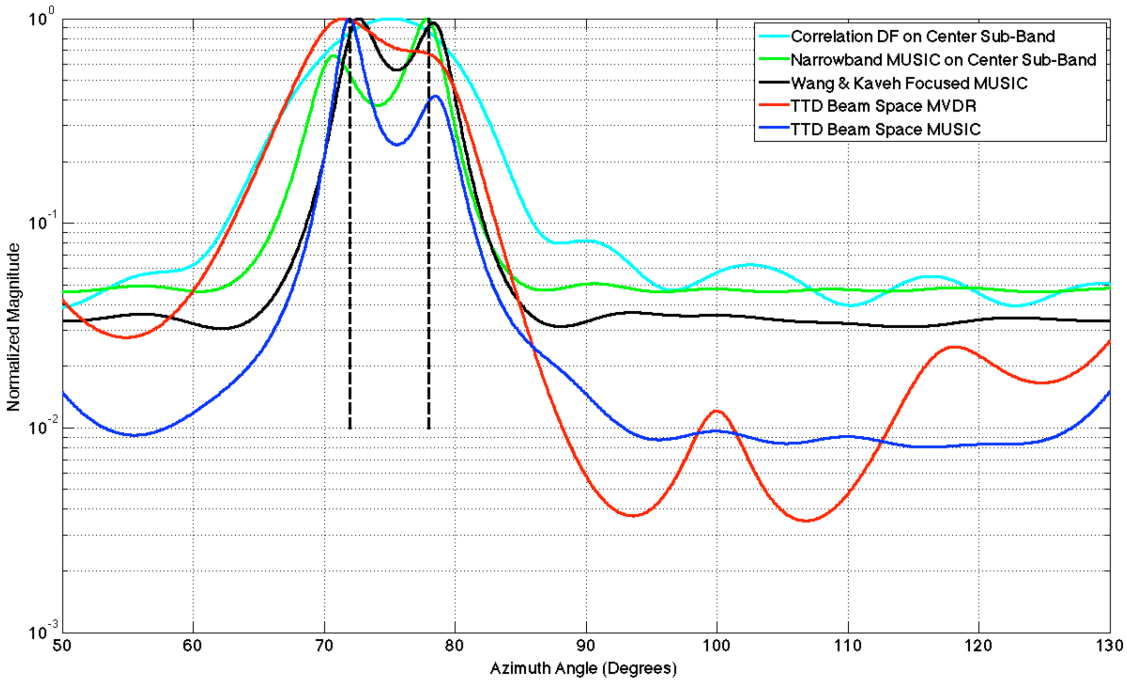

Fig. 51. Two sources SNR = $25dB$.

Note that for this example, narrow band MUSIC performance appears to be very close to that of wideband coherent integration. The spatial spectrum for TTD beam space processing, while perhaps appearing to have peaks not as sharp as those for element space signal subspace processing, does exhibit a low floor providing reliable indication of signal presence in the direction of the incident waveforms. The TTDBF MVDR method is not shown as it performs poorly as compared to TTDBF MUSIC.

Fig. 52 depicts the same case with the only change being that the noise level has been raised to an SNR of $15dB$. The element space narrow band methods fail to resolve the two sources. Interestingly, whereas for high SNR, narrow band MUSIC performance was very close to that of wideband coherent integration subspace processing, now for this

lower SNR its performance appears to be closer to the performance of correlation DF. Wideband CSS resolves the two sources and also exhibits a clearly lower floor than the narrow band methods providing a reliable indication of signal presence in the directions of the incident waveforms. The TTD beam space MUSIC method also resolves the two sources in this example. The TTD beam space method also continues to exhibit a low floor with a clear indication of signal presence in the direction of the two signals.

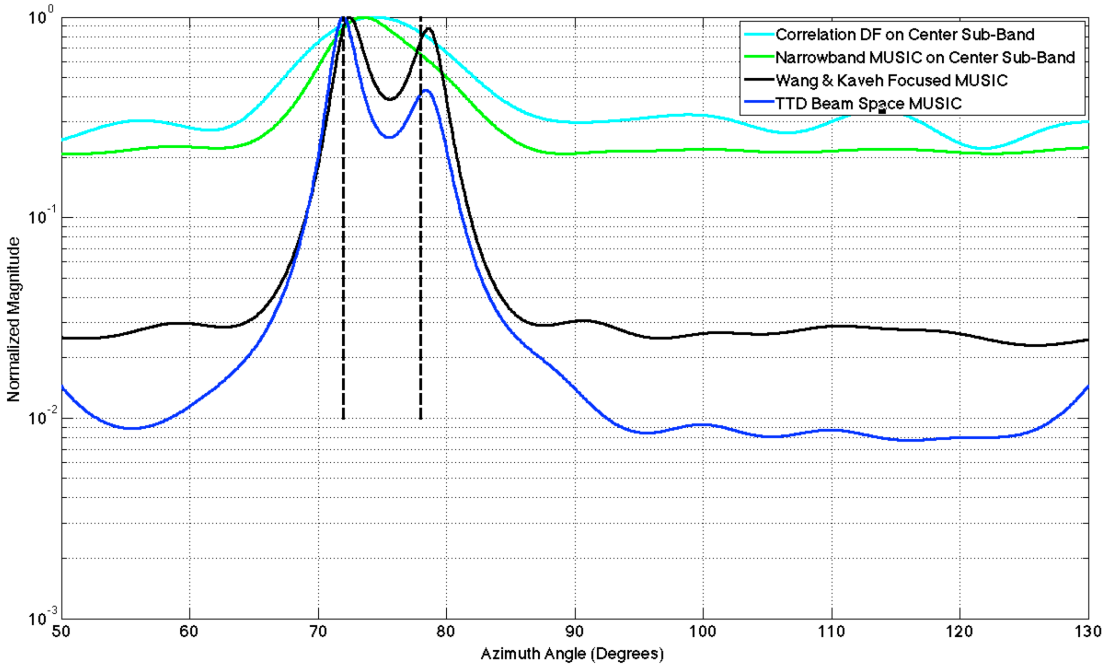

Fig. 52. Two sources SNR = $15dB$.

7.2 Three Signal Example

Next consider three incident wavefronts, two of which are closely spaced with a third disparately spaced. The three signals are an up-chirp at $72°$, a down-chirp at $78°$, and a

convex quadratic chirp at $105°$, all at $25dB$ SNR. The three signal case is significant because the transformation matrices for CSS processing are formed based on a single focal direction, the initial estimate, unless multiple iterations of the algorithm are performed. The initial estimate for CSS in this case is assumed to be given as $75°$. Fig. 53 shows 5 independent runs of the three signals processed by correlation DF. The spectrum clearly indicates signal activity in the directions of the sources, but the closely spaced ones are once again unresolved.

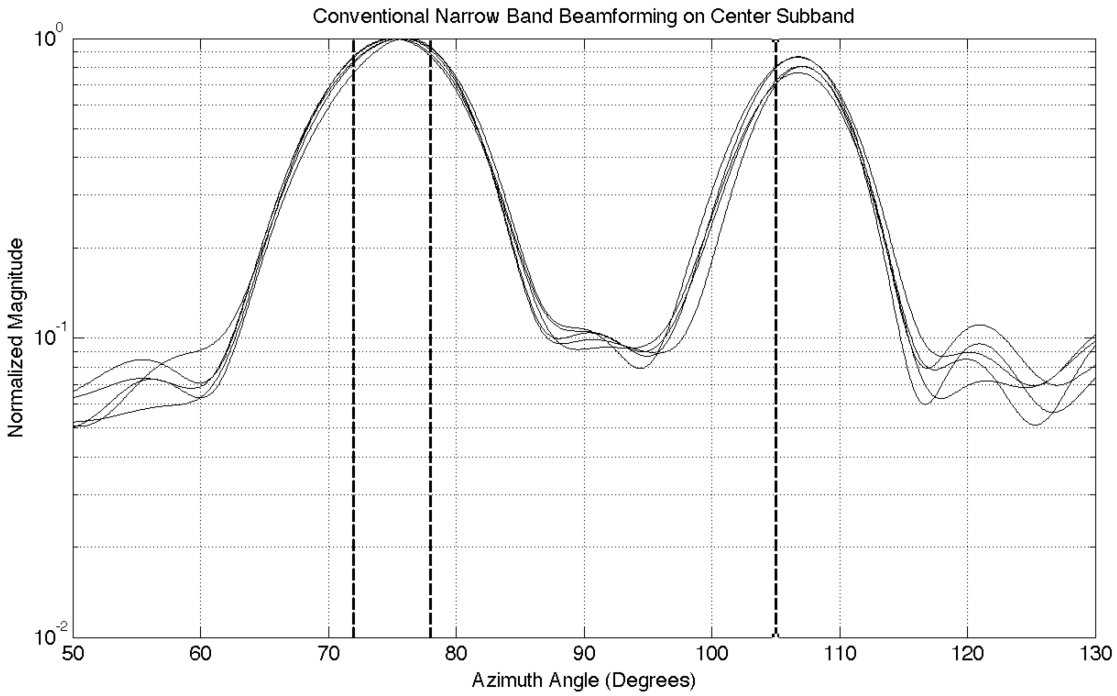

Fig. 53. Three signals $25dB$ SNR center sub-band correlation DF.

Fig. 54 shows the same three signals processed by narrow bandwidth MUSIC in the center sub-band. For the $25dB$ SNR cases, narrow bandwidth MUSIC has varied

performance, for the most part resolving all three sources, but with some significant errors.

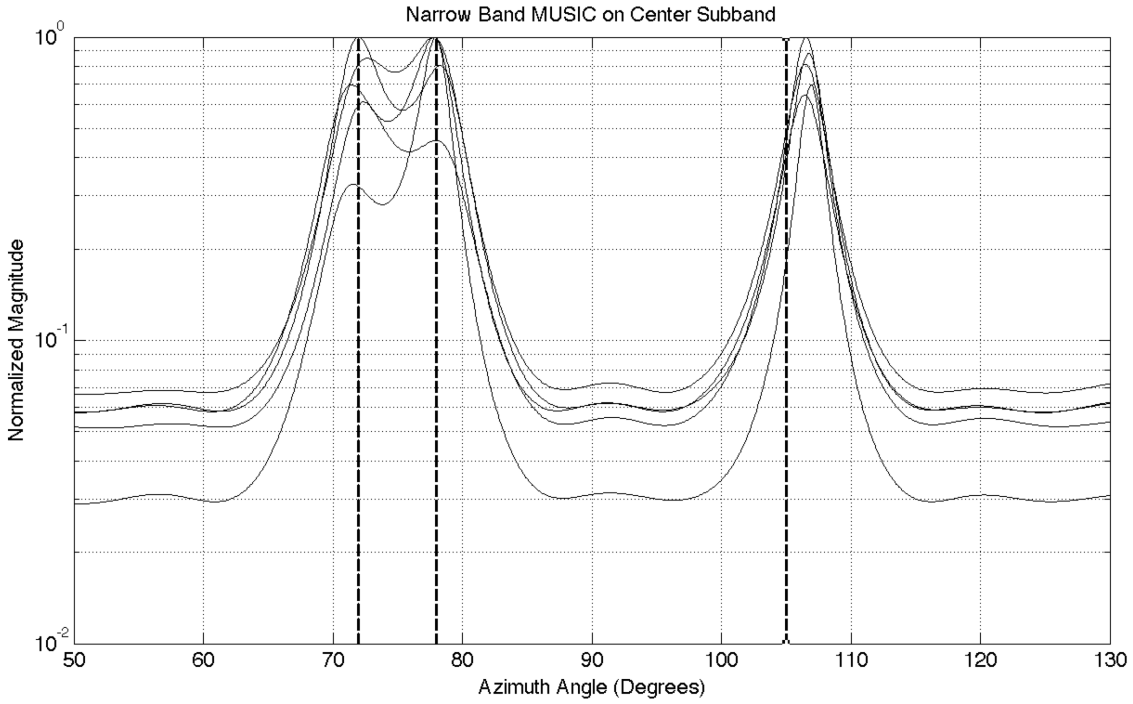

Fig. 54. Three signals $25dB$ SNR center sub-band MUSIC.

Fig. 55 depicts CSS MUSIC spatial spectrum for the three signals. Note once again that the CSS results are ideal assuming perfect knowledge of the noise samples as discussed in Section 2.5.1. The wideband CSS method result is shown for signals at $15dB$ SNR to highlight the multiple independent runs. Since the 3^{rd} incident waveform, the convex quadratic chirp, is displaced from the initial estimate of $75°$, CSS is defocused in the direction of the 3^{rd} wavefront. Even though CSS exhibits a peak near the location of the displaced 3^{rd} signal, the peak represents a significant estimation error. An additional iteration of the algorithm using an estimate near the $105°$ peak to generate additional

transformation matrices could potentially extract the correct spatial spectral information. Obviously to use CSS in a practical application it appears that for any given transformation instance, the spatial spectral data outside some angular interval centered on the initial estimate must be discarded which lends credence to Sellone's robustness boundary formulation [86]. Comparison of the TTD MUSIC result to the Sellone method is addressed in Section 7.3.

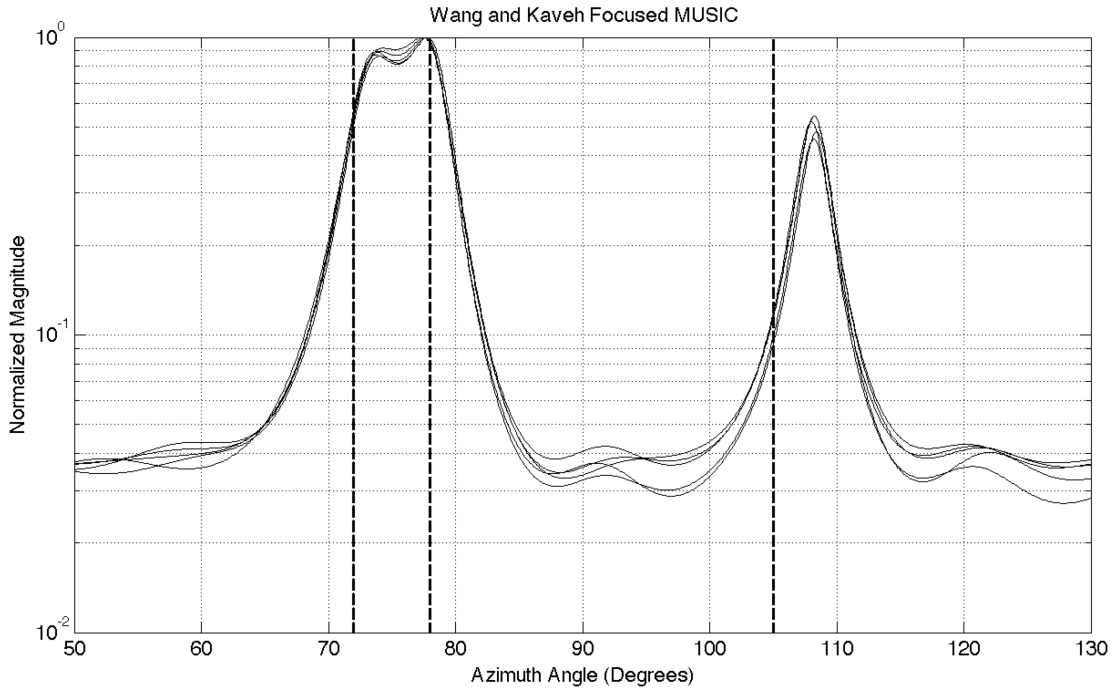

Fig. 55. Three signals $15dB$ SNR CSS MUSIC.

Fig. 56 shows the spatial spectrum for TTD beam space MUSIC. The TTD beam space spatial spectrum exhibits peaks in the directions of all three sources without requiring an initial estimate or iteration. In addition a considerable savings in computational

expense is realized by the TTD beam space method as compared to the element space methods as this experiment demonstrates TTD beam space processing in 8-beam space while the element methods are in 16-element space.

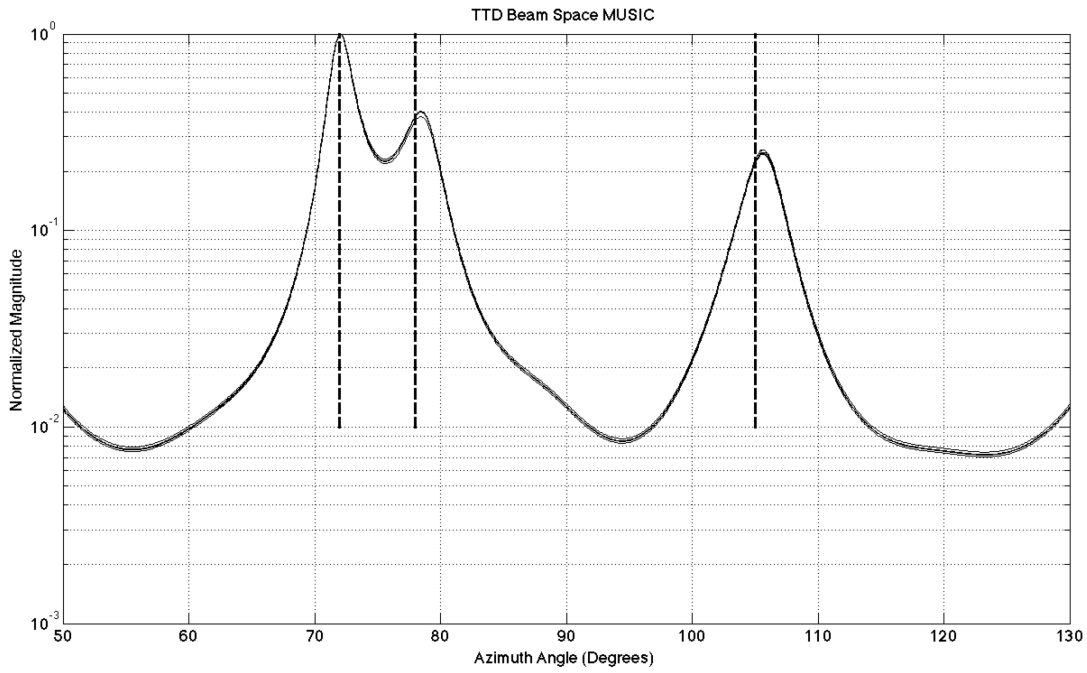

Fig. 56. Three signals $15dB$ SNR TTD beam space MUSIC.

Fig. 57 shows the spatial spectra for 3 signals for all methods plotted together. It clearly shows that for this example of the $25dB$ SNR level of the three sources considered, narrow bandwidth MUSIC still resolved the sources, but CSS is not capable of correct detection of all three sources in a single algorithmic pass. The TTD beam space MUSIC method, on the other hand, correctly exhibits its 3 highest peaks in the directions of the 3 wavefronts.

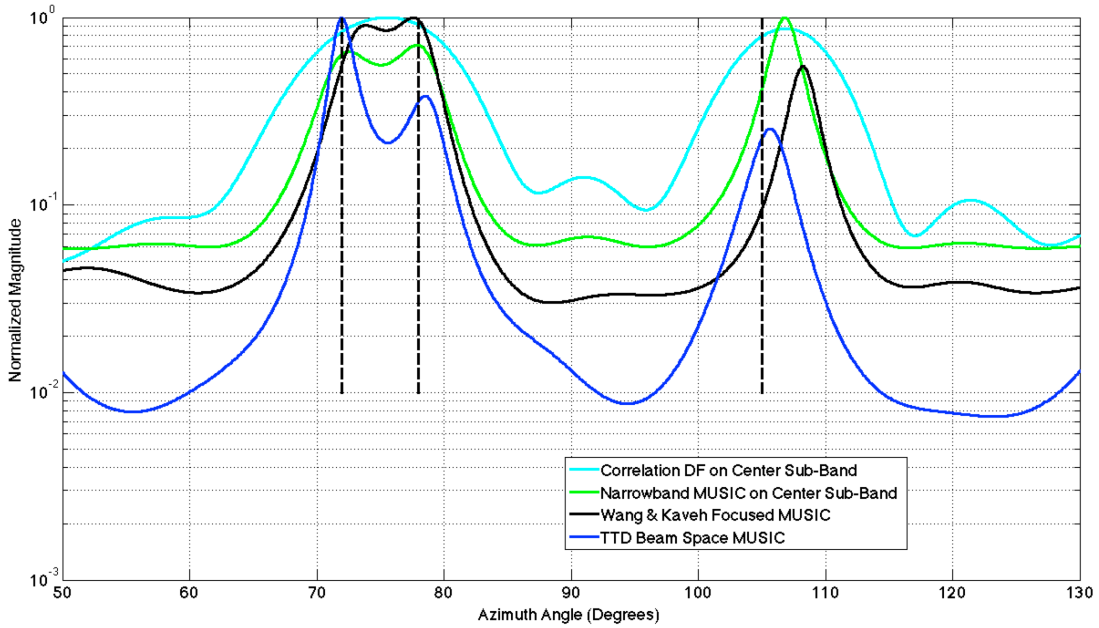

Fig. 57. Three sources, SNR = $25dB$.

Fig. 58 depicts the same configuration of three incident wavefronts but for an SNR level lowered to $15dB$. Note that once again, TTD beam space MUSIC yields accurate peak detections for the incident wavefronts. The narrow bandwidth MUSIC spatial spectrum now exhibits a peak in the direction of the two closely spaced sources, but it does not resolve the sources. It also now exhibits a somewhat greater error near the direction of the displaced wavefront. The initial estimate for calculation of the transformation matrices for CSS is still $75°$. The CSS MUSIC spatial spectrum is similar to the case of the three wavefronts with $25dB$ SNR, resolving the two closely spaced sources and possessing a significant error for the 3^{rd} peak.

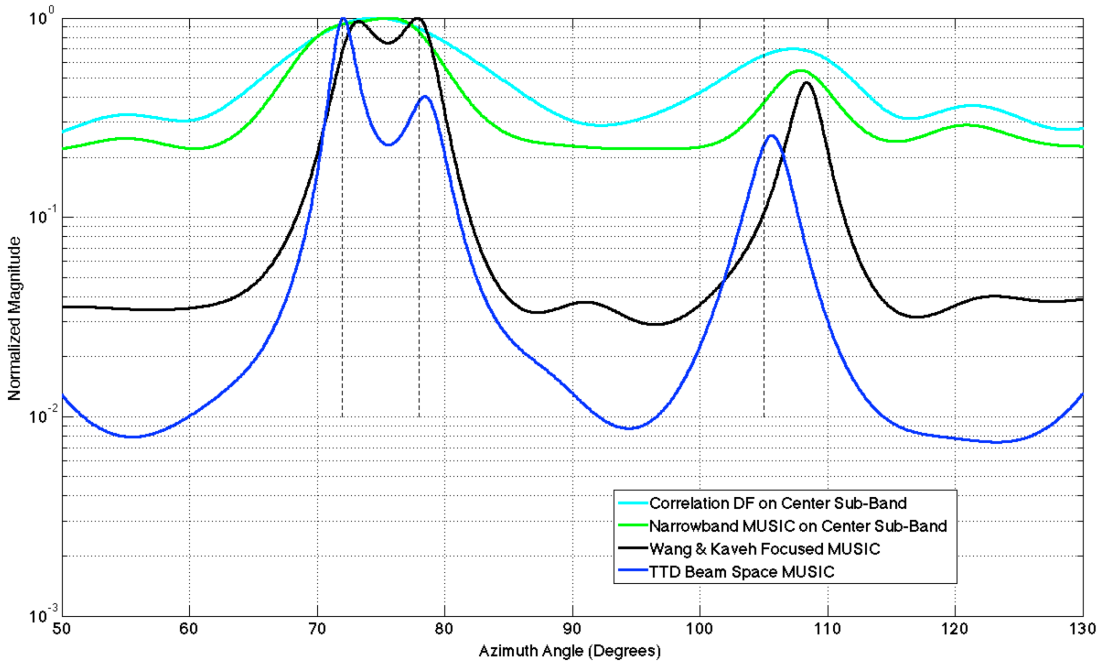

Fig. 58. Three sources, SNR = $15dB$.

These simulation experiments have shown that for appropriate applications requiring high-resolution source location of wideband sources when a limited field of view can be tolerated, the TTD beam space MUSIC method can be used to great advantage. It requires no preliminary course estimation, achieves results in a single algorithmic pass, and provides a significant computational expense savings as compared to element space methods such as wide bandwidth CSS MUSIC.

7.3 Comparison of TTD MUSIC to the Sellone Method

Sellone's R-CSM technique implements robustness boundaries around which the degrees of freedom are said to be concentrated around the source angles. This in turn is posited to improve performance in the robustness regions. The algorithm does not

require a preliminary AOA estimate, but is iterative, with successive iterations narrowing the robustness regions closer to the calculated source locations [86].

The R-CSM method was used to generate spatial spectra with the same data as the simulation of the TTD beam space MUSIC method. The example case examined was that of the 3 source signals described in Section 7.2. The SNR is $25dB$ and the R-CSM algorithm was permitted to operate over four iterations. Parameters peculiar to the R-CSM method were taken from Sellone's paper [86]. Fig. 59 shows the R-CSM spatial spectrum after the 1^{st} iteration. The plots have a linear scale with full semicircular azimuth with boresight at $0°$ as in [86]. Red vertical lines indicate the true AOA's and yellow vertical lines indicate the peaks detected in the spectrum. After the 1^{st} iteration, the R-CSM spectrum exhibits a single prominent peak close to the two closely spaced sources.

Fig. 60 shows the R-CSM spectrum after the 2^{nd} iteration. Two distinct peaks are now visible in the general direction of the two closely spaced sources as the robustness boundaries begin to converge around the source directions. After the 3^{rd} iteration shown in Fig. 61, three peaks are evident as the robustness boundaries continue to converge closer to the source directions. Finally Fig. 62 shows the result after the 4^{th} iteration. The three peaks are relatively close to the source directions.

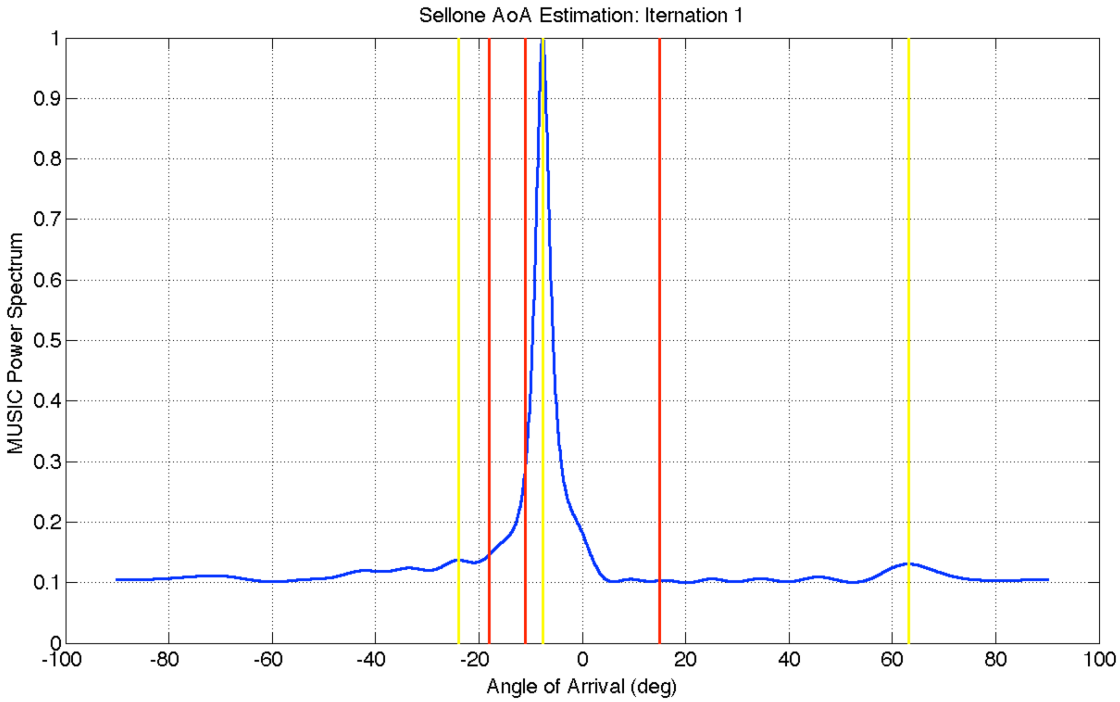

Fig. 59. R-CSM spectrum for 3 sources, 1st iteration, SNR = $25dB$.

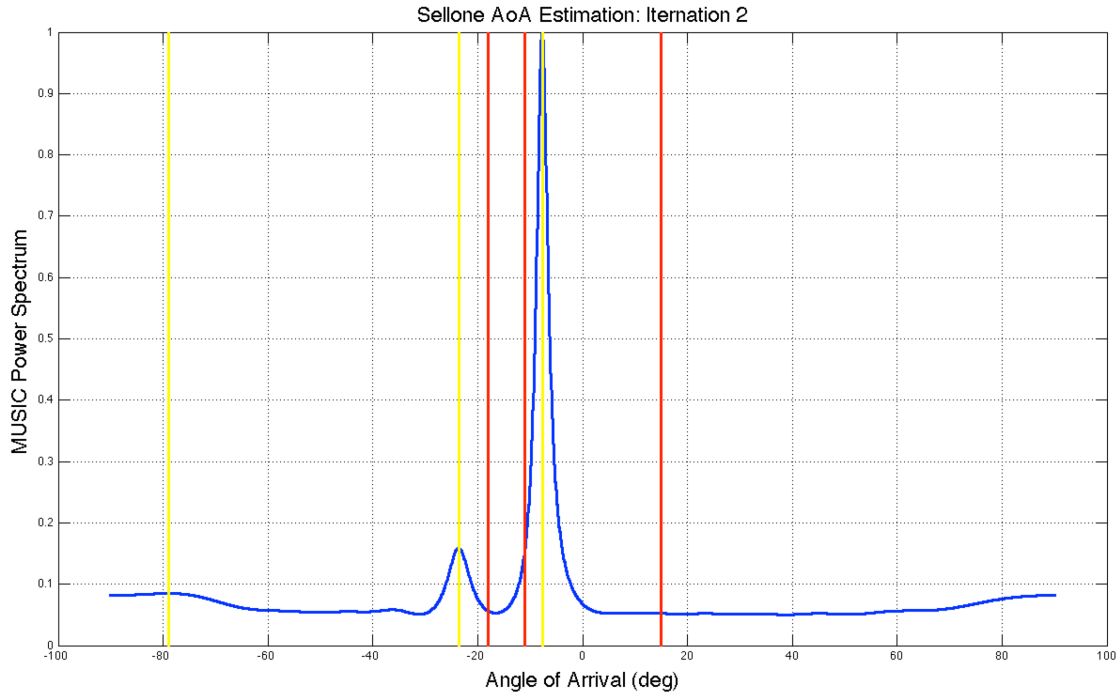

Fig. 60. R-CSM spectrum for 3 sources, 2nd iteration, SNR = $25dB$.

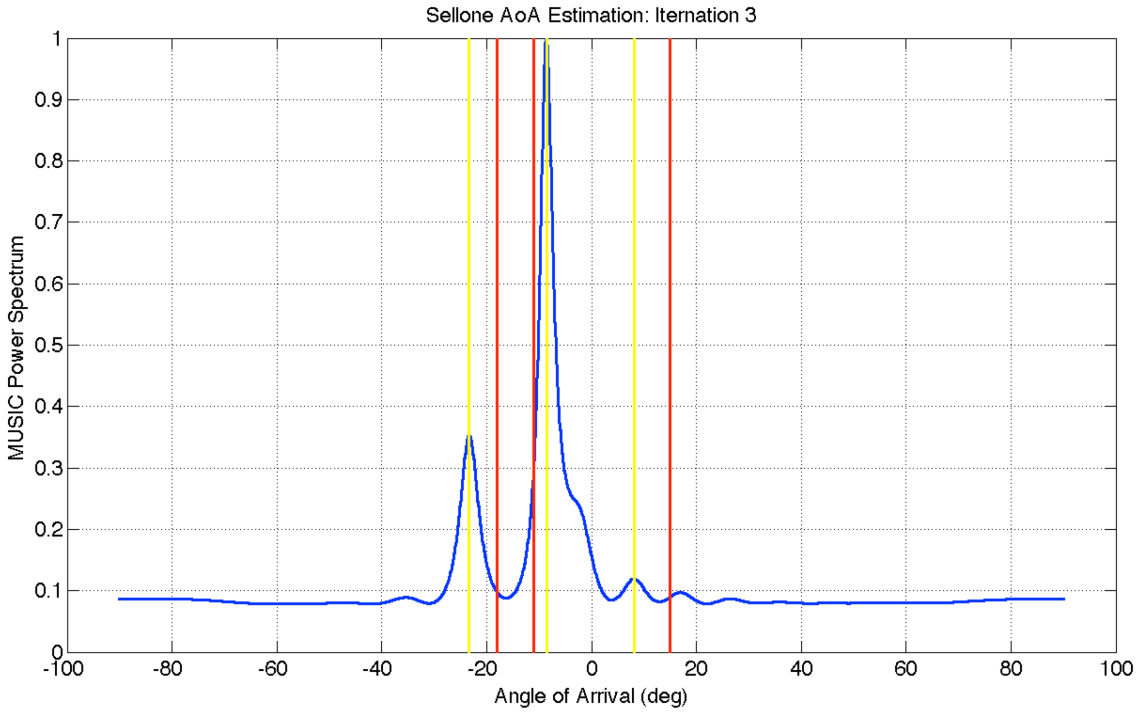

Fig. 61. R-CSM spectrum for 3 sources, 3rd iteration, SNR = $25 dB$.

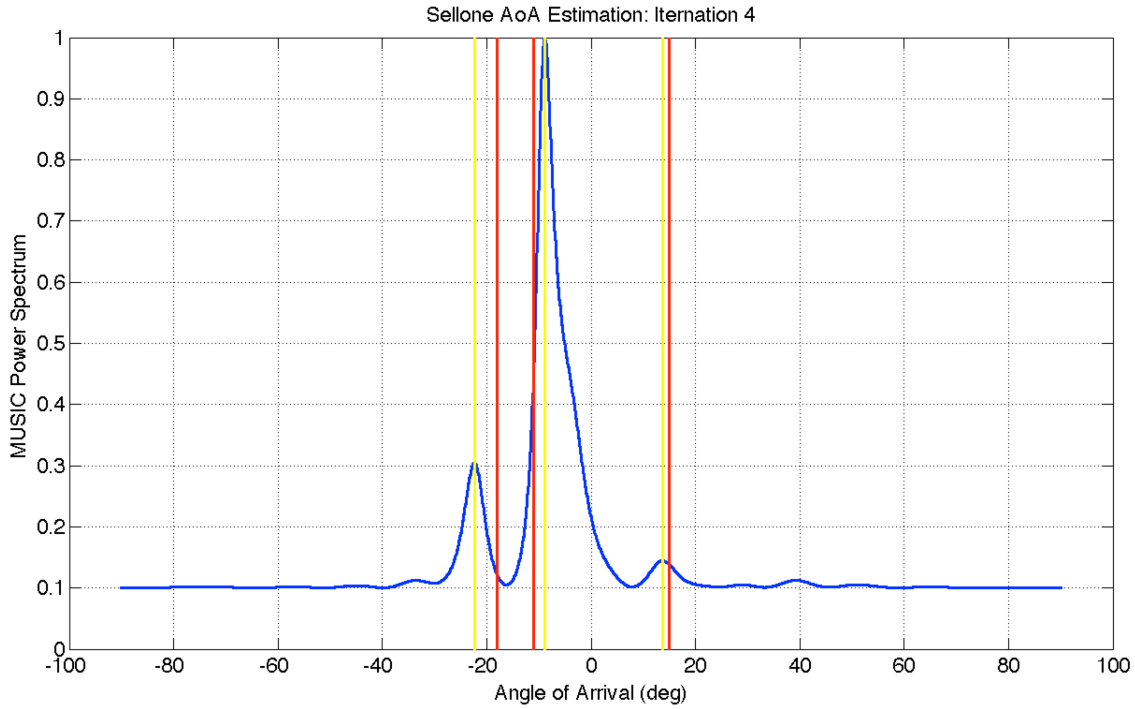

Fig. 62. R-CSM spectrum for 3 sources, 4th iteration, SNR = $25 dB$.

Fig. 63 depicts the R-CSM 4^{th} iteration spatial spectrum plotted together with the TTD MUSIC result on a semi-log scale for comparison. Once again the SNR is $25dB$ for the same three sources as discussed in Section 7.2. The R-CSM spectrum is the same 4^{th} iteration result as that plotted in Fig. 62. By inspection it is evident that the accuracy of the R-CSM result suffers which underscores the challenging nature of this signal set. One advantage of the R-CSM method is that it does not limit the field of view whereas the TTD beam space MUSIC result is for an instantaneous field of view limited to approximately $80°$.

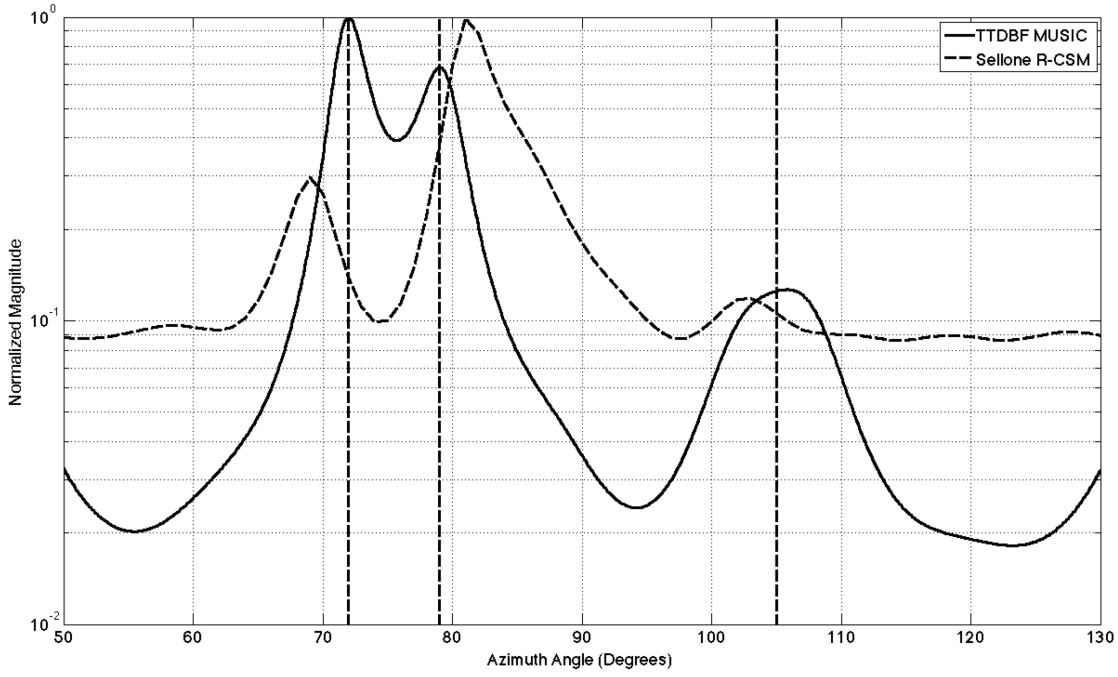

Fig. 63. TTD MUSIC and R-CSM (4 iterations) Methods with SNR = $25dB$.

7.4 Using Minimal Number of Degrees of Freedom

As one of the interesting comments from Gabriel's method [31] dealt with using the minimum degrees of freedom, we present here examples of using only 3 beams and the resulting 3×3 data correlation estimate, $\widehat{\boldsymbol{R}}_B$, for estimation of two closely spaced sources. We first select the beamformer bank direction vector as $[81.1°\ 90°\ 98.9°]$ so that the aggregate pattern exhibits a relatively flat response across the field of view. Fig. 64 shows the aggregate pattern for the three beams with a usable field of view approximately in the interval $[75°, 105°]$ in both rectangular and polar coordinates.

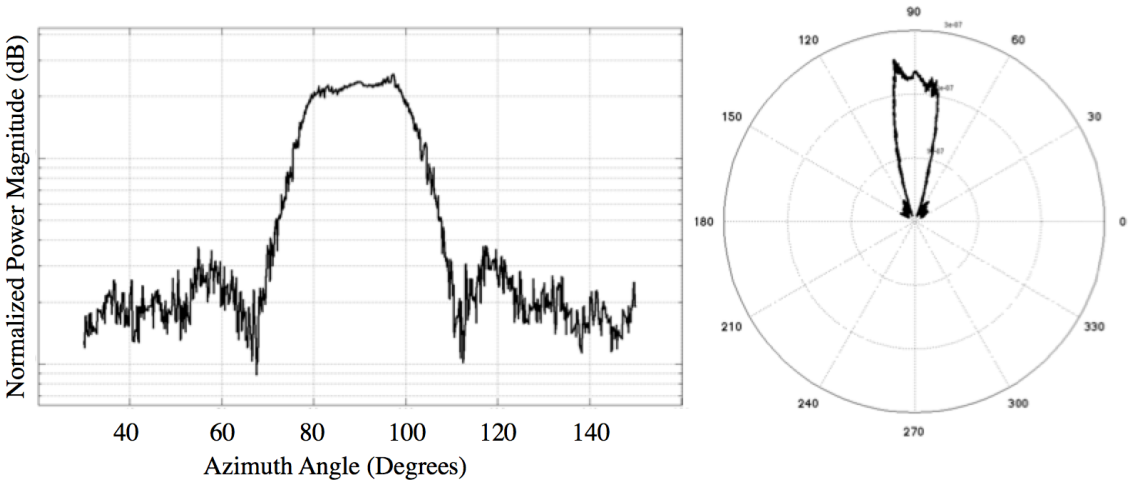

Fig. 64. Field of view for 3-beam bank.

For these simulations we use the same 16-element array, two incident signals, one up-chirp at $86°$ and one down-chirp at $93°$, at various levels of SNR. The initial estimate used to calculate the transformation matrices for CSS was $90°$.

Fig. 65 depicts the result for 5 independent runs of conventional correlation DF on the center sub-band at $25dB$ SNR. Note that all results in this section are plotted on the same $[75°, 105°]$ interval. Fig. 66 depicts the result for 5 independent runs for narrow bandwidth MUSIC on the center sub-band data at $25dB$ SNR.

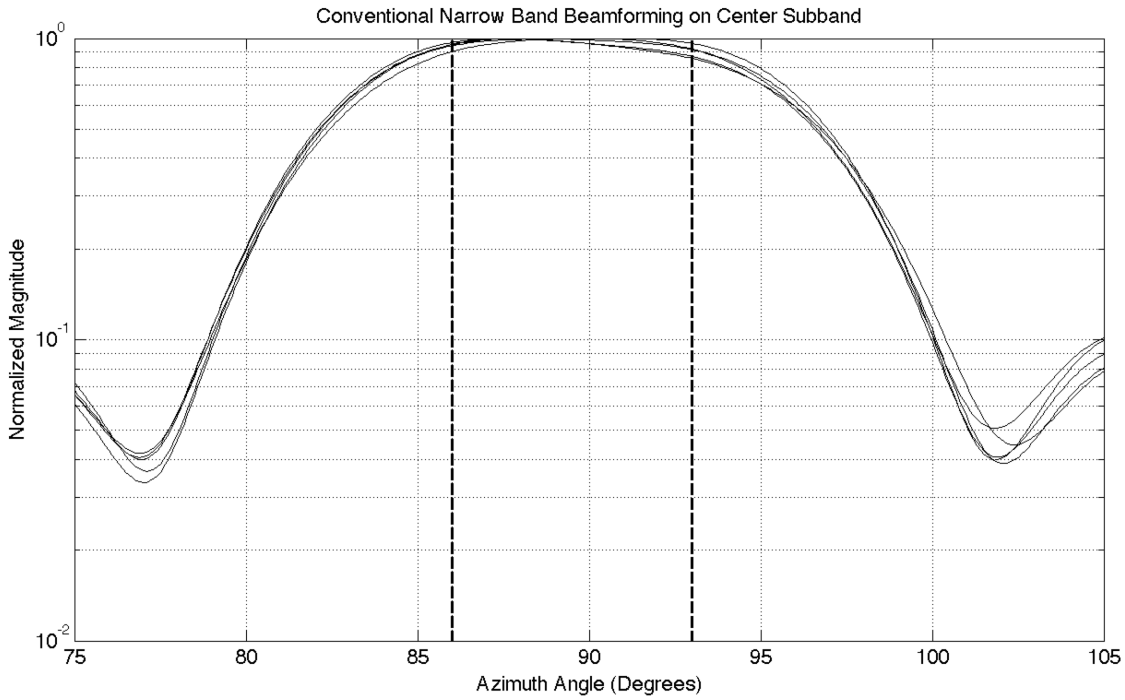

Fig. 65. Two signals $25dB$ SNR center sub-band correlation DF.

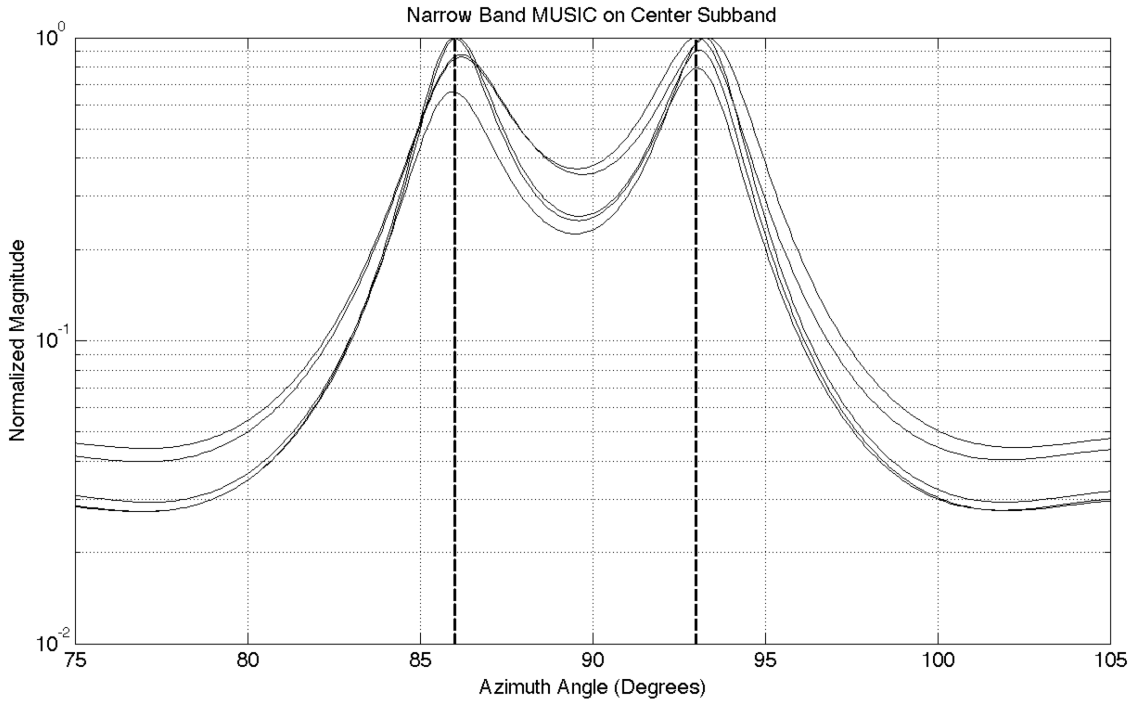

Fig. 66. Two signals $25dB$ center sub-band MUSIC.

Fig. 67 depicts the result for 5 independent runs of CSS at $25dB$ SNR. Observe that performance of narrow band MUSIC and wideband CSS appears similar at this low level of noise.

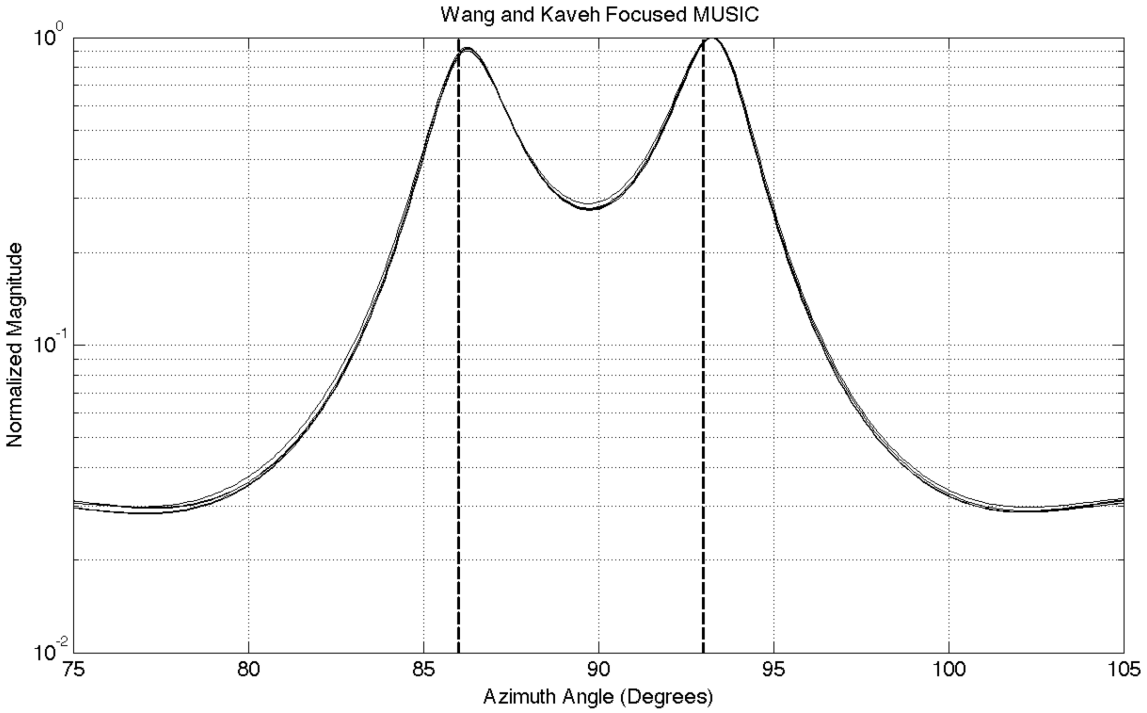

Fig. 67. Two signals $25dB$ CSS.

Fig. 68 shows the result for 5 independent runs of TTD beam space MVDR and Fig. 69 shows the result for 5 independent runs of TTD beam space MUSIC. Note that only 3-beam space was used in the TTD beam space examples while 16-element space was used for the element space methods. For the $25dB$ SNR level, the 3-beam space processing successfully resolves the two sources.

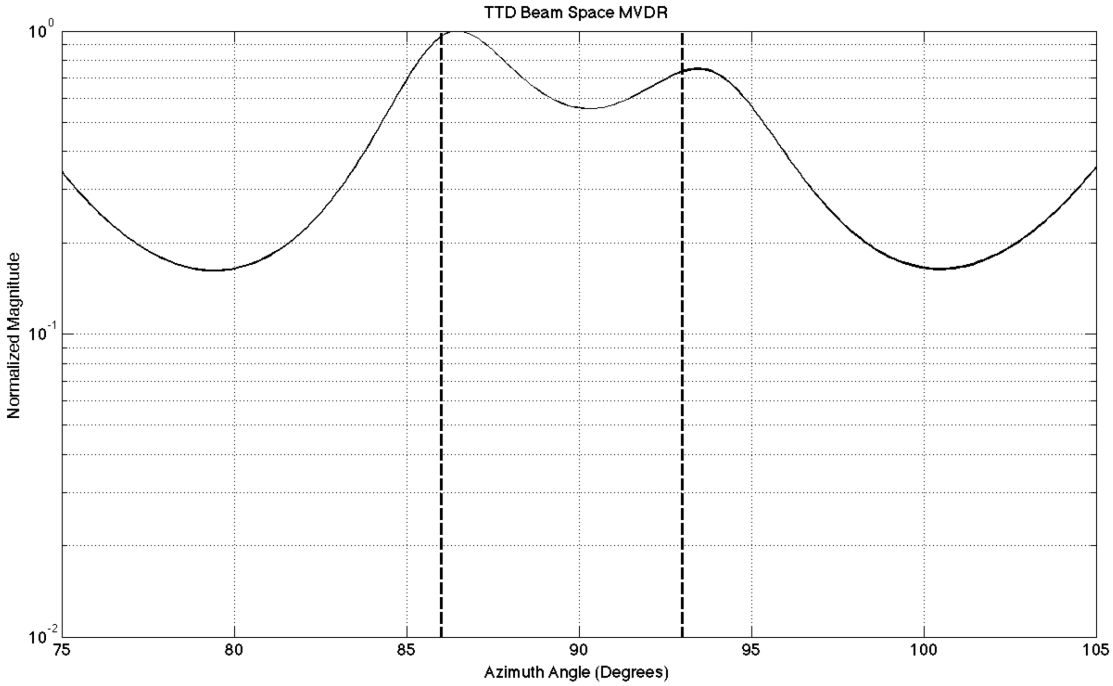

Fig. 68. Two signals $25dB$ 3-beam TTD beam space MVDR.

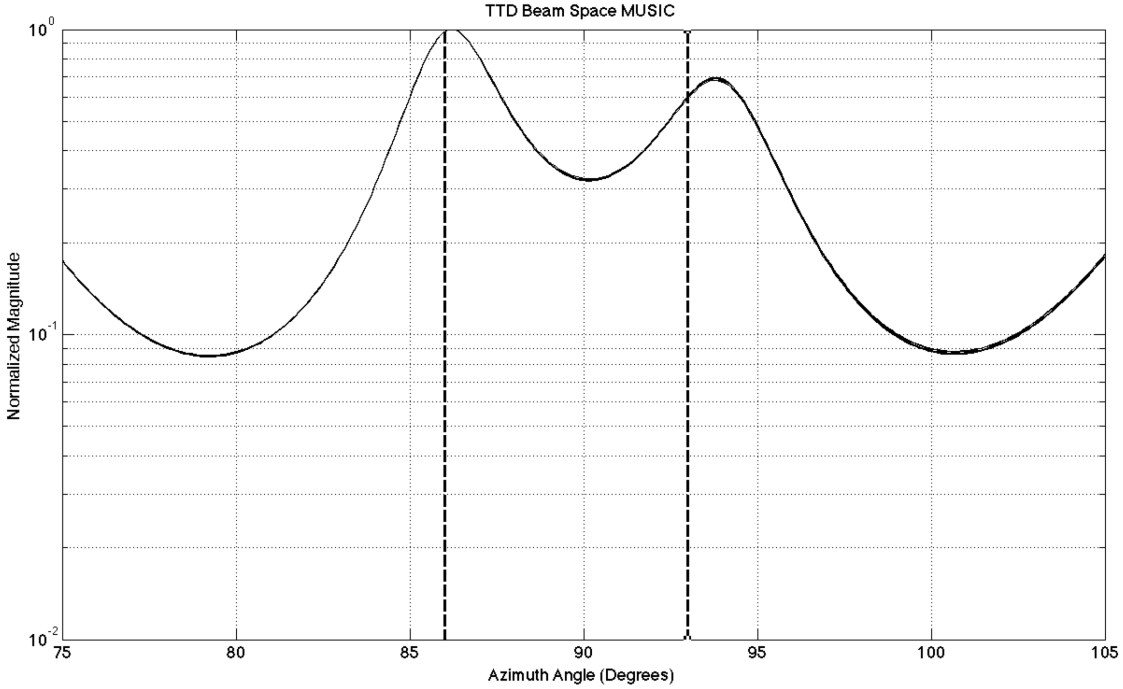

Fig. 69. Two signals $25dB$ 3-beam TTD beam space MUSIC.

The same cases were run for 16-element narrow band correlation DF, MUSIC in the center sub-band, wideband CSS, 3-beam space MVDR and MUSIC at $10dB$ SNR. Fig. 70 shows the result for correlation DF on the center sub-band. Fig. 71 shows the result for narrow band MUSIC on the center sub-band. The narrow band MUSIC method has now failed to resolve the two signals for this noise level.

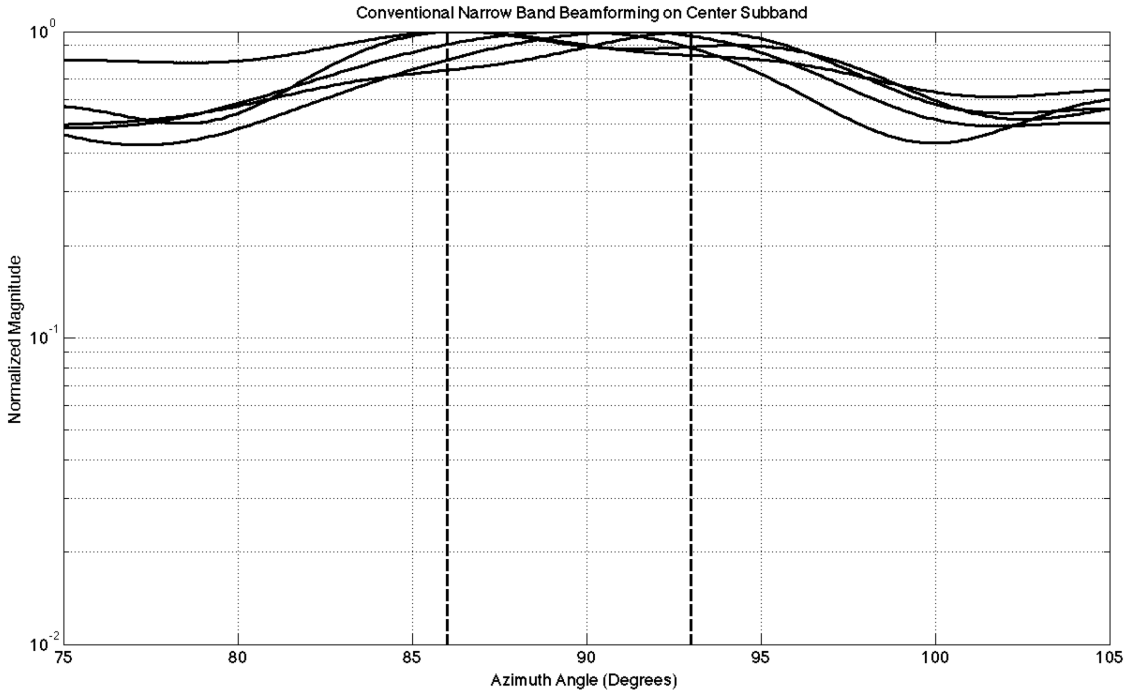

Fig. 70. Two signals $10dB$ center sub-band correlation DF.

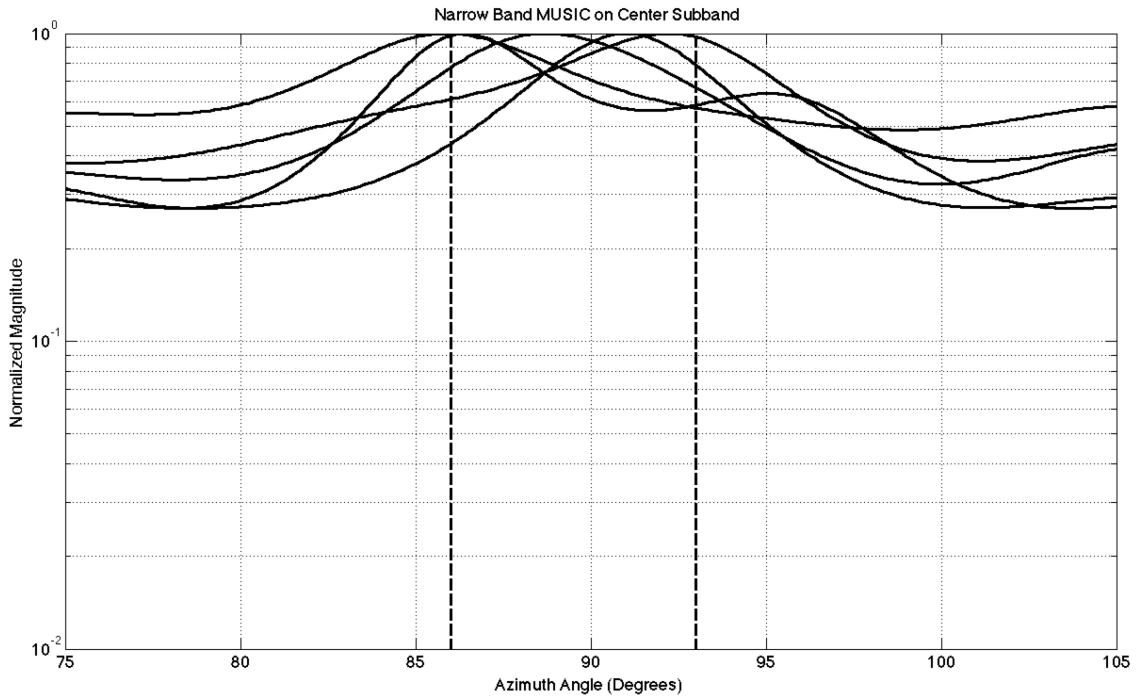

Fig. 71. Two signals $10dB$ center sub-band MUSIC.

Fig. 72 shows the result for the Wang and Kaveh CSS method that still performs very well even at the $10dB$ SNR level. CSS as demonstrated in this example is still quite computationally expensive since it is performed in 16-element space, must integrate over all frequency sub-bands of interest for each processing instance, and has accuracy that depends on the proximity of the sources to the focusing initial angle estimate. The beam space methods utilize a coherent integration of the array manifold over the frequency bandwidth, but this will typically be pre-processed and stored, not required to be re-computed for each processing instance. For the $10dB$ SNR example of 3-beam space TTD MVDR, Fig. 73 indicates that the sources are unresolved.

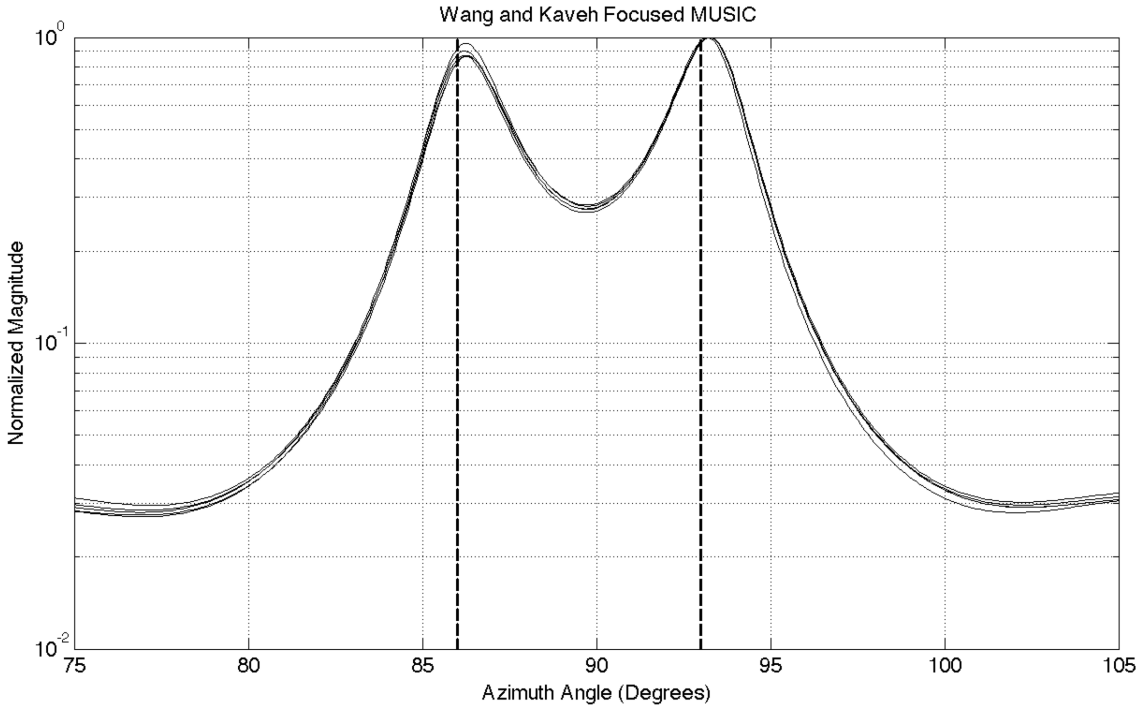

Fig. 72. Two signals $10dB$ CSS.

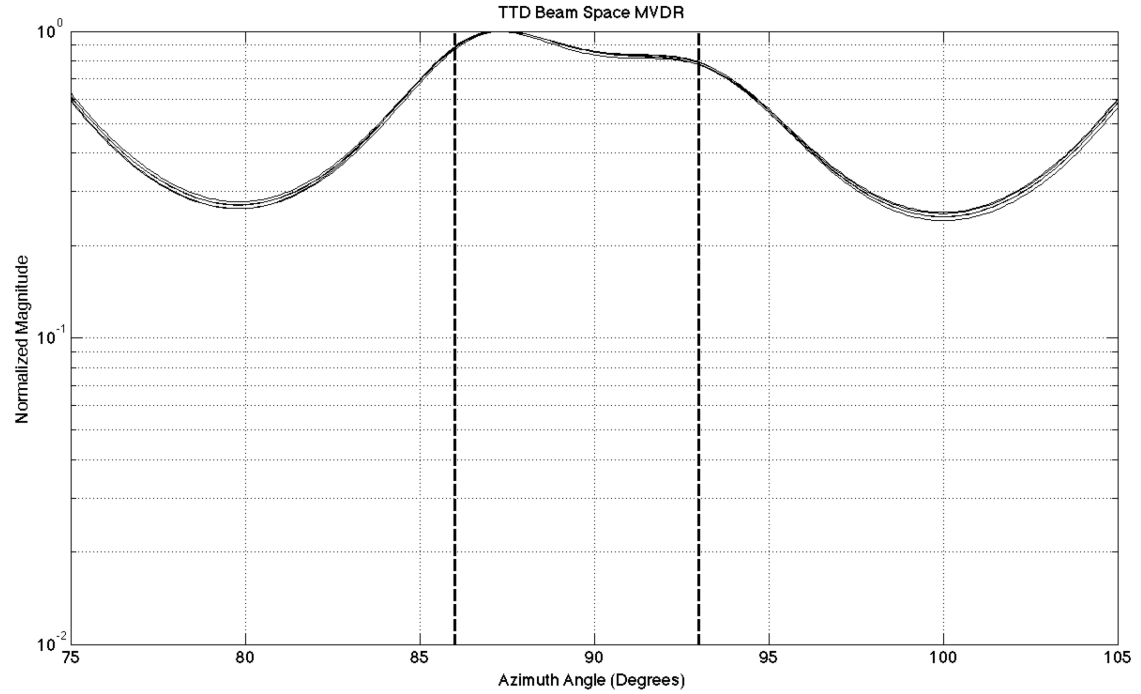

Fig. 73. Two signals $10dB$ 3-beam TTD beam space MVDR.

The $10dB$ SNR example for 3-beam space TTD MUSIC exhibits superior performance to that of 3-beam TTD MVDR having still successfully resolved the two sources as indicated by Fig. 74. The TTD beam space MUSIC method is thus observed to provide good resolution performance, low computational expense and does not require preliminary source estimation, albeit the beamformer bank limits the instantaneous field of view.

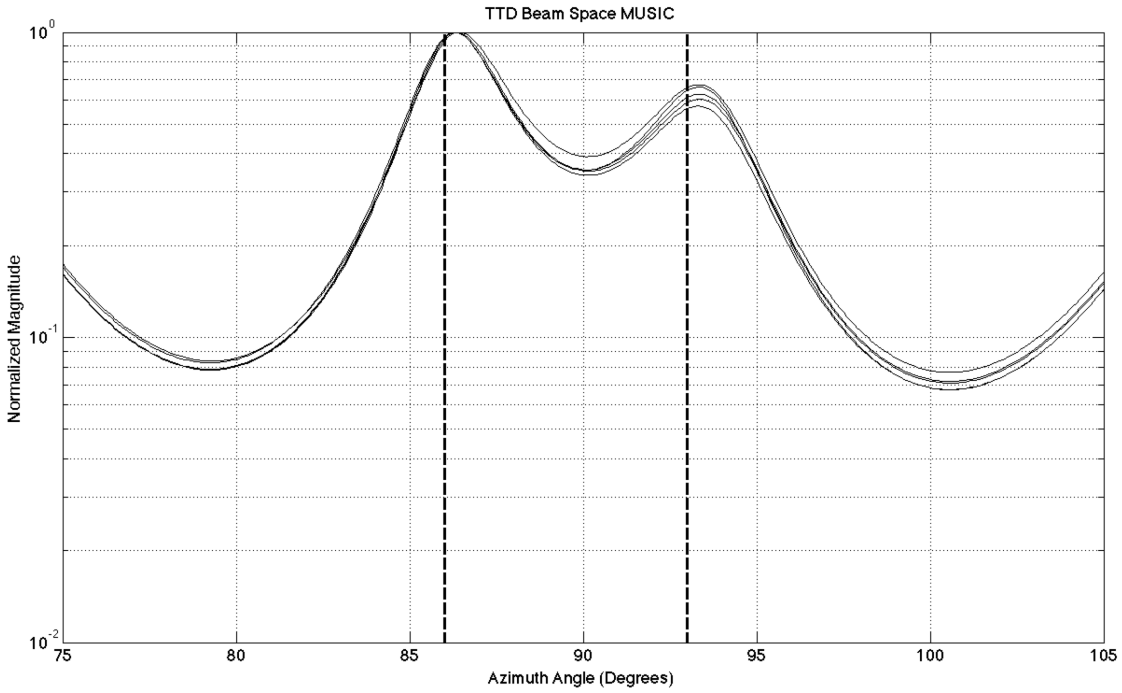

Fig. 74. Two signals $10dB$ 3-beam TTD beam space MUSIC.

7.5 Comparison of Methods to Theoretical Performance Bound

Now consider a comparison of the various methods to the Cramer-Rao Lower Bound (CRLB) using the equations presented in Section 3.4. As in [44] we simulate the bound using the difference, $\Delta\theta = 0.001°$, instead of the differential. Fig. 75 shows the CRLB

plotted as a function of SNR for the two signal case along with the standard deviation calculated for narrow bandwidth correlation DF, narrow bandwidth MUSIC, wide bandwidth CSS MUSIC, and TTD beam space MUSIC. The narrow band methods and CSS were calculated using 16-element space, while the TTD beam space methods were calculated using 8-beam space.

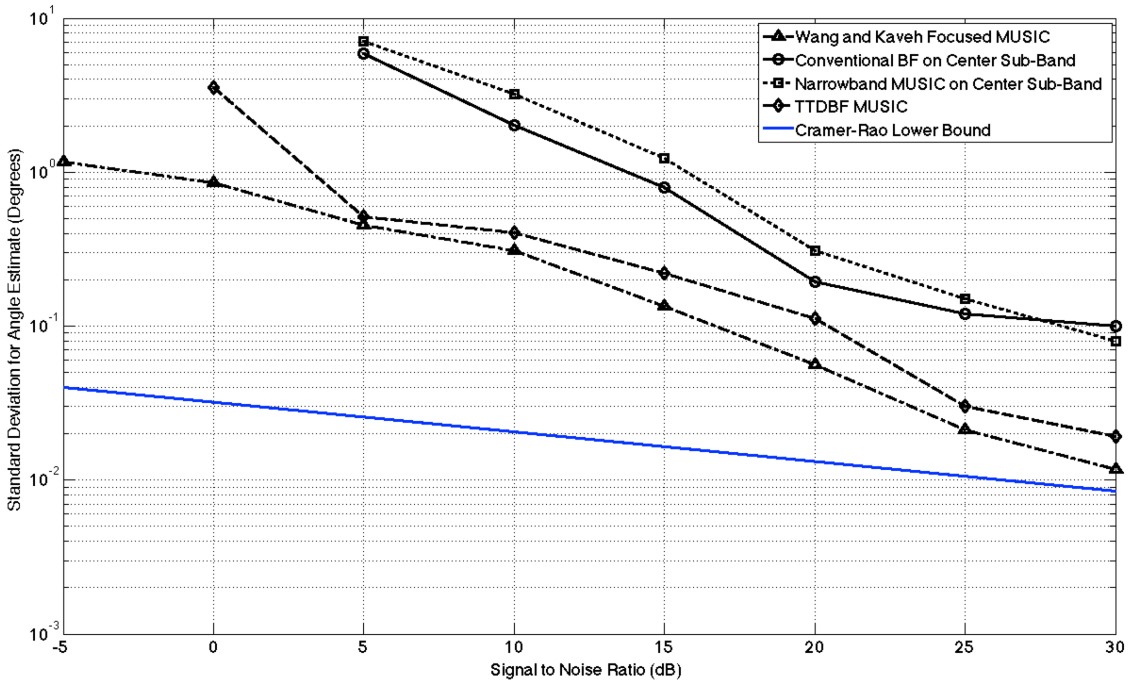

Fig. 75. Cramer-Rao Lower Bound (CRLB) and performance of various source location methods for two-signal case.

The incident waveforms in this example are an up-chirp at $86°$ and a down-chirp at $94°$. The initial estimate for CSS is given as $90°$. A Monte-Carlo simulation of 1000 runs at each SNR level was performed and the error in the peak detections of the 1^{st} waveform for each method were averaged to obtain the results. The plot shows the

standard deviation in peak detection error over 1000 runs across a range of SNR's for 4 methods. The TTD beam space method exhibits performance quite close to that of wideband coherent integration until detection drops off below $5dB$ SNR. The standard deviation performance calculated for both wideband coherent integration and the TTD beam space method is significantly closer to the CRLB than the narrow band methods.

Fig. 76 depicts the standard deviation for error in the peak detections of both sources for the TTD beam space MUSIC method. The peak detections calculated in the Monte-Carlo simulations do exhibit some bias. The mean over all 1000 runs for the magnitude bias calculated for peak detections of resolved peaks for both sources for the TTD beam space MUSIC method is shown in Fig. 77. The mean magnitude of the bias error is seen to be $< 0.5°$ for both estimates for SNR $\geq 10dB$.

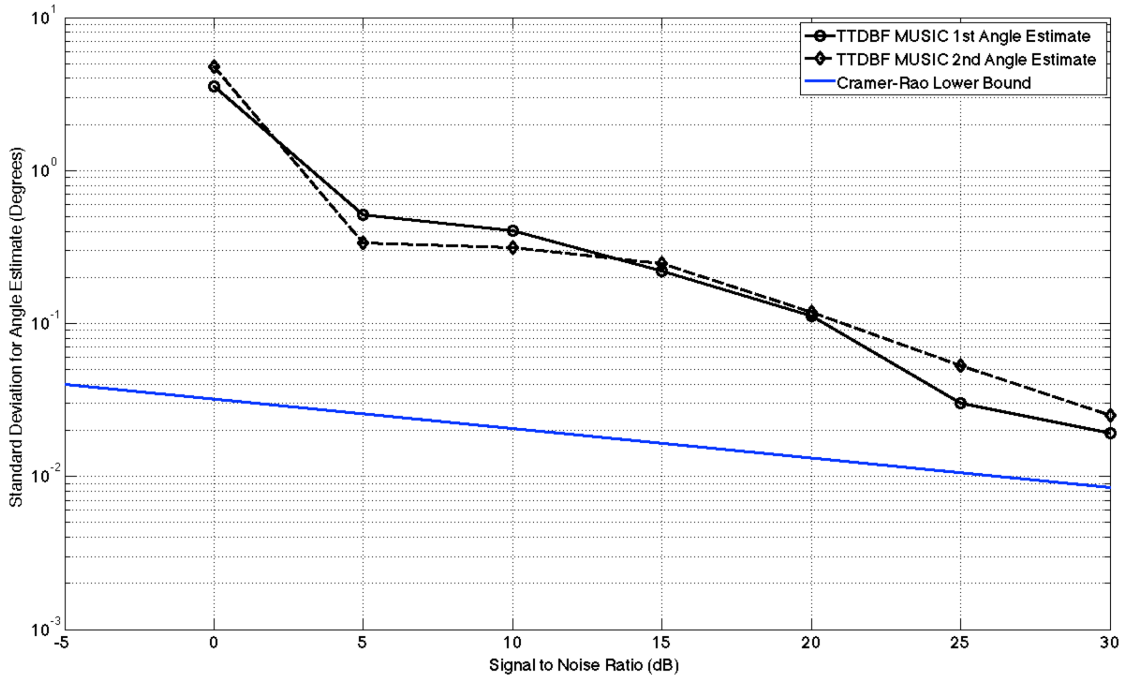

Fig. 76. Standard deviations for angle estimate errors for both sources.

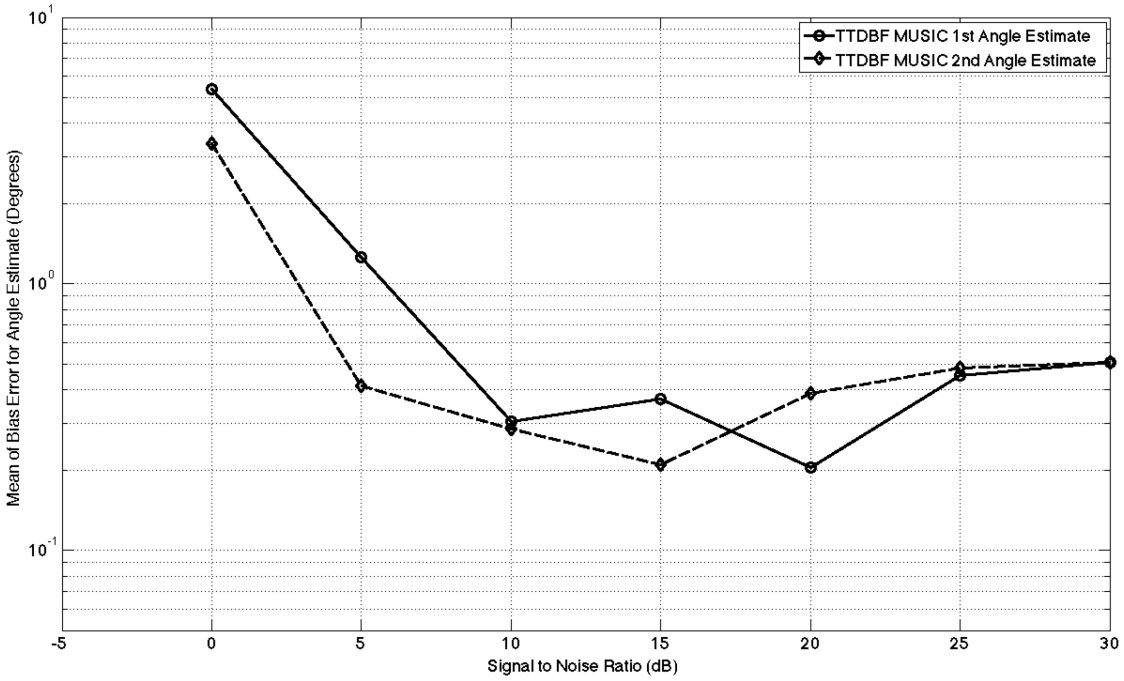

Fig. 77. Bias error for estimate of both sources for TTD beam space MUSIC.

7.6 Simulation Results for TTD Beamformer Bank Optimization

We wish to optimize the TTD beamformer bank for performance of the system. In order to perform such optimizations, a common fitness function and set of constraints was constructed. The fitness function evaluated detection of two closely spaced sources at multiple positions across the field of view by calculating the Mean Square Error (MSE) of the signal detections. For the examples shown, three sets of separate processes were executed in the fitness function to evaluate performance in different regions of the field of view. The three sets of signals were one with signals at $66°$ and $74°$, one with signals at $86°$ and $94°$, and one with signals at $106°$ and $114°$, so that the peak detection for all of these six points was used to calculate the MSE for each fitness function call. Six points is adequate since in order to demonstrate the concept these experiments evaluated the system in a simulated noiseless environment. The beamformer bank was constrained to 8 beams with each beam constrained to point within the system field of view. For each optimization experiment, the starting point of the beamformer bank was that described in the examples in the previous sections. In other words, the starting point corresponds to an arbitrarily constructed uniformly spaced beam bank that covers the desired system field of view. The fitness function value for the starting point is $MSE = 2.975^{\circ 2}$. The Matlab global optimization toolbox graphical user interface (type $optimtool$ on the $Matlab$ command line) was used to perform pattern search [129], simulated annealing [130], and genetic algorithm [131]

optimizations.

The $optimtool$ result for the pattern search optimization displays the best fitness function value for each iteration along with the number of function evaluations for each iteration and is shown in Fig. 78. The optimization terminated due to the arbitrarily set maximum number of fitness evaluations of 2500 being reached with a final fitness function value of $MSE = 0.028^{\circ 2}$ and corresponding beamformer bank steering vector $[53.1° \; 58.9° \; 73.1° \; 79.0° \; 94.9° \; 100.5° \; 107.0° \; 125.0°]$. Note that for concept demonstration purposes, the three sets of signals used in the fitness function evaluate only a very limited portion of the field of view. The performance may suffer in other regions of the field of view. These optimization experiments do not represent a practical final application, only a springboard for potential further study. The author's intention is to indicate that for complex array systems where constraints can be readily identified, such heuristic optimization algorithms may be useful.

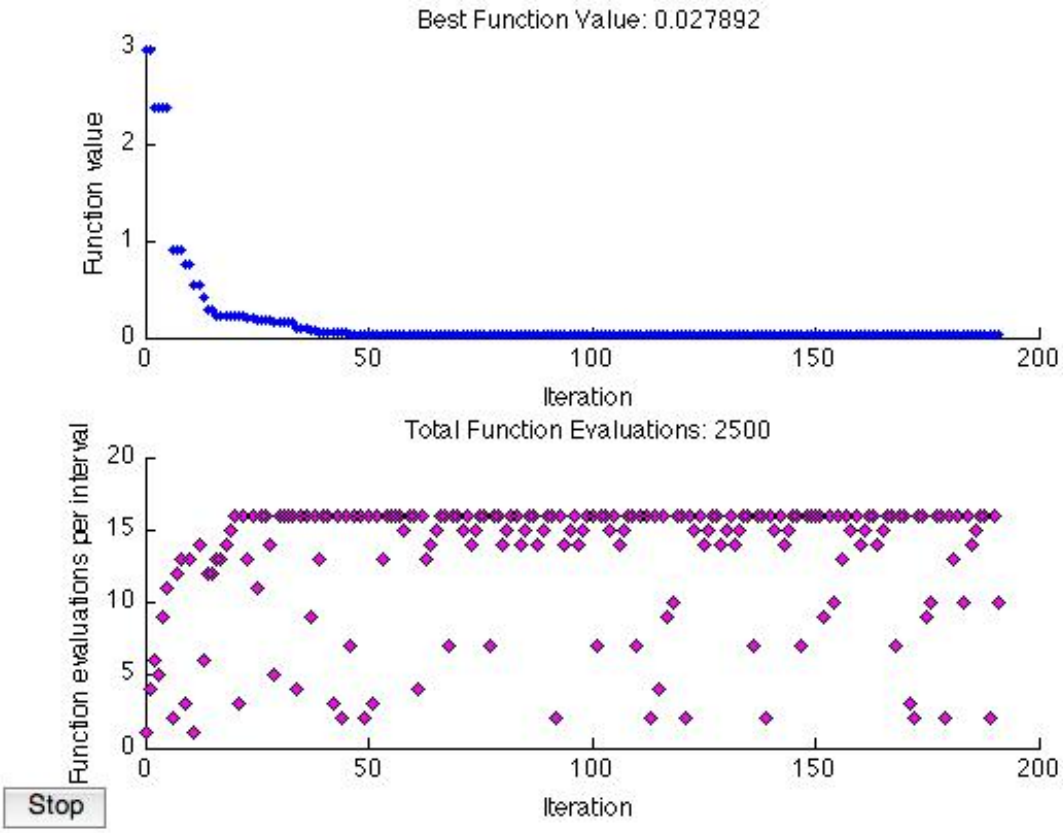

Fig. 78. Optimization results for pattern search.

Next consider an optimization using the simulated annealing process. The state of the simulated annealing optimization at any given point in the process is characterized by the temperature of each variable, in this case each of the eight beamformers in the system. The *optimtool* result for the simulated annealing optimization displays the fitness function value for each iteration along with the final resulting temperature vector and is shown in Fig. 79. Again, the optimization terminated due to the maximum number of fitness evaluations of 2500 being reached with a final fitness function value of $MSE = 0.15^{\circ 2}$ and corresponding beamformer bank steering vector

[50.8° 57.1° 65.2° 72.2° 87.0° 91.1° 107.6° 129.7°].

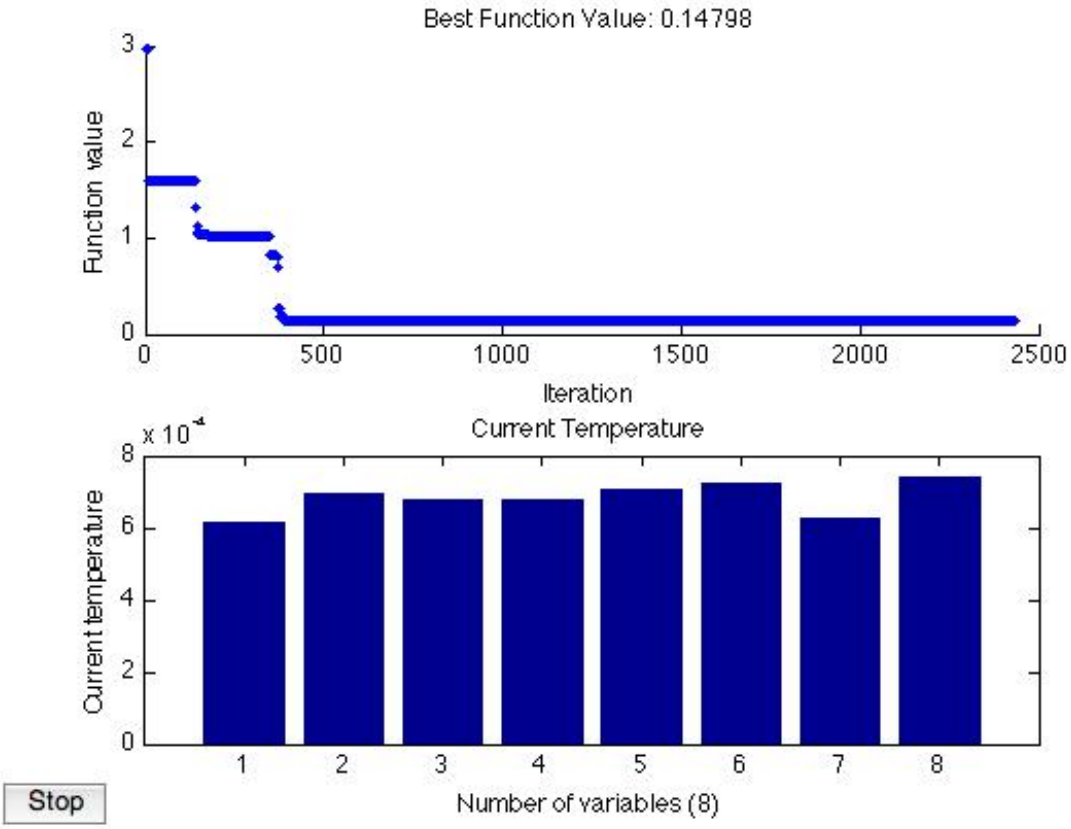

Fig. 79. Optimization results for simulated annealing.

Next consider an optimization by the genetic algorithm process. The *optimtool* result for the genetic algorithm optimization displays the best fitness function value and the mean fitness function value for each generation along with the final resulting best individual beamformer bank vector and is shown in Fig. 80. The genetic algorithm optimization terminated due to a small average change in the fitness function value with

a final fitness function value of $MSE = 0.295^{\circ 2}$ and corresponding beamformer bank vector $[57.5° \ 70.4° \ 76.9° \ 99.9° \ 101.6° \ 111.4° \ 123.5° \ 124.7°]$. It performed 1340 total fitness function evaluations in 67 generations.

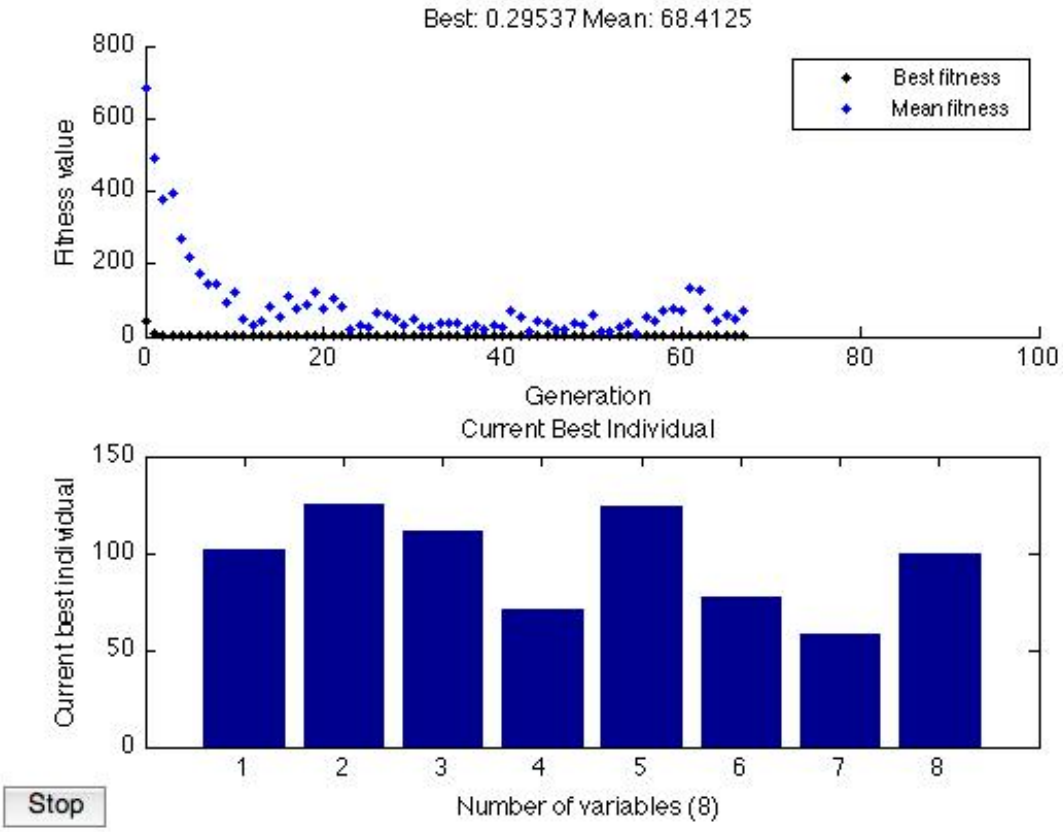

Fig. 80. Optimization results for genetic algorithm.

Table 3 shows the results of all optimization experiments. The genetic algorithm settled into its final state sooner than the other two methods with only 1340 fitness function evaluations as opposed to 2500, but the final performance of its solution was

the worst of the three with a fitness function value of $MSE = 0.295^{\circ 2}$. Pattern search resulted in the best final solution with a fitness function value of $MSE = 0.028^{\circ 2}$, significantly better than the other two, but tied with simulated annealing for the longest process with 2500 total function evaluations.

TABLE 3

FINAL RESULTS FOR ALL OPTIMIZATION EXPERIMENTS

Algorithm	Function Evaluations	Final MSE
Pattern Search	2500	$0.028^{\circ 2}$
Simulated Annealing	2500	$0.15^{\circ 2}$
Genetic Algorithm	1340	$0.295^{\circ 2}$

These optimization results are very limited in scope in order to prove the concept. A similar but much more extensive analysis could be performed for a given system design. The beam space signal subspace processing is amenable to parallel and/or pipelined signal processing hardware configurations that could benefit from optimization of a complex array of multi-processes and data input/output requirements.

7.7 Resolution and Range

The simulation results clearly show resolution performance for TTD beam space methods that is superior to that of the conventional beamformer. In order to quantify the comparison of resolution results consider the airborne ISR application as described in section 1.1. Using the 16-element linear array assume that the element-to-element spacing is set to be $\frac{\lambda}{2}$ for the highest frequency, $f_H = 1.2GHz$, in the desired signal bandwidth of $400MHz$. The aperture size is then

$$D = (M-1)\frac{c}{2f_H} \approx 1.9m \tag{7.1}$$

for speed of light c. This size array is appropriate for the mounting on the fuselage of an ELINT aircraft such as that discussed in Section 5.1. Using two $400MHz$ bandwidth chirp sources and resolution determined by the beam width for the various methods of conventional beamforming on the center sub-band, CSS focused MUSIC and TTD beam space MUSIC, the performance was compared. Fig. 81 shows a plot of the standoff range for which the system is capable versus the source separation. The range to the sources plotted is the maximum at which the given method can resolve the two sources. The plotted range is considered the capable standoff range since the airborne system must be capable of measuring the source locations but be outside of the range of anti-aircraft missiles. If the range is also outside the missile range then it is viable for an operational standoff range.

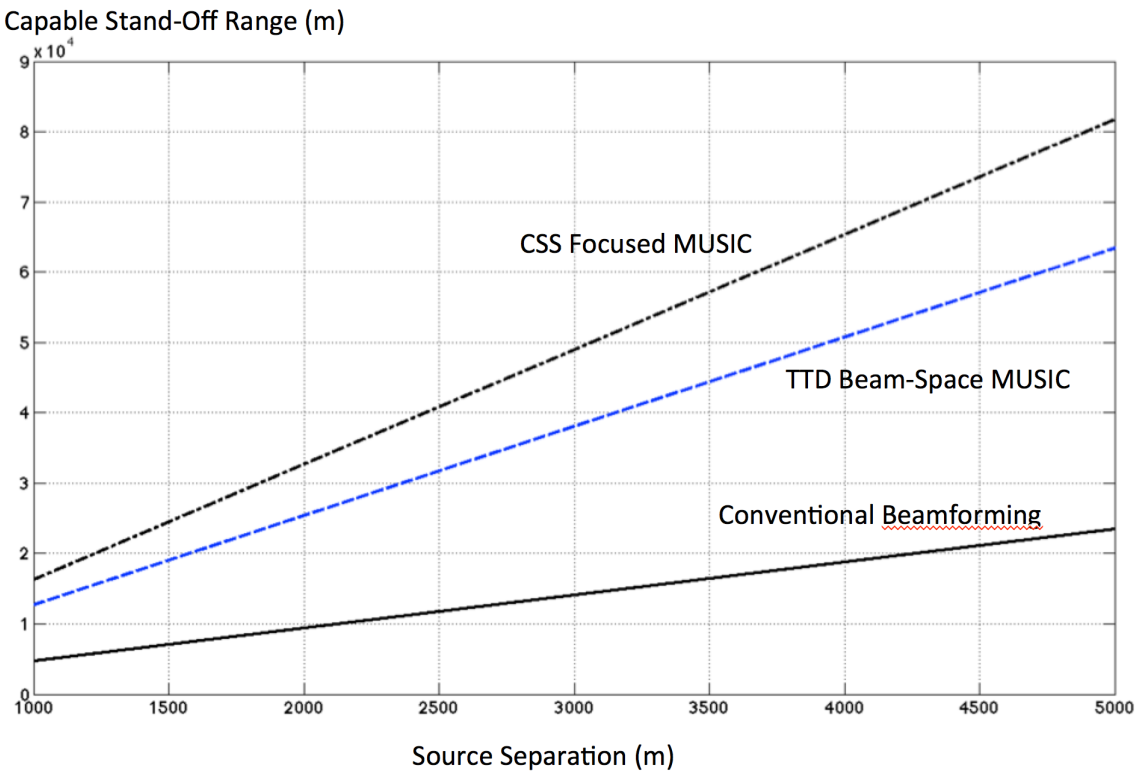

Fig. 81. Comparison of Two Sources Just Resolved Using Various Methods.

The Air Force will execute many future missions of various objectives with Unmanned Aerial Vehicles (UAV's). Fig. 82 shows an image of the US Air Force Predator UAV. The predator UAV and similar vehicles are considerably smaller than a large body manned aircraft. The large body aircraft can typically accommodate a much larger aperture size than a UAV with commensurately higher spatial resolution. As a notional comparison of the resolution performance for different aperture sizes, let us imagine that a large body aircraft can accommodate the $1.9m$ array that we have discussed, but an available UAV could accommodate only a $1m$ length array. Fig. 83 shows the standoff range versus the source separation for TTD beam space MUSIC resolution at these aperture sizes.

The lower resolution for the smaller aperture size for the UAV clearly indicates that the UAV must be closer to the sources to yield comparable performance. However since the UAV is unmanned, a combatant commander may not require strict adherence to the standoff range. Clearly system designers and military users have a number of trade-offs they can make regarding usage of such sensor platforms.

Fig. 82. Predator UAV [image courtesy US Air Force].

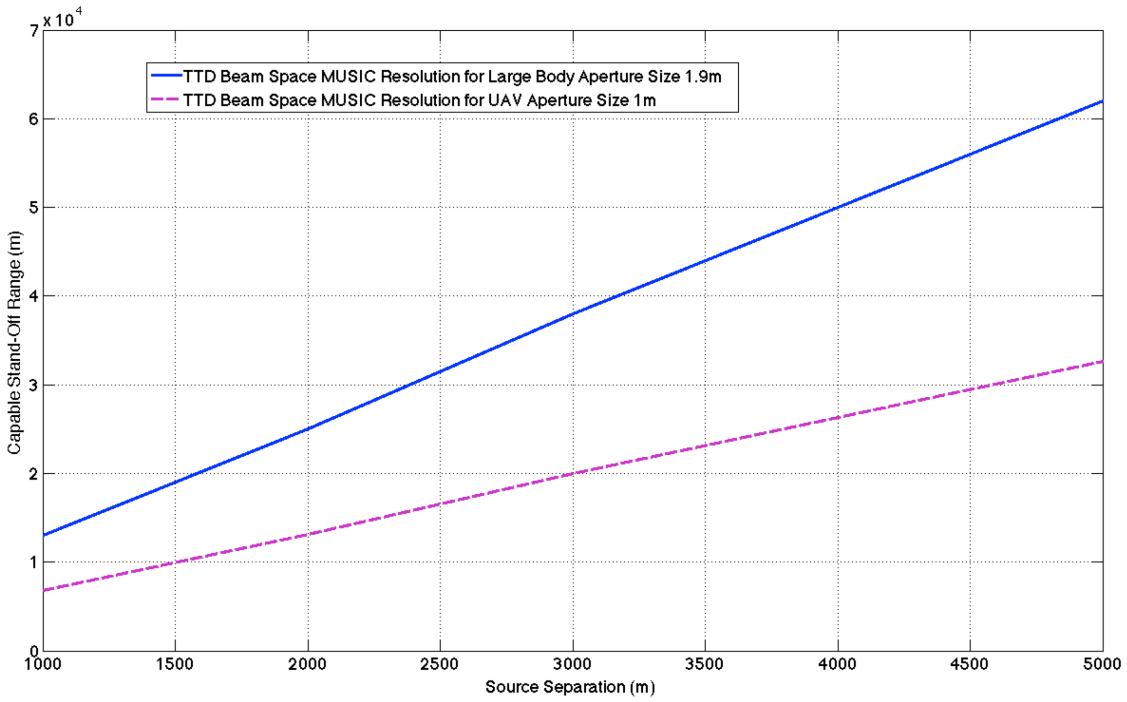

Fig. 83. A large body aircraft may accommodate a larger array than a UAV with commensurately higher resolution, however, the UAV may not require strict adherence to the stand-off range.

Note that these results are for an azimuth estimation system and that the source separation is in the azimuth of the airborne platform. Fig. 84 shows a representation of the azimuthal plane with an example of an apparent azimuthal source separation that is different than the actual source separation. The apparent source separation for an azimuth only system is the measurement between lines of bearing parallel to the platform velocity. If the system calculates geo-location as well as AOA by some means such as integrating over time as the platform moves as discussed in section 5.1 then the actual source separation can be readily found.

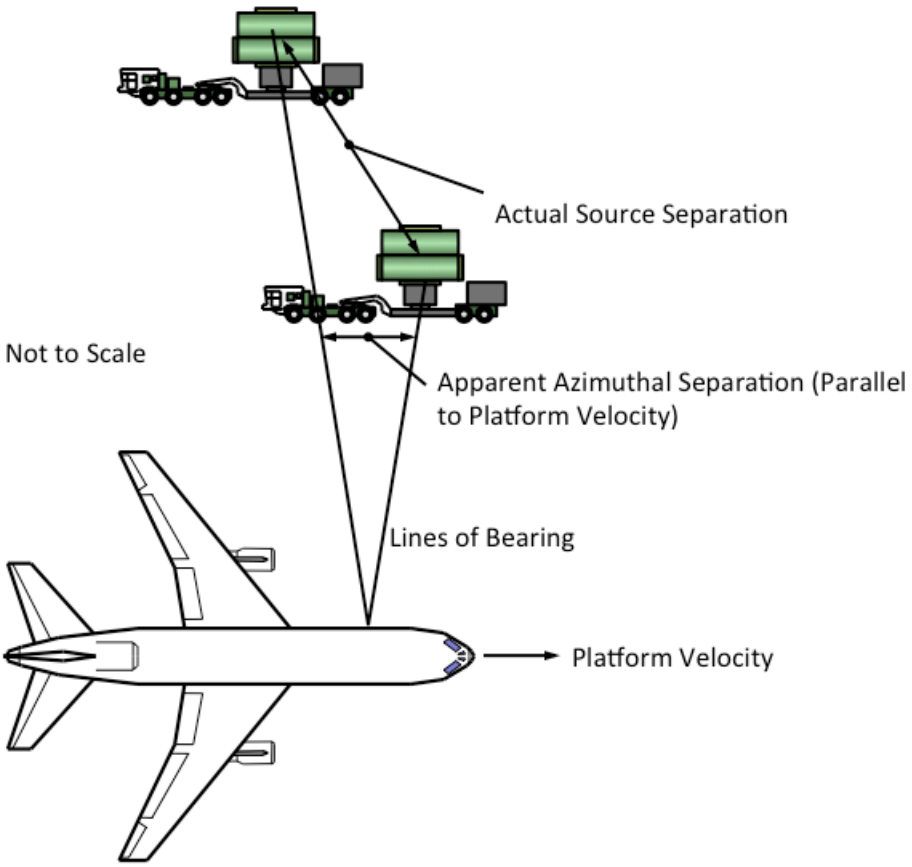

Fig. 84. Apparent Source Separation.

Notice in Fig. 81 that CCS Focused MUSIC has the best performance with the greatest capable stand-off range for all source separations, but recall that it must be focused to the region near the sources of interest and has declining performance in regions spatially separated from the focused region. The TTD beam space method has performance superior to conventional methods, but not as good as the CCS focused method. Recall however that TTD beam space requires no preliminary estimate, has good performance across the field of view, and is computationally low-cost.

8 Summary and Potential Future Research Areas

Wide bandwidth signals are important in many application areas. Communications systems use spread spectrum waveforms to implement multiple user access for limited frequency bands, consumer demand for streaming video and other data intensive uses has fueled an abundance of broadband wireless networks, radar systems incorporate wide bandwidth waveforms to achieve high-resolution, and military systems often spread the bandwidth of signals in order to reduce the probability of the signal being detected. Along with these and other reasons for the proliferation of wide bandwidth signals, the need to perform RF source location for such signals arises as well. Conventional narrow bandwidth methods may fail to perform adequately, particularly for long ranges or high noise levels. The previous wideband methods suffer from various limitations to include the requirement to perform preliminary course AOA estimation, the requirement to perform iteration of the algorithm, various limitations on the type of array or applicable signal type, and general high cost of computation.

This dissertation presented a novel method of signal subspace processing in the beam space of a true time delay beamformer bank. The method performs high-resolution

wide bandwidth RF source location that requires no preliminary estimate, performs the processing in a single pass of the algorithm for the entire field of view, and is capable of achieving significant savings in computational expense as compared to previous methods for cases when the number of beamformers in the true time delay beamformer bank is less than the number of array elements. A potential drawback of the method for certain applications is that the beamformer bank limits the instantaneous field of view. An application that is appropriate for a limited field of view and that needs high-resolution wide bandwidth source location capability is the airborne electronic intelligence application.

This dissertation reviewed previous methods and introduced a number of innovations. It presented the novel method of TTD beam space MUSIC and compared its performance to that of conventional, previous narrow and wide bandwidth methods. It also investigated the theoretical performance limitation for measurement error, discussed optimization of the array and signal processing configuration to maximize performance given certain constraints, and considered various aspects of its practical application.

The root-MUSIC method, originally introduced by Barabell [92], utilizes the roots of the MUSIC spectrum polynomial to estimate source directions and is typically limited to uniform linear arrays. As a logical extension to the root-MUSIC method one could propose a similar polynomial root method using uniformly spaced beams in TTD beam space. This idea was preliminarily explored, but results were not complete in order to

include in the dissertation. A thorough analysis is reserved for future investigation.

One area for future research is an analysis of extension to array configurations other than uniform linear. The equations presented for signal subspace processing in true time delay beam space are suitable for arbitrary array configurations using the construct of the antenna manifold mapped to the beam space manifold, but a thorough analysis of the implications for a 2D or conformal array has not been performed.

Another potential area for future investigation is optimization of array and signal processing configurations. This area was very lightly broached in this investigation and that only to show the potential for utility of the global optimization methods for performance enhancement when complex configurations are difficult to optimize manually. This was essentially an academic exercise used to introduce the topic since we assumed a uniform linear array and the techniques would be much more appropriate for a configuration such as a complex conformal array.

The treatment of polarization and multipath is another area for potential future research. The literature contains extensive treatises on these for the narrow bandwidth case for signal subspace processing. Extension of the narrow bandwidth treatment to the wideband case should be relatively straightforward.

The signal processing of spectrographic data as opposed to simply time-based data using the methods herein presented is a potential topic for future research. Spectrographic data manifests as a 2-Dimensional waveform of signal spectra over time. The simultaneous combination of signal processing for time and frequency domains

corresponds well with the framework of the TTD beam space concepts.

The bias exhibited by the method, for example as shown in Fig. 77, is a topic for additional study. One possible explanation is the non-uniformity of the aggregate beamformer bank response as displayed in Fig. 38. A very straightforward experiment would be to redesign the beamformer bank with optimal uniformity of the aggregate response across the field of view and observe whether the bias of the estimate is affected.

APPENDIX A

ORTHOGONALITY OF THE BEAMFORMER BANK

Some authors have indicated that orthogonality of the beamformer bank should play a role in beam space signal processing. See for example [138] and [139]. As a cursory examination of this assertion in the context of the modeled examples of this dissertation, a nearly orthogonal beamformer bank was generated. The near orthogonality is achieved by adjusting the beam directions so that each beam's first null falls on the location of its nearest neighbor beams' peaks. The beamformer bank generated using this criterion, with all other parameters equivalent to the bank of Fig. 37, is shown in Fig. 85. The beam steering direction vector for this bank is $[39.7° \; 56.4° \; 71° \; 83.5° \; 96.5° \; 109° \; 123.6° \; 140.3°]$. Since the beam width increases away from boresight, the spacing between beam pattern peaks is necessarily non-uniform. A dark green vertical dashed line indicates the peak location of each beam. Compare this to the bank of Fig. 37 that has uniform peak spacing so that the analogy in beam space to the ULA in element space holds.

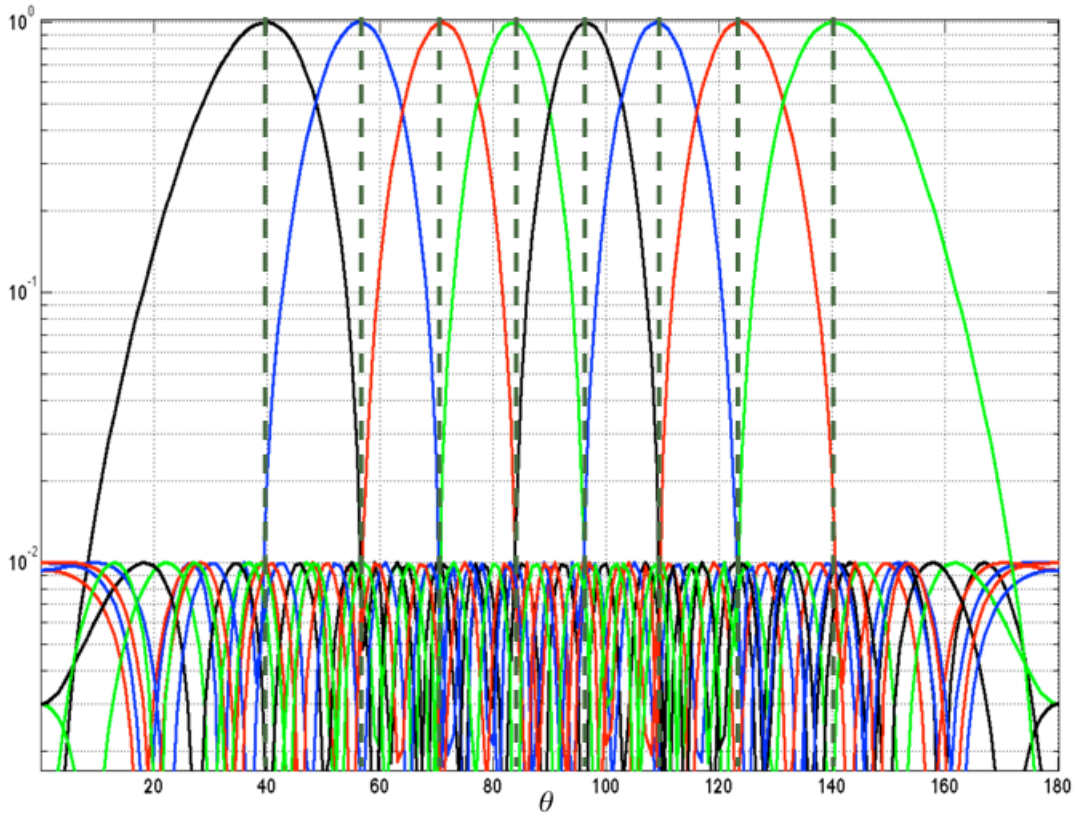

Fig. 85. Nearly Orthogonal Chebyshev TTD Beamformer Bank.

Fig. 86 depicts the aggregate beam pattern for the beamformer bank shown in Fig. 85 in both rectangular coordinates and polar coordinates. Note the severe non-uniformity as compared to the aggregate pattern of Fig. 38. Rather than the orthogonality criterion, the beamformer bank investigated in Chapter 7 used uniformity of the aggregate pattern and uniformity of the peak-to-peak spacing as criteria. Although the orthogonality criterion results in a beamformer bank with a wider field of view, its aggregate beam pattern lacks the uniformity of response across the field of view. Relative advantages and disadvantages of using these alternate criteria, as well as a

thorough analysis of the performance of beam space processing using a nearly orthogonal bank are topics for further study.

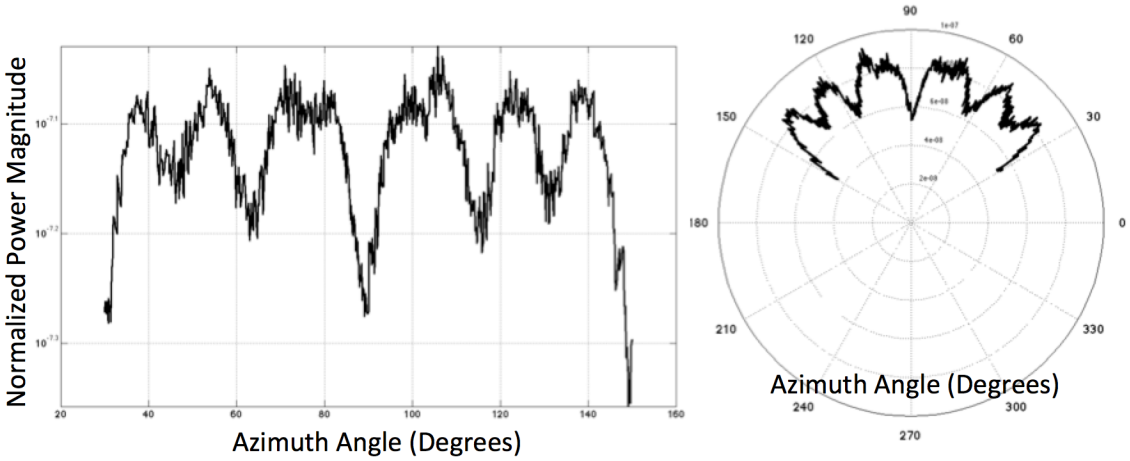

Fig. 86. Aggregate beam pattern for nearly orthogonal Chebyshev TTD beamformer bank.

APPENDIX B

MANIFOLD DERIVATION

The wideband antenna manifold derivation is performed by first considering the linear model as described in equation (3.13). For a single source, $l = L = 1$, the wideband signal model in equation (3.8) can be written as,

$$s_1(t) = \sum_{j=1}^{J} \alpha_{j,1} e^{i2\pi f_j t} \ . \tag{B.1}$$

For simplification of notation, the single wideband signal is modeled as,

$$s(t) = \sum_{j=1}^{J} \beta_j(t) = \sum_{j=1}^{J} \alpha_j e^{i2\pi f_j t} \ . \tag{B.2}$$

where,

$$\beta_j(t) \stackrel{\text{def}}{=} \alpha_j e^{i2\pi f_j t} \ . \tag{B.3}$$

Following from equation (3.13) the jth frequency component of the beam space manifold for *L*=1 is given by,

$$\boldsymbol{\Phi}_{jB}\left(\boldsymbol{W}_{M\times 1}\circ\boldsymbol{\Phi}_{js}\big|_{l=1}\right)=$$

$$\begin{bmatrix}1 & e^{-i2\pi f_j\frac{d}{c}\cos\theta_{B:k=1}} & e^{-i2\pi f_j\frac{d}{c}(2)\cos\theta_{B:k=1}} & \dots & e^{-i2\pi f_j\frac{d}{c}(M-1)\cos\theta_{B:k=1}}\\ \vdots & & \vdots & & \vdots\\ 1 & e^{-i2\pi f_j\frac{d}{c}\cos\theta_{B:K}} & e^{-i2\pi f_j\frac{d}{c}(2)\cos\theta_{B:K}} & \dots & e^{-i2\pi f_j\frac{d}{c}(M-1)\cos\theta_{B:K}}\end{bmatrix}\left(\begin{bmatrix}w_1\\ \vdots\\ w_M\end{bmatrix}\circ\right.$$

$$\left.\begin{bmatrix}1\\ e^{-i2\pi f_j\frac{d}{c}\cos\theta_{s:l=1}}\\ \vdots\\ e^{-i2\pi f_j\frac{d}{c}(M-1)\cos\theta_{s:l=1}}\end{bmatrix}\right)\in\mathbb{C}^{K\times 1}\,. \tag{B.4}$$

Define, $\boldsymbol{\phi}_{js}\overset{\text{def}}{=}\boldsymbol{\Phi}_{js}\big|_{l=1}=\begin{bmatrix}1\\ e^{-i2\pi f_j\frac{d}{c}\cos\theta_{s:l=1}}\\ \vdots\\ e^{-i2\pi f_j\frac{d}{c}(M-1)\cos\theta_{s:l=1}}\end{bmatrix}$. After applying the Hadamard product,

and using $\theta_s\overset{\text{def}}{=}\theta_{s:l=1}$ for a single source,

$$\boldsymbol{\Phi}_{jB}\left(\boldsymbol{W}_{M\times 1}\circ\boldsymbol{\phi}_{js}\right)=$$

$$\begin{bmatrix}1 & e^{-i2\pi f_j\frac{d}{c}\cos\theta_{B:1}} & e^{-i2\pi f_j\frac{d}{c}(2)\cos\theta_{B:1}} & \dots & e^{-i2\pi f_j\frac{d}{c}(M-1)\cos\theta_{B:1}}\\ \vdots & & \vdots & & \vdots\\ 1 & e^{-i2\pi f_j\frac{d}{c}\cos\theta_{B:K}} & e^{-i2\pi f_j\frac{d}{c}(2)\cos\theta_{B:K}} & \dots & e^{-i2\pi f_j\frac{d}{c}(M-1)\cos\theta_{B:K}}\end{bmatrix}\begin{bmatrix}w_1\\ w_2e^{-i2\pi f_j\frac{d}{c}\cos\theta_s}\\ \vdots\\ w_Me^{-i2\pi f_j\frac{d}{c}(M-1)\cos\theta_s}\end{bmatrix}\in$$

$\mathbb{C}^{K\times 1}$,

$$\boldsymbol{\Phi}_{jB}\left(\boldsymbol{W}_{M\times 1}\circ\boldsymbol{\phi}_{js}\right)=\begin{bmatrix}\sum_{m=1}^{M}w_me^{-i2\pi f_j\frac{d}{c}(m-1)\cos\theta_{B:1}}e^{-i2\pi f_j\frac{d}{c}(m-1)\cos\theta_s}\\ \vdots\\ \sum_{m=1}^{M}w_me^{-i2\pi f_j\frac{d}{c}(m-1)\cos\theta_{B:K}}e^{-i2\pi f_j\frac{d}{c}(m-1)\cos\theta_s}\end{bmatrix}\in\mathbb{C}^{K\times 1}. \tag{B.5}$$

The vector $\boldsymbol{\beta}_j(t)$ in (3.14) becomes a scalar for L=1, given by $\beta_j(t)$ as defined in (B.3). Now multiplying the expression in (B.5) by $\beta_j(t)$,

$$\boldsymbol{\Phi}_{jB}\left(\boldsymbol{W}_{M\times 1}\circ\boldsymbol{\phi}_{js}\right)\beta_j(t)=\begin{bmatrix}\sum_{m=1}^{M} w_m e^{-i2\pi f_j\frac{d}{c}(m-1)\cos\theta_{B:1}} e^{-i2\pi f_j\frac{d}{c}(m-1)\cos\theta_s}\\ \vdots \\ \sum_{m=1}^{M} w_m e^{-i2\pi f_j\frac{d}{c}(m-1)\cos\theta_{B:K}} e^{-i2\pi f_j\frac{d}{c}(m-1)\cos\theta_s}\end{bmatrix}\beta_j(t)=$$

$$\begin{bmatrix}\beta_j(t)\sum_{m=1}^{M} w_m e^{-i2\pi f_j\frac{d}{c}(m-1)\cos\theta_{B:1}} e^{-i2\pi f_j\frac{d}{c}(m-1)\cos\theta_s}\\ \vdots \\ \beta_j(t)\sum_{m=1}^{M} w_m e^{-i2\pi f_j\frac{d}{c}(m-1)\cos\theta_{B:K}} e^{-i2\pi f_j\frac{d}{c}(m-1)\cos\theta_s}\end{bmatrix}. \tag{B.6}$$

Summing over all frequencies as in equation (3.13) we obtain the equivalent form for *L*=1 case of equation (3.13),

$$\begin{bmatrix}y_1(t)\\ y_2(t)\\ \vdots \\ y_K(t)\end{bmatrix}=\begin{bmatrix}\sum_{j=1}^{J}\beta_j(t)\sum_{m=1}^{M} w_m e^{-i2\pi f_j\frac{d}{c}(m-1)\cos\theta_{B:1}} e^{-i2\pi f_j\frac{d}{c}(m-1)\cos\theta_s}\\ \sum_{j=1}^{J}\beta_j(t)\sum_{m=1}^{M} w_m e^{-i2\pi f_j\frac{d}{c}(m-1)\cos\theta_{B:2}} e^{-i2\pi f_j\frac{d}{c}(m-1)\cos\theta_s}\\ \vdots \\ \sum_{j=1}^{J}\beta_j(t)\sum_{m=1}^{M} w_m e^{-i2\pi f_j\frac{d}{c}(m-1)\cos\theta_{B:K}} e^{-i2\pi f_j\frac{d}{c}(m-1)\cos\theta_s}\end{bmatrix}, \tag{B.7}$$

which can be further written using (B.3) as,

$$\begin{bmatrix}y_1(t)\\ y_2(t)\\ \vdots \\ y_K(t)\end{bmatrix}\stackrel{\text{def}}{=}\begin{bmatrix}\sum_{j=1}^{J}\alpha_j e^{i2\pi f_j t}\sum_{m=1}^{M} w_m e^{-i2\pi f_j\frac{d}{c}(m-1)\cos\theta_{B:1}} e^{-i2\pi f_j\frac{d}{c}(m-1)\cos\theta_s}\\ \sum_{j=1}^{J}\alpha_j e^{i2\pi f_j t}\sum_{m=1}^{M} w_m e^{-i2\pi f_j\frac{d}{c}(m-1)\cos\theta_{B:2}} e^{-i2\pi f_j\frac{d}{c}(m-1)\cos\theta_s}\\ \vdots \\ \sum_{j=1}^{J}\alpha_j e^{i2\pi f_j t}\sum_{m=1}^{M} w_m e^{-i2\pi f_j\frac{d}{c}(m-1)\cos\theta_{B:K}} e^{-i2\pi f_j\frac{d}{c}(m-1)\cos\theta_s}\end{bmatrix}. \tag{B.8}$$

Now re-write the linear equation of (B.7) in matrix-vector form as,

$$\begin{bmatrix} y_1(t) \\ y_2(t) \\ \vdots \\ y_K(t) \end{bmatrix} =$$

$$\begin{bmatrix} \sum_{m=1}^{M} w_m e^{-i2\pi f_1 \frac{d}{c}(m-1)\,(\cos\theta_{B:1}+\cos\theta_s)} & \sum_{m=1}^{M} w_m e^{-i2\pi f_2 \frac{d}{c}(m-1)\,(\cos\theta_{B:1}+\cos\theta_s)} & \dots \\ \vdots & \vdots & \dots \\ \sum_{m=1}^{M} w_m e^{-i2\pi f_1 \frac{d}{c}(m-1)\,(\cos\theta_{B:K}+\cos\theta_s)} & \sum_{m=1}^{M} w_m e^{-i2\pi f_2 \frac{d}{c}(m-1)\,(\cos\theta_{B:K}+\cos\theta_s)} & \dots \end{bmatrix}$$

$$\begin{bmatrix} \sum_{m=1}^{M} w_m e^{-i2\pi f_J \frac{d}{c}(m-1)\,(\cos\theta_{B:1}+\cos\theta_s)} \\ \vdots \\ \sum_{m=1}^{M} w_m e^{-i2\pi f_J \frac{d}{c}(m-1)\,(\cos\theta_{B:K}+\cos\theta_s)} \end{bmatrix} \begin{bmatrix} \alpha_1 e^{i2\pi f_1 t} \\ \alpha_2 e^{i2\pi f_2 t} \\ \vdots \\ \alpha_J e^{i2\pi f_J t} \end{bmatrix}, \tag{B.9}$$

which we now re-write as,

$$\begin{bmatrix} y_1(t) \\ y_2(t) \\ \vdots \\ y_K(t) \end{bmatrix} \stackrel{\text{def}}{=}$$

$$\begin{bmatrix} e^{i2\pi f_1 t} \sum_{m=1}^{M} w_m e^{-i2\pi f_1 \frac{d}{c}(m-1)\,(\cos\theta_{B:1}+\cos\theta_s)} & \dots \\ \vdots & \dots \\ e^{i2\pi f_1 t} \sum_{m=1}^{M} w_m e^{-i2\pi f_1 \frac{d}{c}(m-1)\,(\cos\theta_{B:K}+\cos\theta_s)} & \dots \end{bmatrix}$$

$$\begin{bmatrix} e^{i2\pi f_J t} \sum_{m=1}^{M} w_m e^{-i2\pi f_J \frac{d}{c}(m-1)\,(\cos\theta_{B:1}+\cos\theta_s)} \\ \vdots \\ e^{i2\pi f_J t} \sum_{m=1}^{M} w_m e^{-i2\pi f_J \frac{d}{c}(m-1)\,(\cos\theta_{B:K}+\cos\theta_s)} \end{bmatrix} \begin{bmatrix} \alpha_1 \\ \alpha_2 \\ \vdots \\ \alpha_J \end{bmatrix}. \tag{B.10}$$

The columns of the above matrix represents the array manifold vector at each frequency, f_j, at search angle θ_s over the entire *K* beam space angles $\theta_{B:1}$ … $\theta_{B:K}$, given by,

$$\boldsymbol{a}_B\left(\theta_s, t, f_j\right) \stackrel{\text{def}}{=} \begin{bmatrix} e^{i2\pi f_j t} \sum_{m=1}^{M} w_m e^{-i2\pi f_j \frac{d}{c}(m-1)\,(\cos\theta_{B:1}+\cos\theta_s)} \\ e^{i2\pi f_j t} \sum_{m=1}^{M} w_m e^{-i2\pi f_j \frac{d}{c}(m-1)\,(\cos\theta_{B:2}+\cos\theta_s)} \\ \vdots \\ e^{i2\pi f_j t} \sum_{m=1}^{M} w_m e^{-i2\pi f_j \frac{d}{c}(m-1)\,(\cos\theta_{B:K}+\cos\theta_s)} \end{bmatrix}. \tag{B.11}$$

Typically a search for unknown source angle, θ_s, is performed at each frequency, f_j, using this $\boldsymbol{a}_B(\theta_s, t, f_j)$ and then summing or averaging the results at each frequency. This is equivalent to using equation (B.10) and setting all $\alpha_j = 1, j = 1,2,\ldots,J$. Thus the wideband beam space manifold vector is given by summing over all *j*'s of the vector (B.11) as in,

$$\boldsymbol{a}_B(\theta_s, t) \stackrel{\text{def}}{=} \begin{bmatrix} \sum_{j=1}^{J} e^{i2\pi f_j t} \sum_{m=1}^{M} w_m e^{-i2\pi f_j \frac{d}{c}(m-1)\,(\cos\theta_{B:1}+\cos\theta_s)} \\ \sum_{j=1}^{J} e^{i2\pi f_j t} \sum_{m=1}^{M} w_m e^{-i2\pi f_j \frac{d}{c}(m-1)\,(\cos\theta_{B:2}+\cos\theta_s)} \\ \vdots \\ \sum_{j=1}^{J} e^{i2\pi f_j t} \sum_{m=1}^{M} w_m e^{-i2\pi f_j \frac{d}{c}(m-1)\,(\cos\theta_{B:K}+\cos\theta_s)} \end{bmatrix}. \tag{B.12}$$

To preserve causality, let $t = t_{max}$, the most recent measurement time to obtain the final manifold vector,

$$\boldsymbol{a}_B(\theta_s, t = t_{max}) \stackrel{\text{def}}{=} \begin{bmatrix} \sum_{j=1}^{J} e^{i2\pi f_j t_{max}} \sum_{m=1}^{M} w_m e^{-i2\pi f_j \frac{d}{c}(m-1)\,(\cos\theta_{B:1}+\cos\theta_s)} \\ \sum_{j=1}^{J} e^{i2\pi f_j t_{max}} \sum_{m=1}^{M} w_m e^{-i2\pi f_j \frac{d}{c}(m-1)\,(\cos\theta_{B:2}+\cos\theta_s)} \\ \vdots \\ \sum_{j=1}^{J} e^{i2\pi f_j t_{max}} \sum_{m=1}^{M} w_m e^{-i2\pi f_j \frac{d}{c}(m-1)\,(\cos\theta_{B:K}+\cos\theta_s)} \end{bmatrix}. \tag{B.13}$$

APPENDIX C

TREATMENT OF NOISE COLORATION THROUGH THE BEAMFORMER BANK

The assumption that the noise is white as measured at the antennas does not generally hold as the signals pass through the individual beamformers. Here we demonstrate that the noise samples at the output of each individual beamformer are non-white Gaussian processes. However, the colored noise processes at different beamformer outputs are uncorrelated. From equation (3.10),

$$y_k(t) = \sum_{m=1}^{M} w_m x_m(t - \tau_{B:m,k}(\theta_{B:k}))$$
$$= \sum_{m=1}^{M} w_m \sum_{l=1}^{L} \sum_{j=1}^{J} \alpha_{j,l} e^{i2\pi f_j (t - \tau_{s:l,m}(\theta_{s:l}) - \tau_{B:m,k}(\theta_{B:k}))} + n_k(t), k = 1, \dots, K , \qquad \text{(C.1)}$$

where,

$$n_k(t) = \sum_{m=1}^{M} w_m n_{mk}(t) = \sum_{m=1}^{M} w_m n_{mk}(t) , \qquad \text{(C.2)}$$

is the output of an FIR filter with weights, $w_1, w_2, \dots, w_M$. Since the observation noise, $n_m(t)$, is assumed to be white Gaussian, $n_m(t) \sim N(0, \sigma_B^2)$, for all m, $n_k(t)$ is colored Gaussian, $n_k(t) \sim N(0, \sigma_B^2 \sum_{m=1}^{M} w_m^2)$. It is easy to show that $n_k(t)$ is an Mth order Moving Average (MA) process with finite length autocorrelation function given by ,

$$r_{n_k}(l) = \sigma_B^2 \sum_{m=l+1}^{M} w_m w_{m-l} \; for \; 0 \le l < M-1$$

$$= \sigma_B^2 w_M w_1 \; for \; l = M-1, and$$

$$= 0 \; for \; l \ge M. \qquad \text{(C.3)}$$

However, the noise processes at the output of K individual beamformers, $n_1(t), n_2(t), \ldots, n_K(t)$ are uncorrelated because the zero-mean processes $n_{mk}(t)$'s in equation (C.2) are uncorrelated for different k values, i.e., expected values of all the cross terms are zeros,

$$E[n_{mk} n_{ml}] = E\left[n_m\left(t - \tau_{B:m,k}(\theta_{B:k})\right) n_m\left(t - \tau_{B:m,l}(\theta_{B:l})\right)\right] = 0, for \; k \ne l \; . \qquad \text{(C.4)}$$

Therefore,

$$E[n_k(t) n_l(t)] = (\sigma_B^2 \textstyle\sum_{m=1}^{M} w_m^2) \; \delta_{kl} \; . \qquad \text{(C.5)}$$

REFERENCES

[1] P. Pace, *Detecting and Classifying Low Probability of Intercept Radar*, 2nd Edition, Artech House, 2009.

[2] A. Viterbi, *CDMA: Principles of Spread Spectrum Communication*, Addison-Wesley, 1995.

[3] J. I. Agbinya, Ed., *Planning and Optimisation of 3G and 4G Wireless Networks*, River Publishers, 2009.

[4] P. Tait, Ed., *Introduction to Radar Target Recognition*, No. 18 in Radar, Sonar and Navigation Series, Institute of Engineering and Technology, London, 2005.

[5] D. Adamy, *EW101: A First Course in Electronic Warfare*, Artech House, 2001.

[6] R. Poisel, *Modern Communications Jamming, Principles and Techniques*, 2nd Edition, Artech House, 2011.

[7] R. Purdy, P Blankenship, C. Muehe, C. Rader, E. Stern and R. Williamson, "Radar Signal Processing," *Lincoln Laboratory Journal*, Vol. 12, No. 2, 2000, p. 316.

[8] *Ibid*., p. 299.

[9] *Ibid*., p. 309.

[10] R. Higgins, *Digital Signal Processing in VLSI*, Prentice Hall, New York, 1990.

[11] Xilinx Corporation, Virtex-6 Family Overview, Product Specification DS150 (v2.4) available online at http://www.Xilinx.com, January 2012.

[12] H. Warston and H. Persson, "Ground Surveillance and Fusion of Ground Target Sensor Data in a Network Based Defense," *Proceedings of the 7th International Conference on Information Fusion*, 2004.

[13] OSD/DARPA, Ultra-Wideband Radar Review Panel, *Assessment of Ultra-Wideband (UWB) Technology*, DARPA, Arlington, VA, 1990.

[14] Time Domain Corporation, *Time Domain's Ultra Wideband (UWB): Definition and Advantages*, White Paper available at http://www.timedomain.com/white-papers, March 2011.

[15] R. Fontana, "Recent System Applications of Short-Pulse Ultra-Wideband (UWB) Technology," *IEEE Transactions on Microwave Theory and Techniques*, Vol. 52, No. 9, pp. 2087-2104, 2004.

[16] S. Azevedo and T. McEwan, "Microwave Impulse Radar," *Science and Technology Review*, January 1996.

[17] J. Proakis, "Spread Spectrum Signals for Digital Communications," in *Encyclopedia of Telecommunications*, Wiley, 2003.

[18] M. Stieber, "Radio Direction Finding Network Receiver Design for Low-Cost Public Service Applications," M.S. thesis, Department of Electrical Engineering, California Polytechnic, 2012.

[19] Z. Shi, Y. Li and W. Yuan, "Modeling of Guidance Signal of Anti-Radiation Missile in the Case of Multiple Sources," *Proceedings of the 2006 IEEE International Conference on Mechatronics and Automation*, pp. 2264-2268, 2006.

[20] R. C. de Lamare and R. Sampaio-Neto, “Reduced-Rank Space-Time Adaptive Interference Suppression with Joint Iterative Least Squares Algorithms for Spread-Spectrum Systems,” *IEEE Transactions on Vehicle Technology*, Vol. 59, No. 3, pp. 1217-1228, March 2010.

[21] M. Porretta, P. Nepa, G. Manara, F. Giannetti, “Location, Location, Location,” *IEEE Vehicular Technology Magazine*, Vol. 3, Issue 2, pp. 20-29, June 2008.

[22] N. Friedman, *The Naval Institute Guide to World Naval Weapon Systems*, 5th Edition, Naval Institute Press, 2006.

[23] A. Denk, “Detection and Jamming Low Probability of Intercept Radars,” M.S. thesis, Naval Postgraduate School, 2006.

[24] E. Tuncer and B. Friedlander, *Classical and Modern Direction-of-Arrival Estimation*, Academic Press, Elsevier, 2009.

[25] P. Matthews, “Photonics for Phased Array Systems,” *Proceedings of IEEE Conference on Phased Array Systems and Technology*, pp. 349-352, 2000

[26] W. Ng, “Advances in Wideband Array Signal Processing Using Numerical Bayesian Methods,” Ph.D. dissertation, Department of Electrical and Computer Engineering, McMaster University, Hamilton, Ontario, Canada, 2003.

[27] B. Jung, D. Kim, I. Jeon, S. Shin and H. Kim, “Optical True Time-Delay Beamformer Based on Microwave Photonics for Phased Array Radar,” *Proceedings of IEEE International Conference on Synthetic Aperture Radar*, September 2011.

[28] W. F. Gabriel, “Spectral Analysis and Adaptive Array Superresolution Techniques,” *Proceedings of the IEEE*, Vol. 68, No. 6, pp. 654-666, June 1980.

[29] W. F. Gabriel, “Using Spectral Estimation Techniques in Adaptive Processing Antenna Systems,” *IEEE Transactions on Antennas and Propagation*, Vol. AP-34, pp. 291-300, March 1986.

[30] W. F. Gabriel, “Large-Aperture Sparse Array Antenna Systems of Moderate Bandwidth for Multiple Emitter Location,” Antennas and Propagation Society International Symposium, pp. 238-241, June 1988.

[31] W. F. Gabriel, “Large-Aperture Sparse Array Antenna Systems of Moderate Bandwidth for Multiple Emitter Location,” *IEEE Transactions on Antennas and Propagation*, Vol. 37, No. 1, pp. 16-29, January 1989.

[32] L. H. Gesell, R. E. Feinleib and T. M. Turpin, “An Acousto-Optic Processor to Generate Laser Radar Range-Doppler Images,” SPIE Vol. 1296, pp. 189-200, 1990.

[33] L. H. Gesell and R. E. Feinleib, *True Time Delay Beamforming*, Rome Laboratory Technical Report RL-TR-94-104, August 1994.

[34] L. H. Gesell, T. M. Turpin and M. W. Rubin, “True Time Delay Beamforming Using Fiber Optic Cavities,” SPIE Vol. 2560, pp. 130-139, 1995.

[35] M. Longbrake, J. Buck, P. Buxa, T. Dalrymple, J. McCann, R. Neidhard, P. Watson, K. Zeller, B. Garber and D. Kuhl, “TELA Testbed Time Delay Beam Steering Demonstration,” *Proceedings of the Antenna Measurement Techniques Association*, 2009.

[36] B. Thompson, “True Time Delay Module Finds Needle in a Haystack Frequencies,” Wright-Patterson Air Force Base online press release, Available at http://www.wpafb.af.mil/news , Wright-Patterson Air Force Base, 2011.

[37] T. Dalrymple, AFRL Sensors Directorate, Wright-Patterson Air Force Base, Private communication, 11 June 2013.

[38] J. Chen, K. Yao and R. Hudson, “Source Localization and Beamforming,” *IEEE Signal Processing Magazine*, Vol. 19, Issue 2, pp. 30-39, March 2002.

[39] K. Wagner, S. Kraut, L. Griffiths, S. Weaver, R. Weverda, and A. Sarto, “Efficient True-Time-Delay Adaptive Array Processing,” Proceedings of SPIE, Vol. 2845, August 1996.

[40] M. Hussain, “Principles of Space-Time Array Processing for Ultrawide-Band Impulse Radar and Radio Communications,” *IEEE Transactions on Vehicular Technology*, Vol. 51, No. 3, pp. 393-403, May 2002.

[41] Tuan Do-Hong and Peter Russer, “Beam space Processing with Spatially Interpolated Wideband Beamformers for Wideband Direction-of-Arrival Estimation,” European Conference on Wireless Technology, Amsterdam, pp. 241-244, 2004.

[42] J. Burg, “Maximum Entropy Spectral Analysis,” Ph.D. dissertation, Geophysics Department, Stanford University, Palo Alto, CA, 1975.

[43] R. O. Schmidt, “Multiple Emitter Location and Signal Parameter Estimation,” *IEEE Transactions on Antennas and Propagation*, Vol. 34, No. 3, March 1986.

[44] H. Wang and M. Kaveh, “Coherent Signal-Subspace Processing for the Detection and Estimation of Angles of Arrival of Multiple Wide-Band Sources,” *IEEE Transactions on Acoustics, Speech and Signal Processing*,” Vol. ASSP-33, No. 4, pp. 823-831, August 1985.

[45] H. Jenkins, *Small Aperture Radio Direction Finding*, Artech House, 1991.

[46] S. Lipsky, *Microwave Passive Direction Finding*, SciTech Publishing, 2004.

[47] P. Gething, *Radio Direction Finding and Superresolution*, Peter Peregrinum Ltd., London, 2nd Edition, 1991.

[48] M. Wax, “Detection and Estimation of Superimposed Signals,” Ph.D. dissertation, Stanford University, Palo Alto, CA, 1985.

[49] M. Wax and T. Kailath, “Detection of Signals by Information Theoretic Criteria,” *IEEE Transactions on Acoustics, Speech and Signal Processing*, Vol. ASSP-33, No. 2, April 1985.

[50] R. Kumaresan, L. Scharf and A. Shaw, “An Algorithm for Pole-Zero Modeling and Spectral Analysis,” *IEEE Transacitons on Acoustics, Speech and Signal Processing*, Vol. ASSP-34, No. 3, pp. 637-640, June 1986.

[51] Y. Bresler and A. Macovski, “Exact Maximum Likelihood Parameter Estimation of Superimposed Exponential Signals in Noise,” *IEEE Transactions on Acoustics, Speech and Signal Processing*, Vol. 34, No. 5, pp. 1081-1089, October 1986.

[52] J. Capon, “High resolution frequency-wavenumber spectrum analysis,” *Proceedings IEEE*, Vol. 57, No. 8, pp. 1408-1418, August 1969.

[53] V. F. Pisarenko, "The retrieval of harmonics from a covariance function," *Geophysics Journal of the Royal Astronomical Society*, No. 33, pp. 366-374, 1973.

[54] S. Reddi, "Multiple Source Location: A Digital Approach," *IEEE Transactions on Aerospace and Electronic Systems*, Vol. AES-15, No. 1, pp. 95-105, January 1979.

[55] R. Kumaresan and D. Tufts, "Estimating the Angles of Arrival of Multiple Plane Waves," *IEEE Transactions on Aerospace and Electronic Systems*, Vol. AES-19, No. 1, pp. 134-139, January 1983.

[56] S. M. Kay, *Modern Spectral Estimation Theory and Application*, Prentice-Hall, Englewood Cliffs, NJ, 1988.

[57] A. Paulraj, R. Roy and T. Kailath, "Estimation of Signal Parameters via Rotational Invariance Techniques – ESPRIT," *Proceedings of the 19th Asilomar Conference on Circuits, Systems and Computers*, November 1985.

[58] B. Rao and K. Hari, "Performance Analysis of Root-MUSIC," *IEEE Transactions on Acoustics, Speech and Signal Processing*, Vol. 37, No. 12, pp. 1939-1949, December 1989.

[59] C. Therrien, *Discrete Random Signals and Statistical Signal Processing*, Prentice-Hall, 1992.

[60] P. Stoica and A. Nehorai, "Comparative performance study of element-space and beam-space MUSIC estimators," *Circuits, Systems, and Signal Processing*, Vol. 10, No. 3, 1991.

[61] W. Tidd, Y. Zhao and Y. Huang, "Sequential Beamspace DOA Estimation," *Proceedings of 2011 IEEE International Symposium on Antennas and Propagation*, July 2011.

[62] H. Wang and M. Kaveh, "On the Performance of Signal-Subspace Processing – Part II: Coherent Wide-Band Systems," *IEEE Transactions on Acoustics, Speech and Signal Processing*, Vol. ASSP-35, No. 11, pp. 1583-1591, November 1987.

[63] H. Hung and M. Kaveh, "Focusing Matrices for Coherent Signal-Subspace Processing," *IEEE Transactions on Acoustics, Speech and Signal Processing*, Vol. 36, pp. 1272-1281, August 1988.

[64] A. Shaw and R. Kumaresan, "Estimation of Angles of Arrival of Broadband Sources," *Proceedings of the IEEE International Conference On Acoustics, Speech and Signal Processing*, pp. 2296-2299, April 1987.

[65] T. L. Henderson, "Rank Reduction for Broadband Waves Incident on a Linear Receiving Aperture," *Proceedings of the 19th Asilomar Conference on Circuits, Systems and Computers*, November 1985.

[66] J. Krolik and D. Swingler, "Multiple Broad-Band Source Location Using Steered Covariance Matrices," *IEEE Transactions on Acoustics, Speech and Signal Processing*, Vol. 37, No. 10, pp. 1481-1494, October 1989.

[67] J. Krolik and D. Swingler, "The Detection Performance of Coherent Wideband Focusing for a Spatially Resampled Array," *Proceedings of the IEEE International*

Conference on Acoustics, Speech and Signal Processing, ICASSP 90, pp. 2827-2830, April 1990.

[68] T. Lee, "Efficient Wideband Source Localization Using Beamforming Invariance Technique," *IEEE Transactions on Signal Processing*," Vol. 42, No. 6, pp. 1376-1387, June 1994.

[69] D. B. Ward, Z. Ding and R. A. Kennedy, "Broadband DOA Estimation Using Frequency Invariant Beamforming," *IEEE Transactions on Signal Processing*, Vol. 46, No. 5, pp. 1463-1469, May 1998.

[70] Darren B. Ward, Rodney A. Kennedy and Robert C. Williamson, "FIR Filter Design for Frequency Invariant Beamformers," *IEEE Signal Processing Letters*, Vol. 3, No. 3, pp. 69-71, March 1996.

[71] Tuan Do-Hong, Franz Demmel and Peter Russer, "A Method for Wideband Direction-of-Arrival Estimation Using Frequency-Domain Frequency-Invariant Beamformers," *IEEE International Symposium on Antennas and Propagation*, Vol. 3, pp. 244-247, June 2003.

[72] Darren Ward and Thushara Abhayapala, "Range and Bearing Estimation of Wideband Sources Using and Orthogonal Beamspace Processing Structure," *Proceedings of the IEEE International Conference on Acoustics, Speech and Signal Processing*, May 2004.

[73] Shahrokh Valaee and Peter Kabal, “Wideband Array Processing Using a Two-Sided Correlation Transformation,” *IEEE Transactions on Signal Processing*, Vol. 43, No. 1, pp. 160-172, January 1995.

[74] Shahrokh Valaee, Benoit Champagne and Peter Kabal, “Localization of Wideband Signals Using Least-Squares and Total Least-Squares Approaches,” *IEEE Transactions on Signal Processing*, Vol. 47, No. 5, pp. 1213-1222, May 1999.

[75] Monika Agrawal and Surendra Prasad, “Broadband DOA Estimation Using “Spatial-Only” Modeling of Array Data,” *IEEE Transactions on Signal Processing*, Vol. 48, No. 3, pp. 663-670, March 2000.

[76] Alex B. Gershman and Moeness G. Amin, “Coherent Wideband DOA Estimation of Multiple FM Signals Using Spatial Time-Frequency Distributions,” *Proceedings of the 2000 IEEE International Conference on Acoustics, Speech and Signal Processing*, June 2000.

[77] Aigang Feng, Zheng Zhao and Qinye Yin, “Wideband Direction-of-Arrival Estimation Using Fast Chirplet-Based Adaptive Signal Decomposition Algorithm,” *Proceedings of the 2001 IEEE Vehicular Technology Conference*, October 2001.

[78] Li Cong and Weihua Zhuang, “Hybrid TDOA/AOA Mobile User Location for Wideband CDMA Cellular Systems,” *IEEE Transactions on Wireless Communications*, Vol. 1, No. 3, pp. 439-447, July 2002.

[79] Giacinto Gelli and Luciano Izzo, “Cyclostationarity-Based Coherent Methods for Wideband-Signal Source Location,” *IEEE Transactions on Signal Processing*, Vol. 51, No. 10, pp. 2471-2482, October 2003.

[80] Jean-Pierre Delmas and Yann Meurisse, “Robustness of Narrowband DOA Algorithms with Respect to Signal Bandwidth,” *Signal Processing*, No. 83, Elsevier, pp. 493-510, 2003.

[81] Malcolm Hawkes and Arye Nehorai, “Wideband Source Localization Using a Distributed Acoustic Vector-Sensor Array,” *IEEE Transactions on Signal Processing*, Vol. 51, No. 6, pp. 1479-1491, June 2003.

[82] Huawei Chen and Junwei Zhao, “Coherent Signal-Subspace Processing of Acoustic Vector Sensor Array for DOA Estimation of Wideband Sources,” *Signal Processing* 85, Elsevier 2005.

[83] Yeo-Sun Yoon, Lance Kaplan and James McClellan, “Direction-of-Arrival Estimation of Wideband Sources Using Arbitrary Shaped Multidimensional Arrays,” *Proceedings of the International Conference on Acoustics, Speech and Signal Processing*, 2004.

[84] Huiqin Yan and H. Howard Fan, “A Wideband Kalman DOA Tracking Algorithm,” Fourth IEEE Workshop on Sensor Array and Multichannel Processing, Waltham, MA, July 2006.

[85] Amr El-Keyi, Thia Kirubarajan and Alex Gershman, “Adaptive Wideband Beamforming with Robustness Against Presteering Errors,” Fourth IEEE Workshop on Sensor Array and Multichannel Processing, Waltham, MA, July 2006.

[86] F. Sellone, “Robust Auto-Focusing Wideband DOA Estimation,” *Signal Processing*, Vol. 86, Elsevier, pp. 17-37, 2006.

[87] R. O. Schmidt, “A Signal Subspace Approach to Multiple Emitter Location and Spectral Estimation,” Ph.D. dissertation, Department of Electrical Engineering, Stanford University, Palo Alto, CA, 1982.

[88] *Ibid*., pp. 54-61.

[89] *Ibid*., pp. 62-64.

[90] *Ibid*., p. 51.

[91] *Ibid*., pp. 66-69.

[92] A. Barabell, “Improving the Resolution Performance of Eigenstructure-Based Direction-Finding Algorithms,” *Proceedings of the IEEE International Conference on Acoustics, Speech, and Signal Processing*, pp. 336-339, 1983.

[93] B. Rao and K. Hari, “Performance Analysis of Root-Music,” *IEEE Transactions on Acoustics, Speech, and Signal Processing*, Vol. 37, No. 12, pp. 1939-1949, December 1989.

[94] K. Buckley, “Spatial/Spectral Filtering with Linearly Constrained Minimum Variance Beamformers,” *IEEE Transactions Acoustics, Speech, and Signal Processing*, Vol. ASSP-35, No. 3, March 1987.

[95] Darren B. Ward, Rodney A. Kennedy and Robert C. Williamson, “Theory and Design of Broadband Sensor Arrays with Frequency Invariant Far-Field Beam Patterns,” *Journal of the Acoustical Society of America*,” Vol. 97, No. 2, February 1995.

[96] H. Messer, “The Potential Performance Gain in Using Spectral Information in Passive Detection/Localization of Wideband Sources,” *IEEE Transactions on Signal Processing*, Vol. 43, pp. 2964-2974, December 1995.

[97] Fei Ji and Sam Kwong, “Frequency and 2D Angle Estimation Based on a Sparse Uniform Array of Electromagnetic Vector Sensors,” *EURASIP Journal on Applied Signal Processing*, Vol. 2006, Article ID 80720, 2006.

[98] M. Wax, T. J. Shan and T. Kailath, “Spatio-temporal spectral analysis by Eigenstructure methods,” *IEEE Transactions on Acoustics, Speech and Signal Processing*, Vol. 32, No. 4, pp. 817–827, August 1984.

[99] S. Sivanand, J. Yang, and M. Kaveh, “Focusing Filters for Wide-Band Direction Finding,” *IEEE Transactions on Signal Processing*, Vol. 39, No. 2, pp. 437-445, February 1991.

[100] R. Mucci, “A Comparison of Efficient Beamforming Algorithms,” *IEEE Transactions on Acoustics, Speech and Signal Processing*, Vol. ASSP-32, No. 3, pp. 548-558, 1984.

[101] X. Zheng, N. Kim and A. Siahmakoun, “High-speed programmable true-time-delay optical beamformer based on recirculating loop,” *Proceedings of the Optical*

Fiber Communication Conference, Optical Society of America, Los Angeles, CA, February 2004.

[102] J. Roderick, H. Krishnaswamy, K. Newton and H. Hashemi, "A 4-bit Ultra-Wideband Beamformer with 4ps True Time Delay Resolution," *Proceedings IEEE Custom Integrated Circuit Conference*, 2005.

[103] D. Hunter, M. Parker and J. Dexter, "Demonstration of a Continuously Variable True-Time Delay Beamformer Using a Multichannel Chirped Fiber Grating," *IEEE Transactions On Microwave Theory and Techniques*, Vol. 54, No. 2, pp. 861-867, February 2006.

[104] M. Longbrake, "True Time-Delay Beamsteering for Radar," Air Force Research Laboratory Sensors Directorate, Unpublished manuscript, 2013

[105] M. Skolnik, *Introduction to Radar Systems, 3rd Ed*., New York, NY, McGraw-Hill, 2001.

[106] A. Zverev, *Handbook of Filter Synthesis*, Wiley, 1967.

[107] S. Palit, S. Granieri, A. Siahmakoun and B. Black, "Binary and Ternary Architectures for a Two-Channel 5-Bit Optical Receive Beamformer," IEEE International Topical Meeting on Microwave Photonics, November 2002.

[108] Y. Chen, K. Wu, F. Zhao, G. Kim and R. Chen, "Reconfigurable True-Time Delay for Wideband Phased-Array Antennas," *Proceedings of SPIE*, Vol. 5363, Emerging Optoelectronic Applications, 2004.

[109] H. Lee, H. Jeon, J. Jung, "Optical True Time-Delay Beam-forming for Phased Array Antenna Using a Dispersion Compensating Fiber and a Multi-wavelength Laser," 4th Annual Caneus Fly by Wireless Workshop, June 2011.

[110] N. Wilkins, "Optimization of Multi-DSP Process Configurations Using a Genetic Algorithm," *Proceedings of the International Conference On Signal Processing Applications and Technology*, 1999.

[111] M. Jamali, A. Affo, N. Wilkins, P. Mumford and K. Hahn, "DSP Based Implementation of Direction of Arrival for Wideband Sources," *Proceedings of the IEEE Radar Conference*, 2007.

[112] N. Asaithambi, *Numerical Analysis*, Saunders College Publishing, 1995.

[113] W. Vetterling and B. Flannery, *Numerical Recipes in C++*, Cambridge University Press, 2002.

[114] Atmel Corporation, *Diopsis 740 Dual Core user manual*, Atmel.

[115] M. Jamali, J. Downey, J. Tipping, N. Wilkins and C. Rehm, "Development of a FPGA-based High Speed FFT Processor for Wideband Direction of Arrival Applications," *Proceedings of the IEEE International Radar Conference*, 2009.

[116] J. Sun, D. Goshi and T. Itoh, "Optimization and Modeling of Sparse Conformal Retrodirective Array," *IEEE Transactions On Antennas and Propagation*, Vol. 58, No. 3, pp. 977-981, March 2010.

[117] K. Papadopoulos, C. Papagianni, P. Gkonis, I. Venieris and D. Kaklamani, "Particle swarm optimization of antenna arrays with efficiency constraints," *Progress in Electromagnetics Research*, Vol. 17, pp. 237-251, 2011.

[118] L3 Communications, Randtron Antenna Systems Website, Interferometer Antennas, Available at http://www2.l-3com.com/randtron/infrmtech.htm, 2012.

[119] M. Klein and T. Furtak, *Optics*, 2nd Edition, Wiley, 1986.

[120] W. F. Gabiel, "Spectral Analysis and Adaptive Array Superresolution Techniques," *Proceedings of the IEEE*, Vol. 68, No. 6, p. 661, June 1980.

[121] W. Stutzman and G. Thiele, *Antenna Theory and Design*, pp. 537-542, Wiley, 1981.

[122] A. Poularikas and S. Seely, *Signals and Systems*, 2nd Edition, p. 230, PWS-KENT Publishing Company, 1991.

[123] M. Agrawal and S. Prasad, "DOA Estimation of Wideband Sources Using a Harmonic Source Model and Uniform Linear Array," IEEE Transactions on Signal Processing, Vol. 47, No. 3, pp. 619-629, March 1999.

[124] Y. Grenier, "Wideband Source Location in the Time Domain," pp. 838-842, Maple Press, 1988.

[125] R. O. Schmidt, "A Signal Subspace Approach to Multiple Emitter Location and Spectral Estimation," Ph.D. dissertation, Stanford University, Palo Alto, CA, pp. 27-28, 1982.

[126] R. O. Schmidt, “Multiple Emitter Location and Signal Parameter Estimation,” *IEEE Transactions on Antennas and Propagation*, Vol. 34, No. 3, March 1986.

[127] A. Shaw, M. Jamali and N. Wilkins, “Toward Bandwidth Invariance in the Non-Cooperative Receiver,” *Proceedings of the IEEE Sensor Array and Multi-Channel Workshop*, SAM-06, Waltham, MA, July 2006.

[128] A. Shaw and N. Wilkins, “Frequency Invariant Electro-Magnetic Source Location Using True Time Delay Beam Space Processing,” *Proceedings of the IEEE International Symposium on Phased Array Systems and Technology*, Array-2010, Boston, MA, October 2010.

[129] T. Kolda, R. Lewis and V. Torczon, “A generating set direct search augmented Lagrangian algorithm for optimization with a combination of general and linear constraints,” *Technical Report SAND2006-5315*, Sandia National Laboratories, August 2006.

[130] L. Ingber, “Adaptive simulated annealing (ASA): Lessons learned,” *Control and Cybernetics*, 1995.

[131] D. Whitley, “A genetic algorithm tutorial,” *Statistics and Computing*, Vol. 4, pp. 65-85, 1994.

[132] L. Trefethen and D. Bau, *Numerical Linear Algebra*, SIAM, 1997.

[133] B. Pollachek, “Guardrail turns 40, modernization keeps it going,” Press release by US Army PIO IEW&S Public Affairs, July 2011.

[134] D. Tulchinsky and P. Matthews, “Ultrawide-Band Fiber-Optic Control of a Millimeter-Wave Transmit Beamformer,” *IEEE Transactions on Microwave Theory Technology*, Vol. 49, p. 1248, 2001.

[135] P. Baldonero, M. Bartocci, A. Manna, A. Pantano and F. Trotta, “Design, Simulation and Measure of a Broadband Cavity Backed Combined Spiral Antenna,” *Proceedings of the International Symposium on Microwave and Optical Technology*, 2007.

[136] P. Baldonero, M. Bartocci, A. Manna, A. Pantano and F. Trotta, “Optimization of a UWB Vivaldi Antenna Array and Measurements with a Near Fields STARLAB System and Farfield Anechoic Chamber,” *Proceedings of the International Symposium on Microwave and Optical Technology*, 2007.

[137] R. Ackerman, “Air Force Researchers Set Stratospheric Goals,” *Signal Online*, *Armed Forces Communications and Electronics Association (AFCEA) Journal*, February 2001.

[138] C. Nilsen and I. Hafizovic, “Beamspace Adaptive Beamforming for Ultrasound Imaging,” *IEEE Transactions on Ultrasonics, Ferroelectrics, and Frequency Control*, Vol. 56, No. 10, pp. 2187-2197, October 2009.

[139] W. Tidd, Y. Huang, and Y. Zhao, “Sequential Beamspace Beamforming,” *Proceedings of 2012 IEEE Aerospace Conference*, March 2012.